INVESTIGATION OF ELECTRONIC AND THERMAL TRANSPORT AND OPTO-ELECTRONIC PROPERTIES OF SINGLE GERMANIUM NANOWIRES

THESIS SUBMITTED FOR THE DEGREE OF

DOCTOR OF PHILOSOPHY (SCIENCE)

IN

PHYSICS (EXPERIMENTAL)

BY

SHAILI SETT

DEPARTMENT OF PHYSICS

UNIVERSITY OF CALCUTTA

2019

ACKNOWLEDGEMENTS

I would like to express my gratitude to my supervisor Prof. A. K. Raychaudhuri for the guidance, help, support and inspiration regarding my work as well as life. He has taught me how to question, think and pushed me to put in the best effort in the toughest of situations. Thank you, Sir.

I would like to thank Prof. Barnali Ghosh for her help and support whenever it was warranted.

I would like to acknowledge Dr. K. Das for introducing me to the field of nanowires which subsequently led to my thesis problem. I am thankful to Prof. K. S. Narayan and Dr. G. V. Pavan Kumar, with whom collaborative work was a great boost to my Ph. D research. I am extremely thankful to my collaborator Dr. Achintya Singha, whose lab I had almost turned into mine! He gave me lot of freedom to work and has been of constant help and also a source of knowledge. I have had a lot of collaborations in our group, the *New Nano Lab* itself with seniors and juniors and I would like to thank Dr. Ankita Ghatak, Ravindra Singh Bisht, Subhamita Sengupta and Vishal Aggarwal for their efforts and time in helping me with my research work. Of course I am thankful to everyone in my lab, both seniors and juniors. I acknowledge the support and expertise of all members of the Technical Research Cell, S. N. Bose Centre.

Without whom the course of almost six years would have been a void; my friends – Ransell, Ravi, Poonam, Ritam, Tukun, Dhani, Ankan and Neeraj, they have been a power-source of fun, frolic, support and love. Thanks guys!

It goes without saying, that I acknowledge the support from my mother and father for being there in this journey.

For everyone who has known me the last six years, thanks for teaching me patience and the ability to fight back and face the odds. I acknowledge all of you.

Shaili

SYNOPSIS

Semiconductor nanowires (NWs) constitute a unique class of materials in the nanoscale in which novel phenomenon can be explored. Since the NW dimensions may be tuned to the order of certain physical length scales, its consequence/impact can be observed through associated physical quantities. The thesis work is focused on overcoming the known challenges of working with single Ge NW and also exploring and quantifying the novel phenomena that were observed. We have investigated the electronic, thermal and opto-electronic properties of single Ge NWs and established the physics behind the experimental findings. These have led to exceptional and interesting results such as obtaining a Responsivity in excess of 10^7A/W in a single Germanium NW (diameter ~30nm), self-powered photo-detection, observation of weak localization at low temperature in a doped Ge NW and lowering of thermal conductivity (by more than one order as compared to bulk) in a Ge NW.

During the thesis work we developed a vapor transport method to grow Ge NWs using vapor-liquid-solid method with Au nanoparticle catalyst. The NWs were extensively analyzed structurally and chemically and were found to be mostly oxygen free, highly oriented and single crystalline. We have analyzed the contact nature at the metal/semiconductor (M/S) interface through evaluation of the ideality factor, barrier height and specific contact resistance with temperature. We find that in contrast to the effect of Fermi level pinning in bulk Ge (~0.5eV) which leads to large contact resistance at the M/S interface, in NWs there is indeed suppression of Fermi level pinning.

The ultra-high broadband photoresponse in Ge NWs has been investigated for the first time in this thesis. The physics behind this response in excess of 10^7A/W is attributed to a number of factors, of which, the one unique to Ge is the surface oxide layer. There are trap states (in the sub-stoichiometric Ge oxide layer) that act as recombination centers and on tuning its density we have been able to achieve super-linear photoresponse. Another interesting phenomenon is the effect of a confining potential that develops in the radial direction due to presence of surface states that induce surface band bending. This helps in spatially separating the photogenerated electron-hole pair. The models have been quantified through Poisson-Schrodinger solver in COMSOL platform.

We observed self-powered photodetection in Ge NWs and establish that an axial field exists due to unequal Schottky barrier height and a short channel length (~1-2μm, comparable to the sum of depletion widths at the M/S contact), which assists photodetection. The existence of the axial field due to asymmetric contacts was validated by simulations.

We have developed a rapid and non-contact method to determine the thermal conductivity of a single cantilevered nanowire through a novel application of Raman Spectroscopy, in which the Raman lines act as a local temperature probe and the focused laser acts as a local heat source. Ge NWs show a low thermal conductivity (2 – 4 W/m.K) for diameters between 50-110 nm. This is the first measurement of thermal conductivity in the technological important region of 300K – 600K. The thermal conductivity above Debye temperature is governed by two important scattering mechanisms: boundary scattering and Umklapp scattering. We have suggested a way to estimate approximately the thermal conductivity of Ge and Si NWs using the above observations that can be predicted within a ~ 20% uncertainty.

We have investigated the approach to metal-insulator transition in doped Ge NWs that lie in the metallic regime and establish a size limit for 3d electronic conduction and show the applicability of the scaling laws for a doped semiconductor.

LIST OF PUBLICATIONS

1. S. Sett, K. Das and A. K. Raychaudhuri, "Investigation of factors affecting electrical contacts on single Germanium Nanowire" *J. Appl. Phys.,* 2017, **121**, 124503.

2. S. Sett, K. Das and A. K. Raychaudhuri, "Weak localization and the approach to metal–insulator transition in single crystalline germanium nanowires", *J. Phys.: Condens. Matter,* 2017, **29**, 115301.

3. S. Sett, A. Ghatak, D. Sharma, G. V. Pavan Kumar and A. K. Raychaudhuri, "Broad Band Single Germanium Nanowire Photodetectors with Surface Oxide-Controlled High Optical Gain" *J. Phys. Chem. C,* 2018, **122**, 8564.

4. S. Sett, S. Sengupta, N. Ganesh, K. S. Narayan and A. K. Raychaudhuri, "Self-powered single semiconductor nanowire photodetector", *Nanotechnology*, 2018, **29**, 445202.

5. S. Sengupta, A. Ghatak, S. Sett, M. Sreemany, S. Bysakh, B. Ghosh and A. K. Raychaudhuri "Restoration of perovskite phase in the top layer of thin BTO film by plasma treatment and annealing", *J. Phys. D: Appl. Phys.* 2018, **51,** 085304.

6. S. Leela, G. V. Rohini, K. Saranya, S. Bhattacharya, N. Ahmed, S. Sett and B. Ghosh, "Tunable growth of semiconductor nanostructures by Plasma Enhanced Chemical Vapor Deposition-Synthesis, morphological and Raman studies", *Superlattices and Microstructures*, 2018, **122**, 510-515.

7. S. Sett, M. Banik, R. Mukherjee, and A. K. Raychaudhuri, "Fabrication of large array of uniform metal nanostructures by use of soft sphere lithography and plasma etching", *AIP Conference Proceedings*, 2017, **1832**, 050066.

8. S. Sett, R. S. Bisht, A. Ghatak and A. K. Raychaudhuri, "Surface oxide modification enables super-linear photoresponse in a single Germanium nanowire photodetector". (*Submitted*)

9. S. Sett, V.K. Aggarwal, A. Singha and A. K. Raychaudhuri, "Temperature dependent Thermal conductivity of a single Germanium nanowire measured by non-contact Opto-thermal Spectroscopy". (*Submitted*)

10. S. Sett, V. K. Aggarwal, A. Singha and A. K. Raychaudhuri, "Photoresponse of SOI based horizontal array of Silicon microstructure" *(Submitted).*

11. S. Sett, V. K. Aggarwal, A. Singha and A. K. Raychaudhuri, "Temperature dependent Raman Spectroscopy and Anharmonicity in Ge nanowires." (*manuscript under preparation*)

12. S. Sett and A. K Raychaudhuri, "Quantitative analysis of ultra-high opto-electronic response in a single semiconductor nanowire", (*manuscript under preparation*).

Patent

Title: "A technique to regenerate ferroelectric phase by surface and subsurface engineering of BaTiO3 thin films"
Application No.201731036353 A
Publication Date: 10/11/2017
Names of Inventors: Ankita Ghatak, Subhamita Sengupta, Shaili Sett, A.K.Raychaudhuri and Barnali Ghosh.

Contents

CHAPTER I

INTRODUCTION

The sole purpose of this work is to add knowledge to the field of material sciences and basic condensed matter physics in low dimensions along with the hope of technological applications and betterment of society based on the findings.

A. MOTIVATION

The transport properties of a nanowire (NW) may show quantum effects if the characteristic length scale associated with that particular physical property is of the same scale as the dimensions of the nanowire. NWs provide a platform to study basic physics in low dimensions as we can decouple length scales in either axial or radial directions. A few important length scales associated with the electronic, optoelectronic and thermal transport properties that we encounter in this thesis are:

- Thouless length (L_{th}): The distance an electron travels while maintaining phase coherence.[1] It is the distance an electron diffuses in between successive inelastic collisions; $L_{th} = \sqrt{D\tau_{in}}$, where τ_{in} is the inelastic scattering time and D is the diffusion coefficient. It is defined as, $D = v_F^2\tau/d$ where d is the dimension of the system and v_F is the Fermi velocity.

- Depletion width (W): The length of the space-charge region formed at a metal-semiconductor (MS) junction when they are in contact.[2] It is defined as: $W = \sqrt{2\varepsilon V_b/eN^*}$ where, N^* is the doping concentration of the NW, ε is the dielectric constant of semiconductor and V_b is the built-in voltage.

- Photocarrier diffusion length (L_n): As the name suggests, it is the path length travelled by a photogenerated carrier by the process of diffusion within its lifetime (τ).[3] It is given by, $L_n = \sqrt{D\tau}$.

- Phonon mean free path (λ): It is the path length traveled by a phonon before it gets scattered. In other words, it is the travelling distance between two consecutive phonon scattering events.[3]

A NW is expected to have physical properties that are fundamentally different from its bulk if their physical dimension is comparable to these characteristic length scales. We indicate a few cases where such effects are perceptible.

- A strong phonon boundary scattering in Si NWs[4] of diameter < 100nm reduces its thermal conductivity to twenty times its bulk value. The phonon mean free path plays a crucial role as it is highly reduced due to diffuse scattering from the surface of the NW.

- Semiconductor NWs[5-9] as optical detectors have Responsivity at least three orders of magnitude more than the bulk due to improved charge collection as the carrier diffusion length is comparable to the device length. In fact, there may be lateral confinement of electrons due to band bending at the surface as a result of a large population of surface states. This radial electric field helps in separation of photogenerated electron-hole pairs.[9]

- Phase coherence is observed in nanowires at low temperatures when electron de-phasing mechanisms such as electron-phonon scattering dies out.[10] The inelastic scattering time increases and the Thouless length become comparable to the NW dimensions. This leads to quantum interference of electrons, and hence localization.

Barring the novel phenomena that have been observed at low dimensions, semiconductor NWs provide other unique properties such as ability to integrate in electronic devices, sub-wavelength optical phenomenon and interfacing with biological systems.[11] It also provides high surface to volume ratio for exploring various sensing applications. Semiconductor NWs have the ability to interface well with living tissues for which it is currently being investigated for single cell endoscopy.[12] It is also being used for study of neuron physiology[12]. Nanowires are used in piezo-generation, mechanical resonators, Li-ion battery applications, artificial photosynthesis, in solar cells and in a variety of other multi-disciplinary fields.[11,12] Not only does the field of nanomaterials have rich basic physics, it is also a well-studied material for applications.

B. OPTO-ELECTRONIC PROPERTIES OF NANOWIRES

The basic concept of photoconduction in a semiconductor involves these main parts:[15]

- optical absorption leading to creation of electron-hole (e-h) pair
- separation of e-h pair and capture of free carries leading to trapping or recombination
- carrier transport to electrodes.

In this entire process, three components play a defining role in the carrier dynamics:

- lattice imperfections or defects
- surface states (which are of importance in a NW since it has a large aspect ratio)
- nature of contacts.

Imperfections in the lattice play a crucial role since they can *capture* a free carrier. After a certain time (carrier lifetime defined as $\tau_{life\ time}$) it may recombine with a carrier of opposite charge. Such a site is known as a recombination centre. Or else, the captured carrier may get re-excited thermally to another energy level before recombination occurs. In such a situation, the imperfection acts as a trap. The behaviour of photoconduction on the photo-excitation intensity is governed by these trap states.

A freshly cleaved crystal has "dangling bonds" where a hybrid orbital points to vacuum. Qualitatively, there is surface reconstruction, i.e., the surface buckles and the sp³ hybridized orbitals go back to the single atom s and p components which lie in the band gap.[16] Thus, **surface states** in semiconductors lie in the band gap region due to orbital re-hybridization. Especially in a doped semiconductor, if the surface states do not lie exactly at the middle of the band gap, there will be a surface potential created which acts as a positive feedback to the energetic position of the surface state.[16] This *surface barrier* plays a significant role in carrier trapping in semiconductor NWs.

The **contact** plays a role of maintaining charge neutrality in e photodetector. The contacts replenish charge carriers when photogenerated carriers are drawn out by the opposite contact through an applied bias.[15] In a semiconductor/metal junction, the contact plays a major role since it governs the charge injection process. In case of a NW, if there is a Schottky barrier (SB) at the MS junction, under illumination it gives rise to a Schottky photocurrent.[17] When carriers diffuse into the contact region upon illumination, the barrier height gets lowered. This current generated due to the SB forms a substantial part of the device photocurrent.

Recently it has been established that photodetectors made from single semiconductor NWs[5-8] reach very high Responsivity ($\mathcal{R}$), (defined as the ratio of photocurrent (I_{Ph}) to incident power on the NW (P)) $\geq 10^3$ while, most commercially available detectors made from bulk semiconductors, show $\mathcal{R} < 1$ A/W.[13] Semiconductor photodetectors have a variety of photonic applications where small radiation powers need be detected, due to their ultrahigh Responsivity. The applications of photodetectors widen if the detector can work in a broad spectral range that spans UV-Visible and Near Infrared (NIR).[14] It is envisaged that if single nanowire broad band detectors can be made they will pave the way for integrating such wires into high performance detector arrays and may even act as detectors for on-chip optical communication systems. The current scenario of performance of photodetectors made from semiconductor NWs has been summed up in Table 1.

Table 1. Single nanowire photodetector parameters

Semiconductor	Diameter (nm)	Wavelength range (nm)	Working Bias (V)	Peak Responsivity (A/W)	Year	Ref #
Si NW	80	300-1100	0.1	2.6×10^4	2014	5
ZnO NW	150-300	390	5	6.3×10^7	2007	6
InAs NW	30-75	300-1100	10	4.4×10^3	2013	7
GaN NW	180	380	5	7.7×10^1	2017	8
GaAs NW	90-160	522	4	8.4×10^3	2009	10
Vertical Ge NW	20	1550	1	2.3×10^1	2017	38
Ge NW	50	532	2	2×10^2	2018	37
Al-Ge-Al NW	30	532	0.1	10^6	2018	39
Ge-GeO$_2$ core shell	100	350-900	2	10^4	2018	40
Si NW	80	300-1100	0	10^4	2014	5
Ge-GeO$_2$ core shell	100	350-900	0	10^4	2018	40

The **origin** of this high response in single semiconductor NWs can be narrowed down to a number of factors:

- Enhancement of electric field in the NW for diameters < 100nm, if there is a cladding (oxide) layer.[2]
- Device dimensions (~few μm) comparable to the recombination length.[6]
- Lowering of the Schottky barrier at the metal/NW interface on illumination.[17]
- Effect of radial field caused by a depletion layer at the surface that separates the photogenerated carriers.[6,9]

The **radial field** is caused by surface Fermi level pinning (FLP) that results in *surface band bending* (SBB) in semiconductor NWs. The SBB in these NWs has been probed through photoelectron spectroscopy in Ge,[18] ZnO[19] and GaN[20] NWs. It is interesting to note that in GaN NWs, it has been deduced through photoconductivity measurements that NWs of diameter $\leq$ 80nm[21] are fully depleted. An estimate of the depletion layer width in these NWs and the Schottky barrier height at the surface that

poses a barrier for electrons to migrate to the surface is essential. Photoconductivity in semiconductor NWs is regulated by the depletion region width, photo-excited carrier density and presence of trap states. Thus an important parameter that governs/predicts the performance of a nanowire photodetector is the quality of the natural oxide layer surrounding the NW surface, which controls the surface trap density and predicts the FLP. It is important to point out that the carrier relaxation in semiconductor NWs is dominated through surface recombination,[22] which has been investigated through ultrafast carrier dynamics using femto-second pump-probe THz spectroscopy. The opto-electronic properties of a semiconductor NW may be tuned and controlled through surface modifications. In the context of Si NWs, surface passivation of a NW by growing a shell of a-Si enhanced the carrier lifetime two orders and also the surface recombination velocity S_v by two orders to 4×10^3cm/s.[23]

C. THERMOELECTRIC PROPERTIES OF NANOWIRES

Currently there has been revival in research for development of thermoelectric devices focusing on increasing the efficiencies with nanostructured materials.[24,25] Thermoelectric devices has application in heat waste management and clean energy harvesting, which currently has high cost and low efficiency. Nanostructured materials have the advantage that electrical and thermal property both can be tuned as desired. The aim of the research is to improve and obtain a viable figure of merit,

$$ZT = S^2\sigma/\kappa,$$

where S is the Seebeck coefficient, σ is electrical conductivity and κ is the thermal conductivity. The Seebeck coefficient can be increased if we go to quantum level where the density of states is modified but it is not a cost effective or a viable solution to the current problem. To find a good thermoelectric material is a challenging process since usually by increasing the electrical conductivity, the thermal conductivity also increases (Wiedemann-Franz law).[3] In this regard, semiconductor NWs are an effective class of materials to investigate. Electrical conductivity in these NWs is usually unchanged with respect to bulk and can be controlled through well-established doping processes, while thermal conductivity is naturally low in this geometry as a result of diffuse scattering of phonons at the NW boundary and due to surface roughness.[25,26] Hence, to obtain an appreciable *ZT*, semiconductor NWs which have a much lower κ is a natural choice. Other nanostructured materials like thin film superlattices, Skutterides, Clatharates, nanoparticles etc have an appreciable *ZT* (maximum ZT ~2.4 in p-type Bi_2Te_3/Sb_2Te_3 superlattices) but they suffer from the roadblock of complex chemistry, heavy compounds and toxic lead compounds.

Hence, NWs are a suitable potential option for thermo power generation. For example a 50 nm diameter of Si NW has *ZT* ~0.6.[24]

In a NW, the factor that most effectively can be tuned is the thermal conductivity. The lattice thermal conductivity is defined as,[3]

$$\kappa = \frac{1}{3}Cvl,$$

where *C* is the specific heat capacity per unit volume, *v* is the group velocity, *l* is the mean free path of a phonon given by, $l = v\tau$, where τ is the relaxation time of a phonon scattering process. It is important to understand the various relaxation processes in a material to get an idea of the temperature dependence of thermal conductivity.[27] The resistive scattering mechanisms include Umklapp scattering, impurity scattering and temperature independent boundary scattering. The 3-phonon normal scattering tends to bring back the phonon distribution to equilibrium while the resistive mechanisms displace the phonon distribution function. These relaxation times determine which process dominates over the rest and the thermal conductivity follows that trend. The phonon lifetime due to scattering by boundary forms a significant part of the total scattering time, which is given by,[27]

$$\tau_B^{-1} = \frac{v}{D}\left(\frac{1}{F}\right),$$

where *v* is the group velocity, *D* is the diameter of NW and *F* is the specularity parameter, that determines the extent of reflection from the NW boundary that is diffusive in nature.

A study of phonon dispersion and scattering mechanisms is essential to study the thermal properties of a semiconductor since in the presence of a temperature gradient the dominant heat transport is through phonons. The phonon dispersion curve has optical and acoustic branches, depending on the phase of vibration of the respective atoms. Heat is generally transported through the acoustic modes as they have a larger group velocity.[27] Optical phonons decay into acoustic phonons (as a result of anharmonicity in the lattice potential, which is more pronounced in NWs) and this interaction disturbs the phonon distribution function, which in turn alters the heat conduction, thus affecting the thermal conductivity.[26-28]

D. WHAT IS THE IMPORTANCE OF GERMANIUM NANOWIRES?

It is an elemental semiconductor, lying in Group IV of the periodic table just below Silicon with a cubic diamond structure. Ge got its fair share of fame when the first transistor was built from it in Bell Labs in

1948 that opened the gateway for solid-state electronics. Ge overrides Si in most physical properties which are listed in Table 2. Its availability and ease of synthesis makes it more applicable as compared to other compound semiconductors like GaAs, InAs and InGaAs, where stoichiometry control is essential. Crystalline bulk Ge has been studied extensively in the VIS-NIR region (upto wavelength 1800nm).[30,31] Ge photodetectors based on single crystalline Ge are available commercially. They work in the VIS-NIR region and have peak Responsivity at 800 nm with $\mathcal{R}$ ~0.25 A/W.[13] Ge is also an important infrared optical material, for NIR windows etc. Ge is recognized as a secondary standard thermometer and is used for low temperature sensor applications commercially.

Advances in integrated circuit technology in the past five decades demand electronic devices with higher device density, faster switching rate and lower power consumption. It has been proposed that alternative materials like NWs can be active materials for FETs as well as interconnects, which are not limited by Moore's law[32]. Not only are NWs a topic of considerable current interest in nano-electronics, it is also a problem of basic physics, in which some of the fundamental issues of electronic conduction in semiconductors can be addressed.[32,33] Semiconductor NWs can be prepared high-yield as required for large scale integrated circuit systems. Currently, there are well-controlled NW growth processes available to control dimension, morphology and chemical composition. It offers the potential of parallel production of large number of devices with same physical and chemical properties, since it is possible to have a large throughput.[32]

Considering its superior properties (see Table 2) and also unpredicted phenomenon observed in quasi-one dimensional material, there is a recent surge in study of electrical and opto-electronic properties of Ge NWs. There has been a revival in the study of electronic properties of Ge NWs in recent times due to device scaling and high performance electronics.[34,35] This is because intrinsically, Ge has better electronic properties as compared to those of Si. Ge also offers advantages over Si due to lower processing temperatures as well as larger Bohr radius resulting in stronger confinement. Ge has potential application as an active element in field effect transistors,[36] optoelectronic devices[37-40] and also as Lithium Ion battery anodes.[41]These achievements have promoted more research into development of synthesis and applications of Ge NWs.

We will survey the current scenario of growth, electrical, opto-electronic and thermal property investigation of Ge NWs, while putting it in context to other semiconductor NWs. Our main motivation lies in overcoming the known challenges related to working with Ge and its revival in the field of electronics and opto-electronics in the nanoscale, novelty of performing the experiments in order to surpass the difficulties in single nanowire measurements and to provide a solution to the existing issues.

Table 2. Important properties of Ge and Si.

Property	Germanium	Silicon	Related area of application/interest
Mobility ($cm^2V^{-1}s^{-1}$)	3900	1400	electronics
Effective Mass (m_e)	0.082	0.19	electronics
Carrier concentration (cm^{-3})	2×10^{13}	1×10^{10}	electronics
Thermal conductivity (W/m.K)	58	130	thermo-electrics
Band Gap (eV)	0.66	1.12	opto-electronics
Bohr exciton radius (nm)	24.3	4.9	quantum property

E. ORGANIZATION OF THE THESIS AND MAIN ISSUES INVESTIGATED

1. Growth and characterization

Semiconductor nanowires with different compositions can be synthesized using either direct vapor transport or through solution process. The main process that leads to formation of a NW is anisotropic growth of a crystal. This is usually achieved by using a seed metal catalyst. A lot of research has gone into growth of NWs and their growth kinetics, with Ge being no exception.[42,43] Ge NWs were first grown through a simple direct physical vapor transport mechanism utilizing the Vapor-Liquid-Solid (VLS) mechanism.[44] The first real time in-situ growth of a NW through VLS mechanism was observed in Ge NWs.[45] Further insights into the Ge-Au interface at the tip of the NW have been studied to understand the nucleation process and nanowire growth.[46] It established the nanoscale phase diagram of Ge-Au since it differs from the bulk due to capillary effect and surface tension in the nano-sized metal liquid droplet phase. There in higher Ge content available at a lower temperature in NWs.[47]

Even though VLS growth offers its many advantages like crystallinity, high yield, choice of metal nanoparticle catalyst, preferential site growth, control over diameter, length and morphology, along with doping through use of chemical vapor deposition methods, there are certain shortcomings.[43,48] The most crucial one is, the metal catalyst diffuses into the NW body at high growth temperatures causes impurity states. For example, Au forms deep level acceptor states in Si.[48]

Ge NWs have been well characterized through X-ray photoelectron spectroscopy (XPS) and electron microscopy. Ge NWs grown by VLS method are crystalline with relatively smooth surface (rms roughness ~0.3nm) and well-defined interface with the Au-Ge alloy tip.[49] It appears that the NWs have a native oxide layer that grows instantly on exposure to the atmosphere. The NWs grow a self-limiting oxide layer upto 5nm within 24 hours.[50] The chemical composition of the oxide states have been studied in great detail through the surface sensitive XPS technique, where information upto a depth of few nm is revealed. The XPS spectrum of the 3d state (27-37eV) shows Ge in the 4+ state. Prolonged exposure shows Ge^{2+} and Ge^{3+} states along with an increase in Ge^{1+} species. The oxidation states have chemical shifts of 0.8, 1.8 and 2.7 eV with respect to the Ge^0 peak (29.8eV).[18]

2. Electrical properties

(i) MS contact: Ge began to be replaced by Si inspite of its better electrical properties as Ge has the disadvantage of a chemically unstable native oxide layer. The native oxide layer of Si is a boon since SiO_2 is highly stable and forms a sharp interface. The Si–SiO_2 system possesses the technical ability of low cost and ease of integration compared to other semiconductors. It is used to process a metal-oxide-semiconductor field effect transistor (MOSFET), the basic element of integrated circuits. On the other hand Ge oxide has poor chemical stability since it is water soluble.[51] It is usually of the form of GeO_x (x≤2). In bulk Ge, there is a very high contact barrier at the MS interface[52] as a result of Fermi level pinning (FLP) which makes the barrier height more or less independent of the electrode material. There are highly bunched interface states at the MS contact which pins the Fermi level to ≈ 0.5-0.6 eV.[53] A large barrier formation leads to high specific contact resistance (ρ_C). In general in Ge, metal induced mid gap defect states are thought as the cause for large contact resistance, arising from FLP due to these interface states.[54,55]

In contrast to bulk, the issue of contact resistance and formation of barrier at the metal-semiconductor (MS) contact has not been researched in Ge NWs as extensively. Although limited in number, the reported investigations on formation of contact on Ge NW have made progress, particularly in terms of bringing out the key issues.[56-58] In fact there are clear indications from recent experiments[58] in single Ge NW configuration that there is suppression of FLP leading to a clear dependence of the barrier height and specific contact resistivity (ρ_C) on the metal work function. It has been shown that for Ag which has relatively low work function (≈ 4.26-4.29 eV), the Schottky barrier can be low even in NWs with carrier concentration in the range of $10^{17}/cm^3$ and Ohmic contact can be obtained although ρ_C remains high (>$10^{-2}\Omega.cm^2$).

9

(ii) FET: There are many detailed reports investigating certain unique characteristics observed from Ge NW FETs. It shows hole mobility of 600 cm^2/V.s[36] which is very close to the MOSFET made from bulk Ge. It is a very desirable mobility in an elemental pristine semiconductor nanowire. Interestingly, FETs made from undoped or p-doped Ge NWs, both show p-type gate characteristics. A p-type response can come from metal catalyst incorporation that has deep level acceptor states and intrinsic doping or surface effects.[36,59,60,61] Hysteresis in the transfer characteristics in a FET has been observed and it is claimed that this is due to water molecules strongly bound to slow surface states in surface oxide layer of Ge.[18]
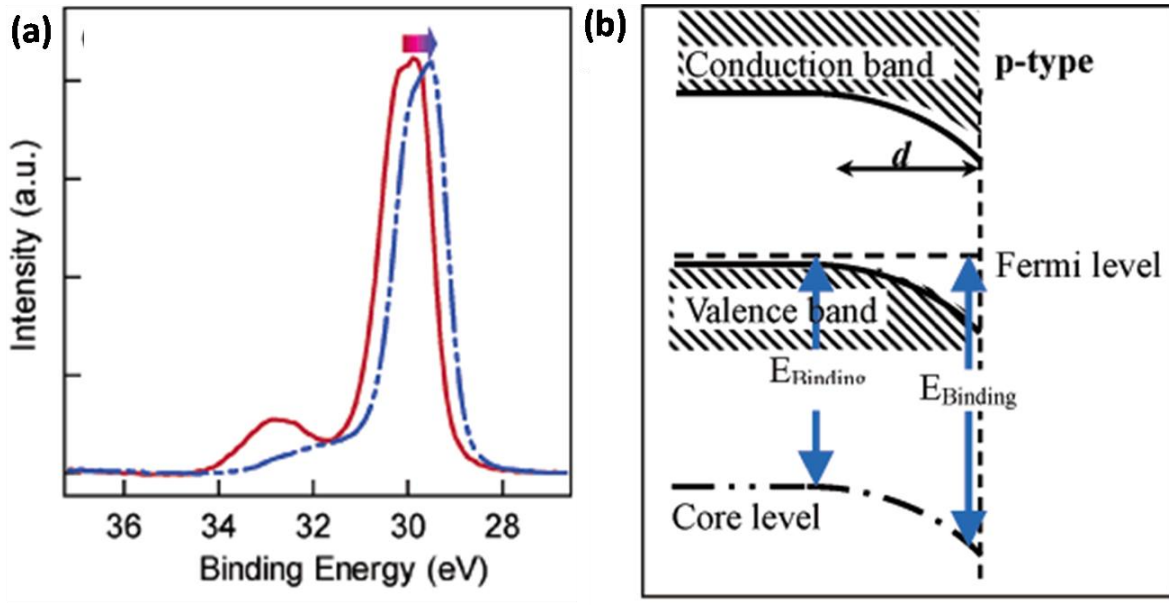

Figure 1. (a) XPS spectra of Ge NWs (3d spectra) before (red) and after (blue) annealing, showing a shift in the Binding Energy to a lower eV when the oxide is removed. (b) Schematic illustration of band bending for a Ge NW due to Fermi level pinning of surface states (in the oxide layer). BE in the core of Ge NW is lower than BE at the surface due to band bending upwards as shown by arrows. [Reprinted with permission from Ref# 18]

It has also been shown that vacuum annealing at 450^{0}C eliminates hysteresis for p-type Ge NW FETs though it re-appears when exposed to air. This cycle is reproducible as long as the air exposure is brief (few mins).[18] It is proposed that H$_2$O molecules adsorbed on the surface oxide layer are responsible for the hysteresis. To support the claim, XPS was performed on the NWs, under test conditions. The XPS measurement on an oxide stripped Ge NW shows that the binding energy (BE) shifts by ~0.1-0.3eV for the Ge^0 3d state.[18] Band bending causes a decrease in the energetic distance between the Ge 3d core-level to the Fermi level (see Figure 1). This decreases the BE of the Ge 3d level relative to bulk Ge in a NW. Oxide removal at the surface through annealing eliminates the interface states and reduces/removes band

bending. Thus, these cause shifting of the Ge peaks (see Figure 1) towards that of energetic value of bulk Ge, as seen from XPS spectra. So, with surface band bending, the energetic gap between the Ge 3d core level and Fermi level will be modified once the oxide is removed. In p-type Ge NWs, since band bending is downwards, the BE of a NW with oxide is more than the bulk/core of Ge (see Figure 1(b)). XPS clearly reveals band bending in Ge NWs due to FLP by surface states in the oxide layer inferred from the shift in binding energy (-0.3eV) of the NWs on annealing.

Surface band bending (SBB) has also been observed in other semiconductor NWs[19-21]. In ZnO SBB[19] has been probed through UV- photoelectron spectroscopy and it has been found that for a bare ZnO NW, SBB is ~1.5eV with depletion width ~ 40nm for NWs in the diameter range 150-350nm. The SBB arises due to surface defects in the NW (like oxygen deficiency), which chemisorbs atmospheric O_2 by capturing free electron from the surface thereby forming a depletion region. This leads to band bending near the surface. In GaN NWs, it has been deduced through photoconductivity measurements that the NWs of diameter $\leq$ 80nm are fully depleted due to SBB.[21]

(iii) Low temperature electrical conductivity: There is the only report so far concerning conventional electrical transport measurement at low temperature in single Ge NW recently.[62] It shows that the transport mechanism is hopping in nature. Barring this, no other conductivity measurements in doped or undoped NW have been performed. Thus, the effect of size on electronic conduction in Ge NWs has not been investigated before, which is of utmost importance. It sets a size scale to observe and investigate quantum properties in these electrically superior NWs.

3. Opto-electronic property

Previous reports of photodetectors made from single Ge NWs[37,39,40], have been investigated only around the visible range of the spectrum with wavelength < 532nm. The only report in the NIR region at 1550nm of a Ge NW has $\mathcal{R}$~23A/W.[38] The highest Responsivity reported in Ge NW (at 532nm) is around 2×10^2 A/W at 2V bias.[37] which discusses the presence of "slow states" associated with the Ge oxide surface and "fast states" at the interface between the Ge/GeO_x.

An investigation of absorbance of single Ge NW (using photocurrent as a detection tool) showed that the photo-absorption in Ge NW depends on its diameter and differs qualitatively from bulk[63] as it shows a peak around 600-800nm (depending on the diameter) and drops for wavelength > 1000nm. The change in spectral dependence was related to leaky resonance mode in NWs with lengths comparable to light wavelengths. Very recently there has been a report on an axial metal−semiconductor−metal (Al−Ge−Al)[39] heterostructure, which shows Responsivity ~10^6A/W, similar to what we have also achieved in this thesis. They describe a charge trapping model with surface states at the GeO_x layer. The photogenerated

electrons are trapped in the oxide layer. Hence it effectively modulates the conductivity. This *photo-gating* effect driven by the trap states prolong the carrier lifetime and is one of the important reasons for such a high photoresponse. In another very recent study of ultra-fast carrier dynamics in Ge NW,[22,64] it is proposed that electrons are trapped in the surface states of Ge NW that lies below the Fermi level. This gives rise to hole accumulation at the surface and hence band bending. This observation corroborates well with results from XPS analysis, atomic probe microscopy as well as electrical measurements as discussed in section 2(ii).[61]

Recently, there has been report on a single Si NW based photodetector that shows a zero-bias Responsivity $\sim10^4$A/W at 514 nm.[5] Another recent report on core-shell type self-powered single Ge NWs showing Responsivity $\sim6\times10^3$A/W.[40] However, there has been no other report of a self-powered nanowire photodetector. The previous reports[65,66] on films that show zero bias photodetection have an unequal barrier heights or an asymmetry at both contacts. It is known to be the main cause for photodetection. A quantitative modeling and/or nature of the built-in potential is missing, especially for the case of NWs, where both contacts are qualitatively similar.

4. Thermal conductivity

Semiconductor NWs show large reduction of κ as has been measured experimentally as well as theoretically.[4,26] These NWs show very low thermal conductivity compared to its bulk thereby increasing the figure of merit *ZT*, which is essential for thermoelectric applications. The reduced thermal conductivity in NWs is due to dominance of boundary scattering that decreases the mean free path of the phonons. The dominance of boundary scattering becomes more prominent as go to lower NW diameters. In Si, the thermal conductivity goes down from 130W/m.K to 44W/m.K as we go from bulk to NW (diameter ~100nm). A 56nm diameter NW has $\kappa = 26$W/m.K and a 22nm diameter NW has $\kappa = 8.5$W/m.K in single Si NW.[4] The surface roughness of the NWs is a very important parameter and can modify its thermal conductivity by an order or more[28] through enhanced phonon surface scattering. Work has been done in artificially roughening Si NWs to reduce thermal conductivity by an order, till it reaches the amorphous limit.[29] Artificially roughened Si NWs have κ ~few W/m.K that is two orders respect to that of bulk Si.

While most work done so far has been on Si NWs only, even in the bulk form, Ge has a lower thermal conductivity of 58W/m.K as opposed to Si (130W/m.K).[67] The main focus is to reduce the thermal conductivity and, from simulations the predicted value for smooth Ge NWs, of diameter ~100nm is 12.5W/(m.K),[28] which is much lower than that of Si NWs (~ 40W/(m.K)) for the same diameter and surface roughness.[26] There is only one report of thermal conductivity measurement in a single Ge NWs

showing values of 2.26 + 0.60/−0.39W/m.K for a 20nm NW at 300K.[68] This value is ~ 40% lower than the predicted value of a 20nm Ge NW (3.7W/m.K)[26] of surface roughness 0.3nm, which is usually the value for VLS grown NWs.[49] A basic study of thermodynamic and thermal properties of Ge NWs is lacking, which will be a stepping stone to seek out the current issues related to Ge NWs as well as the issue of high efficiency thermoelectric materials.

F. WHAT WOULD BE OF SIGNIFICANT VALUE ADDITION TO THIS AREA?

Considering the recent developments related to understanding the hysteresis and p-type behavior in Ge NWs, shows us how important surface characterization can assist in understanding and revealing the physics behind the unique observed phenomena. The surface oxide though detrimental for the FET, is useful for optoelectronic applications since it causes SBB. The origin of a high response (highest reported till date is $\mathcal{R} \sim 10^7$A/W for ZnO NWs[6] in the UV region) in semiconductor NWs is most importantly due to the radial field caused by SBB.[6,40] Though, the impact of a confining potential on photoconduction properties are known, the nature of the field or a quantitative analysis has not been investigated. Another factor that seems to be a likely cause of such high Responsivity is impact ionization[69,70] due to very high electric field at the depletion region that produces multiple electron-hole pairs through avalanche mechanism. We have analyzed each of these factors in detail which has enabled a quantitative understanding of photoconduction mechanism in Ge NWs and semiconductor NWs in general.

An important parameter that has not been investigated before in the context of Ge NWs is the ideality factor (η) associated with contact junctions.[71] The barrier formation at a MS interface is extremely sensitive to the surface. Formation of electrical contacts to NWs leads to various chemical (exposure to resists, etchants) as well as physical (ion milling) damage. These make the barrier far from ideal which leads to non-ideality in the junction.[72] Since the contact plays a crucial role in all electronic devices, a quantitative temperature dependent study of the contact parameters is essential. For device applications of Ge, since the International Technology Roadmap for Semiconductors 2014 gives an upper limit of $10^{-8}\Omega.cm^2$ for specific contact resistance (ρ_C), achieving a low ρ_C on Ge in this range is a very desirable as well as a challenging task.

The effect of size on electronic conduction in Ge NWs has not been investigated before and it is felt that a study of this issue will be an important addition in this area. Since no significant work has been done on low temperature electrical conduction in Ge NWs, a study of weak localization in doped NWs would be

interesting to observe from a basic physics point of view. Also, one can also establish a size limit for the validity of scaling theories of localization in Ge NWs.[10]

The numerically predicted thermal conductivity of a 100nm Ge NW at 300K is ~ 12.5W/m.K[28] and it is ~ three times less than Si NW of the same dimension. In this light, the thermal properties of Ge NWs need to be investigated. The measurement of thermal conductivity of nanostructures was developed through advances in nano- micro fabrication. A micro-fabricated structure[4] is designed to build suspended SiN membrane with SiN beams, and platinum lines acting as heater as well as electrical contacts to the nanowire/nano-sheet, which are placed on the suspended structure by a nano-manipulator. This micro-chip device has accurate measurements but relies heavily on state-of-art nanofabrication facility. This method has been used widely used to determine the thermal conductivity of Si NWs,[4] Graphene,[73] CNT[74] and other nanomaterials. There are certain sources of errors that need to be combated while measurement of thermal properties through a micro-chip device such as:

- Presence of thermal contact resistance between metal contact pad and nanowire
- Presence of surface oxide that leads to poor electrical and thermal contacts
- Joule heating if contact resistance is very high
- Heat flow through other high conductivity paths
- Systematic errors due to electrical measurements

Thus, a simpler, rapid, non-contact method is favorable. A technique derived from the opto-thermal Raman method has been recently developed to measure thermal conductivity in NWs that requires local heating as well as measurement through Raman Spectroscopy using a continuous laser.[75] It is simplistic, rapid and overcomes errors arising due to thermal contact resistance measurement and other systematic errors related to electrical probes in a NW. It has proven to be an accurate method with measurement of thermal conductivity of Si NWs.[75] There has been just one experimental report[68] on the thermal conductivity in Ge NWs that is ~ 40% lesser than the predicted value. Hence, an experimental study on the thermal conductivity in Ge NWs through the newly developed Raman opto-thermal method is warranted with a proper investigation aiming to rule out all discrepancies and also scope for improvement of the experimental set-up at its nascent stage.

G. THESIS LAYOUT

This thesis investigates a cross-section of important physical properties of a single Ge NW. Some discussions presented here maybe carried over to specific Chapters for sake of completeness. It focuses on

the study of some of the transport properties of Ge NWs and its revival in the field of opto-electronics as well as thermal transport. We have tried to incorporate a balance of basic physics and applications of Ge NWs. It includes the approach to weak localization in Ge NWs and the study of thermodynamic properties like thermal expansion and thermal conductivity. Ge NWs have great potential for application in broadband photodetectors and it has been probed from a fundamental as well as applications point of view. The thesis work is focused on overcoming the known challenges of working with single Ge nanowire and also exploring and quantifying the novel phenomenon that was observed. The novelty of the thesis is that it has investigated the properties of the NWs by measurements on single NW through conventional electrical method as well through an original application of Raman Spectroscopy. **Chapter 2 focuses on the growth of crystalline Ge NWs** through direct vapor transport method. The NWs have been extensively characterized by electron microscopy and the oxide layer has been investigated in details through XPS. It is the foremost part of the thesis. **The design and development of device and experiments for single NW is discussed in Chapter 3** which is a prominent part of the thesis. **In Chapter 4, we investigate the effect of electrical contacts to single Ge NWs** as it is fundamental for device applications. **In Chapter 5, we have worked harmoniously with the recent developments in photoconductivity of Ge NWs**. This is an extensive study that not only leads to the highest reported Responsivity but also a clear understanding of the physics of ultra-high photoresponse and effects of surface and interface states. We proceeded further to establish the nature of radial field while in **Chapter 6 we discuss the phenomena of self-powered photodetection. Chapter 7 is dedicated to the measurement of thermal properties** of a single Ge NW through Raman Spectroscopy. **In Chapter 8 we study the approach to weak localization in Ge NWs.** Finally, Chapter 9 has a brief discussion on the main observations of this thesis along with concluding remarks.

REFERENCES FOR CHAPTER I

[1]F. Gebhard, The Mott Metal-Insulator Transition (Springer, Heidelberg, 2000).

[2]H. K. Henisch, *Semiconductor Contacts: An Approach to Ideas and Models* (Oxford-UK, 1984)

[3]C. Kittel, *Introduction to Solid State Physics* (John Wiley & Sons, 8th edition, 2007)

[4]D. Li, Y. Wu, P. Kim, L. Shi, P. Yang and A. Majumdar, *Appl. Phys. Lett.*, 2003, *83*, 2934.

[5] K. Das, S. Mukherjee, S. Manna, S. K. Ray and A. K. Raychaudhuri, *Nanoscale,* 2014, *6*, 11232-11239.

[6]C. Soci, A. Zhang, B. Xiang, S. A Dayeh, D. P. R. Aplin, J. Park, X. Y. Bao, Y. H. Lo and D. Wang *Nano Lett.* 2007, *7,* 1003.

[7]Z. Liu,T. Luo, B. Liang, G. Chen, G, Yu, X. Xie, D. Chen and G. Shen. *Nano Res.* 2013, *6,* 775.

[8]X. Zhang, Q. Liu, B. Liu, W. Yang, J. Li, P. Niu and X. Jiang, *J. Mater. Chem.C*, 2017, *5*, 4319.

[9]S. Thunich, L. Prechtel, D. Spirkoska, G. Abstreiter, A. Fontcuberta-i-Morral, and A. W. Holleitner, *Appl. Phys. Lett.* 2009, *95*, 083111

[10]P. A. Lee and T. V. Ramakrishnan, *Rev. Mod. Phys.* 1985, *57*, 287.

[11]P. Yang, R. Yan and M. Fardy, *Nano Lett.* 2010, *10*, 1529–1536.

[12]N. P. Dasgupta, J. Sun, C. Liu , S. Brittman, S. C. Andrews, J. Lim, H. Gao, R. Yan and P. Yang, *Adv. Mater.* 2014, *26*, 2137–2184.

[13]Thor Labs website https://www.thorlabs.com/thorproduct.cfm?partnumber=FDS1010 (accessed March 2019)

[14]R. R. Pierre, M. Robson, M. K. Azizur-Rahman, M. Kuyanov, *J. Phys. D: Appl. Phys.* 2017, *50*, 123001.

[15]R. H. Bube, *Photoelectronic properties of semiconductors,* (Cambridge University Press)

[16]A. Zangwill, *Physics at Surfaces,* (Cambridge University Press, 1987)

[17]Y. Ahn, J. Dunning and J. Park *Nano Lett.* 2005, *5,* 1367-1370.

[18]D. Wang, Y-L. Chang, Q. Wang, J. Cao, D. B. Farmer, R. G. Gordon and H. Dai, *J. Am. Chem. Soc.* 2004, *126*, 11602-11611

[19]C. Chen, J. R. D. Retamal, I-W. Wu, D. H. Lien, M. W. Chen,Y. Ding,Y. L. Chueh, C-I. Wu and J. H. He, *ACS Nano,* 2012, *6* 9366-9372

[20]H. Y. Chen, R. S. Chen, N. K. Rajan, F. C. Chang, L. C. Chen, K. H. Chen, Y. J. Yang and M. A. Reed, *Phys. Rev. B.* 2011, *84*, 205443

[21]R. Calarco, M. Marso, T. Richter, A. I. Aykanat, R. Meijers, A. v.d. Hart, T. Stoica, and H. Luth, *Nano. Lett.* 2005, *5*, 981-984.

[22]R. P. Prasankumar, S. Choi, S. Trugman, S. T. Picraux and J. Taylor, *Nano Lett.* 2008, *8*, 1619−1624.

[23]Y. Dan, K. Seo, K. Takei, J. H. Meza, A. Javey, and K. B. Crozier, *Nano Lett.* 2011, *11*, 2527–2532

[24]A. Ali, Y.Chen, V.Vasiraju and S. Vaddiraju, *Nanotech.* 2017, *28*, 282001

[25]Z. Zhang and J. Chen, *Chin. Phys. B* 2018, *27,* 035101

[26]P. Martin, Z Aksamija, E Pop and U Ravaioli, *Phys. Rev. Lett.*, 2009, *102*, 125503

[27]*Thermal Conductivity: Theory, properties and applications,* Edited by T. M. Tritt (Kluwer Academic / Plenum Publishers, New York, 2004)

[28]P. N. Martin, Z. Aksamija, E. Pop and U. Ravaioli, *Nano Lett.* 2010, *10*, 1120—1124.

[29]J. Lim, K. Hippalgaonkar, S. C. Andrews, A. Majumdar, and P. Yang, *Nano Lett.* 2012, *12*, 2475

[30]R. Newman and W. W. Tyler, Photoconductivity in Germanium; *General Electric Research Lab*: New York, 1959.

[31] W. Kaiser and H. Y. Fan, *Phys. Rev.* 1954, *93*, 977.

[32]C. Thelander, P. Agarwal, S. Brongersma, J. Eymery, L. F. Feiner, A. Forchel, M. Scheffler, W. Riess, B. J. Ohlsson, U. Gösele, and L. Samuelson, *Mat. Today*, 2006, *9*, 28-35

[33]W. Lu and C. M. Lieber *Nat. Mater.* 2007, *6*, 841

[34]F. Leonard, A. A. Talin, B. S. Swartzentruber, and S. T. Picraux, *Phys. Rev. Lett.* 2009, *102*, 106805

[35]A. B. Greytak, L. J. Lauhon, M. S. Gudiksen, and C. M. Lieber, *Appl. Phys. Lett.* 2004, *84*, 4176–4178

[36]D. Wang, Q. Wang, A. Javey, R. Tu, H. Dai, H. Kim, P. C. McIntyre, T. Krishnamohan, and K. C. Saraswat, *Appl. Phys. Lett.* 2003, *83*, 2432–2434

[37]Y. H Ahn and J. Park*, J. Appl. Phys. Lett.* 2007, *91*, 162102.

[38]H. Otounye, W. Kim and W. D. Lu *Appl. Phys. Lett,* 2017, *110*, 173104.

[39]P. Staudinger, M. Sistani, J. Greil, E. Bertagnolli and A. Lugstein, *Nano Lett.* 2018, *18*, 5030−5035.

[40]S. Mukherjee, K.Das, S. Das and S.K. Ray, *ACS Photonics*, 2018, *5*, 4170-4178

[41]T. Kennedy, E. Mullane, H. Geaney, M. Osiak, C. O'Dwyer, and K. M. Ryan, *Nano Lett.* 2014, *14,* 723

[42]B. A. Wacaser, K. A. Dick, J. Johansson, M. T. Borgstrom, K. Deppert, and L. Samuelson, *Adv. Mater.* 2009, *21*, 153−165

[43]W. Lu and C. M. Lieber*, J. Phys. D: Appl. Phys.* 2006, *39* 387-406

[44]Y. Wu and P. Yang, *Chem. Mater.* 2000, *12*, 605-607

[45]Y. Wu and P.Yang*, J. Am. Chem. Soc.* 2001, *123*, 3165-3166

[46]Y-L Chueh et. al., *Nano Lett.* 2010, *10*, 393-397

[47]H. Lu and X. Meng, *Scientific Reports* 2015, *5*, 11263

[48]Y. Wu, Y. Cui, L.Huynh, C.J. Barrelet, D. C. Bell, and C. M. Lieber, *Nano Lett..* 2004, *4*, 433-436

[49]J. Lim, K. Hippalgaonkar, S. C. Andrews, A. Majumdar and P. Yang, *Nano Lett.* 2012, *12*, 2475−2482.

[50]T. Hanrath and B. A. Korgel, *J. Phys. Chem. B*., 2005, *109*, 5518-5524

[51]Kingston, R. H. *J. Appl. Phys.* 1956, *27*, 101−114.

[52]T. Nishimura, K. Kita, and A. Toriumi, *Appl. Phys. Lett*., 2007, *91*, 123123

[53]A. Dimoulas, P. Tsipas, A. Sotiropoulos, and E. K. Evangelou*, Appl. Phys. Lett.* 2006, *89*, 252110

[54]J. Tersoff, *Phys. Rev. Lett.* 1984, *52*, 465–468

[55]J. F. Wager and J. Robertson, *J. Appl. Phys*. 2011, *109,* 094501

[56]F. Leonard and A. A. Talin, *Nat. Nanotechnol*. 2011, *6*, 773–783

[57]M. M. Kolenik-Gray, T. Lutz, G. Collins, S. Biswas, J. D. Holmes, and V. Krsti, *Appl. Phys. Lett.* 2013, *103*, 153101

[58]C. Y. Tsai, S. Y. Yu, C. L. Hsin, C. W. Huang, C. W. Wang, and W. Wu, *Cryst. Eng. Comm.,* 2012, *14*, 53–58

[59]S. Barth, M. M. Kolesnik, K. Donegan, K. Krsti, and J. D. Holmes, *Chem. Mater.* 2011, *23*, 3335–3340

[60]M. Simanullang, G. B. M. Wisna, K. Usami, W. Cao, Y. Kawano, K. Banerjee, S. Oda, *J. Mater. Chem*. C. 2016, *4*, 5102−5108.

[61]S. Zhang, E. R. Hemesath, D. E. Perea, E. Wijaya, J. L. Lensch-Falk, and L. J. Lauhon, *Nano Lett*., 2009, *9*, 3268-3274

[62]H. Kamimura, L. S. Araujo, O. M. Berengue, C. A. Amorim, A. J. Chiquito and E. R. Leite, *Physica E* 2012, *44* 1776–1779

[63]L. Cao, J. S. White, J. S. Park J. A. Schuller, B. M. Clemens and M. L. Brongersma, *Nat. Mat.,* 2009, *8*, 643

[64]Y. Li, R. Clady, A. F. Marshall, J. Park, S.V. Thombare, G. Chan, T. W. Schmidt, M. L. Brongersma and P.C. McIntyre, *ACS Photonics*, 2015, *2*, 1091−1098

[65]D. Li, X. Sun, H. Song , Z. Li, H. Jiang, H. Chen, G. Miao and B. Shen *Appl. Phys. Lett*. 2011, *99*, 261102

[66]H. Y. Chen, K. W. Liu, X. Chen, Z. Zhang, M. M. Fan, M. M. Jiang, X. H. Xie, H. F. Zhaoa and D. Z. Shen, *J. Mater. Chem. C* 2014, *2*, 9689

[67]J. A. Carruthers, T. H. Geballe, H. M. Rosenberg and J. M. Ziman, *Proc. R. Soc. Lond. A* 1957, *238*, 502-514

[68]M. C. Wingert, Z. C. Y. Chen, E. Dechaumphai, J. Moon, J-H Kim, J. Xiang and R. Chen, *Nano Lett*. 2011, *11,* 5507−5513

[69]S. Assefa, F. Xia and Y. A. Vlasov, *Nat. Lett*. 2010, *80,* 464

[70]C. Yang, C. J. Barrelet, F. Capasso and C. M. Lieber, *Nano. Lett*, 2006, *6*, 2929-2934

[71]R. T. Tung, *Phys. Rev. B* 1992, *45*, 13509

[72]Tung R T *Appl. Phys. Rev*. 2014, *1*, 011304

[73]W. Jang, W. Bao, L. Jing, C. N. Lau and C. Dames, *Appl. Phys. Lett*. 2013, *103,* 133102

[74]L. Lu, W. Yi, and D. L. Zhang, *Rev. Sci. Instrum*., 2001, *72*, 2996

[75]G. S. Doerk, C. Carraro, and R. Maboudian, *ACS Nano*, 2010, *4*, 4908.

CHAPTER II

GROWTH AND CHARACTERIZATION OF GERMANIUM NANOWIRES

We have grown single crystalline Germanium Nanowires through a non-toxic physical vapor deposition technique using gold nanoparticles as catalyst. The challenges involving an unwanted oxide layer during growth was overcome by use of reducing agents. The NWs have been well characterized quantitatively to obtain necessary information about the spatial and chemical composition of the oxide layer.

A. INTRODUCTION

The growth of single crystalline materials is a thermodynamically driven dynamic process which depends strongly on the control of growth parameters. The processes of crystal growth like vapor, liquid and solid have been well studied over the last hundred years.[1] Each process has its challenges and is favorable for a particular class of materials. The process of crystal formation is a dynamic equilibrium process which provides the driving force as the crystal formation occurs in the direction of lowest Gibbs free energy.[2] The liquid to solid phase transformation process, like Czochralski process, is the most well known for growth of mono-crystalline Silicon and other semiconductor materials. The vapor to solid phase transformation involves growth by sublimation and vapor transport. The growth of nanowires by vapor transport was first achieved in 1964 by Wagner and Ellis[3], when they grew Silicon whiskers from an impurity seed particle. The growth mechanism was explained as Vapor-liquid-solid (VLS) mechanism,[2-9] a method by which, an impurity seed particle alloys with the source material at a relatively low temperature, and this acts as a site for preferred deposition of the source vapor. This leads to formation of a supersaturated solution and a nucleation process occurs which causes precipitation and hence growth in the facet of the minimum surface energy. The change in Gibbs free energy when nucleation occurs[2,9],

$$G_1 = -n\Delta\mu, \tag{1}$$

which is the energy released by the chemical potential going from the vapor to liquid phase in the alloy droplet. The energy required to create new interfaces is given by,

$$G_2 = l_{vs}h\sigma_{vs} + l_{ls}h\sigma_{ls}, \tag{2}$$

where l is the perimeter length of the nucleus, h is the height of the nucleus and σ is the interface energy. The change in Gibbs free energy, $\Delta G = G_1 + G_2$, can be minimized by the shape and placement of the nucleus, which, incidentally is minimum at the three phase boundary (TPB) line – at the interface of the

liquid alloy droplet and the solid crystal.[9] Incorporation of vapor atoms into the crystal occurs through the liquid alloy and nucleation occurs at the three phase boundary where the crystal growth occurs, thus adding a new layer to the existing crystal. The schematic of this process are shown in Fig. 1. Thus, depending on the interface energies, a preferred growth direction is obtained. The basic needs for the VLS method are transportation of the source material to a relatively cooler growth zone, where, there is supersaturation and nucleation, leading to "formation of spontaneous fragments of the stable phase" of the crystal. The liquid surface is rough and has more accommodation coefficient as compared to the solid and hence a preferred site for deposition.[2] Unidirectional growth at the three phase boundary is a consequence of the anisotropy in the nucleation processes at different interfaces. The axial growth occurs by this mechanism because the precipitation is catalyst mediated at the liquid/solid (L/S) interface.
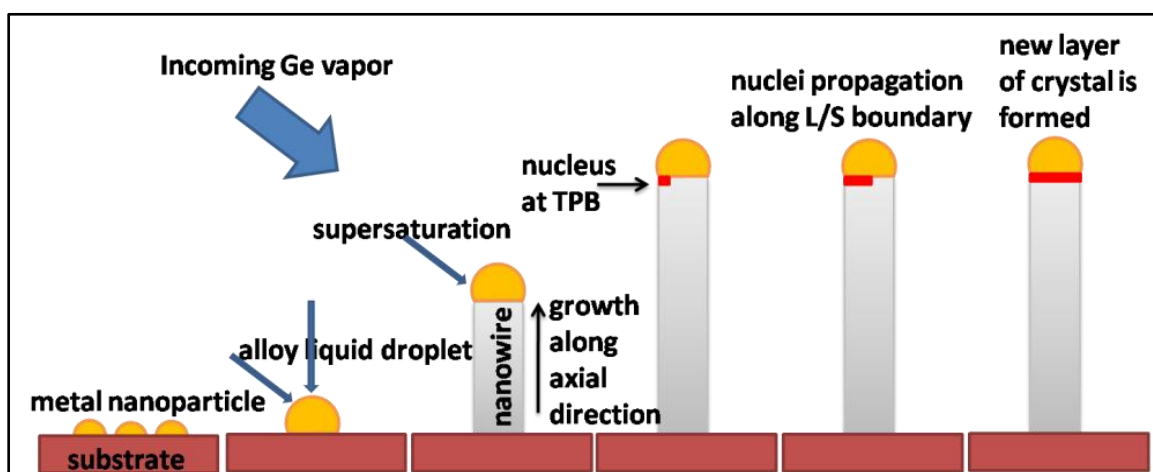

Figure 1. Growth schematic of VLS mechanism.

The growth of semiconductor NWs is well-researched field and each method has its share of advantages and drawbacks. Nanowires grown by the VLS method are oriented, single crystalline with preferred deposition site as well as controllable diameter of NW.[10] It is a simple and direct process of growth with a large output. It allows selectivity of growth at targeted sites. We can control diameter of NW through the metal nanoparticle diameter.[11] Sometimes, direct vapor deposition on the NW sidewalls may occur, known as radial growth, but it can be negated through use of H_2 gas for passivation, lower growth temperature or by insitu mild HCl gas etching.[9] There is an open choice for using the metal nanoparticle[12], which decides the growth temperature and the particle size determines the NW diameter. The disadvantage of this type of growth is that, the catalyst adds impurity to the NW known to cause deep level traps in Si NWs.[12]

The type of vapor transport to the substrate can occur through physical vapor transport or by chemical means. Hence, hazardous chemical precursor gases like SiH_4 and GeH_4 may be used. But physical transport involves using the vapors of the source material only. Even though, chemical route may be advantageous as it provides options of doping[13] during growth by using the dopant precursor gas, it suffers disadvantages in terms of environment and health hazards on exposure to these harmful and toxic gases. In VLS growth, smooth NWs (with surface roughness ~0.3nm)[14] are formed as opposed to top down methods like metal assisted etching in which large surface roughness exists. These advantages have lead to NW growth by VLS mechanism through the non-toxic physical vapor transport to become the preferred one.

B. EXPERIMENT

The growth process is carried out in a dual zone furnace (Fig. 2(a)) with Au nanoparticle as the seed impurity and inert gas as a carrier.[15,16] We have calibrated the dual zone furnace initially to get the preferred site for growth of the NWs. The temperature profile inside the dual zone furnace is given in Fig. 2(b). The growth temperature depends on the phase diagram of Ge-Au, and beyond its eutectic temperature, we get growth of NWs. The eutectic point of Au-Ge is at 361^0C with Au:Ge::28:72 by atomic percent. It is known that the eutectic point reduces (by 22^0 for 20 nm Au nanoparticle-Ge NW) since surface energy of the nanoparticle (NP) is much larger than bulk.[17] The Au NPs were formed by a method of dewetting an ultrathin Au film grown by e-beam evaporation technique on a clean Si (100) wafer in an ultrahigh vacuum chamber (10^{-5} Pa) followed by annealing.[18] This causes breakage of the thin film due to surface tension and they form clusters through agglomeration on subsequent cooling.[19] The Au NP distribution is governed by the thickness of the Au layer and annealing temperature. We have grown 8-9 nm Au film (A) and 5-6 nm Au film (B) measured by an insitu quartz crystal thickness monitor and annealed the film at 400^0C for 30 mins. The SEM images of these two Au NP distributed on the Si substrate in shown in Fig. 3a and 3b. The NPs are far apart in (A), while in (B), they are more closely packed. But in both cases the particle distribution is non-uniform, with a large number of particles with diameter ~ 100nm. We then proceed to decrease the annealing time in film B to 15 mins at 400^0C. The SEM image of this film is given in Fig. 3c. With these growth conditions we get a uniform density of NPs, with Gaussian distribution centered about 10 nm. The Au NP distribution has been characterized through Atomic Force Microscopy.
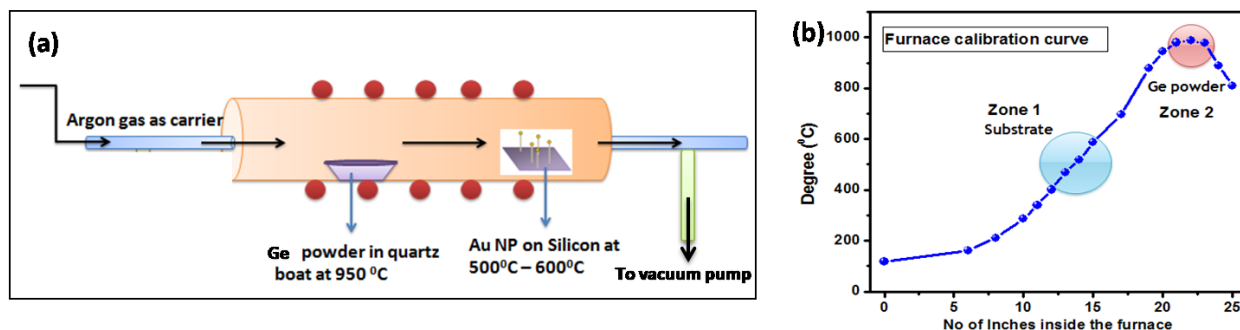
Figure 2. (a) Schematic of the experimental setup. (b) Calibration of furnace showing the two zones.
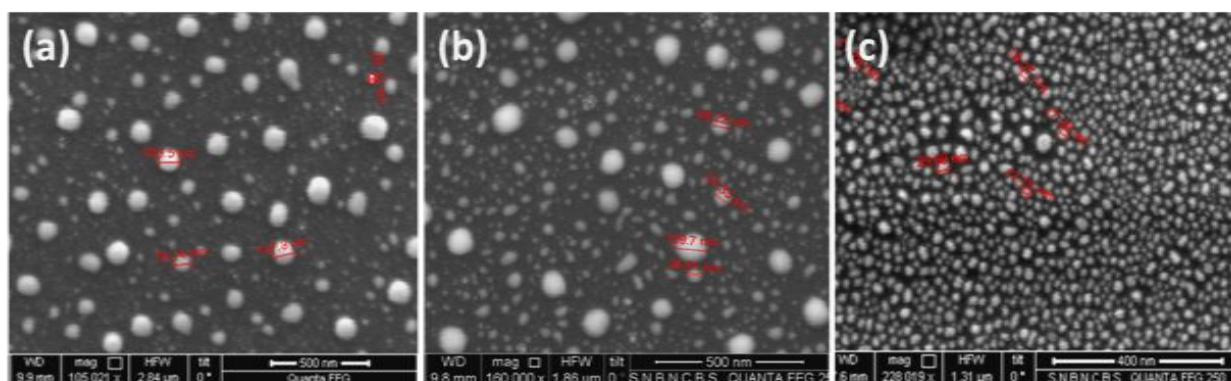

Figure 3. SEM image of Au NP on Si substrate under different growth conditions. Panel C shows the optimized growth of Au NPs

The Si wafer with Au NPs is placed vertically (through a quartz stand) at $400 - 500^0$C along the downstream of the carrier gas flow. The furnace is evacuated first and when the source temperature greater than 950^0C is reached, the gas flow is started. The melting temperature of Ge is 938^0C, so beyond this temperature, we get evaporation of Ge. The carrier gas transports the Ge vapors to a relatively cooler Au NP substrate, where through the VLS mechanism growth of NWs occur. The growth time is ~ 30 mins. The gas flow continues upto an hour post growth, after which, the chamber is evacuated again, till it reaches room temperature.[18] The Ge NWs grow as a dense bunch on the Si substrate with diameters varying from $10 - 150$ nm and length ~ few microns as shown in SEM image, Fig. 4a. We have got targeted growth of the NWs at the site of Au NP only (see Fig. 4b). The growth process though simple, needs careful control of the important parameters like substrate temperature and flow rate. The flow rate of the carrier gas is kept below 0.5 sccm, as a very high rate can cause a film deposition on the substrate (see Fig. 4c). The substrate temperature controls the alloying and precipitation. It is quite critical and when sufficient temperature is not reached, the growth of NWs is not achieved. We have used Argon as the carrier gas as well as Ar/H_2 mixture gas as discussed later.
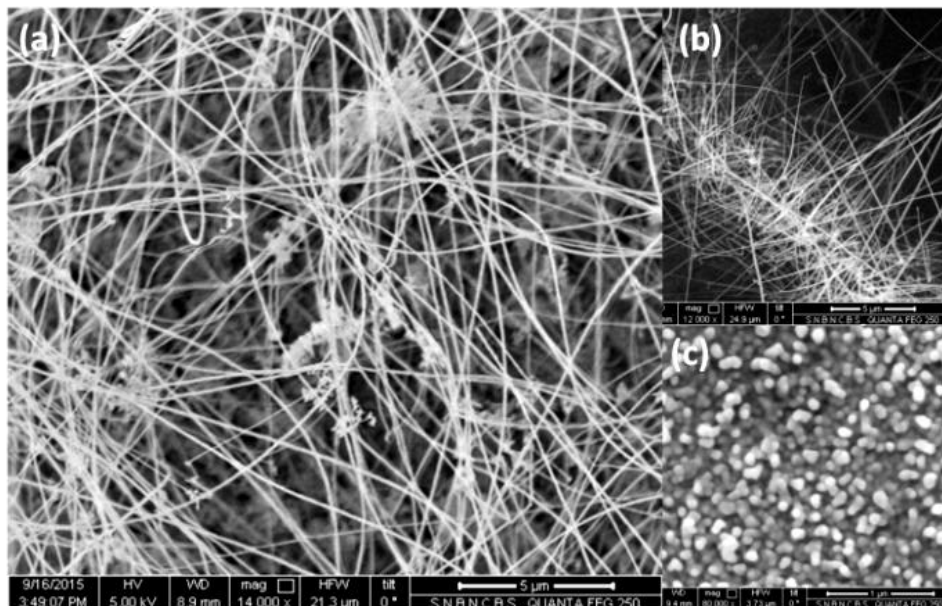
Figure 4. SEM image of a bunch of NWs (a) on the Si substrate and (b) at targeted region only. (c) Ge film grown on the Au NP substrate due to high flow rate.

C. CHARACTERIZATION TOOLS

The Ge NWs were characterized using the usual nano-characterization tools with extensive Transmission Electron Microscopy (TEM) associated studies. We have also used X-Ray Photoelectron Spectroscopy (XPS) to identify the chemical valence states of Ge in the native oxide layer, which is essential for analysis of the opto-electronic properties. It not only serves as a tool for characterization, it helps us quantify the chemical and spatial composition of the nanowire for a better understanding of its physical properties.

The advent of new-age technology allows us to probe into the details of nanostructures. Imaging techniques includes Scanning Electron Microscopy (SEM) and Transmission Electron Microscopy (TEM) and TEM associated techniques like High Angular Annular Field (HAADF) Imaging. Characterization has been performed through X-Ray Diffraction (XRD), EDX (Energy-dispersive X-Ray Spectroscopy), Atomic Force Microscopy (AFM), Electron Energy Loss Spectroscopy (EELS) and X-Ray Photoelectron Spectroscopy (XPS).

1. XRD

X-Ray diffraction is a basic characterization tool to determine the crystal structure of a material. It follows the Bragg law where the wavelength used is ~ atomic spacing. Usually, Cu $K_{\alpha 1}$ line ($\lambda = 1.54A^0$) is used as the source. On interaction with sample, which is placed on a goniometer, the diffracted X-rays are then detected, processed and counted. Conversion of the diffraction peaks to d-spacing helps us to identify the element. The peak position obtained can be used to correlate with standard reference of International Centre for Diffraction Data (ICDD) and ascertain the composition.

2. SEM

It is an imaging technique with an electron beam that is scanned onto a sample, and scattered electrons are used to construct an image. The focused electrons interact to produce secondary electrons, back-scattered electrons, auger electrons X-rays and cathodoluminiscence. A field emission electron gun is used as source to inject highly focused beam of electrons through an accelerating grid, condenser lens, objective aperture and scanning coils and finally through an objective lens and then scanned onto the sample, kept on a motorized stage. The beam is scanned over the sample in a raster pattern in synchronization with a cathode ray tube. Usually the secondary electrons are detected using an Everhart-Thornley detector. Their intensity is proportional to the signal detected. The image obtained is black and white, corresponding to the intensity of the spot, which brings contrast to the image. Through SEM we can study the topography and morphology of a sample. SEM has a large depth of field (few mm) that allows a large amount of the sample to be imaged at once. It also has a very high resolution (1-10 nm depending on the source used and the pixel size of CCD).

3. EDX

The X-Rays produced by the interaction of the primary electron beam with the sample are essential for elemental identification and is used for elemental quantification through EDX. The X-Ray energy from each shell in an element is unique and serves as an accurate method for chemical analysis. Characteristic X-rays come from electron transitions between core shells. An electron is first knocked out in order to create a vacancy, which gets filled up by X-ray emission. The number and energy of the X-rays emitted can be measured by an energy dispersive spectrometer. The specific energy of the X-ray peak has to be identified for each element. It is a very useful tool for elemental identification. EDX setup is also available with the TEM where spatially resolved EDX can also be performed in Scanning Transmission electron microscope (STEM) mode, which gives us chemical composition of a nanomaterial mapped spatially.

4. Raman Spectroscopy

The spectral analysis of inelastic scattering of light by the vibrating molecules in a material is known as Raman Spectroscopy. Raman scattering is caused by the polarization induced in a molecule by the oscillating electric field of an incoming radiation. It acts as a secondary source for electromagnetic radiation. The polarisability being a second rank tensor gives three components of the induced dipole moment. If the polarisability depends upon vibrational frequencies, these terms will modulate the incident electric field. Hence, the molecular vibration affects the polarisability.

The polarized electrons radiate at the frequency of their oscillations. The scattered radiation of the induced dipole moment consists of three components with the angular frequencies ν, $\nu-\Delta\nu$ and $\nu+\Delta\nu$ which corresponds to Rayleigh, stokes-Raman and anti-stokes scattering respectively. Since only 1 in 10^7 photons shows inelastic scattering, a highly intense laser beam is used for this purpose, with a very sensitive detection system.

5. XPS

In XPS, the kinetic energy (K.E) of the electrons is detected for an unit energy interval and the number of electrons gives the counts. The electrons are detected by an electron spectrometer which is controlled by a variable electrostatic field. When soft X-Rays interact with a material, the K.E. of the emitted electrons is given by the Photoelectric effect, $K.E. = h\nu - B.E. - \phi_s$ where, B.E. is the binding energy of the atomic orbital from which the electron originates and ϕ_s is the spectrometer work function. Since mean free path of electrons in solids is few A^o, the electrons producing peaks in the XPS spectra originate from only the top few atomic layers. This makes XPS a *unique* surface-sensitive technique for chemical analysis. There can be a variety of K.E. depending of the available final states, but each final state has a different probability of cross-section. Each element has a unique set of binding energies and it can be used to identify elements as well as their concentration in the surface. Variations in the elemental binding energy arise from shifts in the chemical potential of the compound.

The major components of the XPS system are an X-Ray source, X-Ray monochromator, energy analyzer, ion-gun for sputter etching and vacuum chamber. The X-Ray used is Al K_α line of energy 1486.6eV, falling at 45^0 on the sample. The base vacuum is kept at $\sim 10^{-8}$ Pa. The XPS spectrum is a plot of the number of electrons versus electron binding energy in a small energy interval. Composition as well as the chemical states of the Ge in the Ge NWs was examined as a function of film thickness through XPS depth profiling. For surface cleaning and depth profiling, sample surface was etched with Ar^+ ion at 2 keV with a grid voltage of 120V for different time intervals to sputter out the films over an area of $\sim$

200μm×200μm. The sputtering rate of the surface is ~1 nm/min. The surface charge effects were compensated by calibrating the energy scale of high resolution Ge 3d in reference to the adventitious carbon at 284.5 eV in B.E. scale. The recorded high resolution Ge 3d photoelectron peaks were resolved into their respective Gaussian fits after background subtraction.

6. TEM

TEM as the name suggests, analyses the transmitted beam of electrons through a thin (<100nm) specimen. A much higher energetic beam of electrons (100-200KV, as compared to 5-20kV in SEM) are used, hence resolution is better. The transmitted beam is magnified through stage lens and objective aperture and viewed in a screen, which can be recorded by a CCD camera. The image contrast is obtained due to variation of intensities in the transmitted beam. Either the transmitted beam (bright field imaging) or the diffracted beam can be used for imaging (dark field imaging). Nanostructures can be imaged in great detail and crystal structure, atomic positions and other information can be gathered. For example, a high resolution image shows the crystal planes. From a good quality HRTEM image we can obtain the periodic plane spacing. A 120kV (Tecnai G 2, TF-20, ST) was employed to study the structure and phase locally on a single Ge NW.

In TEM both the imaging and diffraction techniques can be used. The **SAED** maps the specimen in the reciprocal lattice and we get an image of atomic positions. It gives a Fourier Transform of the periodic crystal lattice. From this pattern, the structure, orientation, lattice spacing, atomic position and information related to crystallinity or defects can be obtained.

Another type of imaging associated with TEM, is imaging by **HAADF** detector in the STEM mode. In this mode, the electron beam is focused at a spot (~few 100nm away from the sample to avoid damage), and then raster scanned over the sample. The HAADF detector relies on the inelastic scattered beam which it collects from an annulus around the beam. It detects according to the angle of scattered electrons transmitted from the sample. The intensity of a HAADF image depends on the atomic number of the element. Thus a lighter element will appear dark while a heavier one, bright, thus, providing an elemental contrast image.

Along with this, TEM is equipped with an **EDX** with spatial resolution down to 0.1 nm (depending on the size of the beam spot). This gives an opportunity to study an EDX line profile, which exactly gives the spatially resolved chemical composition.

EELS is an analytic technique for advanced material analysis and is equipped with a TEM. It is based on inelastic scattering of energetic electrons. The scattered beam loses energy and is bent through a small

angle (5 - 100 milliradians). The typical electron energy-loss spectrum has an intense peak occurs at 0 eV known as the zero-loss peak. These are due to transmitted electrons that have been elastically scattered. The low-loss region (< 50 eV) has peaks coming from a plasma resonance. At higher energy losses (> 50 eV), there are characteristic peak called ionization edges. When a core electron absorbs energy from the primary electron beam, it goes to excited state. This leads to a sharp rise and gradual fall in the electron energy loss spectrum. The ionization edges are used for analysis of elements. The peak onset gives the ionization energy which helps in elemental analysis. EELS is a very useful technique to find the oxidation states of the element in a sample. It utilizes the inelastic scattered electrons to study the bonding state of an element. The energy loss of an electron after interaction with the sample is recorded in a known energy window (characteristic of that element). It can help determine the valence state of an element in a compound. The TEM-based Gatan parallel detection electron energy loss spectrometer was used study the chemical binding states of Ge NWs.

7. AFM

Atomic force microscopy has been derived from scanning tunneling microscopy which is based on the principle of quantum mechanical tunneling. Here, short range forces between the AFM tip and the sample helps in mapping its surface. The apparatus consists of a cantilever on whose free end a tiny tip is attached. When the tip scans over the sample surface, the attraction/repulsion of the tip to the sample due to Van der Waals forces causes a vertical movement of the cantilever. This is detected by a laser beam which is reflected of the back of the cantilever to a position sensitive photodetector. Subsequently this is converted to a contrasting image on screen. The amount of force depends on the distance between the tip and sample and also on the spring constant of the cantilever. The AFM can be operated in three modes: Contact, Tapping and Intermediate. It is useful for mapping the surface of a sample. It gives the surface topology of the sample. We have used AFM to study the morphology of the nanowire surface.

D. RESULTS AND DISCUSSIONS

Ge NWs form a native oxide layer on exposure to atmosphere within a span of a few hours to a self limiting thickness ~ 5nm. The oxide layer is known to be unstable as it not formed purely of stoichiometric hexagonal GeO_2, but rather sub-oxide GeO_x (x<2). Thus, Ge/GeO_2 interface has been a subject of much debate with respect to its composition.[20-23] Studies have been done on growth and characterization of Ge NWs and a clear understanding of the surface characteristics of Ge NWs post growth (after exposure to atmosphere) is important to understand its physical properties. Work has been done on processes of removal of the oxide layer (by mild acid etching followed by surface passivation)[21]

and its effects on the electrical properties.[20] XPS studies have been performed in Ge NWs, to determine the content of the oxide layer, which suggest that there is indeed a presence of GeO_x in the oxide layer.[22]

The physical dimensions, chemical composition and spatial composition of the NWs have been investigated through nano-characterization tools. The NWs grown through the VLS mechanism, have a signature of an Au NP sitting at the tip of the NW.[24] It can be seen from the SEM image (Fig. 5a) marked in a red circle. The eutectic based VLS growth leads to the separation of the Au enriched tip, which is shown in the TEM image in Fig. 5(b). However, the bulk of the wire is expected to have a finite amount of Au in the body of the NW. The exact content of the Au is not known though it is expected that it will vary along the length so that near the tip, the concentration of Au will be more.[18] The NWs grown from vapour phase are thus not intentionally doped. A discussion regarding this has been presented in Chapter I, Section B (ii).
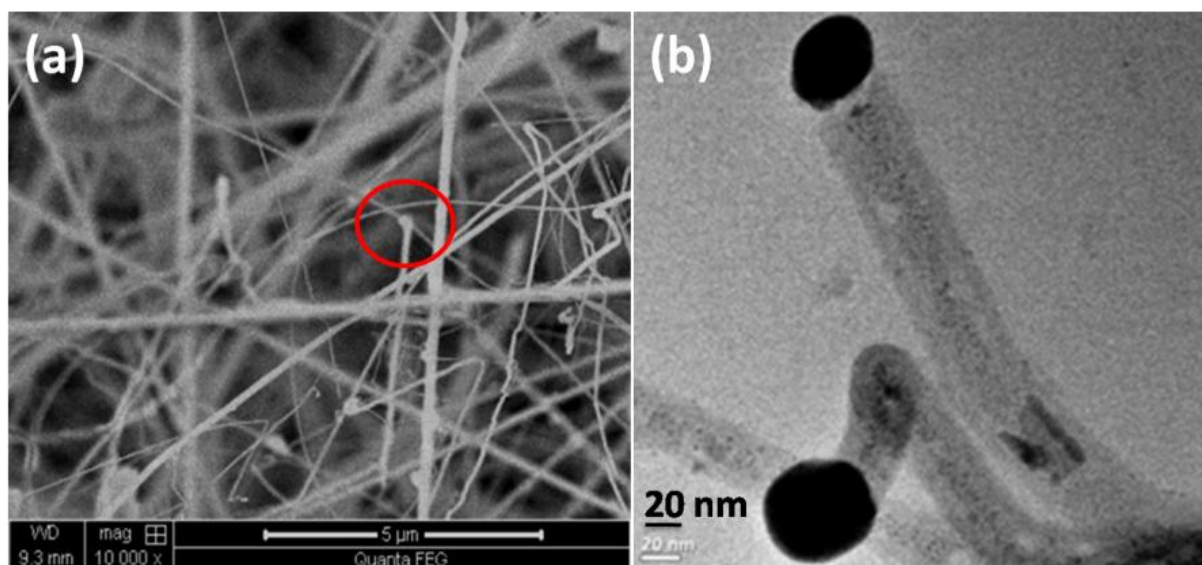

Figure 5. (a) SEM image showing an Au NP at the tip of a Ge NW.[24] (b) TEM image showing Au tip as a black circle on a Ge NW.

The SAED pattern as shown in Figure 6a, confirms cubic nature of the NW with parallel planes along <111> direction only (ICDD, Ref. Code:00–003-0478). The SAED pattern has also been taken along different spots on the Ge NW, and it remains unchanged, thus establishing the crystalline nature of the NWs.[25] The HRTEM image (Fig. 6b) also agrees with the SAED analysis, showing d-planes with spacing of 0.326 nm which corresponds to <111> direction. It also shows an oxide layer around ~5-10 nm thick (depending upon the NW diameter) on both sides.
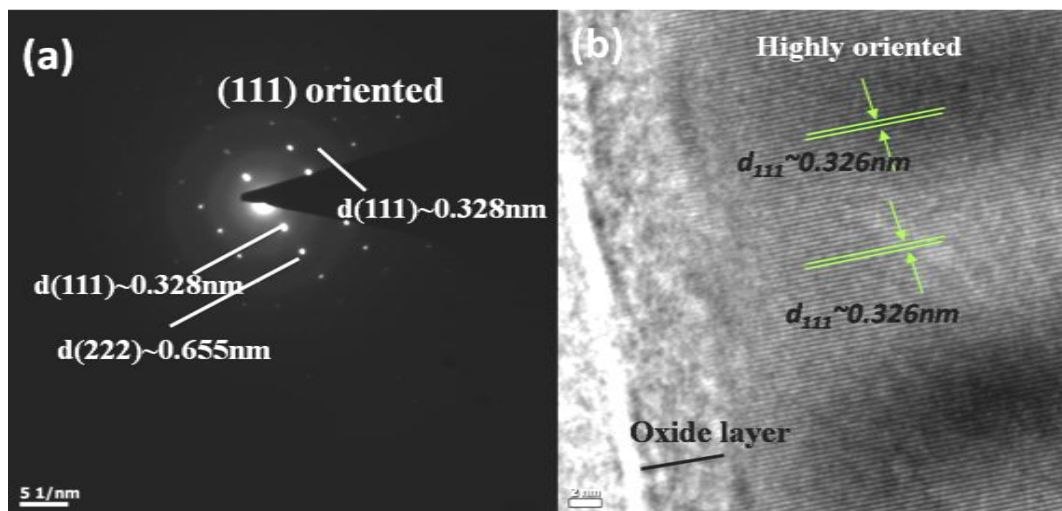
Figure 6. (a) SAED pattern of a Ge NW showing highly oriented planes along (111) direction. (b) HRTEM image of a Ge NW with distance between parallel d-planes~ 0.326 nm, and an oxide layer marked in black.[25]
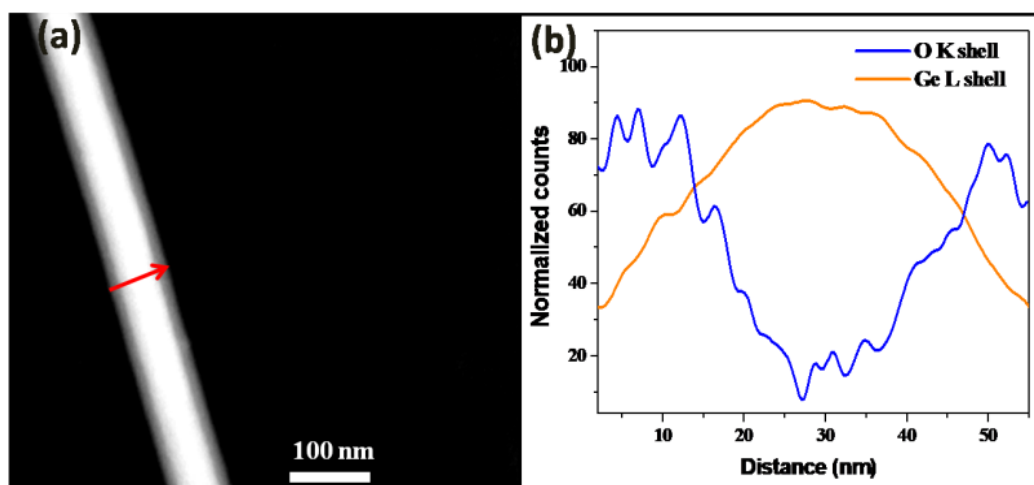

Figure 7.(a) The HAADF image of a Ge NW, showing the direction marked with red arrow, along which line EDAX profile was taken. (b) Line Edax of a single Ge NW taken in STEM mode with O and Ge concentration profile along the radial direction as marked by arrow.

The HAADF detector for imaging in Fig. 6a shows presence of a thin layer (~5nm) on a NW of diameter ~ 45 nm at a lower contrast compared to the bulk portion of the NW, which appears bright.[25] The spatial position of the Ge oxide was investigated using EDAX line profile of a Ge NW taken in Scanning TEM (STEM) mode along the radial direction shown by a red arrow in Fig. 7a. The plot of the Line EDAX profile shows Oxygen concentration (from the K shell) at the two ends of the NW to be maximum, while

the Ge concentration profile (from the L shell) is almost complementary to it. The maximum Ge concentration lies from 15-45 nm in the line EDAX profile. There is a finite size of the electron beam for each step size taken for the line profile which causes spatial broadening of the line scan leading to an apparent larger thickness of the oxide layer compared to the actual thickness. Nevertheless, it is established that the surface of the NW is surrounded by an oxide layer, while the core made up of purely Ge.[25]

We have performed Electron Energy Loss Spectroscopy (EELS) using TEM to get information on the chemical binding states of Ge and nature of the oxide layer. The EELS spectrum was analysed using multiple Gaussian peak fitting. The EELS spectrum of Ge L edge (Fig. 8a) shows a broad spectrum. The spectrum of Ge L edge corresponding to the transition of Ge 2p has been fit using standard Gaussian fitting, which shows Spin-orbit splitting into $2p_{3/2}$ (L_3) and $2p_{1/2}$ (L_2) at 1217 and 1247 eV respectively. Apart from these elemental peaks of Ge, there is another peak whose edge is 1222 eV and this corresponds to the binding energy of Ge other than metallic state.[26] The O K edge spectra corresponding to the transition of O 1s is shown in Fig. 8b. Splitting can be observed in the O K edge which shows two peaks, one of which is the K edge from O 1s orbital at 532 eV. The other peak shows absorption edge below 530 eV, which corresponds to binding energy of metal oxides. Thus it can be inferred from the EELS spectrum analysis that the Ge NW has oxygen, which is surface absorbed as well as in the form of GeO_x ($x \leq 2$). The details of the composition and chemical binding states of Ge have been analysed through X-ray Photoelectron Spectroscopy and are discussed in Chapter V, where it is appropriate.
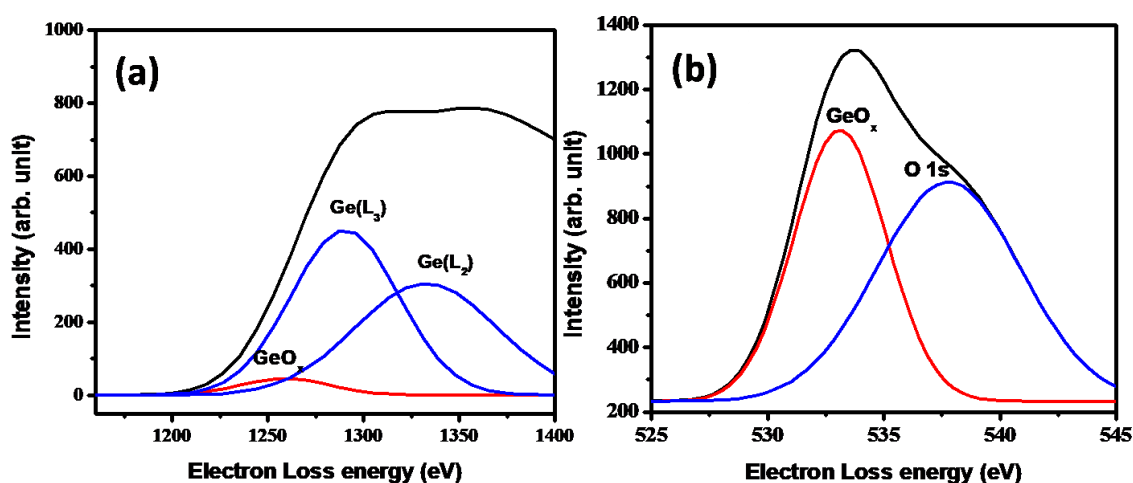

Figure 8.(a) EELS spectrum showing the Ge L_3 (1247 eV) and L_2 (1217 eV) peaks and a shallow oxide binding energy loss peak, with edge at 1220 eV. (b) EELS spectrum showing two peaks with an edge at 532 eV from O 1s orbital and the other peak corresponding to a metal oxide peak, with edge below 530 eV. Blue lines show elemental peaks, red line shows oxide peaks and black line is the experimental data.

An oxide layer can be formed post growth on the NW naturally which is ~ 2-5 nm thick.[21,22] Oxide growth can also occur in the NW during the growth period. To prevent oxidation of NW during growth, we have used 5% H_2 gas mixed with Argon as the carrier gas. It prevents and reduces any oxidation of gas phase or solid phase Ge by residual O_2. We have also used Titanium pieces which act as a getter and forms TiO_2 if any O_2 gas is present. This ensures no oxide layer growth during the actual growth of NWs. We have again performed all the characterizations and seen that the oxide layer is negligible by use of the reducing gas and oxygen getter during the growth process.
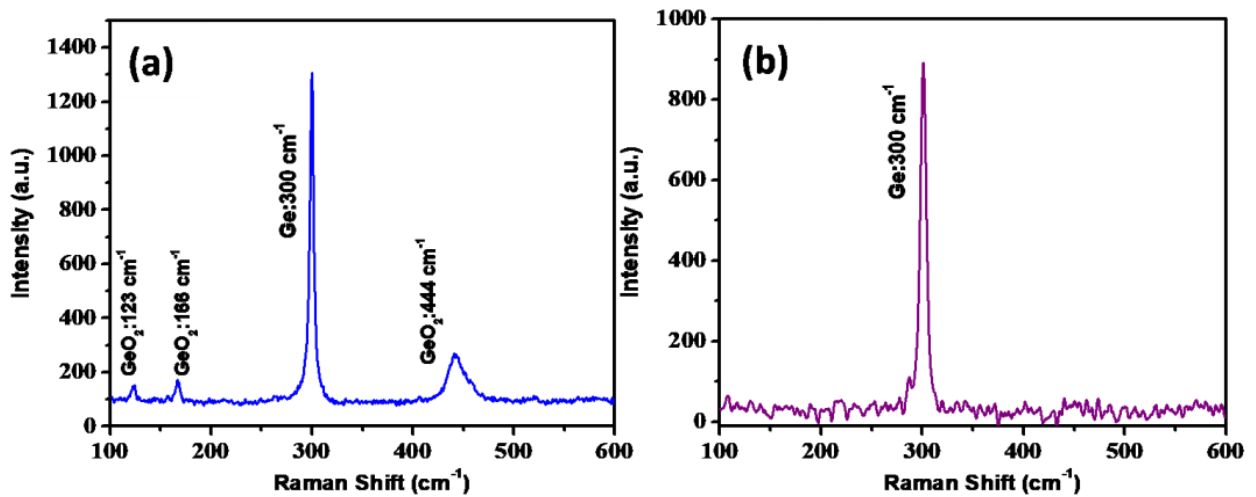

Figure 9. (a) Raman Spectrum of a single Ge NW of diameter 105nm showing oxide peaks. (b) Ge NW of diameter 93 nm with peak Raman peak at ~300 cm^{-1}, grown in reducing environment.

A comparison of the NWs grown by VLS mechanism through a normal process and the ones grown in a reducing environment is performed by Raman Spectroscopy. The room temperature Raman spectra of single NW (see Fig. 9), clearly shows a huge difference in the spectra – in one only a pure Ge peak[27] with Raman Shift at 300.2±0.5 cm^{-1} while the other one has the Ge peak along with three other peaks. The Ge Raman peak shift comes from the LO/TO degenerate mode. The other peaks have been identified as GeO_2 peaks[28] which have α-quartz type of structure with E1 modes at 123.3±0.2 and 167.0±0.3 cm^{-1}, and A1 modes at 262.4±0.6 (not clearly visible in this scale) and 444.4±0.4 cm^{-}. The Raman spectra have been taken on at-least eight different NWs and an average value of the peak position is given. Thus, with the modified growth conditions, we can get a pure crystalline Ge NW, without any oxide layer.
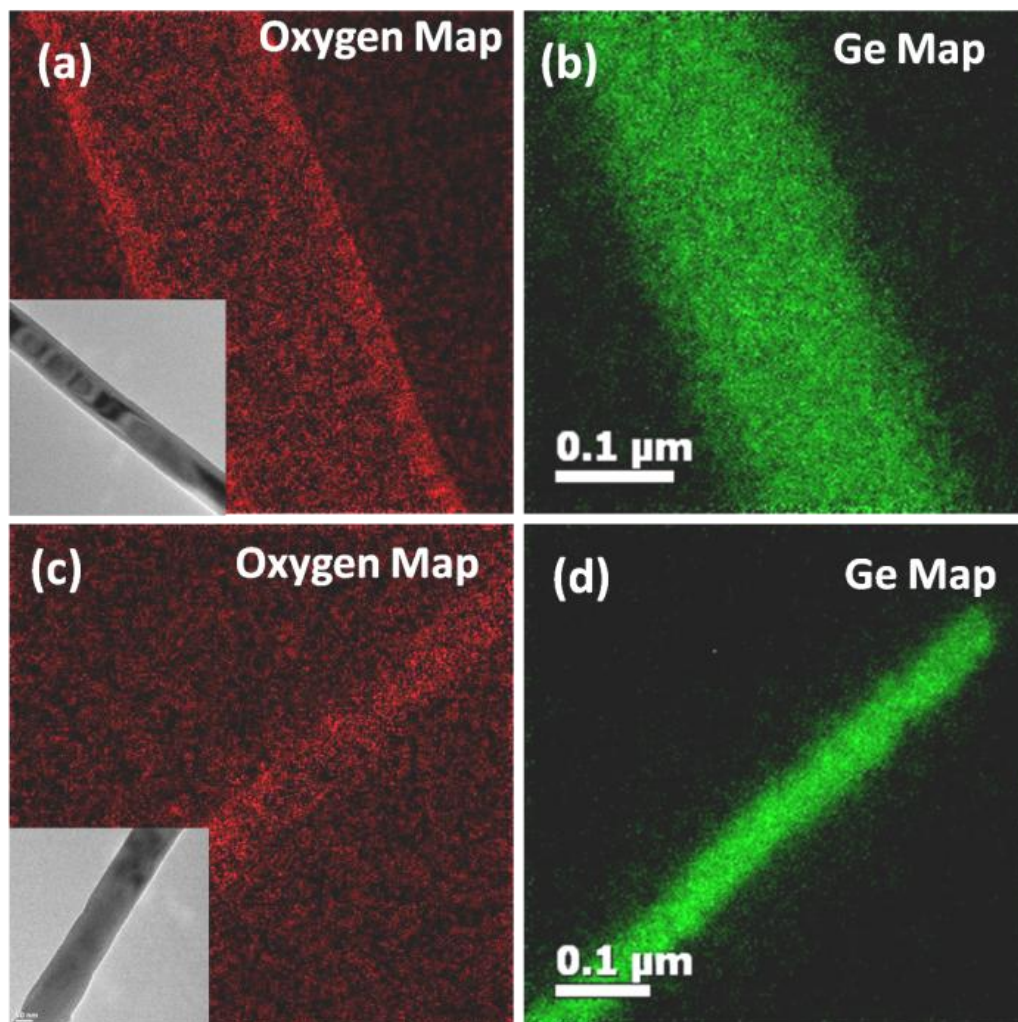
Figure 10. (a) and ((b) and showing the EELS mapping of O and Ge in the oxide rich NWs. (c) and (d) shows the EELS mapping of Oxygen and Ge map of the Ge NWs grown in a reducing environment. Insets show the TEM image of the NW under investigation.

We have also performed an EELS mapping on the NWs. The previously grown Ge NWs, as shown in Fig. 10a, has Oxygen (O has been quantified through the K shell) distribution throughout sample, with more density of O at the sides of the NW. The background for the EELS spectrum also has Oxygen, coming from the alcohol solvent and oxidization of the carbon grid on which the TEM sample is placed. In the NW grown in reducing environment (see Fig. 10c), O content is very low and is almost equivalent to the background noise and uniformly distributed throughout the NW. In both cases (see Fig. 10b and 10d), the Ge (Ge has been quantified through the L shell) is highly dense with uniform distribution, though, in the reducing growth environment, Ge shows higher density (there are brighter and denser green spots).

The removal of Ge oxide post growth is also possible through dilute HF etching. The Raman Spectra of an ensemble of Ge NWs, etched with 1% HF solution as a function of etching time is plotted in Fig. 11. The GeO_2 peak intensities slowly decrease as we increase the etch time. The NWs are completely stripped of its oxide layer beyond 10 sec of etching in the acid solution.
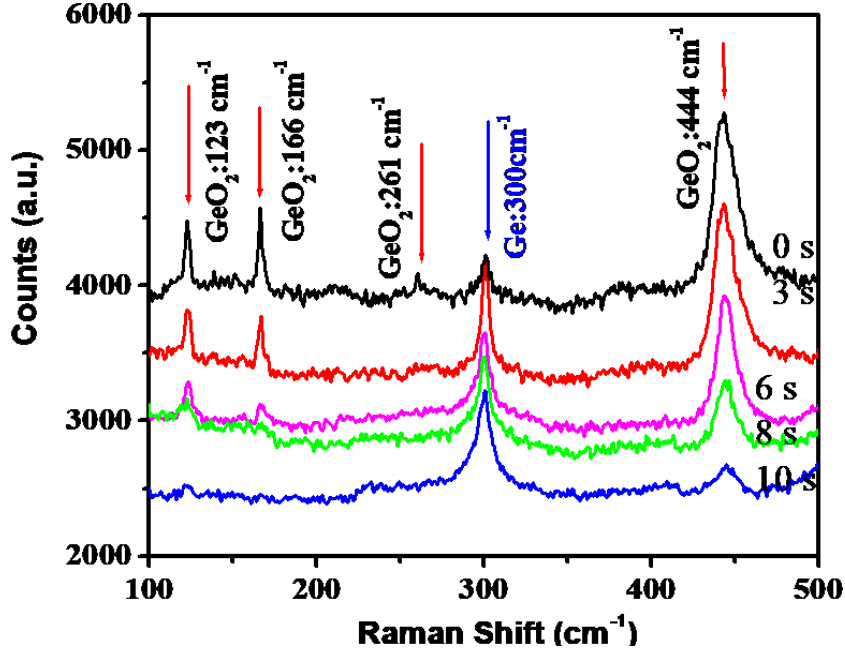

Figure 11. Raman Spectrum of the Ge NWs with etching time of 0, 3, 6, 8 and 10 seconds.

The surface roughness is an important parameter especially for surface characterization of NWs. We have used AFM to quantify the surface roughness of a Ge NW. The diameter fluctuation can be quantified through a rms height deviation (*h*). The surface mapping of a NW was taken in tapping mode down to a 300nmX300nm scan area. Initially, the AFM tip was scanned over a larger area to first identify a nanowire. Then, the area was magnified and at each step, the surface mapping was done (see Figure 12). Finally, when ~80% of the scan area was covered by the NW, we mapped the area and Section analysis was performed along the diameter of the NW (as shown in Fig. 12(c)). The section analysis data was converted into an x-y data file and fit using a Spline fitting function in Mathematica. The section data and spline fit data was subtracted to get the error which is the fluctuation in the diameter of a NW as shown in Figure 13. This rms height *h* is then extracted from the error plot. We have taken an average of all the section analysis performed on multiple NWs. We get rms surface roughness of a Ge NW, *h*= 0.48 ±0.09 nm.
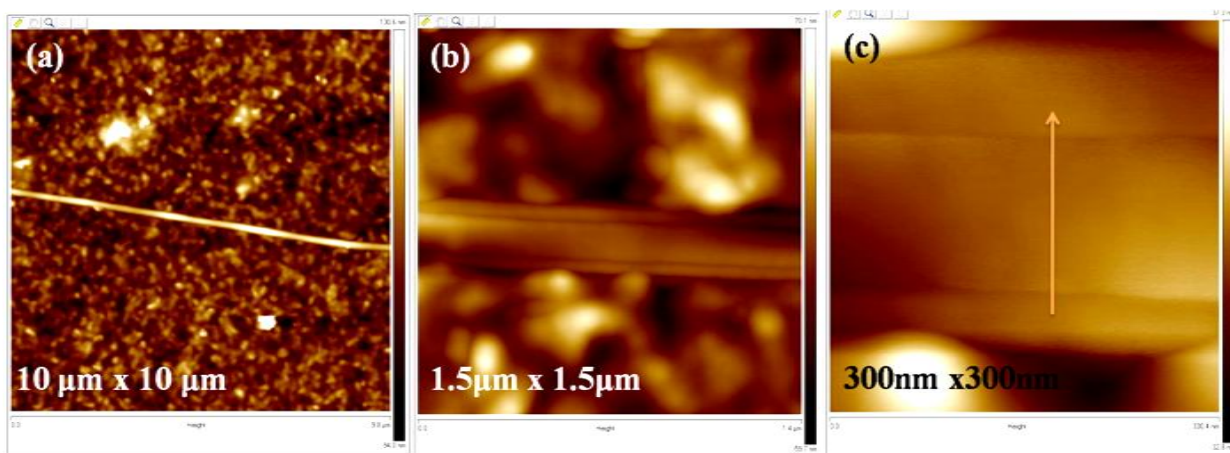
Figure 12. AFM image of a Ge NW at different magnifications with (c) showing the arrow along which section analysis was performed.
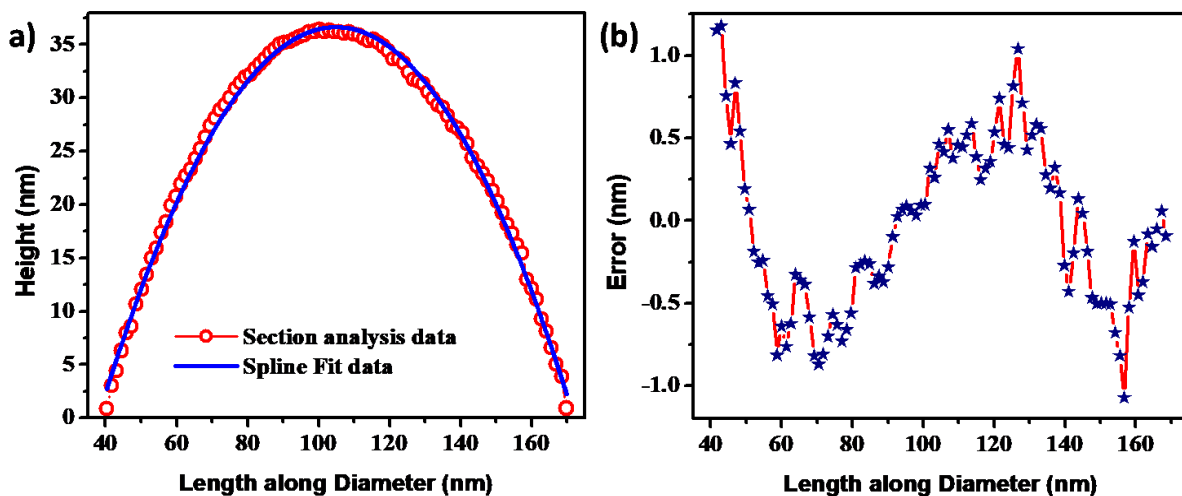

Figure 13. Section analysis data and Spline fit data of a diameter section. (b) The diameter fluctuation in a nanowire.

E. CONCLUSIONS

We have grown single crystalline highly oriented Ge NWs by the VLS method, with Au NP as a catalyst. The growth of unwanted oxide on the Ge surface during growth can be avoided by growing it in a reducing environment. The oxide layer can also be etched out completely by mild acid etching. The modified growth process with use of H_2 mixed with carrier gas and also use of an oxygen getter successfully prevents formation of oxide layer. Through EDAX in Scanning TEM mode we see that the

oxide layer exists at the surface of Ge. The Ge oxide formation post growth is unavoidable and a thin native oxide layer, 1-5 nm (self-limiting) forms. All these techniques were necessary to determine the morphology, crystal structure and composition in Germanium nanowires. These studies form an essential part of the thesis as utilizing specific information from each of these specialized equipments, we have been able to support our experimental findings, that is discussed as and when deemed appropriate.

REFERENCES FOR CHAPTER II

[1]R. A. Laudise, *The Growth of Single Crystals*, (Englewood Cliffs, N.J.: Prentice-Hall, 1970).

[2]B. A. Wacaser, K. A. Dick, J. Johansson, M. T. Borgstrom, K.Deppert, and L. Samuelson, *Adv. Mater.*, 21, 153–16, 2009

[3]R. S. Wagner and W. C. Ellis, *Appl. Phys. Lett.* 4, 89, 1964

[4]W. Lu and C. M. Lieber, *J. Phys. D: Appl. Phys*. 39, R387-R406, 2006

[5]S. Kodambaka, J. Tersoff, M. C. Reuter, and F. M. Ross, *Phys. Rev. Lett,* 96, 096105, 2006

[6]H. Wang, L. A. Zepeda-Ruiz, G. H. Gilmer and M. Upmanyu, *Nat. Commun*. 4, 1956, 2013

[7]E. I. Givargizov, *Journal of Crystal Growth* 31, 20—30, 1975

[8]A. M. Morales and C. M. Lieber, *Science*, 279, 208, 1998

[9]W. Lu and J. Xiang, *Semiconductor Nanowires: From Next-Generation Electronics to Sustainable Energy, Chapter 1*(Royal Society of Chemistry, 2014)

[10]N. Wang, Y. Cai, R.Q. Zhang, *Materials Science and Engineering,* R 60, 1–51, 2008

[11]K. A. Dick, *Progress in Crystal Growth and Characterization of Materials*, 54, 138-173, 2008

[12]Y. Wu, Y. Cui, L. Huynh, C. J. Barrelet, D.C. Bell, and C. M. Lieber, *Nano Lett*. 4, 433-436, 2004

[13] J. Wallentin and M. T. Borgström, *J. Mater. Res*., 26, 2011, 2142

[14]J. Lim, K. Hippalgaonkar, S. C. Andrews, A. Majumdar and P. Yang, *Nano Lett*., 12, 2475−2482, 2012

[15]Y. Wu and P. Yang, *Chem. Mater*., 12, 605-607 605, 2000

[16]Y. Wu and P. Yang, *J. Am. Chem. Soc*., 123, 3165-3166, 2001

[17]H. Lu and X. Meng, *Scientific Reports,* 5, 11263, 2015

[18]S. Sett, K. Das and A. K. Raychaudhuri, *J. Appl. Phys.* 121, 124503, 2017

[19]R. Mukherjee, S. Das, A. Das, S. Sharma, A. K. Raychaudhuri and A. Sharma, *ACS Nano* 4 3709, 2010

[20]T. Hanrath and B. A. Korgel, *J. Phys. Chem. B*, 109, 5518-5524, 2005

[21]T. Hanrath and B.A. Korgel, *J. Am. Chem. Soc*., 126, 15466-15472, 2004

[22]D. Wang, Y. Chang, Q. Wang, J. Cao, D. B. Farmer, R. G. Gordon and H. Dai, *J. Am. Chem. Soc*. 126, 11602-11611, 2004

[23]R. H. Kingston, J. Appl. Phys. 27, 101, 1956

[24]S. Sett, K. Das and A. K. Raychaudhuri, *J. Phys.: Condens. Matter* 29, 115301, 2017

[25]S. Sett, A. Ghatak, D. Sharma, G. V. Pavan Kumar and A. K. Raychaudhuri, *J. Phys. Chem. C*, 122, 8564−8572, 2018

[26]J. Oh and J. C. Campbell*, J. Electron. Mater*., 33, 364, 2004

[27]J. H. parker Jr, D. W. Feldman, M. Ashkin, *Phys. Rev*., 155, 712, 1967

[28]P. Gillet and A. L. Cleach*, J. Geophys. Research,* 95, 21635-21655, 1990.

CHAPTER III

DESCRIPTION OF EXPERIMENTS: SINGLE NANOWIRE DEVICE FABRICATION, AND ELECTRICAL, OPTOELECTRONIC AND THERMAL MEASUREMENT SETUPS

We have used a combination of electron beam lithography and photolithography to achieve metal electrode connections to single nanowire devices. The process is well known, though challenging as completing such a task successfully needs careful and precise experimentation, with each step playing an equally important role as the others.

We have used single Ge nanowire (NW) devices for electrical and optoelectronic measurements. Solely electrical measurements were executed for temperature dependent contact property study and electronic transport study. We have used a variable temperature insert in a closed cycle cryostat from room temperature to ~ 6 K. For a quick low temperature conductivity measurement we have used a home-made dipstick, which we insert in liquid N_2. Opto-electronic measurements were performed in ambient conditions (25^0C and atmos. pressure) in a dark room with an optical set-up. The thermal measurements were done on ensemble as well as single NW which were as-grown or dispersed on a substrate. Thermal measurements were done in humidity controlled atmosphere through a micro-Raman Spectrometer setup, equipped with a temperature controlled sample stage and a microscope objective lens.

A. SINGLE NANOWIRE DEVICE FABRICATION

Micro and nano fabrication has developed with integrated circuit manufacture. The advantages of using the electron beam to pattern was studied in the sixties, where the minimum feature size possible was ~20nm,[1] which was not limited by diffraction limit of optics. In the following decades, machines dedicated to nanofabrication was developed which currently gives a linewidth of 5nm and a pitch of 14nm.[2]*Lithography* or "writing on stone" is this method of fabricating a desired patterned on a substrate in the context of device fabrication. The principle of lithography involves using/drawing a mask to pattern a device and its realization. There is mainly three forms lithography, barring soft lithography namely photolithography (PL), X-Ray lithography and electron beam lithography (EBL). In all these forms, a

sensitive material (resist) is coated on a substrate which we need to pattern and on exposure to an external agent (light, X-ray or electron beam), changes its chemical bonding. This changes its solubility property and according to the tone of the *resist*, is removed by *developing* in a suitable solvent. Thus we get a patterned substrate on which we deposit a desired material followed by *lift-off* in a solvent. The schematics are shown in Fig. 1. These are the basic steps involved in lithography, be it of any type. We will look at the details of only the two forms, PL and EBL in details followed by the process of single nanowire (NW) device fabrication.
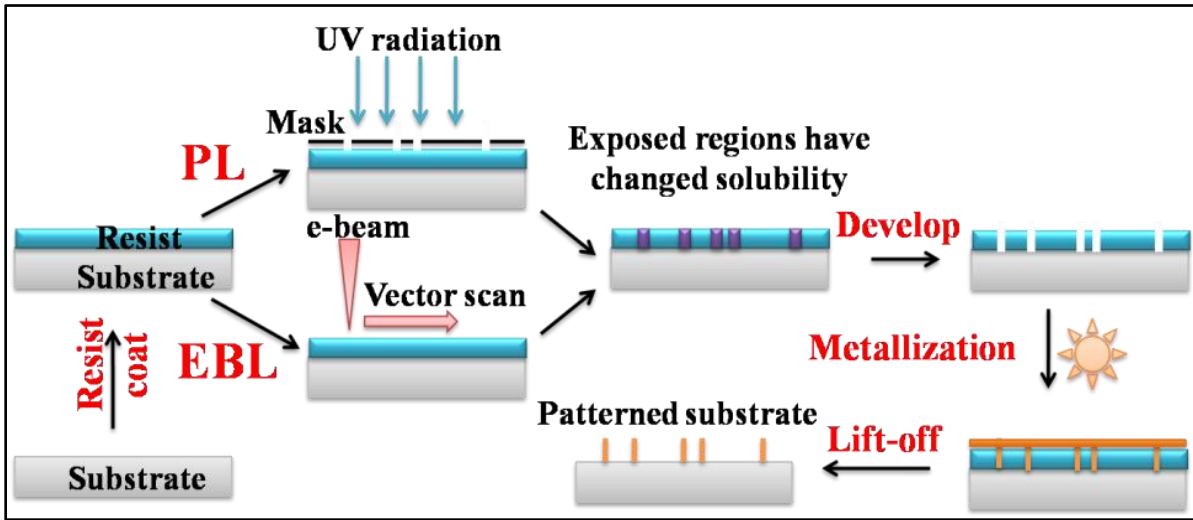

Figure 1. Schematics of the patterning process using PL and EBL.

1. Hierarchy of steps involved

The single Ge NW devices were fabricated by the following procedure. The as grown Ge NWs on the Si wafer were dispersed in ethanol and sonicated. This ensures that the NWs are freed from the substrate and are evenly distributed in ethanol. The dispersion was then drop-cast (50-100μl) onto SiO_2(300nm)/Si substrates which have larger pre-existing connection pads made by photolithography. The NWs are then identified as to which is optimal for the nature of our work and has been anchored on to the substrate through Focused electron beam (FEB) deposited Platinum (see Fig. 2). Two square blocks of Pt are deposited on both ends of the NW, which has dimensions around 500nm X 500nm. This anchoring has a dual purpose. It prevents the NW from moving/displacement while spin-coating procedure and also serves as a marker while pattering with EBL. The 2-p and 4-p contacts (with Cr/Au or Ni) to the NWs were made by multiple step electron beam lithography followed by metallization and lift off. We have also used FEB deposited Pt as the electrode material. The work flow of single NW device fabrication is given in Fig. 2.

The single nanowire device fabrication has been performed inside a cleanroom. It is necessary to have a clean, dust free working environment for device manufacture at nano-regimes using lithography techniques since a dust particle (diameter <0.5μm) can hamper the synthesis/fabrication process. A clean room has a controlled environment with a very low level of air-borne pollutants such as dust, aerosol particles and chemical vapors. The level of contamination is specified by the number of particles per cubic meter at a specified particle size. Air coming from an outside source is filtered to eliminate dust, and the inside air is re-circulated through HEPA (High efficiency particulate air) filters and/or ULPA (ultra-low particulate air) filters that remove contaminants produced from within the cleanroom. People entering and leaving the cleanroom have to do so through airlocks including an air shower stage and have to wear protective clothing. We have a Class 1000 (Federal Standard 209E) cleanroom where, particulates of diameter <0.5μm, is maximum of 1000/cm^3.
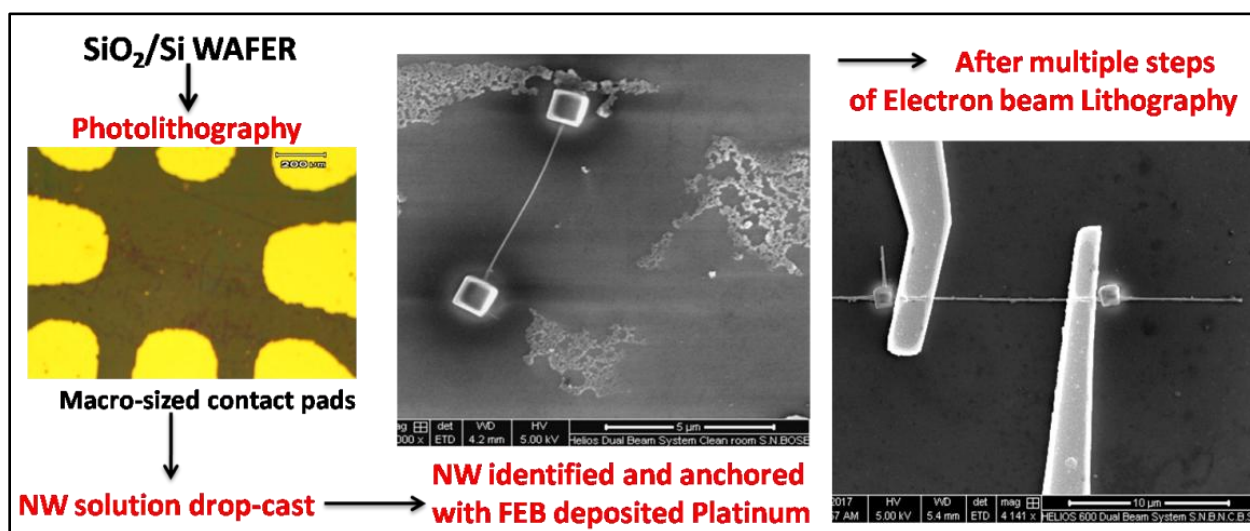

Figure 2. A flow chart showing the steps used for single NW device fabrication.

B. PHOTOLITHOGRAPHY

We have used photolithography to design the macro-sized contact electrodes on which we can make electrical connections. We have used the contact method in which, a mask is placed in direct contact with a substrate on a chuck. The chuck is connected to a vacuum system. The contact method is advantageous since proximity effects due to diffraction do not hamper the accuracy of the pattern. We can go down to 0.1 μm resolution using this method. The photo-mask is patterned according to the need of design necessary for the device. We have used a plastic sheet on which the design has been printed by solid ink, which was available commercially (shown in Fig. 3a). For the resist we use SU-8 (2000), which is a negative photoresist. It is an epoxy dissolved in an organic solvent accompanied by a photo-acid

generator. On exposure to UV radiation (Hg lamp with emission at 435.8nm), the polymer cross-links and on curing, forms microstructures that have high mechanical stability. The process and recipe[3] followed by us given in the following section.

Sample Cleaning

Substrate cleaning is the foremost and an important part of the process. It determines the sticking capability of the organic layer on the substrate. We have used insulating SiO_2(300nm) on top of Si substrate (001 orientation, lightly p-doped withρ in between 1-10Ωcm). Typically 0.5x0.5cm wafers have been used. We have used Trichloroethylene (TCE) to remove grease and organic material on the substrate. It was followed by washing in de-ionized water and this cycle was repeated with acetone and ethanol. The substrate was blow dried with de-humidified air.

Development of pattern

The clean substrate is placed on a rotating platform which is connected to a vacuum chuck. The resist is drop-cast with a micropipette (~ 100μL) and spun for a specific time. The spinning speeds depend on the thickness of the layer. Typically a speed of 2000-2500rpm is used which gives a thickness of ~2.2-2.4μm.We use a pre-baking also known as soft bake for 15 mins at 90-100^{0}C. This is usually done to remove excess solvent in the spin-coated resist film.

A mask is placed and the resist-coated wafer is then exposed to UV radiation followed by post-bake. The exposure time depends on the film thickness and the light intensity. It has been optimized to 90 seconds in our machine/setup. The formation of the cross-linking in the resist is a two-step process. The activated monomers are formed on exposure and polymer formation, which is catalyst mediated process requires a temperature of 60-70^{0}C, at which the wafer is post-baked for 10 mins. Thus, the regions exposed to light, become mechanically stable and resistant to the *developer* (1-Methoxy-2-propyl acetate), which is essentially a solvent the can dissolve the unexposed SU-8 film. This is thus a negative resist, which means, the part in which light does not fall is etched out. A developed wafer is shown in Fig. 3b. An optimum etching time determines the sharpness of the pattern and also the degree of under-cutting due to lateral etching.

Metallization

The developed wafer is then taken for metallization. If at all there are any remnant resist on the desired area of the pattern, it may be removed by an O_2 plasma etch. It is not a necessary step in PL but has been performed systematically during EBL and is discussed later. The resist patterned wafer is then loaded in an evaporation chamber. We have used physical vapor deposition methods like e-beam evaporation

(EBE) or thermal evaporation. For high-melting point materials like Ni, to achieve reasonable deposition rate, resistive heating is not sufficient. In such materials, localized heating by an electron beam can cause evaporation. A hot filament emits electrons by thermionic emission and electrons are accelerated through a potential difference of several kV, which are guided by a magnetic field via the Lorentz force to strike the material to be evaporated, that is kept in a graphite crucible. In case of thermal evaporation, as name suggests, the target material is evaporated by resistive/Joule heating kept in a Tungsten/Molybdenum boat. Metals like Cr and Au have been thermally evaporated. The substrate is mounted on a holder perpendicularly on top of the material. The vacuum in the chamber is kept $< 10^{-6}$ mbar, which allows deposition since the mean free path of the evaporating particle is determined by the number of gas molecules in the chamber. A high vacuum system consisting of a rotary pump connected to an oil diffusion pump and/or a turbo-molecular pump was used. A mean free path of $\sim$ 30cm needs a vacuum $\sim 10^{-3}$ mbar if particle size is $\sim$0.3 nm. The EBE chamber had an ultra high vacuum of $\sim 10^{-8}$ mbar. The vacuum also prevents impurities from deposition and prevents target particles from chemically combining. The film thickness was determined during evaporation by a quartz crystal thickness monitor. We have usually deposited a layer of Cr $\sim$ 5nm followed by Au ($\sim$ 80 nm) on the patterned substrates thermally and Nickel film ($\sim$60nm) deposited by EBE.
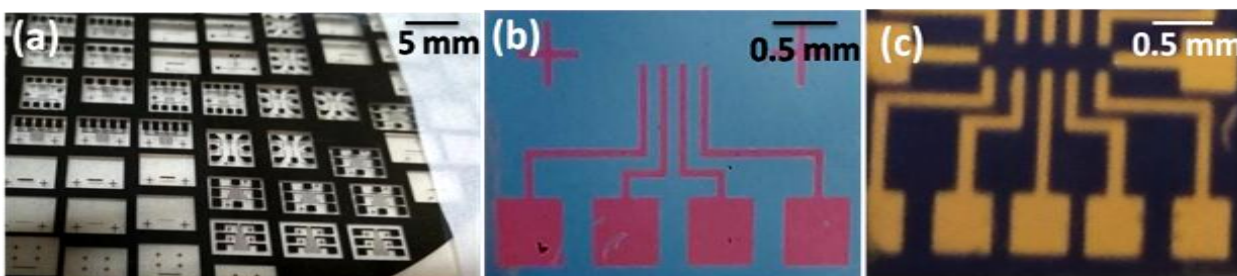

Figure 3. (a) A PL mask. (b) A developed pattern on SiO_2/Si, with blue region in which resist persists and the purple region which has developed, showing a 4-p pattern. (c) A patterned wafer with Au which appears yellow.

Lift-off

Post metallization, the entire substrate is covered with desired metal film. Thus, a *lift-off* process is necessary, that removes metal from the unwanted regions and keeps it in the region of negative mask. The metal which is on top of SiO_2 (which was etched out as it was unexposed), sticks to the substrate. While the metal on top of the regions that have resist, on dipping in a remover (solvent for the cross-linked polymerized SU-8) is washed away. It is a diffusion limited process and may need ultra-sonic treatment for proper removal of resist (since it is mechanically very stable and resistant). Thus, as the underlying

resist layer washes away, the metal film is also removed from the regions. So, it works as a negative resist i.e. regions which were unexposed (black region of the mask) has metal layer while the exposed regions have no metal film. Post lift-off, the wafer is washed in ethanol for removal of remnant organic material. A patterned wafer fabricated by PL is shown in Fig. 3c.

C. ELECTRON BEAM LITHOGRAPHY

To design the nano-sized contacts to a NW upto to the larger PL fabricated electrodes, we have used EBL. It works on the same principle as the PL but instead of the UV radiation, there is a highly focused electron beam which can alter the solubility of the resist, and thereby be developed. The EBL system is a modified and upgraded version of a Scanning Electron Microscope (SEM) coupled with beam control from the pattern generator and software to draw the desired pattern. Here, a pre-patterned mask is not necessary and the pattern we need can be dawn using a Computer Aided Design (CAD) program. It also has a beam blanker for deflecting the beam. As opposed to SEM, the electron beam is vector scanned instead of raster scanned. It does not scan areas which are not to be exposed. Instead, the beam is rapidly deflected between exposed features and is draws/fills one feature at a time. Commercial available high end nanofabrication tools are dedicated for EBL only. We have used the Helios dual beam system for our work (see Fig. 4) It has a special feature of a Focused Ion Beam (FIB) along with the usual field emission (FE) electron source. It is equipped with a Beam Blanking System and Nanometer Pattern Generating System (NPGS).
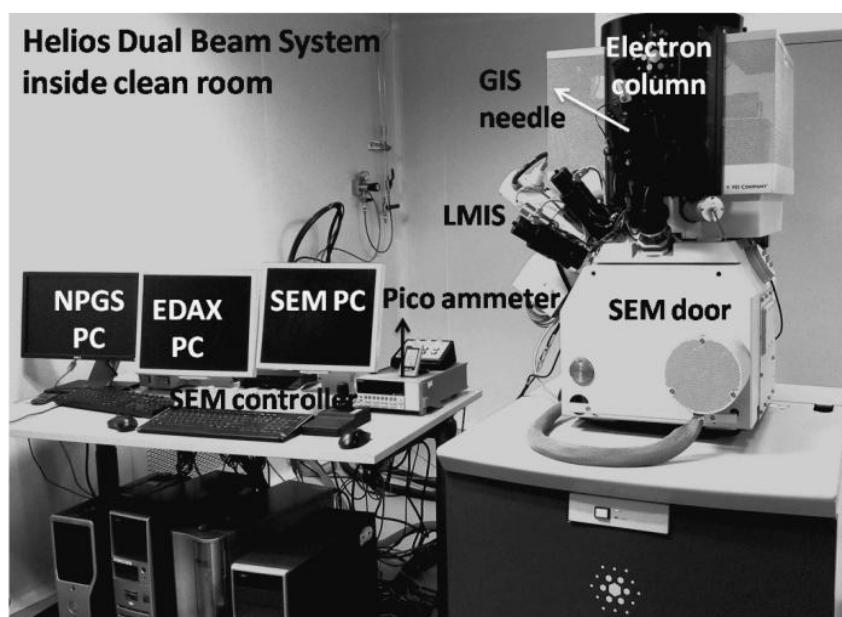

Figure 4. Helios dual beam system.

Process

The process for patterning using EBL is similar to PL, expect, here we can draw/design our own mask with the CAD program, which then gets scanned onto the resist coated substrate. We have used a double layered Poly methyl methacrylate (PMMA), a positive resist of different molecular weight. PMMA is a long chain polymer that is broken into smaller, soluble fragments by the electron beam. A double layer is advantageous for lift-off purposes. If we use a single layer, during development, there is lateral etching which leads to undercutting, and the pattern becomes less accurate. Also, during the lift-off process, if there is a single layer, the metal on the patterned region tends to get removed. Hence, we use a double layer of resist. For the resist, we use 5% PMMA 350K and PMMA 950K, dissolved in chlorobenzene. The first layer is spun at 3000rpm and baked at 180^0C for 90seconds followed by the second layer of 950K at 6000rpm at 120^0C for 45 mins. The resist coated wafer is then transferred to the EBL machine. The spin speed, temperature, time etc has been optimized for best output results.

Pattern generation and writing

Prior to scanning any pattern, it is important that the SEM is calibrated properly. It involves checking gun and column alignment, calibrating and setting up the beam current, and adjusting beam focus and astigmatism. The optics and expertise to create a finely focused electron spot is essential. The factors that are under control of the user in pattern generating are: electron beam energy, dose, current and development time. The factors that influence these are backscattering of electrons (proximity effect), forward elastic scattering (that broadens the beam), and during development, overdevelopment due to capillary forces and line edge roughness caused by statistically fluctuating effects at small dimensions[5]. Thus, every step needs to be optimized to obtain the perfect desired design onto the wafer.

After a series of dose, current and working voltage tests, we have optimized certain important parameters. Usually a voltage of 20keV has been used with Dose of 200-250μC/cm^2. The current varies, depending upon the pattern dimensions. For designing electrodes that connect directly onto the NW, which has a feature size of ≤ 1μm in one direction, we use 11pA of current. Typically for patterns which are around 100μm, we have used 690-1400pA current. We have used NPGS software for designing the electrodes/connections, which has been converted to a file which the NPGS uses to control and deflect the e-beam. A precise control is obtained by adjusting the electrical deflection of the beam to the stage whose position is monitored using two laser interferometers.

Pattern drawing through CAD is simple. Marking the position such that there is exact mapping of the area we draw and the area that gets exposed by e-beam needs careful operation. Thus, it is essential to use markers so that a relative co-ordinate system can be used to draw the pattern with respect to the wafer.

Once, the pattern is drawn and the co-ordinates setup, we need to run the file in the NGPS software. Care should be taken not to expose the wafer before or after patterning.

The developing time is very critical, since the solubility rate of the exposed resist is quite high. We have used a mixture of methyl isobutyl ketone (MIBK) and Isopropyl alcohol (IPA) in the ratio 1:2 as a developer. The etch time is typically 3-5 seconds and at each time it is best to check the developed pattern through an optical microscope to determine whether the desired pattern is developed optimally. The exposure time (t) depends on the dose (D), current (I) and area of exposure (A) as, $DA = It$, so a low exposure will lead to an under-developed pattern, which means that the partial remnants exist at the undesired regions. While, a longer exposure time will lead to overdeveloping and the pattern will not be sharp and may merge into neighboring ones if the gap between them is less (of the scale of the pattern). These situations may also exist due to lesser/longer developing times. Exposure and development are interconnected to each other. It is so because, longer chain polymers may also be soluble if the developing time/strength is increased.

Even though there may be an optimum time for development, there are chances of remnant resists in the patterned region which are not visible through the optical microscope. So, as a precautionary measure, we use oxygen plasma etching to remove it. An inductively coupled plasma reactive ion etcher (ICP-RIE), SI 500 by Sentech Instruments was used for this purpose. With ICP power of 200 W and a process pressure of 0.6Pa, the etch rate of PMMA was determined to be ~350nm/min. Thus, an etching time of 2 seconds is enough to remove a few nm of remnant resist. PMMA is readily etched by O_2 by a purely chemical process. In the last step of the EBL process, which is connecting the NW to an electrode, we have used Ar plasma to clean-up the remnant resist, since O_2 may cause reactive etching on the Ge NW surface. Ar gas was chosen because it is non reactive and will not cause any chemical damage since it etches by ion milling/sputtering. In some cases, we have etched the Ge NW surface (which is exposed post development) with a dilute (1%) HF solution for a few seconds to remove/etch unwanted oxide.

D. FOCUSED ELECTRON BEAM DEPOSITED METAL

The Helios dual beam system can also pattern insitu using its electron beam assisted metal deposition. In the presence of a metal-organic precursor gas, a focused e-beam (FEB) can pattern directly insitu on the sample. Metal-organic gas molecules are adsorbed on a substrate, which on irradiation by an e-beam, dissociate into nonvolatile components and form a deposit. It consists of a nano-composite material: metal nanoparticles (~ few nm) embedded in a matrix of amorphous carbon. Here we have used the precursor

methyl-cyclo-penta-dienyl tri-methyl platinum ($C_9H_{16}Pt$) which is solid at room temperature and needs a warm-up period prior to deposition. The pattern can be drawn on the Helios dual beam SEM control software. The electrodes to a NW can also be fabricated through this process. We have also used this method to pattern Pt anchors at the ends of a NW, which act as markers during the EBL process.

E. A GLIMPSE INTO THE SINGLE NW DEVICE FABRICATION BY EBL

A preview of the multiple EBL steps showing connection to a single NW is given in Fig. 5. For the final connection to the NW, we have in certain cases also used FEB deposited Pt as the electrode material. SEM image of three single NW devices of 4-p, 2-p with EBL and a 2-p with FEB deposited Pt is shown in Fig. 6.
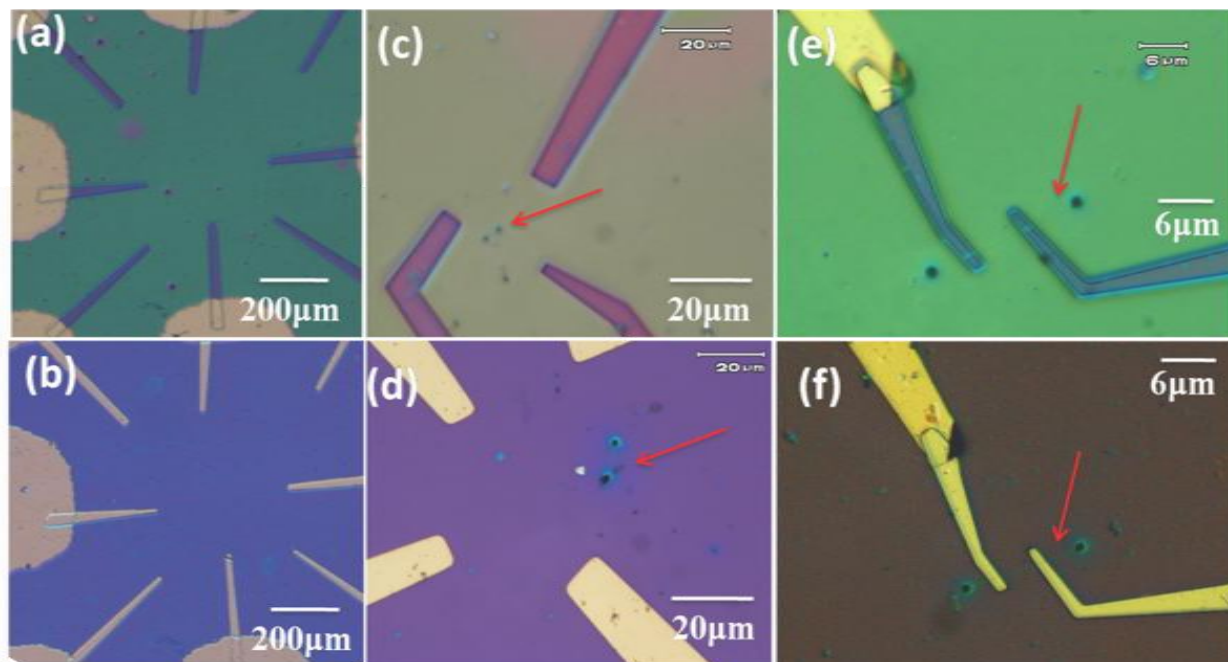

Figure 5. This image shows the multiple steps of EBL performed for a single Ge NW connection. Panel (a), (c) and (e) show optical images of resist coated wafer after EBL writing and development. Panel (b), (d) and (f) show wafers post metallization. The red arrow marks the position of the NW, while the black dots are the FEB deposited anchors to the NW.
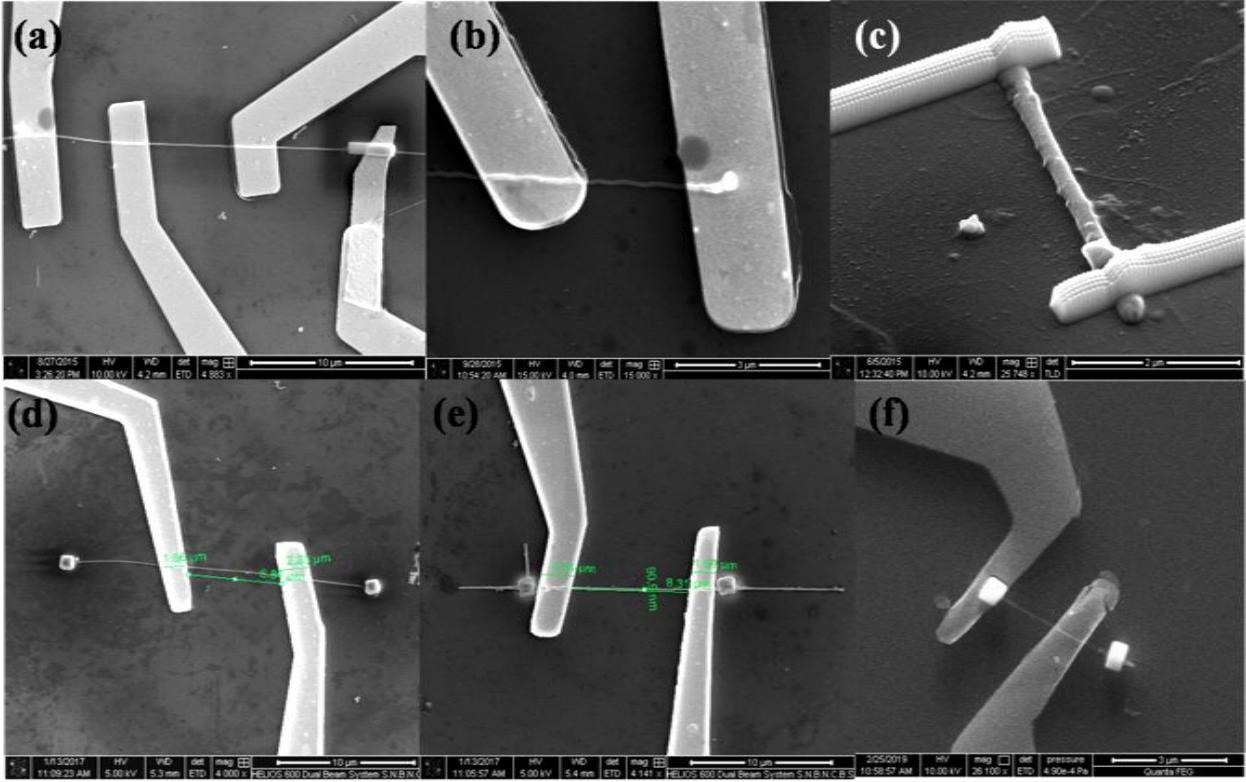
Figure 6. SEM image of single Ge NW device in (a) 4-p configuration, (b) 2-p configuration and (c) 2-p configuration using FEB deposited Pt.[4] SEM image of three other NWs in 2-p configuration fabricated using EBL with Cr/Au electrodes in (d) and (e) and (f) connected with Ni.

F. DEVICE PREPARATION

Single Ge NW devices were used for electrical and opto-electronic measurements. The sample (5mm x 5mm) was always mounted on a thin (~1 mm) mica sheet with GE-varnish to provide good thermal anchor at cryogenic temperatures while keeping electrical insulation. Electrical connections to a Ge NW were made on the macroscopic (~2mm x 2mm) metal contact pads (see Figure 7(a)). An enameled Cu wire (Gauge number: 39) was dipped partially in ortho-phosphoric acid and the two ends etched out. One end is attached to the metal electrodes through a conducting silver epoxy paste (sheet resistance ~0.02 Ω/sq.). The sample is dried for 6-8 hrs before any measurements are done. The other end of the Cu wire is soldered onto a printed circuit board. From here, banana or BNC connectors are used to connect to the required instrument. While handling and connecting a single NW device, we have always used an antistatic wrist band. It is an antistatic device used to safely ground a person to prevent the buildup

of static electricity on their body, which can result in electrostatic discharge. These discharges are sufficient to damage sensitive electrical components like a single NW.

G. EXPERIMENTAL SET-UPS

1. Low temperature set-up

Electrical measurements upto 77K was taken in a homemade dip-stick. The home-made dipstick has four stainless steel rods connected to a base on which PCB electrical connections have been made. A Pt-100 is used as a temperature sensor and a 50Ω Manganin wire wound on the base plate is used as a heater. These are drawn internally through hollow SS pipes onto a probe head and eventually connected to a Lakeshore Temperature controller. The sample is mounted on the base (see Figure 7(b)) and electrical connections from it are attached to the PCB at the base which is connected to the probe (internally through the hollow SS pipes). Connectors from the probe directly go to the sourcemeter through a banana connector. A bigger SS hollow cylinder is used as the probe carrier connected to vacuum through bellows by a rotary pump (10^{-3} mbar pressure). Flanges with rubber O rings are used to keep the system airtight and maintain vacuum. This evacuated probe is dipped in liquid Nitrogen kept in a dewar. The schematic of the device is shown in Fig 2.

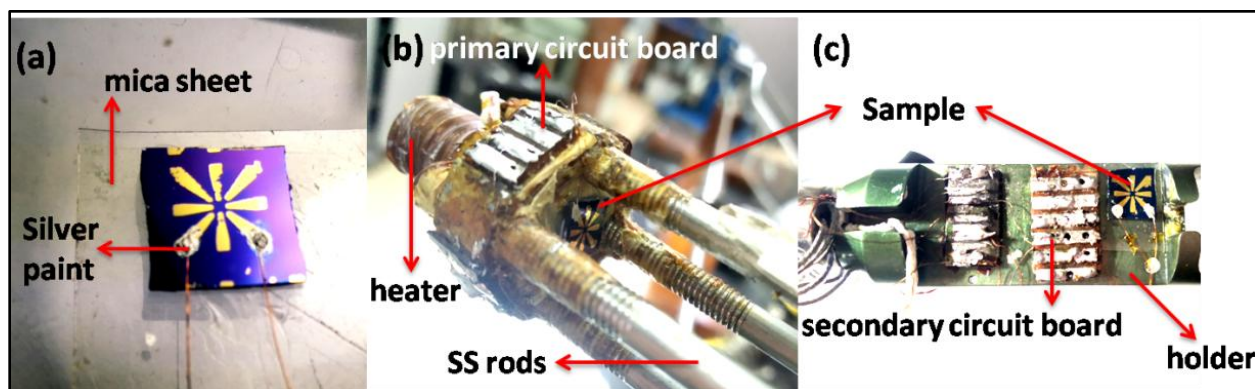**Figure 7.** (a) A sample ready for measurement with larger contacts connected to contact electrodes by silver epoxy. (b) Sample mounted on the home-made dipstick. (c) Sample mounted on the variable temperature insert.

The electrical measurements were taken from 300K to 6K using a cryogen free variable temperature insert (CF-VTI) in a closed cycle He cryostat, which cools through a two-stage Grifford-McMohan

cryocooler. Temperature was controlled through a Cernox sensor connected to a Resistance heater through PID in a Lakeshore Temperature controller. Other temperature sensors located in the VTI system can be monitored through a LabView program. The outer jacket of the VTI system has a radiation shield and is kept under high vacuum (10^{-6} mbar). The cryocooler cools down the second stage to ~ 4.2 K. At this temperature, the closed circuit pure He gas flow can be started. There is a reservoir of pure He maintained to the correct working pressure through which the closed gas circuit is connected. The He gas flow is controlled through a needle valve. Circulation of this He takes place through a closed circuit through a scroll pump. This enables operation of the VTI from 4.2K to 300K, once base temperature is reached and He gas starts flowing continuously. The VTI system has a 16-pin Fischer connector for the different thermometers placed at various cooling stages. The VTI has a 30mm vertical sample access bore made of stainless steel. The probe has a 6 pin Fischer connector, which has two heater leads and the four for calibrated Cernox sensor. The probe also has another 11 pin Fischer connector, with eight connections made on a PCB at the sample platform. The sample is placed on this platform (see Figure 7(c)) and a silicone heat sink compound was used to glue the sample to the heating stage. Banana connectors are used from the probe head to the sourcemeter. The image of the VTI is shown in Fig. 8.

Figure 8. (a) Schematic of the home made low temperature dip-stick. (b) Cryogen free VTI system.

We have measured the Voltage at a fixed current as a function of sample temperature. From this we extract the resistance and in turn the resistivity or conductivity. We have measured *I-V* characteristics at a fixed temperature from 300K to 6K at an interval of 20K. A source meter was used for taking electrical data which was automated using a programme written in C^{++} through a GPIB interface.

2. Optical set-up

Opto-electronic studies were performed in ambient conditions using a standard Xenon light source with a monochromator in the range 300-1100nm. A schematic of the experimental setup is shown in Fig. 9. The Xenon light source characteristics have emission lines beyond 800nm, which results in a low minimum in light intensity at certain wavelengths. The system in the wavelength range upto 1100nm was calibrated using a Si detector with NIST traceable calibration. At longer wavelengths we used broad band source (range 300-2600nm with peak at 1000nm, intensity at 1800nm is ½ of that at 1000nm) with a fiber-coupled output and a band stop filter that blocks radiation with wavelength < 980nm. The electrical measurements were taken by a sourcemeter or by current amplifier input of a lock-in amplifier (LIA) with chopper modulated illumination. The sample was placed inside a dark chamber with electrical leads connecting to a sourcemeter or LIA. For these measurements we have used LabView program to collect the I-t and I-V curves under illumination and in dark using a GPIB interface. From these, we get the photocurrent as a function of intensity and Responsivity as a function of wavelength.
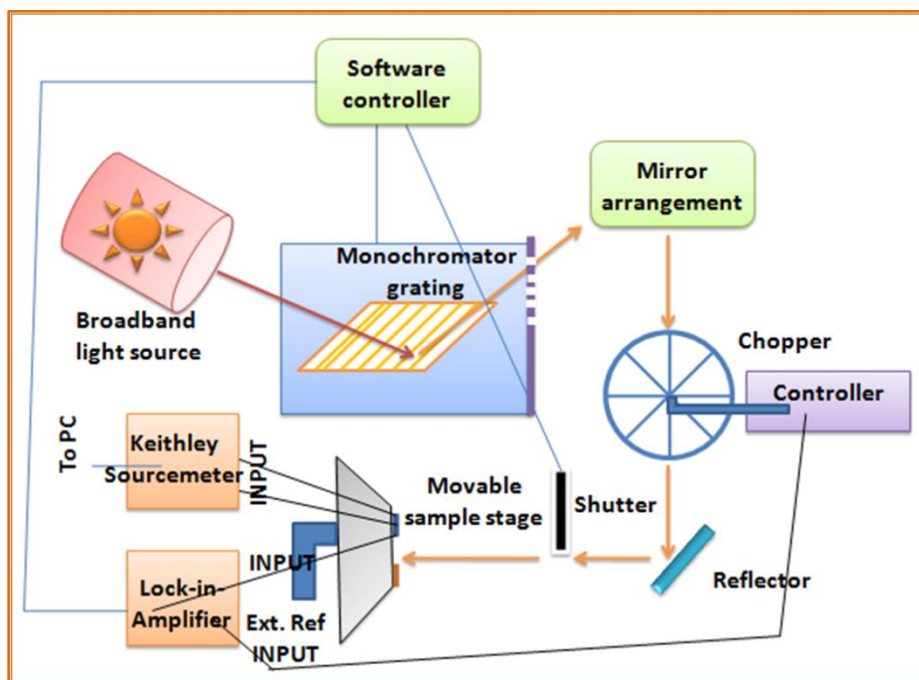

Figure 9. Schematic of opto-electronic setup.

3. Raman Spectroscopy set-up

Raman spectra of an ensemble of NWs as well as a single Ge NW was recorded using a Lab RAM HR spectrometer with 1800 gr/mm grating and Peltier cooled CCD detector. An argon-ion laser wavelength

488 nm was used as excitation light source with 100X objective and a numerical aperture of 0.9 was used to focus the laser and collect scattered intensity. The experimental setup is shown in Fig. 10. The temperature variation of the substrate from 83K to 900K was carried out in a vacuum chamber connected to a PID controlled heating stage, with N_2 vapor cooling facility (Linkham THMS600). We have recorded the Stokes line in this experiment. The spectrometer was calibrated with a Si (001) oriented single crystal, with known Raman line at 520.7cm^{-1}. The room was maintained at a temperature of 25^{0}C with humidity controlled to < 35%. (We have used the Raman Spectroscopy set-up in Bose Institute, Kolkata.)
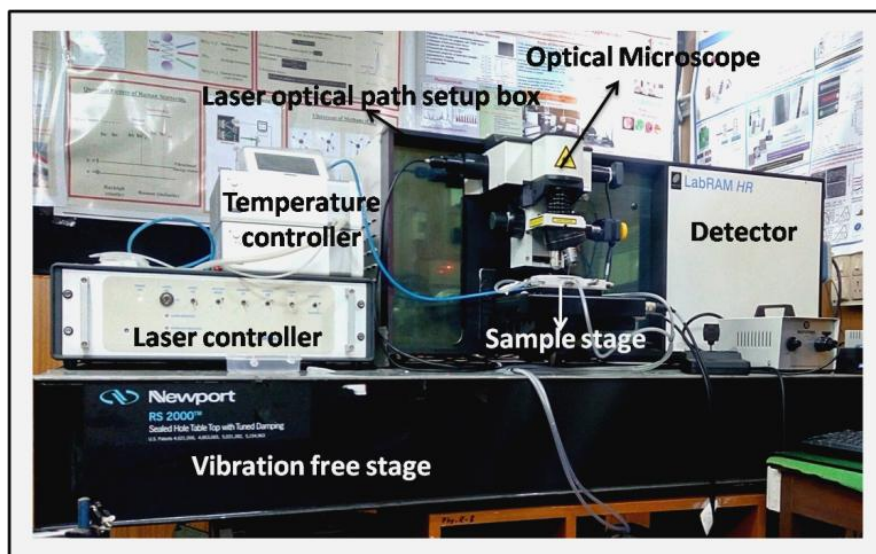

Figure 10. Raman Spectroscopy setup at Bose Institute, Kolkata (courtesy Dr. Achintya Singha)

The Ge NWs on Si wafer was placed on a temperature controlled stage with an optical window. The NW was first identified through a 100X objective lens and then focused through the laser. The FWHM of the laser is ~700nm, and needs careful handling to focus onto a single NW. The room was completely dark while collecting the scattered intensity through a notch filter that blocks the Rayleigh intensity. The Raman spectrometer gives the intensity as a function of the wavenumber in cm^{-1}. The temperature dependent Raman spectrum was recorded from 80K to 800K at regular intervals. The Raman data has been collected at the lowest possible laser power ~4-6 µW to avoid any local heating that may give rise to peak broadening and/or peak shift. We get the peak position as a function of temperature from this measurement. The power of the laser, falling through the microscope is measured through a flux-meter.

Raman Spectroscopy has been used a probe to determine the local temperature rise in a NW and will be discussed in Chapter VIII in the context of the study of thermal properties in a single nanowire.

H. REMARKS

The use of electron beam lithography for making single Ge NW devices was successfully implemented and is a challenging task. It requires careful experimentation at each step, as all the steps are equally important to obtain the final product of a single Ge NW connected to metal electrodes. Since there are multiple steps of EBL involved, the process becomes tedious and tough. In some cases, two EBL sessions and in others three sessions were necessary, depending on the placement of the NW. Connections to FEB deposited Pt are one level simpler since we do not have to deal with EBL on top of the NW. Usually, the final level connection is most interesting. Since the gap between two electrodes ~ few microns and the electrode size ≤ 1μm, it is critical not to overexpose or even overdevelop. Thus, once in a span of six months, we have had to do a calibration check, to optimize the current and dose, which will give the best pattern with a reasonable pitch post lift-off. Along with it, maintenance and calibration of the machine is an important part of EBL. Since we are dealing with a NW of say 5 μm length and diameter ≤ 100 nm, a machine shift of even ~ 100 nm is destructive to the pattern. For every machine, there are certain short comings related to the shift of the e-beam focus, with respect to the kV and current. In certain cases, if we need a current shift from 1400pA to 170pA, there may be a shift in the e-beam centre point which may not coincide with the centre of the pattern designed. With regular machine handling, it becomes clear which current shifts cause error and which do not and care should be taken in these subtle things. Thus, keeping the shift in mind, the pattern may be designed in such cases. This may also happen if we change the kV. Thus, to prevent such unforeseen and uncontrolled errors, it is advisable to do multiple steps, where, in one step a particular range of current is used that do not cause any beam shift. Even though, this lengthens the process of preparing a single Ge NW device, it preserves accuracy.

All the measurements experimental setups were calibrated by the user prior to experiment.

REFERENCES FOR CHAPTER III

[1]T. G. Mollensted and R. Speidel, *PhysikaZische Blatter*, 16, 192, 1960

[2]C. Vieu, F. Carcenac, A. Pepin, Y. Chen, M. Mejias, A. Lebib, L. Manin-Ferlazzo, L. Couraud and H. Launois, *Appl. Surf. Sc.*164, 111–117, 2000

[3]R. Basori, Ph.D thesis, submitted to Calcutta University (2016).

[4]S. Sett, K. Das, and A. K. Raychaudhuri, *J. Appl. Phys*., 121, 124503, 2017

[5]X. Zhao and S. Lee*, J. Vac. Sc. Techn. B* 32, 06F505, 2014

CHAPTER IV

STUDY OF ELECTRICAL CONTACTS TO SINGLE GERMANIUM NANOWIRES

Making contact to Ge nanowire (NW) poses a formidable challenge and it is due to some fundamental nature of the Ge surface that leads to Fermi level Pinning. We have done an extensive investigation on this issue to find a way to make low resistance contact to Ge NW. We have shown that there is suppression of Fermi level pinning in metal contacted Germanium nanowires. We have also been able to achieve one of the lowest reported values of specific contact resistance on a Ge NW. We find that the barrier height at the metal/nanowire interface is inhomogeneous and has a Gaussian distribution that leads to large temperature dependent ideality factor.

A. INTRODUCTION

One of the issues that need to be addressed in a semiconductor device is the junction characteristics of the semiconducting material and the metal contact electrode which is governed by the barrier height and contact resistance. The type of contact formed at the metal-semiconductor (MS) junction affects the charge injection process. A barrier forms when a metal comes in contact to a semiconductor surface. The nature of contact and the barrier formation depends on the distribution of the energy states at the interface region that lies in the band gap region.[1] In general, the barrier height (φ) will depend on where the Fermi level (E_F) lies in the spectrum of interface states. Ideally in absence of interface states the barrier height will be determined by the work function of contacting materials as per the simple Schottky-Mott rule given by,

$$\varphi = \varphi_m - \chi_{sc} \tag{1}$$

for n-type systems and

$$\varphi = \chi_{sc} + E_g - \varphi_m \tag{2}$$

for p-type materials, where φ_m is the work function of the contacting metal, χ_{sc} is the semiconductor electron affinity and E_g is the semiconductor band gap. Even in presence of interface states (that occur almost always) if they have a uniform spectral distribution the variation of the barrier height with charge

density at the interface is gradual and the barrier height follows the Schottky-Mott rule.[1] A schematic diagram of barrier height formation in presence of uniform density of interface states is shown in Fig. 1a.

However, a wide spectrum of experimentally observed Schottky barrier height (SBH) data goes beyond the simple Schottky-Mott rule. In many semiconductors like bulk Ge there are dense bunching of interface states near the mid gap region.[2,3] When a metal is brought in contact with such a surface the charge distribution to bring the Fermi levels in alignment brings the E_F in the region where there are highly bunched interface states and the Fermi level gets pinned (FLP) (see Fig. 1b). In this case the barrier height becomes independent of the charge density and work function of the contacting material. This had been first proposed by Bardeen in the context of explaining work function independent barrier formation in bulk Ge and is applicable when the density of surface levels lies within the band gap and are sufficiently high.[4] It has been seen experimentally that even for an elemental semiconductor like Si, contacted with different metals, the SBH does not follow this Schottky-Mott rule.[5] This variation can be traced upto the sharp dependence of the SBH on the atomic structure of the MS interface.
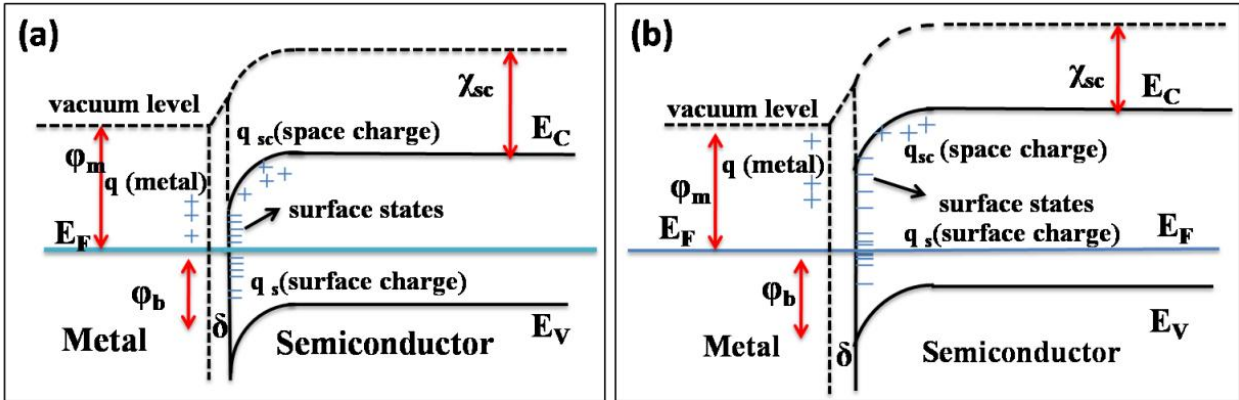

Figure 1. (a) MS junction with uniform distribution of interface states. (b) MS junction with densely bunched interface states.

It has been shown through experiments and numerical calculations that the chemistry of formation of the SB at the metal/semiconductor interface is the cause for variation of SBH.[6] Even though, apparently it may seem that the MS junctions are ideal, they may not be atomically smooth. The extent of SBH sensitivity to various physical and chemical factors can be understood from the following examples. Even a difference in the orientation of atomic planes of two interfaces- type A and type B in NiSi$_2$/Si(111), causes a barrier height difference of 0.14 eV.[9] The Ni-Si hybridization is the main cause for this difference, which for one case, has presence of unpaired electrons that can be compared with dangling bonds on the surface of a nanowire. The formation of a SB depends on the initial stages of the metal layer

deposition due to formation of defect state levels at the interface,[7,8] induced indirectly by the adatoms. Hence, a layer of adsorbed oxygen at the MS interface can modify the SB formation dynamics. It is immensely sensitive to the surface of the semiconductor material as well as the environment for metal deposition. Surface treatments like plasma etching can impart energy which causes surface modification as well as disorder in the semiconductor.[9] These treatments are essential for nanowire devices fabricated by electron beam lithography, where remnant resists needs to be etched out for better lift-off. Structural inhomogenity can also affect the SBH at the MS interface, like point defects near the MS interface, inhomogeneous interface structure or even compound phases at the interface.[9] These make the SB far from ideal, which requires different and unique analysis for each MS system.

The process of contact formation has been investigated in the bulk in technically important semiconductors like Si, Ge, GaAs etc. using metals with different work functions. In general in Ge, metal induced mid gap defect states are thought as the cause for large contact resistance, arising from FLP at 0.5-0.6eV due to interface states.[2,3] The strategy for prevention of defect state formation led to use of very thin insulating layers (e.g., TiO_2, ITO, ZnO and other insulators) that limit the spread of the electron wave functions of the metals into Ge, thus reducing formation of metal induced interface states. It has been shown that these insulators in low thickness (1-10nm) can reduce the value of specific contact resistivity ρ_C to lower than $10^{-8}\Omega.cm^2$ and this is particularly effective when the Ge is heavily doped[15-17] with carrier density in excess of $10^{20}/cm^3$.

One important aspect that we sought to answer is whether in doped NWs of low or moderate resistivity, we can establish a clear relation between ρ_C and φ with the nanowire resistivity (ρ_{NW}). This is a useful development from the work reported before[13] where this has been investigated in NWs of higher resistivity. There are clear indications of suppression of FLP leading to a dependence of ρ_C and φ on metal work function. We also wanted to study the contact behavior with different metal electrodes, hence varying work functions. Another very important parameter (and its temperature dependence) that has not been investigated before in the context of Ge NWs is the ideality factor (η) associated with contact junctions. The present investigation thus sought to answer a cross-section of these important issues that arise when a single Ge NW is made into a device using metal contacts made by lithography followed by lift-off.

B. EXPERIMENTAL METHOD

We have measured the *I-V* curves for the Metal-Semiconductor-Metal (MSM) single nanowire devices that were measured as a function of temperature from 300K down to 30K. The *I-V* curves are non-Ohmic

since there exists a barrier at the MS interface as discussed in Section A. A typical *I-V* curve at room temperature and as a function of temperature is shown in Figure 2 so that the non-Ohmic nature can be appreciated. The nanowire length often limits the feasibility of 4-p configurations as it needs a longer wire. 2-p measurement has the drawback of contribution from the contact resistance being included with the nanowire resistance. To separate out the contact contribution, the 2-p configuration has been treated as a Metal-Semiconductor-Metal (MSM) device. We show below that an analysis based on MSM device allows us to separate out the contact resistance contribution.
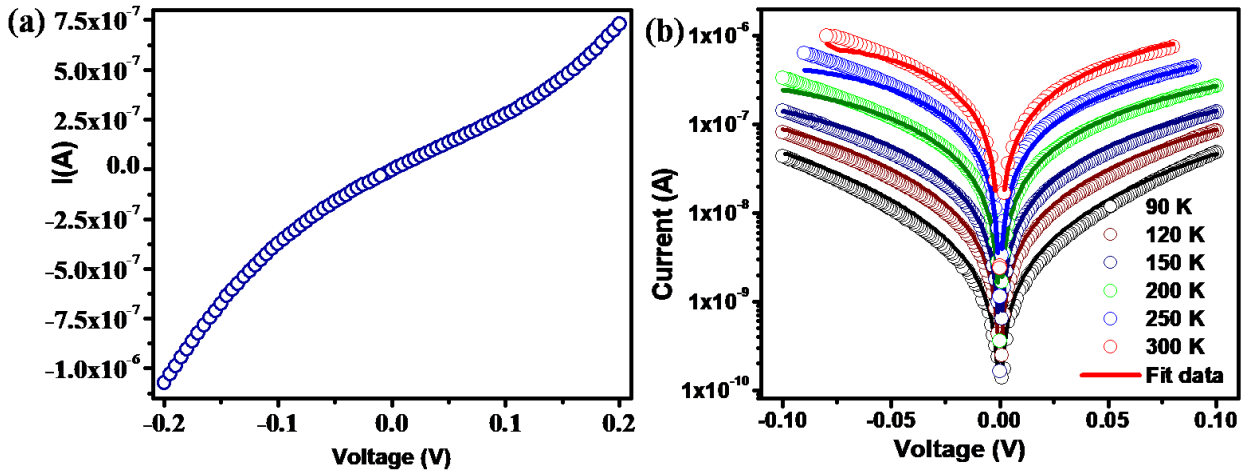

Figure 2. (a) A typical I-V curve at room temperature. (b) *I-V* characteristics as a function of temperature with solid line fitted to equation 5.

We analyzed the *I-V* data using the MSM model for back-to-back Schottky diodes connected by a NW in between with resistance of R_{NW}.[14] This method has been effectively used in previous studies[15,16] to determine the NW resistivity and separate out contribution due to the contact resistance. For an ideal Schottky diode, the thermionic emission (TE) at the MS junction gives the *I-V* characteristics as,

$$I = I_0 \exp\left(\frac{-\varphi}{kT}\right)\left\{\exp\left(\frac{qV}{kT}\right) - 1\right\} \tag{3}$$

where, I_o is defined as, $I_0 = AA_R T^2$, where A_R is the Richardson constant and A is the area of contact, V is the applied voltage, φ is the barrier height at the contacts and k is the Boltzmann constant. An important parameter that governs the nature of charge injection at the MS interface is the ideality factor (η) which we assume unity. We will use the non-ideal case to maintain generality in our discussions. In case of a series resistance R connected with the diode, the equation modifies to,[14]

$$I = I_o \ \exp\left(\frac{-\varphi}{kT}\right)\left\{\exp\left(\frac{q(V-IR)}{\eta kT}\right) - 1\right\} \tag{4}$$

For two back-to-back non-ideal diodes with a series resistance R_{NW} in between the two ends, this equation takes the form of the modified Richardson-Dushmann equation[17] which is given by,

$$I = I_0\left(\exp\left(\frac{qV'}{\eta kT}\right) - 1\right)\frac{\exp\left(\frac{-q(\varphi_1 + \varphi_2)}{kT}\right)}{\exp\left(\frac{-q\varphi_2}{kT}\right) + \exp\left(\frac{-q\varphi_1}{kT}\right)\exp\left(\frac{qV'}{\eta kT}\right)} \tag{5}$$

where, , $V' = V - IR_{NW}$, φ_1 and φ_2 are the barrier heights at the two contacts. The total resistance of the device is thus: $R_{Tot} = R_{NW} + 2R_c$, where R_c is the contact resistance at the MS interface. This method allows us to separate out the R_c and R_{NW} from a 2-terminal (referred as 2-probe) measurement of $I - V$ (The two contacts are nearly symmetrical and we assume the same value of R_c for both contacts. The slight asymmetry of the contacts arises due to unequal transfer lengths at both the contacts, which could not be avoided during fabrication). We have then determined the specific contact resistivity, $\rho_c = R_c A_c$ where $A_c = \pi\beta dw$, and d is the NW diameter, w is the length of electrode covering the NW and β is the fraction of the NW covered by the electrode (we have used $\beta = 0.75$ for our calculations).[13] The SBH at both junctions is within 20% of each other and we have taken an average barrier height, φ.

C. RESULTS AND DISCUSSIONS

1. Evaluation of method

By using the modified Richardson-Dushmann we can decouple the contact effects from the true resistance of the NW in case measurement cannot be done in a 4-p configuration. This method has been effectively used in previous studies[16,17] to determine the NW resistivity and separate out contribution due to the contact resistance. This method also allows extraction of the R_{NW}, R_c as well as average contact barrier height φ, which are important parameters needed for analysis of the barrier.

To validate the analysis using equation (5), we used the following procedure. For the sample A, we have made four contact electrodes and resistance of the NW was measured in both 4-p and 2-p configurations. We have measured resistance as a function of temperature. The R_{NW} can be easily obtained from the 4-p data and it can also be obtained from equation (5) from the 2-p data. It can be seen from Fig. 3(a), that the value of resistance obtained from both the methods show identical results. We have also calculated the contact resistance R_c in both ways. From the experimental data, we get R_c by subtracting the 2-p from the

4-p data. R_c has been determined from the fit data by subtracting the 2-p data from R_{NW} (as obtained from fit to equation (5)). These two methods also agree very well as shown in Fig. 3(b). This establishes that the analysis of the *I-V* data using the model is a valid procedure and we can use it not only to find ρ_{NW} but also the contact parameters (barrier height, ideality factor and the contact resistance) that we need for the present investigation.
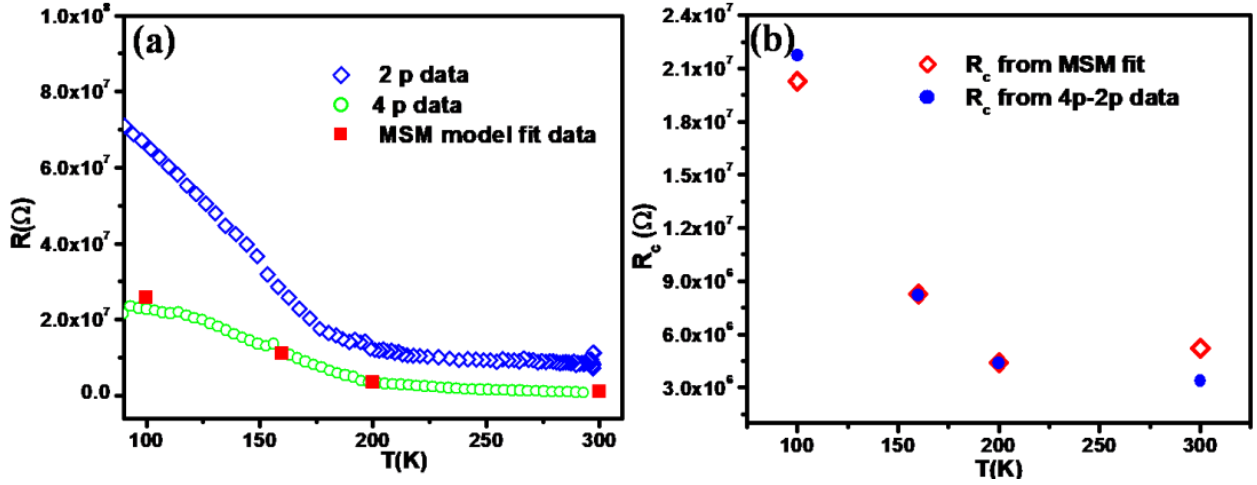

Figure 3. (a)Resistance verses temperature for the Ge A, showing R_{NW} determined from the MSM model fit and that measured from the 4p configuration. The 2p data are shown for comparison. (b) Contact resistance versus temperature for Ge A extracted by MSM method and from 4p-2p data.

2. Analysis of *I-V* characteristics

The *I-V* curves for at least ten single nanowire MSM devices were fit to the modified Richardson-Dushmann equation. A representative *I-V* characteristic as a function of temperature has been fit to equation (5) and is shown in Fig. 2b. At each temperature we used MSM model to analyze the *I-V* data to separate out R_{NW}, R_C, η and φ at the contacts. All the relevant data for room temperature (RT) have been summed up in Table 1. The R_{Tot}, R_{NW} and R_c obtained by fitting the *I-V* data for the NW sample D1 and has been plotted in Fig. 4a as a function of temperature. This NW has a room temperature resistivity $\rho_{NW} \approx$ 1.6×10^{-4} Ω.cm which is low and a relatively low specific contact resistance $\rho_c \approx 2.98 \times 10^{-6} \Omega.cm^2$. However, the contact resistance in this NW is found to be more dominant compared to the NW resistance itself. Previous temperature dependent resistivity measurements in Ge NWs have been done by 2-p method only and the effect of contact resistance were not discussed.[18,19] In the present investigation we evolved a mechanism that allows a method to separate out the contact contribution.

58

Table 1. Physical dimensions of the Ge NWs studied and fit parameters of the *I-V* curves at room temperature to the MSM model.

NW Name	Diameter (nm)	Length (μm)	Electrode	Nanowire resistivity ρ_{NW} (Ω.cm)	Specific contact resistivity ρ_c (Ω.cm^2)	Barrier Height φ (eV)	Ideality factor (η)
E	35	2.0	Cr/Au	3.1×10^{-2}	3.4×10^{-4}	0.246	2.36
1	65	2.0	Cr/Au	3.5×10^{-4}	9.9×10^{-7}	0.202	1.00
D1	90	1.9	Cr/Au	1.6×10^{-4}	2.98×10^{-6}	0.161	1.00
D1a[a]	90	1.9	Cr/Au	1.6×10^{-4}	1.25×10^{-6}	0.143	0.97
D2	90	4.5	Cr/Au	5.4×10^{-3}	4.1×10^{-4}	0.284	1.55
D2a[b]	90	4.5	Cr/Au	8.1×10^{-4}	6.9×10^{-6}	0.148	0.97
A	90	5.1	Cr/Au	2.4×10^{-1}	1.3×10^{-2}	0.325	7.3
A1	30	1.2	Cr/Au	4.9×10^{-2}	6.2×10^{-4}	0.298	3.1
M1	60	1.8	Ni	3×10^{-1}	4.6×10^{-3}	0.282	4.1
M1a[c]	60	1.8	Ni	1×10^{-2}	1.5×10^{-4}	0.252	2.25
N1	65	3.2	Pt	6.5×10^{-2}	1.09×10^{-3}	0.238	2.05

[a,b,c] Refer to the same NWs after annealing.

There is the only report so far concerning conventional electrical transport measurement at low temperature in single Ge NW only recently that shows that the transport mechanism to be hopping in nature.[20] The temperature dependent resistivity data for all the NWs is shown in Fig. 4b, which have been determined after the MSM fitting apart from NW A, in which the 4-p data is plotted. It is seen that ρ_{NW} of different Ge NWs vary by more than three orders of magnitude at RT, from 0.2mΩ.cm to 0.2Ω.cm. At RT the intrinsic resistivity of bulk Ge is ~ 46Ωcm. This indicates that NWs are not intrinsic and unintentional doping has occurred during growth from the Au catalyst as discussed in Chapter 2. The ρ-T data for the NWs shows semiconducting behavior with activated type of transport down to 200K, followed by a plateau region where there is saturation and carriers are mostly extrinsic and at very low temperatures,

due to carrier freeze out, the resistivity, $\rho \to \infty, T \to 0$. Measurement could not be taken upto 6K because the device resistance goes to the order of Giga-Ohms. The temperature region beyond 200K has been fit by the Arrhenius equation, $\sigma \sim e^{-E_a/kT}$ which gives activation energy (E_a) for the carriers. The E_a for all the NWs studied gives a value of ~ 106 ± 15 meV. The activation energy shows value less than that of the band gap energy (660meV) indicating presence of defect states in the band gap region. This has also been observed for disordered metals which shows activated transport due to trapping/de-trapping of electrons from defect states.[21] Some NWs that are highly doped have a negative temperature coefficient (NTC) of resistivity.[22] However they are metallic in nature because they do not show an activated behavior and shows a finite conductivity at zero temperature (see the low T limiting region in Fig. 4). Its resistivity saturates to a finite value as $T \to 0$. Such a behavior is in conformity with heavily doped bulk semiconductor like Si and Ge close to the insulator-metal transition boundary.[23] The behavior is similar to that of highly resistive disordered metallic alloys that also show NTC behavior despite being metallic.[24] For heavily doped semiconductor (bulk) the NTC arises from weak localization. The present chapter focuses on the study the effect of contact properties of Ge NWs and a detailed analysis of the temperature dependence of the resistivity of the NWs is beyond its scope and is discussed in Chapter VIII.
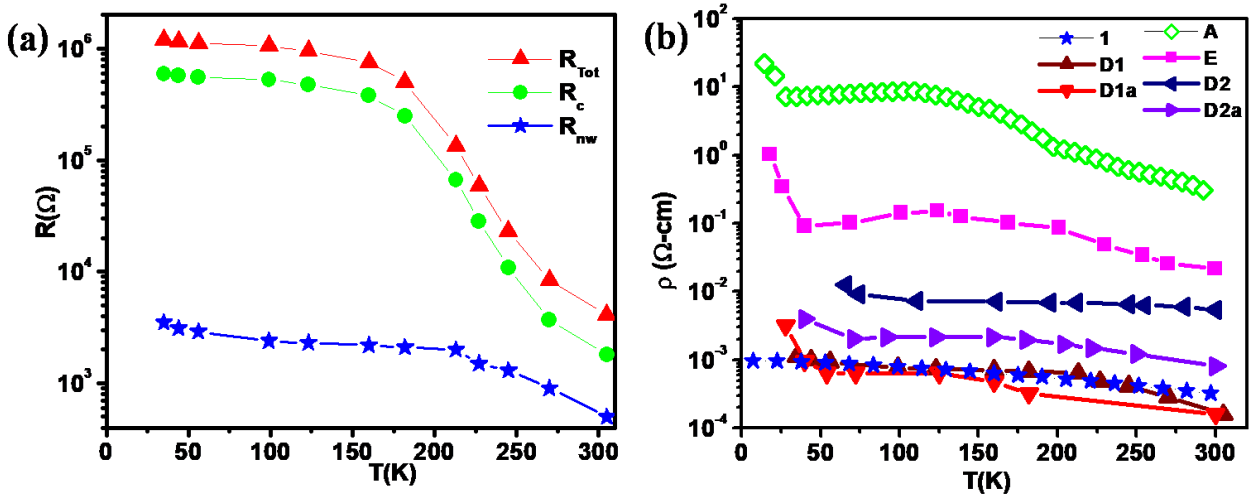

Figure 4. (a) Resistance verses temperature for the D1 NW, showing the NW resistance (R_{NW}) and the contact resistance (R_C) which has been determined by fitting. The total measured resistance R_{tot} is also shown. (b) Resistivity (ρ_{NW}) verses temperature (T) for all the Ge NWs studied. The sample names are the same as in table 1 which has the details. The NW names are written next to the corresponding curves.

3. Contact parameters as a function of nanowire resistivity

Both room temperature specific contact resistance ρ_c and Schottky barrier height φ are plotted as a function of nanowire resistivity ρ_{NW} (Fig. 5) at room temperature. The contact resistivity increases with the NW resistivity. The dependence of ρ_c on ρ_{NW} is almost linear. For ρ_{NW} lying from 10^{-4} to $10^{-1}\Omega.cm$, ρ_c lies in the range 10^{-6}-$10^{-2}\,\Omega.cm^2$. For the majority of the NWs, we have chosen Cr/Au contact as this is mostly used in making contacts to NWs and also Cr which makes the first contact to Ge, has relatively low work function (~4.5eV) compared to Au (~5.3eV), Ni (~5.1eV) or Pt (~5.6eV in polymer form). We use Cr also as a buffer layer because it sticks better to the SiO_2 substrate with a layer of Au (60-80nm) on top as it is less prone to oxidation as compared to Ag and Ni. In another NW, namely *N*, we have used Ni (~60nm) contact electrodes. Ni has a work function which is just lower than Au, but higher than Cr. This gives us a diversity of the types of contact material to a single Ge NW, which helps us to better evaluate the contact effects. In one of the NWs (sample name *P*), we also used Focused electron beam (FEB) deposited Platinum as the electrode material. This was done with a view to have an evaluation of such precursor deposited contacts and compare them with more conventional e-beam patterned metal contacts. The values of the contact resistance have an approximate linear dependence of ρ_c on ρ_{NW} and it is expected to be maintained even if the contact electrode material is different from the ones we have investigated.

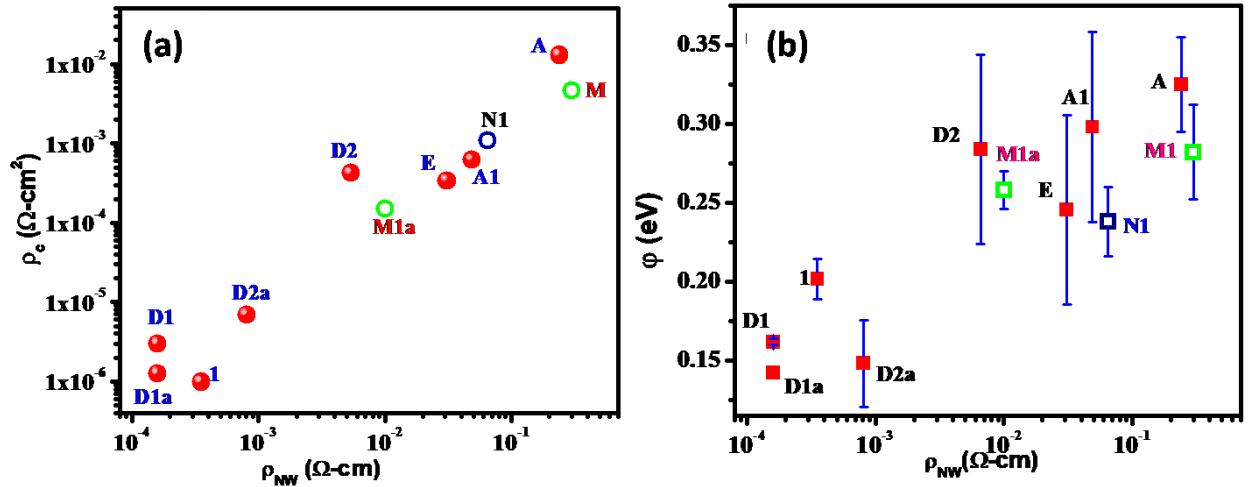**Figure 5.** (a) Specific Contact resistance (ρ_C) and (b) barrier height (φ) as a function of ρ_{NW} at 300 K. The Cr/Au contact materials are marked in red dots, Focused Electron Beam deposited Pt in blue and the Ni contacted NW is in green.

The lowering of ρ_c on reducing ρ_{NW} is expected to arise from larger carrier density of the NWs of less resistivity. At RT, the contact resistance ρ_c goes up as the barrier height φ goes up. The contact barrier also has a clear dependence on ρ_{NW}. For $\rho_{NW} < 10^{-3}\Omega.cm, \varphi < 0.2$ eV. However, for $\rho_{NW} > 10^{-3}\Omega.cm$, the barrier rises to beyond 0.25 eV. This value is still less than that seen in bulk Ge, where FLP leads to a large barrier height (0.5-0.6 eV)[17,18] irrespective of the contact materials. Recent report of suppression of FLP in Ge NW[13] shows that while for materials like Au that has work function in excess of 5 eV, the barrier height even in NW can be very high, in the vicinity of 0.4 eV. In Cr/Au contact the metal in contact with Ge is Cr that has a work function of 4.5-4.6 eV. The Schottky barrier within the vicinity of 0.15 eV to 0.2 eV observed in Ge NW (with relatively low resistivity) follows with the expectation that in Ge NW with side contact, there is indeed suppression of FLP.

4. Lowering of SBH upon annealing

We have investigated the effect of annealing on resistivity and contact parameters on two NWs with Cr/Au electrodes that have same diameter. We chose D1 close to the open tip (where the Au catalyst remains attached after growth) and D2, further away (~6 μm from the tip) which is expected to have less Au in it as explained in section 2. They have resistivities differing by an order (see Table 1). Their specific contact resistances differ by two orders. These NWs were vacuum annealed at 370° C (which is just above the eutectic temperature of Au-Ge) for an hour and the two NWs after annealing are designated as D1a and D2a. In both NWs annealing leads to a substantial reduction in contact resistances. For D1, which has lower resistivity, ρ_c comes down from $2.98 \times 10^{-6}\Omega.cm^2$ to $1.25 \times 10^{-6}\Omega.cm^2$, and there is no change in ρ_{NW}. Annealing leads to improvement of contact only. In case of the high resistivity NW D2, there is reduction of ρ_{NW} from $5.4 \times 10^{-3}\Omega.cm$ to a low value of $8.1 \times 10^{-4}\Omega.cm$ and ρ_c reduces from $4.1 \times 10^{-4}\Omega.cm^2$ to $6.9 \times 10^{-6}\Omega.cm^2$. The reduction in ρ_c in both the samples arises from reduction in the contact barrier. In case of sample D2 there is a large reduction in φ by nearly a factor of two and it reaches a value of 0.148 eV at RT which is the lowest barrier potential seen by us in the study. It is likely that the annealing leads to redistribution of Au atoms by diffusion in the contact regions leading to improvement of the contacts.

To ascertain the generality of our results, we have investigated the method of annealing with the Ni contacted Ge NW following the same principle of vacuum annealing near the Ni-Ge formation temperature of 400⁰C.[25] From Table 1, we can see the reduction in ρ_c from 4.6mΩ-cm² to 0.15mΩ-cm² on annealing and also a decrease in is φ by 24 meV. ρ_{NW} reduces by an order, from 0.3Ω-cm to 0.01Ω-cm. Annealing not only improves the electrical contacts, it helps in reducing defects in the NW and increases the mobility which in turn is reflected in the reduction of NW resistivity. Thus our investigation shows

that vacuum annealing at a relatively low temperature (that preserves the contacts as well) is an effective way to lower the contact resistance and the barrier. More details on annealing is given in Chapter V, Section 9 when discussing the opto-electronic properties of annealed single nanowire photodetectors.
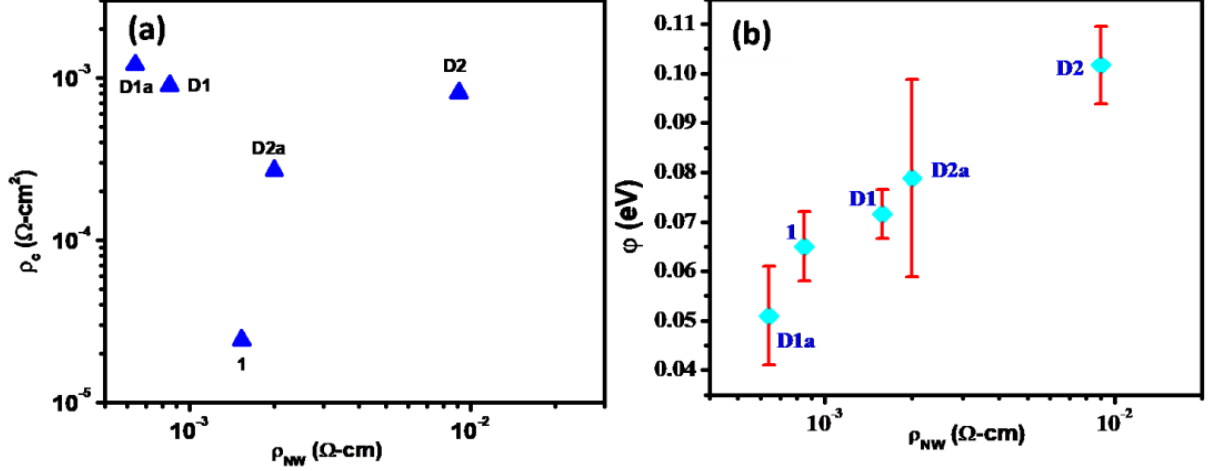

Figure 6. (a) Specific Contact resistivity (ρ_C) and (b) barrier height (φ) as a function of ρ_{NW} at 77 K.

5. Contact parameters evaluated at 77K

The dependence of ρ_c and φ on ρ_{NW} at 77 K is shown in Fig. 6. There is substantial augmentation of ρ_c on cooling. Though ρ_c still increases as ρ_{NW} increases, the good correlation between the two seen at 300 K is no longer strictly valid. Interestingly however, is the observation that the average barrier height (φ) shows softening on cooling. Enhancement of ρ_c on cooling along with softening of barrier height may appear self- contradictory if attention is not paid to the temperature factor. The apparent contradiction is resolved (as discussed quantitatively below) that the factor that determines ρ_c is not φ alone but the ratio, $\frac{\varphi}{k_B T}$, k_B being the Boltzmann constant. As a result even if φ is suppressed as T is decreased, if its rate of decrease is lower than that of T, then the ratio $\frac{\varphi}{k_B T}$ increases leading to enhancement of ρ_c on cooling. This can be evaluated quantitatively using the following equation of ρ_c,[26]

$$\rho_c = \frac{k_B \eta}{q T A_R} e^{\frac{2\varphi}{k_B T}}, \tag{6}$$

where, A_R is the Richardson constant, φ is the average barrier heights and η is the ideality factor of the diode. We have plotted ρ_c (normalized by the value at RT) as a function of T for two NWs D1 and D2

using equation (6) along with φ as a function of T in Fig.7. It can be seen that even if φ is suppressed on cooling the ρ_c actually goes up.
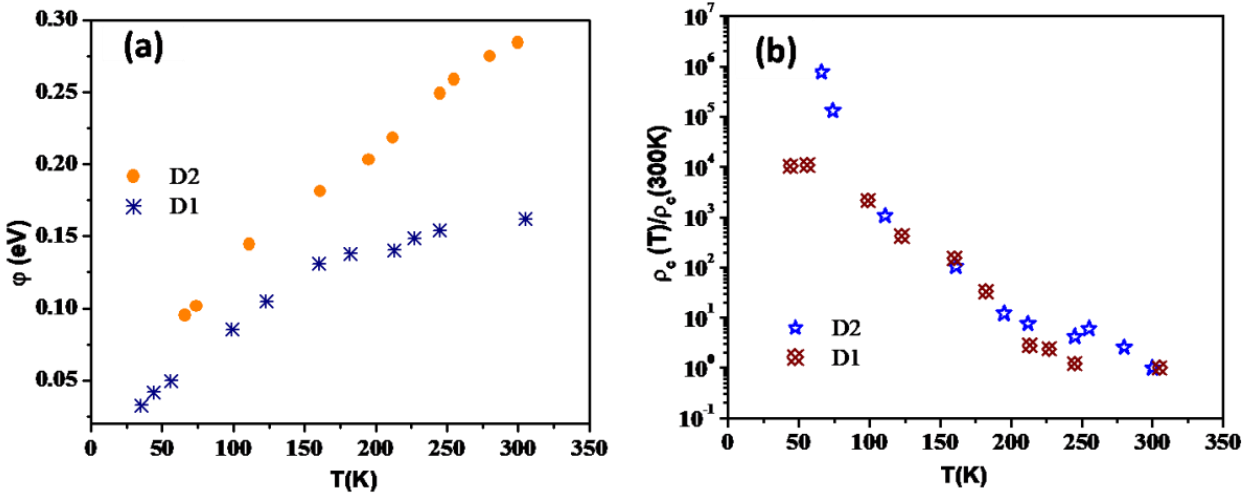

Figure 7.(a) Barrier height increasing as we increase temperature in NWs D1 and D2. (b) The normalized value of ρ_c from equation 6.

6. The Ideality factor

An important parameter that controls the quality of the contact is the Ideality Factor. In a junction the ideality factor η is close to 1 when the junction is defect-less and the current is mostly diffusion controlled. With recombination of carriers at the defect sites, η rises and $1 \leq \eta \leq 2$. In general,[26] $\eta > 1$ can occur due to one or more of the following reasons: (a) Interface states at a thin oxide between metal and semiconductor, (b) tunneling currents when the semiconductor is heavily doped, (c) image forces and (d) generation recombination current within the space charge region. We obtain the value of η by fitting the *I-V* curves using equation (5). The ideality factor at 300 K for the NWs A1 and E which has the lowest diameter (~30-35 nm) has η slightly larger than 2. It has been reported[27] that, as the diameter of a Ge NW decreases below a certain length scale ~30nm, when the depletion layer at the contact region is larger, η can reach a large value in vicinity of even 3. Thus observation of larger $\eta > 1$ in these two cases is expected given the narrow diameter of the wire. In NW D2 on annealing, the value of η reduces from 1.5 to 1 as the contact improves and the contact resistance comes down, which is also true for NW N, where there is sufficient lowering of η. In Fig. 8, we show the dependence of η on ρ_{NW}. It can be seen that for low resistivity the ideality factor is indeed close to 1 at RT, whereas for high resistive NWs, it deviates from unity to a higher value. Barring a few of the NWs, in the contacts in most of the NWs, η is not much different from its ideal value. In fact, even in the FeB deposited Pt electrode, whose MS junction is far

from ideal, η ~2.2, which is acceptable, considering the Pt is actually a network of Pt nanoparticles embedded in a carbonaceous matrix with a very high work function of 5.6eV.[28] In some of the NWs investigated, there is a presence of a thin oxide layer of thickness ~ 5nm, which causes η to deviate significantly from unity. The value of η is not always ideal for experimental situations as the assumption of homogeneous barrier height is not valid. The validity of equation 2 (where we introduce the ideality factor) depends on the homogeneity of SBH. For practical cases the transport through inhomogeneous SBH can be considered as parallel conduction through 'patches', which correspond to regions of lower SBH which are embedded in an uniform barrier height region.[9] The SB is inhomogeneous as in most cases the atomic structure varies from region to region in the MS interface. The variation of ideality factor from sample to sample and its dependence on processing may be attributed to variation in distribution of 'patches'. The size of these patches is in nanometer regime, which is well within the limits of our contact area. Using the dipole layer approach to determine the local potential at the MS interface, a bias dependant SB comes into play, which causes η to be greater than one.[26]As a result the deviation may exist, even if there are contributions from one or more of the factors stated above. We have shown that, upon annealing, we can make the ideality factor come closer to its ideal value of unity, even if deviations were present a priori.
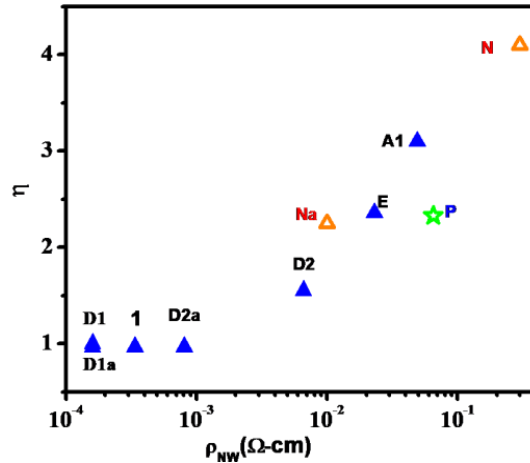

Figure 8. The ideality factor at room temperature for all the NWs investigated. The Cr/Au contact materials are marked in blue filled symbol, Focused Electron Beam deposited Pt in green symbol the Ni contacted NW is in orange symbol.

7. Temperature dependence of contact parameters: Inhomogeneous Barrier

The temperature dependence of ideality factor has not been investigated in all the NWs. For E and N, ideality factor is quite high (η> 2) at room temperature, and it goes to a much higher value at low

temperatures. For some NWs, MSM fitting gives $\eta \gg 1$ and hence carrier injection is not by simple thermionic emission. High ideality factors can be also be attributed to tunneling current due to presence of oxide layers on the Ge NWs. Our fitting does not support this conduction mechanism which may be due to insufficient doping levels or low applied bias, which prevents tunneling. The NWs on cooling down show suppression of φ and enhancement of η (see Fig. 9). The lowering of SB with temperature can be well understood from the concept of an inhomogeneous barrier and high η at low temperature. As temperature is lowered, only those regions of SB allow carrier flow, which has low barrier height. This effect has been observed in other NWs also.[29,30] As temperature is lowered, carriers get lower energy to cross the SB and hence most of the transport occurs through the regions of low SBH and a large η. This is also reflected in our devices, where ideality factor is much greater than 1 at low temperature (77 K) as shown in Fig. 9(b). The increasing ideality factor and a decreasing SB as temperature reduces confirm the presence of an inhomogeneous barrier with certain broad regions of low SBH.

The temperature dependence of both the important parameters have been investigated in the context of MS junctions in the past and comprehensive model[31] based on Gaussian distribution of barrier heights that appear to explain most of the data in the bulk. In this model there is a spatial inhomogenity in the contact barrier arising from roughness in the contact region which is expected as the MS contact in most systems are not formed on atomically smooth interfaces. This is also the case for contact formed on Ge NW that is seen to have a corrugated surface. The length scale of the corrugation is smaller than the contact region length scale. In these situations the barrier height (and the effective band bending that leads to depletion layer at the interface and formation of the barrier) can be assumed by a Gaussian distribution with a mean value φ_m (at RT or in high T limit) and a width σ_S.
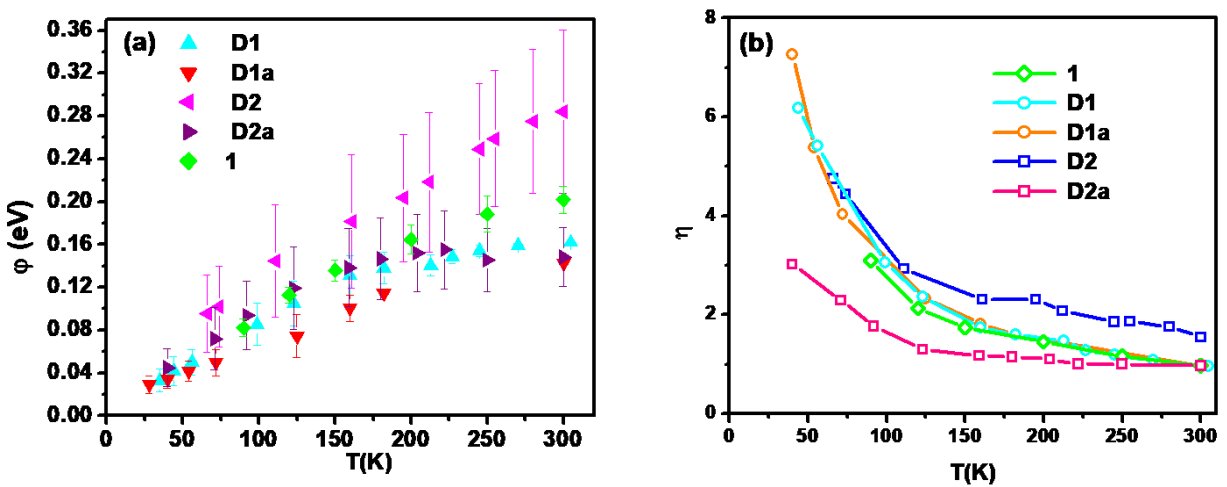

Figure 9. Temperature dependence of (a) barrier height (φ) and (b) ideality factor (η).

The distribution of barrier height at the MS interface can be determined from its temperature dependence given by,[31]

$$\varphi = \varphi_m - \frac{\sigma_s^2}{2k_B T}.$$ (7)

We find that for T > 100K there is approximately $1/T$ dependence. The parameters obtained from the fit to equation (7) are shown in Table 2. It shows that annealing in D1 and D2 leads to decrease of the distribution width and this makes the barrier relatively more uniform. Annealing also leads to decrease of mean barrier height. The contact resistance decrease on annealing due to homogenization of the barrier which we can see from the Gaussian distribution parameters. Annealing also causes reduction of the ideality factor and brings it closer to unity.

The ideality factor η shows strong temperature dependence and is much enhanced as the NWs are cooled down as shown in Fig. 9b. The temperature dependence of the ideality factor can be modeled[30] using bias dependence of the mean barrier height as well as its distribution. This can be expressed using two parameters, γ_2 and γ_3, which are the coefficients that quantify the bias dependence of the barrier distribution through the relation,

$$\Delta\varphi_m(V) = \varphi_m(V) - \varphi_m^0 = \gamma_2 V$$ (8.1)

$$\Delta\sigma_s^2(V) = \sigma_s^2(V) - \sigma_{s0}^2 = \gamma_3 V,$$ (8.2)

where, $\Delta\varphi_m$ and $\Delta\sigma_s^2$ are variation in barrier height and standard deviation respectively due to bias dependence and φ_m^0 and σ_{s0}^2 are the zero bias barrier height and standard deviation respectively. The bias dependence of the parameters leads to a temperature dependent η given by,[31]

$$\eta = 1 + \gamma_2 - \frac{\gamma_3}{2k_B T}.$$ (9)

The observed T dependence of the ideality factor can be seen to follow this behavior (equation 9). The fitting parameters γ_2 and γ_3 are shown in Table 2. Both γ_2 and γ_3 are negative which indicates that mean barrier height as well as the barrier distribution reduces as the bias is reduced. To find out the validity of our fitting parameters, we have determined the variation in barrier height and standard deviation by using equation (8.1 and 8.2) and taking the maximum value of the bias which we have used in the experiment (refer to Table 2). The values of $\Delta\sigma_s^2$ and $\Delta\varphi_m$ are much less than φ_m, indicating a very weak dependence of the barrier height on the bias voltage. This implies that equation (7) is not changed much due to the bias dependence.

Table 2. Fit parameters for the barrier height and ideality factor with temperature.

NW Name	φ_m(eV)	σ^2_s (eV^2)	γ_2	γ_3(eV)	$\Delta\varphi_m$ (eV)	$\Delta\sigma^2_s$(eV^2)
D1	0.200±0.003	0.0020± 0.0001	-0.923	-0.048	0.009	0.0048
D1a	0.178±0.009	0.0019± 0.0002	-1.000	-0.049	0.004	0.0002
D2	0.34±0.02	0.0039± 0.0005	-0.215	-0.045	0.086	0.0180
D2a	0.181±0.007	0.0012± 0.0002	-0.405	-0.017	0.010	0.0004
1	0.256±0.007	0 .0030± 0.0001	-0.922	-0.045	0.092	0.0045

D. CONCLUSIONS

The present investigation carried out on single Ge NWs grown by vapor phase shows that metal contacts through e-beam lithography can lead to reasonably low specific contact resistances ~$10^{-6}\Omega.cm^2$ in NWs with resistivity in the order of $10^{-4}\Omega.cm$. The study has been performed on NWs with resistivity in the range of 10^{-1} to $10^{-4}\Omega cm$ with metals of work function between 4.5 to 5.6eV. With increase in NW resistivity the specific contact resistivity increases. It is noted that the specific contact resistances achieved in low resistivity Ge NW is the lowest reported, although it is about two orders larger than that achieved in bulk Ge using intervening insulating layer. The junction characteristics were modeled using a Thermionic Emission model and the barrier height and the ideality factors were obtained. The barrier is Schottky in nature and the observed data are in agreement with suppression of Fermi level pinning observed before in Ge NW. The ideality factors of the junctions in the Ge NWs are close to unity at room temperature showing good quality junction. It is found that the contact barrier heights also depend on the NW resistivity and a low contact barrier of nearly 0.15 eV can be obtained. The barrier height shows suppression and the ideality factors shows enhancement on cooling down. The temperature variation was explained using a model that predicts $1/T$ dependence for both barrier height as well as ideality factors which have been observed. From the temperature dependence the mean barrier height as well as the spread of the barrier has been obtained.

The investigation carried out gives us a way to quantitatively assess contacts on Ge NWs and also opens the possibility of using this analysis to fabricate very low resistance and low barrier height contacts through suitable innovations.

REFERENCES TO CHAPTER IV

[1]H. K. Henisch, *Semiconductor Contacts: An Approach to Ideas and Models* (Oxford-UK, 1984)

[2]J. Tersoff *Phys. Rev. Lett.* **52,** 465-468 (1984)

[3]J. F. Wager and J. Robertson, *J. Appl. Phys.* **109,** 094501 (2011)

[4]J. Bardeen, *Phys. Rev*. **71,** 717 (1947)

[5]Raymond T. Tung, *Applied Physics Reviews* **1**, 011304 (2014)

[6]L. J. Brillson, *Contacts to Semiconductors* (Noyes Publications, New York, 1993)

[7]L. J. Brillson, *Phys. Rev. Lett.* **40**, 260 (1978)

[8]W. E. Spicer, I. Lindau, P. Skeath, C. Y. Su and P. Chye, *Phys. Rev. Lett*. **44**, 420 (1980)

[9]R. T. Tung, Phys. Rev. Lett., **52**, 461 (1984)

[10]S. Gupta, P. P.Manik, R. K. Mishra, A. Nainani , M. C. Abraham and S. Lodha, *J. Appl. Phys*. **113,** 234505 (2013).

[11]A. Agrawal, N. Shukla, K. Ahmed and S. Datta, *Appl. Phys. Lett.***101,** 042108 (2012)

[12]P. P. Manik, R. K. Mishra, P. V. Kishore, P. Ray, A. Nainani , Y. C. Huang, M. C. Abraham, U. Ganguly and S. Lodha*, Appl. Phys. Lett*. **101,** 182105 (2012)

[13]M. M. Kolenik-Gray, T. Lutz, G. Collins, S. Biswas, J. D. Holmes and V. Krsti, *Appl. Phys. Lett*. **103,** 153101 (2013)

[14]Z. Zhang, K. Yao, Y. Liu, C. Jin, X. Liang, Q. Chen, and L. Peng *Adv. Funct. Mater*, **17**, 2478–2489 (2007)

[15]K. Das, S. Samanta, P. Kumar, K. S. Narayan and A. K. Raychaudhuri, *IEEE Trans. Electron. Devices*. **61,** 1444-1450 (2014)

[16]R. Basori R and A. K. Raychaudhuri*, Nano Micro Lett*. **6,** 63-69 (2014)

[17]H. Norde*, J. Appl. Phys*. **50,** 5052–5053 (1979)

[18]G. Gu, M. Burghard, G. T. Kim, G. S. Dusberg, P. W. Chiu, V. Krstic, S. Roth and W. Q. Han*, J. Appl. Phys*. **90,** 5747-5751 (2001)

[19]L. S. Araujo*,* H. Kamimura, , O. M. Berengue and A. J Chiquito, *Phys. Procedia* **28**, 62 – 66 (2012)

[20]H. Kamimura, L. S. Araujo, O. M. Berengue, C. A. Amorim and A. J. Chiquito and E. R. Leite, *Physica E*. **44,** 1776–1779 (2012).

[21]T. Yamada, H. Yabutani, T. Saito and C. Y. Yang, *Nanotechnology* **21,** 265707 (2010)

[22]S. Sett, K. Das and A. K. Raychaudhuri, *J. Phys.: Condens. Matter* **29**, 115301 (2017)

[23]B. Kramer and A. MacKinnon*, Rep. Prog. Phys*. **56,** 1469 (1993)

[24]P. A. Lee and T. V. Ramakrishnan, *Rev. Mod. Phys*. **57,** 287 (1985)

[25]J Tang, C-Y Wang, F Xiu, Y Zhou, L-J Chen and K L. Wang, *Advances in Materials Science and Engineering*, **2011**, 316513, (2011)

[26]R. T. Tung, *Phys. Rev. B* **45,** 13509 (1992)

[27]F. Leonard, A. A Talin, B.S. Swartzentruber and S. T. Picraux, *Phys. Rev. Lett.***102,** 106805 (2009)

[28]M. Chakravorty, K. Das, A. K. Raychaudhuri, J. P. Naik and P. D. Prewett, *Microelectron. Eng*. **88,** 3360-3365 (2011)

[29]H. Asi, K. Cinar, E. Gur, C. Coskun and S. Tuzemen, *Int. J. Phys. Sci.,* **8** 371-379 (2013)

[30]J-H. Shin, J. Park, S. Y. Jang, T. Jang and K. S. Kim, *Appl. Phys. Lett.,* **102**, 243505 (2013)

[31]J. H. Werner and H. H. Guttler, *J. Appl. Phys*. **69,** 1522-1533 (1991)

CHAPTER V

INVESTIGATION OF OPTO-ELECTRONIC PROPERTIES OF SINGLE GERMANIUM NANOWIRES

In this chapter we present results of our extensive investigations on opto-electronic properties of optical detectors made from a single strand of Ge nanowire (NW). These detectors are configured as metal-semiconductor-metal devices. The investigations were carried out for device characteristics in the dark as well under illumination of varying wavelength from UV (300 nm) to NIR (1100 nm) as well as of varying illumination intensity from ~5µW/cm^2 to ~2000µW/cm^2. The principal result that we obtained is Responsivity ($\mathcal{R}$) is in excess of 10^7 A/W that can be achieved in single Ge NW photodetector with a bias < 2V at low illumination intensity range of ~ few µW/cm^2. The observed peak of $\mathcal{R}$ =3X10^{7}A/W is one of the highest Responsivity seen in any single NW photodetector reported till date.

We have also investigated the illumination dependence of the NW photodetectors where the photocurrent generally shows sub-linear dependence on illumination intensity. However, we find that a proper heat treatment in vacuum that controls the surface oxide can lead to super-linear intensity dependence. We have carried out an investigation on this issue and discussed the role of surface oxides and surface states in determining the kinetics of photodetection which we support through a numerical model.

We also discuss the likely causes that lead to such a high photo-response and use simulations wherever applicable to validate our claims.

A. INTRODUCTION

In recent years there have been considerable interests in low level optical radiation detection in photodetectors that use semiconductor nanowires (NWs).[1-5] In table 2 chapter I, we gave a collection of published results of single NW photodetectors till date. For the sake of ease of reading we reproduce the table here as Table 1 and include main results obtained in single Ge NW photodetectors. It can be seen that in single NW photodetectors (when the diameter falls below 100 nm) irrespective of the material the Responsivity ($\mathcal{R}$) enhances by orders of magnitude. Before this work the highest reported peak $\mathcal{R}$ was ~6x10^{7}A/W in ZnO[2] in the UV region and ~10^4 over a broader band width in Si NW.[1]

Table 1. Single nanowire photodetector parameters.

Semiconductor	Diameter (nm)	Wavelength range (nm)	Working Bias (V)	Peak Responsivity (A/W)	Year	Ref #
Si NW	80	300-1100	0.1	2.6×10^4	2014	1
ZnO NW	150-300	390	5	6.3×10^7	2007	2
InAs NW	30-75	300-1100	10	4.4×10^3	2013	3
GaN NW	180	380	5	7.7×10^1	2017	4
GaAs NW	90-160	522	4	8.4×10^3	2009	5
Vertical Ge NW	20	1550	1	2.3×10^1	2017	6
Ge NW	50	532	2	2×10^2	2007	7
Ge NW	30	300-1100	2	10^8	2018	this work

In a photoconductor, the Responsivity is directly proportional to the carrier mobility. This investigation on Ge NW was carried out with this motivation that since carrier mobility μ is larger compared to that in Si it can give rise to higher $\mathcal{R}$ in the same parameters space. Also its band gap being smaller, it is expected to perform at longer wavelengths extending well into NIR region of the spectrum. The only report of a semiconductor NW at 1550nm is of a Ge NW with $\mathcal{R} \sim 23$A/W.[6] As can be seen from Table 1 that other semiconductor NWs with diameters ≤ 100nm can reach extremely large photo-response with $\mathcal{R} > 10^3$A/W.[1-3] For example, Si[1], ZnO[2], InAs[3] and even for molecular material like Cu:TCNQ[8], provided the distance between electrodes is around a μm or less (see Table 1). Among the single NW photodetectors that show very high Responsivity only InAs[3] and Si[1] have been tested for broad band application in the wavelength range 300 nm to 1100 nm. InAs NW with diameter in the range 30-75 nm grown by MOCVD, with illumination intensity of 1.4 mW/cm^2 and at a bias of 15V, shows a value of $\mathcal{R}$ = 4.4 x 10^3 A/W.[3] In a previous investigation from our group[1] it was observed that in a single Si NW detector, $\mathcal{R} > 1.5$x 10^4 A/W is achieved in a 80 nm diameter nanowire in the spectral range 450-1000nm with a small bias of only 0.3V with illumination intensity of few mW/cm^2.

The photoconductive gain (G_{Pc}) (defined as the ratio of (I_{Pc}) to the incident number photons of frequency (ν) in unit time) in these NW devices reach a very high value $\sim10^6$ -10^8, which often reduces at higher illumination intensity.[2] The origin of this high photocurrent gain has been introduced in Chapter I, Section B and will be discussed in later sections. We have investigated the role of the surface states in Ge NWs and show that they have two important contributions: they cause surface band bending that leads a radial field caused by a depletion layer at the surface.[9,10] This effective radial field acts to separate out the electron-hole pair created by the optical illumination. The other is presence of trap states that controls the carrier generation-recombination kinetics and the dependence of photocurrent on illumination intensity.

B. EXPERIMENTAL PROCESS AND PARAMETERS FROM EXPERIMENT

The details of experimental work have been given in Chapter III. All measurements were taken at room temperature and under ambient atmospheric conditions. Performing the experiment in ambient atmosphere to vacuum, changes the device current by a small amount ($\sim3\%$). Thus, humidity and air do not have any significant effects on the electrical characteristics. The stability of the NW photodetectors was checked and there is negligible degradation of the photodetector performance for ~2000 cycles (beyond which we have not tested the device). Representative data of a current v/s time (*I-t*) curve in nanowire (N1) with 240 ON/OFF cycles are shown in Fig. 1.

In this section we recapitulate some of the important issues and point out the parameters that are used to quantitatively evaluate the photodetector characteristics. The main experiments consist of measuring the following:

- Device current (I) as a function of bias (V) at a fixed wavelength (λ) by with different illumination intensities ($\mathcal{I}$) by turning illumination ON and OFF referred to as ($I - t$) curves.

- The ($I - V$) curves in dark and under illumination of variable intensities ($\mathcal{I}$),

- Spectral dependence of photocurrent (PC) in the spectral range 300-1100 nm for a fixed bias. The PC is defined as $I_{pc} \equiv \left(I_{light} - I_{dark}\right)$ for a given bias, illumination intensity and wavelength. I_{light} is the device current under illumination and I_{dark} the device current in dark at same bias voltage.
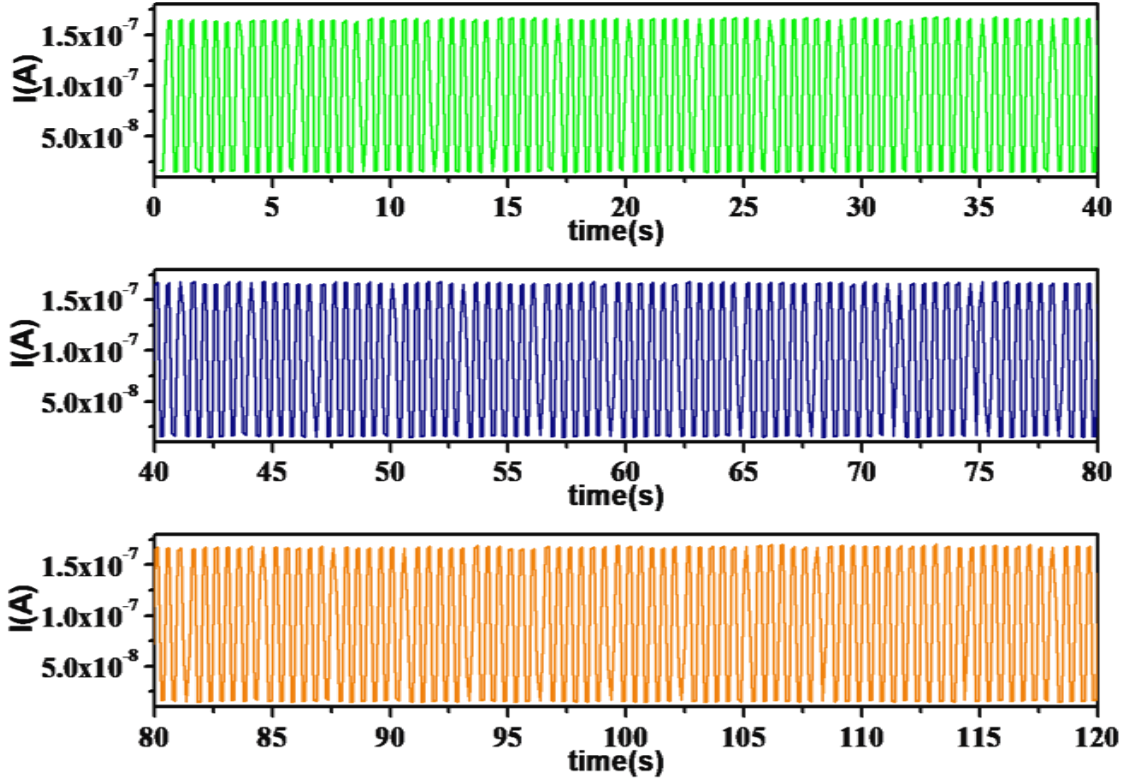
Figure 1. *I-t* curves for nanowire N1 at 2V bias voltage with illumination ON/OFF.

Using the above measurements we derive a number of device parameters which are:

- Responsivity ($\mathcal{R}$),
- Photocurrent gain (G_{Pc}),
- Specific Detectivity (D^*).

Responsivity is the ratio of the photocurrent I_{pc} to incident power (P), given by

$$\mathcal{R} = \frac{I_{pc}}{P} \tag{1}$$

The power incident on the nanowire (P) for a particular intensity, $\mathcal{I}$ (measured in W/cm^2) has been calculated using the relation, $P = \mathcal{I} \times \mathcal{A}$, where $\mathcal{A}$ is the collection area of the nanowire. It is defined as $\mathcal{A} = \pi l d$, where l is the length of the NW between two electrodes and d is the diameter of the NW. The illumination spot size is ~1mm in radius and illuminates the entire device. The illumination of the whole device cannot be avoided given the small size of the device (~ 2×10^{-7} mm^2).

G_{Pc} at a given wavelength or frequency (v) is defined as the ratio of the photo-generated carriers per unit time (I_{Pc}) to the incident number photons of frequency (v) in unit time (P/hv). This is given by:

$$G_{Pc} = hv I_{pc}/eP = \left(\frac{hv}{e}\right)\mathcal{R}. \tag{2}$$

The parameter G_{Pc} is a dimensionless quantity, while $\mathcal{R} = \left(\frac{e}{hv}\right)G_{Pc}$ has the unit of Ampere/Watt (A/W). A simpler way to write the Gain is, $G_{Pc} \equiv \frac{N_{carrier}}{N_{photon}}$, where $N_{carrier}$ is the number of electron-photon pairs generated in the device per unit time due to number of photons falling on to it in unit time, N_{photon}.

The internal factors as well as device parameters links the opto-electronic parameters through G_{Pc}.[11] In a two terminal metal-semiconductor-metal (MSM) detector the Gain in related to the device parameter $\tau_{transit}$ (carrier transit time) and the material parameter $\tau_{life\ time}$ (carrier lifetime) so that $G_{Pc} \equiv \frac{N_{carrier}}{N_{photon}} = \frac{\tau_{life\ time}}{\tau_{transit}}$. Here $\tau_{transit}$ is the time a carrier takes to reach an electrode in the MSM device (separated by a distance, l) under a bias V. If μ is the carrier mobility and the carriers are to diffuse over a length l, the transit time is the carrier diffusion time and $\tau_{transit} = \frac{l^2}{\mu V}$. Now, $\tau_{life\ time}$ is the life time of a carrier before recombination so,

$$\tau_{life\ time} = \frac{d_{avg}^2}{D}, \tag{3}$$

where, d_{avg} is the average recombination length and D is the Diffusion coefficient for an electron/hole. Using Einstein's relation on electron mobility ($D = \mu\frac{k_B T}{e}$), we get

$$\tau_{life\ time} = \frac{d_{avg}^2}{D\mu\left(\frac{k_B T}{e}\right)} \tag{4}$$

G_{Pc} will then have a simple definition given by:

$$G_{Pc} \equiv \frac{N_{carrier}}{N_{photon}} = \frac{\tau_{life\ time}}{\tau_{transit}} = \frac{d_{avg}^2}{\mu\frac{k_B T}{e}} / \left(\frac{l^2}{\mu V}\right) = \frac{eV}{k_B T}\left(\frac{d_{avg}}{l}\right)^2 \tag{5}$$

In this case the gain G_{Pc} is given by the ratio of two length scales. In the single nanowire devices l is typically, ~1µm and $d_{avg} > l$ which ensures G_{Pc} can be a large quantity ($\gg 1$).

The photodetector capability to detect low intensity illumination will be limited by the noise in the current through the device. In this context the parameter that quantifies the performance of the opto-electronic detector is the Specific Detectivity (D^*) which is defined as:

$$D^* = \sqrt{\mathcal{A}\Delta f}/NEP. \qquad\qquad (6)$$

Here $\mathcal{A}$ is the area of the NW exposed to incident radiation, Δf is the signal bandwidth and NEP is the power at which the signal to noise ratio is unity. NEP includes shot noise, flicker noise and thermal noise. In most calculations of NEP, only the shot noise is calculated to determine the NEP. This is not the true value of the NEP, which should be experimentally determined as the power at which the photocurrent to dark ratio is unity. Making NEP the Shot noise only underestimates NEP and enhances D^*.

C. RESULTS

1. Detector characteristics in dark and evaluation of MSM device parameters

Dark characteristics of the photodetectors have been obtained from $I-V$ data in the dark and its analysis as a MSM device with model of back to back Schottky diodes using the modified Richardson–Dushmann[12,13] equation as discussed in Chapter IV. We have studied six photodetectors made from Ge NWs with diameters ranging from 30-90 nm. Dark $I-V$ data are given in Chapter IV. Here we reproduce some of them in Figure 2.
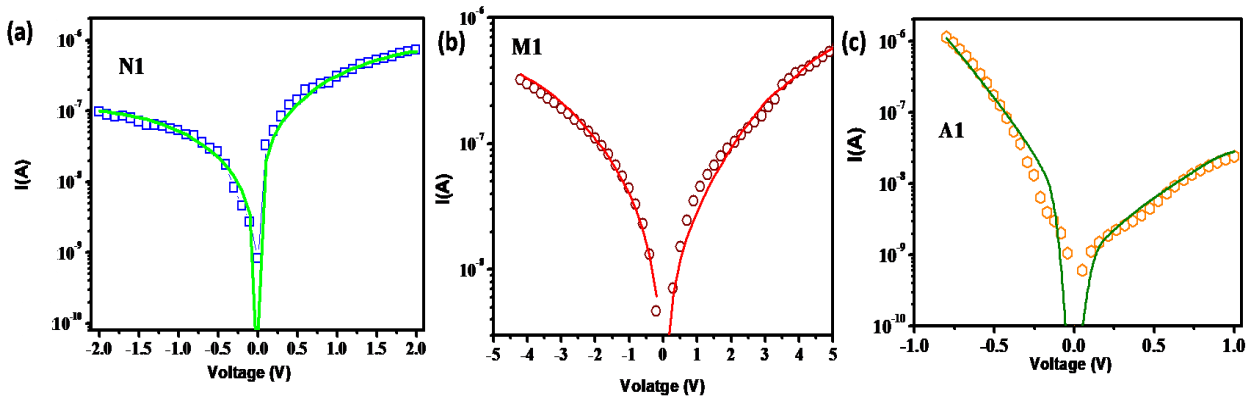

Figure 2. *I-V* characteristics in dark for (a) N1, (b) M1 and (c) A1.

Table 2 gives the summary of all the samples measured and parameters obtained from experimentally measured dark $I-V$ data. This table contains data also from Table 1 in Chapter IV. However, discussions will be focussed on three NWs: A1 with diameter 30 nm, N1 with diameter 65 nm and M1 with diameter 62 nm. These are highlighted in the table 2 with bold fonts. We note that the $I-V$ curves are asymmetric and this arises due to asymmetry in Schottky Barrier Height (SBH) at the contacts. In

Table 2, we have shown the average barrier height, $\phi \equiv (\phi_1 + \phi_2)/2$, where ϕ_1 and ϕ_2 have been obtained from the modified Richardson-Dushmann fit to the data. (Chapter IV has a detailed discussion on these issues).

Table 2. Device parameters in dark.

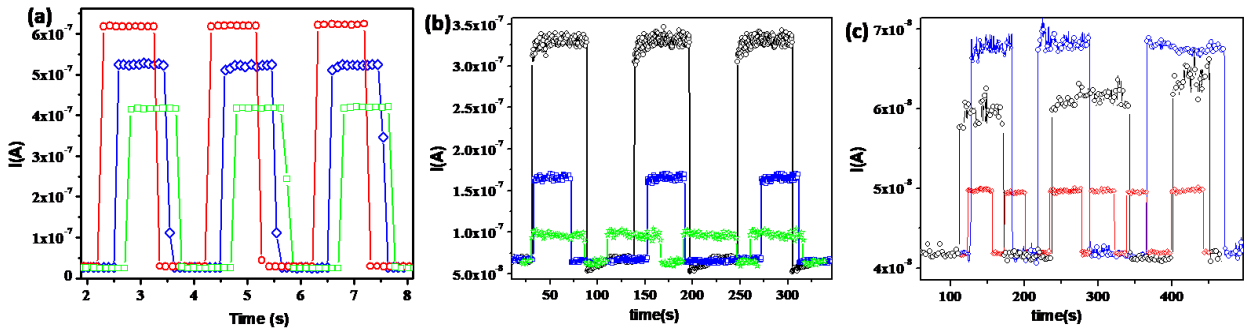| NW	Diameter (nm)	Length (μm)	Electrode	ρ_0 (Ω-cm)	Average SBH (eV)
D1	90	2	Cr/Au	0.0001	0.160
F	70	1.4	Pt	0.175	0.285
N1	**65**	**3.2**	**Pt**	**0.065**	**0.237**
M1	**62**	**1.8**	**Ni**	**0.3**	**0.280**
M1$_a$	62	1.8	Ni	0.01	0.258
A1	**30**	**1.2**	**Cr/Au**	**0.049**	**0.300**

Figure 3. The *I-t* curves of (a) N1, (b) A1 and (c) M1 are shown for 1V bias at 650 nm light of different intensities.

2. Photodetector characteristics under illumination

In Figure 2 the *I-t* curves of photodetectors based on 3 Ge NWS (a)N1 (b)A1 and (c)M1 are shown for a fixed bias at 650 nm light of different intensities. The graph shows the nature of time response we obtain from these detectors. For sample N1 where the data have been taken in scales of ~ 1sec (ON/OFF time),

the finite response at ON/OFF can be seen in scale of fraction of seconds. For other devices, the data time scale being long, the device response time scale cannot be seen. For sample A1 there are longer tails for rise time as well as small "negative" response at fall which may arise from capacitive effects[1] at the MSM contacts that it has a very high value of SBH (0.3ev). This will be discussed later in Section C, 6.

In Figure 3(a) we show the $I - V$ data in dark and under illumination for one representative device N1 and in Figure 3(b), we show the photocurrent I_{pc} obtained from the $I - V$ data. The figure and the Table 3 show the extent of I_{pc} obtainable from these single Ge NW devices. Figure 4 has the contour plots of N1, A1 and M1 that show both bias and the illumination intensity dependence of the device current. In fact with a moderate bias (~1-3V) and a moderate intensity of illumination ($\leq$ 1mW/cm^2) the NW devices give rise to $I_{pc} \approx 0.1$-1 μA. We have not used higher biases or illumination intensities as a preventive measure from electro-migration which occurs at current densities ~10^{6}A/cm^2.
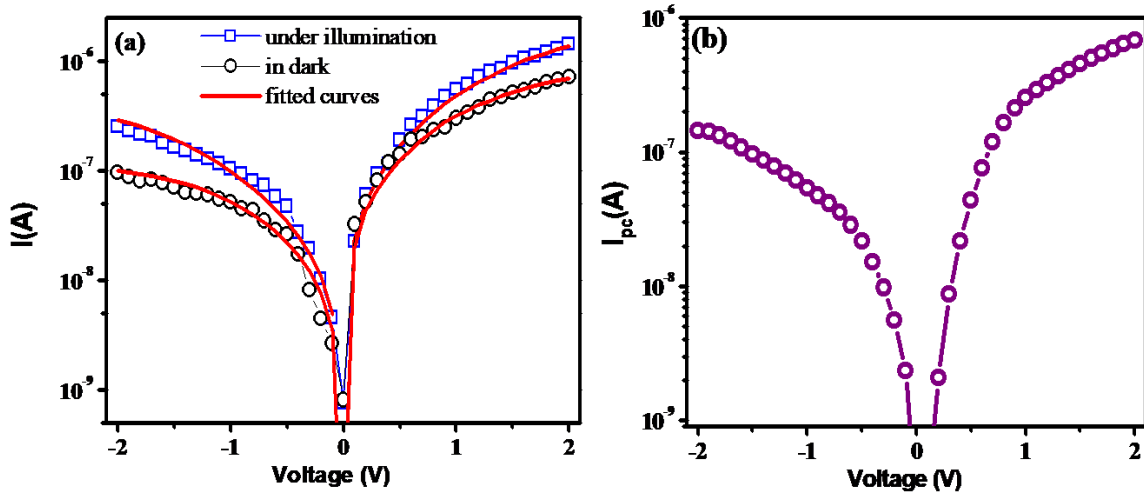

Figure 4. (a) *I-V* characteristics of device N1 in dark (black) and under illumination (blue) at λ=650nm and intensity ~ 100μW/cm^2.Red lines showing fitted curves. (b) The Photocurrent of N1 for the same.

In Table 3 we have summarized all the relevant optical-detector device parameters for the single Ge NW devices measured. The parameters have been measured/calculated at illumination wavelength of 650nm. This is the range in which the response is around the peak and this is also the middle of the spectral range. We find that there is indeed a trend that reduction in the diameter enhances the response. This could not be made more quantitative as there are effects of other parameters like the SBH at the contact (lower SBH enhances device current) and also the nanowire resistivity (lower ρ_o makes the response higher).

Table 3. Photodetector device parameters measured at wavelength 650nm.

NW	Bias (V)	I_{dark} (A)	I_{pc} (A)	*Max. G_{pc}*	Intensity ($\mu W/cm^2$)	G_N (m^2/V)	d_{avg} (μm)	α
D1	0	3.52×10^{-7}	1.13×10^{-7}	7.1×10^5	8.2	-		-
F	0.5	3.3×10^{-9}	2.5×10^{-7}	1.1×10^6	136	1.9×10^{-6}	215	0.68
N1	1	3×10^{-7}	3.3×10^{-7}	5×10^6	19.4	5.1×10^{-5}	1131	0.33
M1	3	1.8×10^{-7}	1.3×10^{-7}	1.0×10^7	7.2	6.5×10^{-6}	404	0.58
M1$_a$	0.1	3.8×10^{-7}	2.1×10^{-7}	1.8×10^6	960	5.8×10^{-5}	1207	1.38
A1	1	2.4×10^{-8}	6×10^{-8}	1.0×10^7	10.5	1.5×10^{-5}	612	0.40

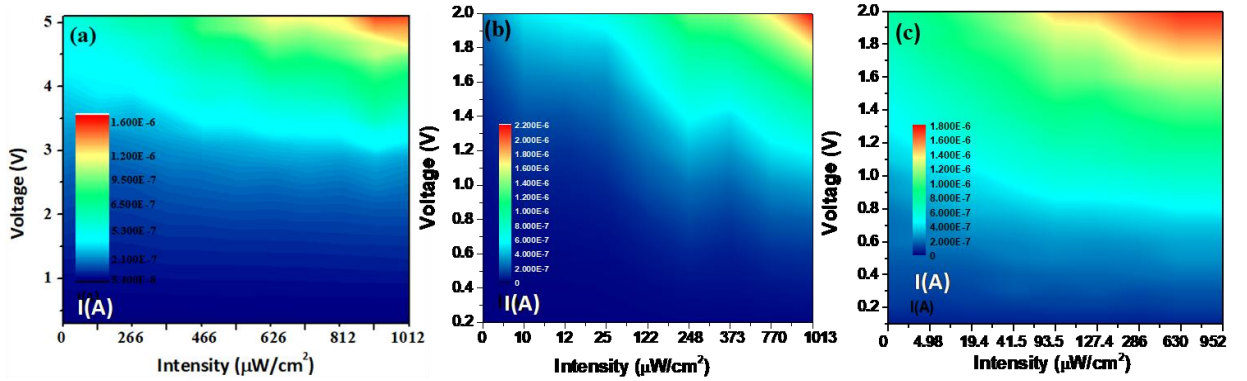*#Maximum $G_{pc} \sim 10^8$ obtained in A1 at 2V bias.*

Figure 5. Contour plot of device current as a function of bias with light intensity for (a) M1, (b) A1 and (c) N1 respectively at $\lambda = 650$nm.

We show the spectral dependence of Responsivity in Figure 6 for A1 (diameter 30 nm) at a bias of only 2V. Over the spectral range of 400-1100nm, $\mathcal{R} > 10^7$ A/W. This result also shows the efficacy of using single Ge NW as a photodetector. More discussions on the nature of the photoresponse are given in Section C, 5.
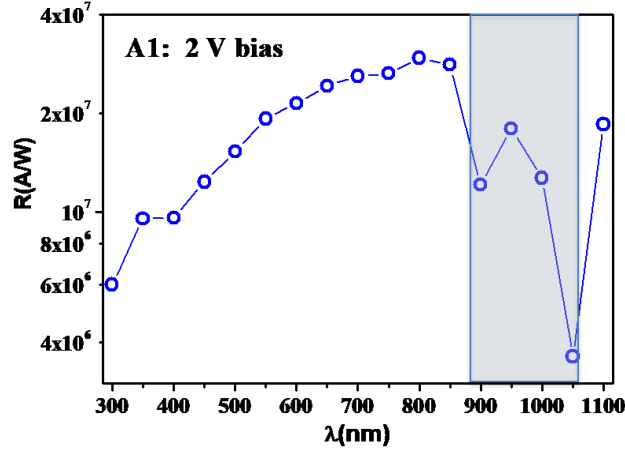
Figure 6. Spectral dependence of Responsivity of the photodetectors at different bias taken with illumination intensity ranging from 50 – 600 µW/cm². The shaded region has very low source intensity.

It can be seen from Table 3 that G_{pc} in all the detectors is well above 10^5. In two of them it is above even 10^7 A/W. In device D1 we find that there is high $G_{pc} \sim 7 \times 10^5$ even at zero bias. This makes a self-powered detector, which we have investigated in Chapter VI. At a bias of 2V in NW A1, we have achieved G_{pc} $\sim 10^8$ which is commendable and the highest reported till date in a broadband single nanowire photodetector, surpassing ZnO NW[2]. As can be seen from equation 5 that the gain G_{Pc} is dependent on the transit time between electrodes ($\tau_{transit} = \frac{l^2}{\mu V}$). Since the devices have different lengths and the data have been gathered with different bias, to factor out these effects we redefined the following quantity as a normalized gain G_N that is dependent only on internal parameters of the NW like the recombination length d_{avg} given by,

$$G_N \equiv \left(\frac{l^2}{V}\right) G_{Pc} = \left(\frac{e}{k_B T}\right) d_{avg}^2 . \tag{7}$$

The normalized gain G_N has a unit of (m^2/V) is shown in Table 3. In Fig. 7 we have plotted G_N as a function of ρ_0. The quantity varies by nearly 2 orders from $\sim 10^{-4}$ to $\sim 10^{-6}$ for the nanowires used and expectedly dependent on the resistivity ρ_0. As ρ_0 decreases there is an enhancement of G_N. Samples F and M1 that have high values of ρ_0 and lowest $G_N < 10^{-6} m^2/V$. Samples M1$_a$ (that has been obtained by annealing M1 which will discuss later on) and A1 have lower values of ρ_0 leading $G_N > 10^{-4} m^2/V$. Since the intensities are not similar at the maximum G_N is achieved, the ρ_0 dependence is not strictly followed.
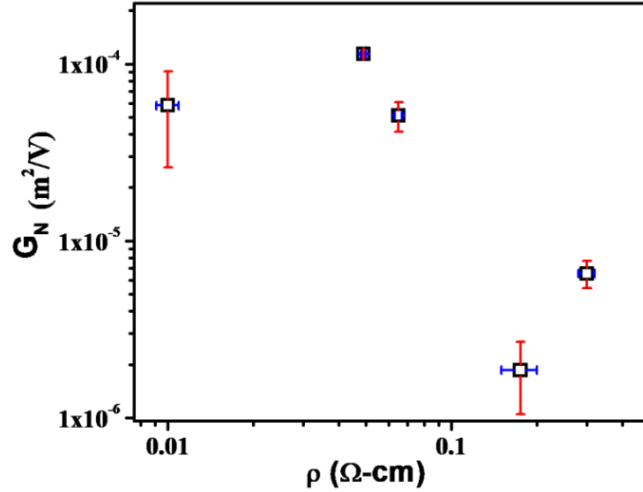
Figure 7. Normalized Gain (G_N) versus Resistivity (ρ) of the nanowire photodetectors.

3. Recombination length and absence of recombination at surface

There are two important length scales determined by the physical device that would determine the performance of the device. The fundamental length scale (depending intrinsically in the material) in a photodetector is the recombination length d_{avg}. One physical length scale is l, the device active length between the two electrodes. As can be seen from equation 5 that when d_{avg} is comparable to l, the carriers are effectively collected before they recombine. This also leads to enhancement as the axial fields (arising from the band bending at MS contacts) can enhance charge collection efficiency. More conventional bulk photodetectors generally have $d_{avg} \ll l$. The carriers recombine mostly before reaching electrodes thus reducing severely the gain. The other length scale is magnitude of d_{avg} with respect to the diameter d. The diameter is the smallest length scale in the system and the surface is expected to be a place for carrier recombination. But if $d_{avg} \gg d$, carrier recombination does not occur at the surface. If the recombination occurs in defects in bulk of the NW then one would expect the recombination length should be inversely correlated to the resistivity of the NW.

Equation 5 embodies the fact that we assume that the gain arises only from conventional mechanisms of a photoconductor. Using $\frac{k_B T}{e} \approx 25$ meV at room temperature, we can obtain d_{avg}. These are also shown in Table 3. It can be seen that the $d_{avg} \sim$ 200-1200 μm. This is a non-physical value and it arises because we assume the Gain to be completely independent of other factors. As embodied in Eqn. 5, in a bulk photoconductor, this is the only factor that can give rise to Gain. Inversely, to get an upper bound for the Gain in a NW due to diffusion of photogenerated carriers only, we calculate the Gain using, $d_{avg} \sim 5 \mu m$[14]

in a Ge NW with $l \sim 1\mu m$ and bias = 1V. We get, $G_{Pc} = 10^3$. This is an upper limit that one would get from photoconductive mechanisms. Any value of $G_{Pc} > 10^3$ *must* arise due to other factors. Thus, in a NW, calculating d_{avg} based on experimental value of $G_{Pc} \gg 10^3$ completely overestimates the recombination length and one would need other enabling mechanisms.

Clearly, there is a translation from bulk photoconductivity when we enter the nano-regime. Indeed, there is a need for other mechanisms in the system that pushes the Gain and contributes to photocurrent. The most potent enabling mechanism will be that which stretches the carrier recombination time by a field that can separate the two photo-generated electron-hole pairs. We shall later explore whether there could be an internal field as in the case of a p-n junction type photodetector, or a radial field that separates the electron-hole pair that has been proposed for ZnO NWs.[2] We will discuss the factors for $G_{Pc} \gg 10^3$ in details in Section D, as we move ahead in this Chapter.

In Ge, it is known that $d_{avg} \sim 4\text{-}5\mu m$,[14] which is $\gg$ diameter of a NW. This establishes the fact that in the single NW photodetectors the recombination of carriers do not occur at the surface. We show below that this is an important ingredient that leads to effective enhancement of the gain and large Responsivity. If the NW recombination would have been surface nucleated one would never get high optical response in NW photo detectors. In fact the enhancement of response as the NWs become narrower would not have happened. We also discuss how the surface recombination is inhibited in narrow NWs.

4. Quantification of photoconductivity and photo induced SBH lowering

The analysis of the $(I - V)$ curves (fits to the experimental data are shown as solid line in Fig. 2a) allows us to determine the evolution of R_{NW} with illumination intensity. This helps to determine the extra carrier density (Δn) generated by illumination. The analysis also gives us a measure of the lowering of barrier height on illumination. This is an important factor that adds on to the photocurrent and enhances it. Let R_o be designated as the value of resistance of NW in dark and from it we obtain the resistivities (ρ_o), given in Table 2. A comparison of the resistivities of the NWs with bulk[15] will give an approximate carrier concentration (n_o) in the NWs. The enhancement in conduction of the NW (Δg_{NW}) under illumination has been derived from the relation, $\Delta g_{NW} = (R_{NW}^{-1} - R_0^{-1})$. Both R_{NW} and R_o have been obtained from experiment. The ratio (δ) of the change in conductivity of the NW on illumination to that in dark $(\delta = \Delta g_{NW}/R_o^{-1})$ is shown in Fig. 8a for the selected NW devices. Substantial change in the photoconductivity compared to dark is observed. Assuming that mobility does not change upon illumination, δ is the change in the carrier concentration on illumination $(\Delta n/n_0 \equiv (n - n_0)/n_0)$, n_0 being the carrier concentration in dark. At high illumination intensity ($> 20 \ \mu W/cm^2$), $\Delta n > n_0$. It can be

seen in Fig. 8a that within an order the relative changes in the photo-conductivity in the NWs are similar. Interestingly when beyond a certain intensity $\Delta n > n_0$, the rate of change of carrier concentration on intensity is enhanced. It may happen that the creation of excess carriers may come from photo-ionization of dopant sites in the NWs being unintentionally Au doped during growth. In Fig. 8b, we plot the SBH as obtained from the fit, where it shows reduction of the SBH as a function of illumination intensity. The initial barrier height, ϕ in dark for NW A1 is larger compared to that of the NW N1 and M1, although they are of comparable order. In case of NW N1 and M1, the lowering of the SB height $|\Delta\phi| \approx 0.02$ eV and that for the NW A1 is $|\Delta\phi| \approx 0.06$eV for illumination intensity ~ 1mW/cm^2.

To assess the reduction in the barrier height that occurs due to diffusion of carriers in the MS contact region, we estimate $|\Delta\phi|$, from change in the chemical potential due to the change in carrier density due to diffusion. The carrier diffusion upper limit is given by the change in the carrier concentration $\Delta n/n_0$ due to photo generated carrier which we estimated before. Thus we estimate an upper limit of the SB height lowering due to the photo generated carriers as:[16]

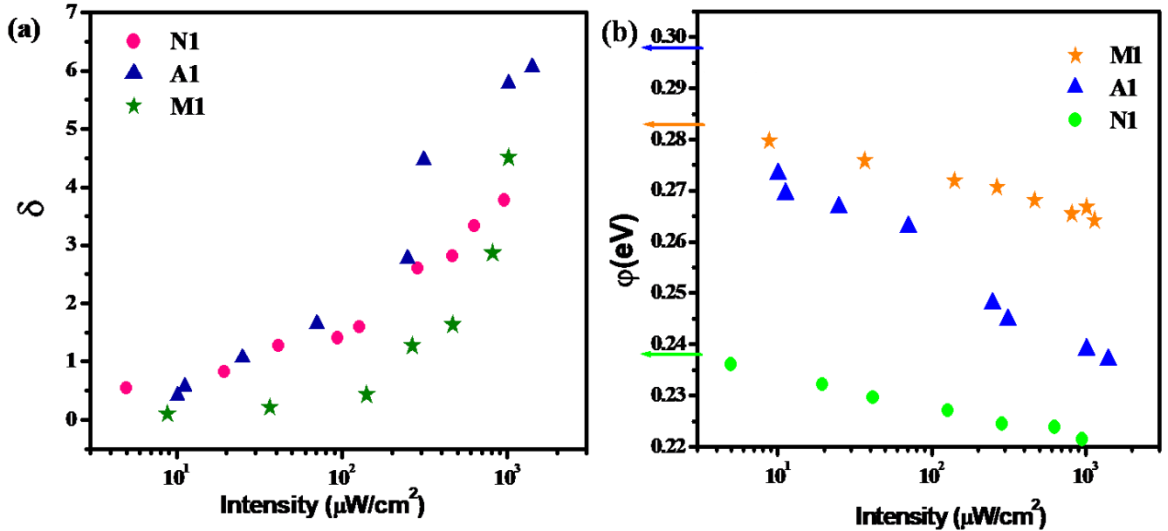$$|\Delta\phi| = \frac{k_B T}{e} ln(\frac{n_0 + \Delta n}{n_0}) \tag{8}$$

Figure 8. (a) The ratio δ (relative change in conductance on illumination) as a function of illumination intensity at 650 nm light. (b) The barrier heights as deduced from analysis of the data as a function of illumination intensity. The barrier height at dark is marked with arrow on y-axis.

The ratio $(n + n_0)/n_0)$ has been obtained from the experimentally measured δ as mentioned before. Comparison with observation shows that the values of $|\Delta\phi|$ though comparable to the estimated values, are consistently lower (~ 10meV) at 1mW/cm^2. This is expected; the calculated $|\Delta\phi|$ is an upper limit

which assumes that all the photogenerated carriers diffuse into the contact region. In reality, a smaller fraction will diffuse in, because some part of the photogenerated carriers recombine in the depletion region and in traps. The comparison establishes that the diffusion of carriers in the MS contact region leads to changes in the chemical potentials which lower the barrier height. The reduction in ϕ is an important effect which adds on to the photocurrent of the NW photodetector.

5. Ultrahigh spectral response in UV-Vis-NIR region

A simple measure of the sensitivity of the single Ge NW can be appreciated from the following observation. A photocurrent ~ 50 nA is detected in a single Ge NW (A1) with area of light collection ~ 10^{-9} cm^2 at 2V bias in a room dimly lit with white light (from a CFL). The same photocurrent is obtained by a commercial Si photodetector with collection area of 1 mm^2. This immediately shows that the Responsivity of the nanowire detector is larger than a commercial detector by few orders which is approximately the ratio of the collection areas of the Si detector and the Ge NW detector.
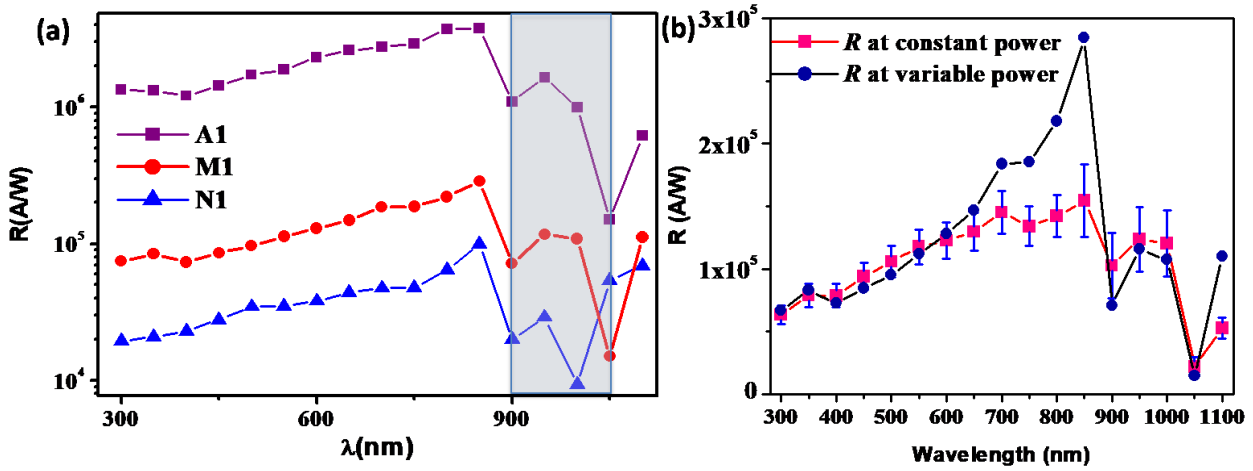

Figure 9. (a) Spectral dependence of Responsivity of the Nanowire photodetectors at different bias taken with illumination intensity ranging from 50 – 600 μW/cm^2. The shaded region has very low source intensity. (b) Spectral dependence of Responsivity in M1 shown at a constant intensity of 500 μW/cm^2 (pink curve) while the blue curve shows spectral dependence of Responsivity at available intensities, depending upon the source output power characteristics.

The major result of the present investigation is ultra large $\mathcal{R}$ obtained in the photodetectors made from a single Ge NW. The spectral dependence of $\mathcal{R}$ for some of the selected devices is shown in Figure 9(a). The photoresponse of the NWs ($\mathcal{R}$ ~10^7 A/W) are orders of magnitude higher compared to those of photodetectors made from bulk Ge crystals ($\mathcal{R}$ < 1 A/W).[17] The spectral response of the NWs extend to

similar ranges although the value of $\mathcal{R}$ differ by two orders of magnitude. At a bias of 1V for NW N1, $\mathcal{R} > 10^4$ A/W over the broad spectral range of 300 nm to 950 nm peaking. For NW M1, $\mathcal{R} > 10^5$ A/W has been achieved with the 3V bias and same spectral range. At 1V bias, for NW A1, $\mathcal{R} > 10^6$ A/W. In the photodetector with diameter 30 nm NW (A1), the value of $\mathcal{R}$ is at least an order larger compared to that of the detector with diameter 65 nm (N1) at same bias of 1V. This observation of $\mathcal{R}$ measured in different semiconductor single NW photodetectors shows that on decreasing the diameter, there is enhancement of $\mathcal{R}$.

The dips in $\mathcal{R}$ as shown in Fig 6 and Fig. 9(a) in the shaded region are due to source characteristics as we use a Xenon lamp source, which has very strong emission lines in the NIR region interposed with regions of low emission intensity. Since photoresponse is power dependent (like in other semiconductor NWs and as we shall see in Section C, 11), $\mathcal{R}$ follows the characteristic nature of the source intensity and the spectral dependence (as seen in Fig. 9(a)) of the NW partly arises from it. In Fig. 9(b), $\mathcal{R}$ has been calculated at a constant intensity ($J = 500\mu W/cm^2$) in M1 at a bias of 3V. The Responsivity at constant power/intensity should follow the absorption characteristics in a Ge NW, which is different from bulk Ge due to leaky mode resonances[18] and varies with diameter. It is no longer a constant (at energy >> band gap of Ge, 0.66 eV corresponding to 1850 nm), like bulk Ge. The absorption efficiency decreases beyond 800nm[18] and falls << 1 in the near infra-red region. The Responsivity for wavelength > 900nm reflects this fall in absorption in a Ge NW. The large uncertainty in Responsivity curve in the wavelength range > 900nm (see Fig. 4) arises mostly from fluctuations in the Xenon power source as we validate during calibration (shown as error bar in Fig. 9(b)).

To check the efficiency of the NW photodetector at longer wavelengths, we measured the photocurrent in the broad band NIR region from 980-2600 nm using a white light source. The I_{Pc} obtained from broad band source in NIR region is ~1 μA as shown in Fig. 10a for both the nanowires along with the spectral response. This is much larger than the dark current and the noise limit. The broad band source used has peak emission at 1000nm from which we determine its intensity ~1.5 mW/cm^2. The photocurrent is of the order ~μA in both NWs, is quite large and can be assumed to have partly originated from illumination in the NIR region beyond 1100 nm and upto 1800 nm, which is the band gap of Ge.

Photoconductivity measurements though performed at individual wavelengths in the NIR region (beyond 1100 nm), cannot be quantified due to lack of a proper intensity calibration as well as source characteristics lower than 1μW/cm^2 in the wavelength range of 1100-1600nm. Still, since we attempted to make measurements, the representative data on one of the NW, N1 is shown for extensiveness in Fig. 10(b).
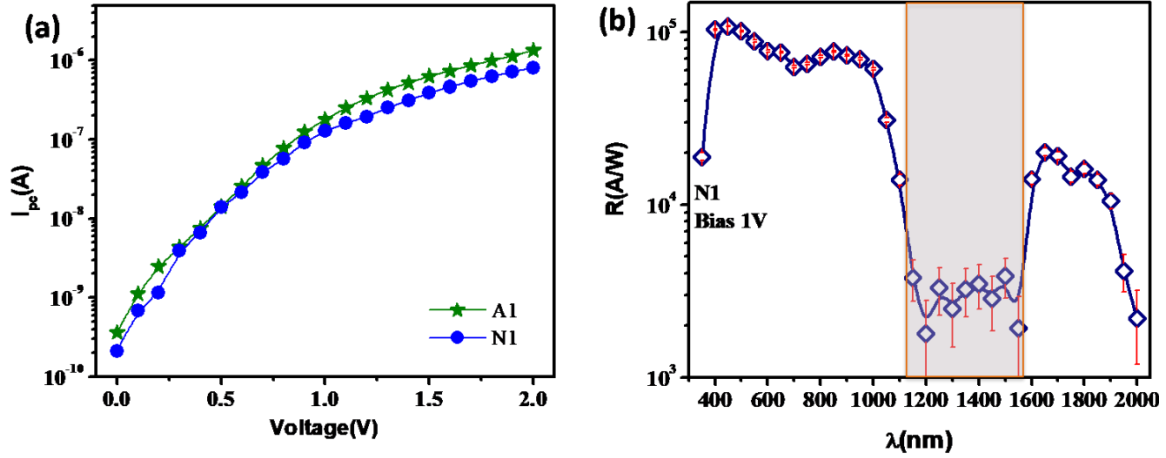
Figure 10. (a) The photocurrent at longer wavelengths in the NIR region measured with a broad band source (980nm -2600nm). (b) Responsivity of N1 at 1V bias taken upto λ =2μm. The shaded region has very low source power.

6. Photon detection limit analysis

The effectiveness of the photodetector in presence of noise is an important factor, which is often measured by the Specific Detectivity, $D^* = \sqrt{\mathcal{A}\Delta f}/NEP$ as defined before. The signal bandwidth Δf is selectable by the user and often is limited by the parasitic capacitance.[19] It has been shown by previous investigations done from our group on single Si nanowire photodetectors that the time response of these MSM devices is determined mostly by the stray capacitances from long contacts and also junction capacitances.[19] These limit the band-width to less than 1 KHz. It is likely that the intrinsic response is much faster. The rise time (t_r) of the photodetector (not intrinsic lifetime of charge carriers) can be calculated from the -3dB bandwidth (f_{3dB}) using the relation,[11]

$$f_{3dB} = 0.35/t_r \tag{9}$$

Fig. 11 shows (I_{pc}/I_{max})% versus frequency for NW D1. f_{3dB} is the frequency at which (I_{pc}/I_{max})% is $1/\sqrt{2}$ of its 100% value. This gives a rise time of ~7 *msec* for photodetector D1. Other NWs show similar t_r ~ 5 -15 *msec*.

In the device configuration used by us the measured Δf is ≤ 1 KHz. We thus take an upper limit of the band width =1 KHz. As a realistic estimate we take *NEP* as the power at which the signal to noise ratio just reaches unity. For the NW N1, *NEP* is 6x10^{-15} W and for NW A1 device it is 0.3x10^{-15} W. The observed values of D^* ranges from 10^{11}cmHz$^{1/2}$/W to 10^{13}cmHz$^{1/2}$/W and is appreciable, since

commercial bulk Ge detector has $D* \sim 10^{14} cm^{1/2} Hz/W$.[17] This ensures that making the detector size in nanometre domain does not degrade its performance by extra noise. The value of $D*$ is comparable to most single NW photodetectors.[1]
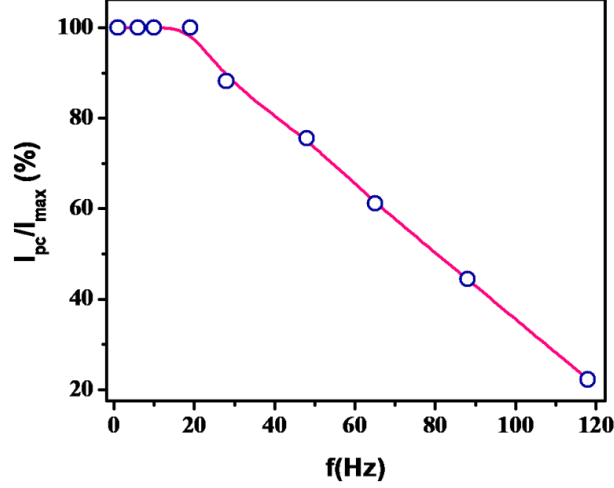

Figure 11. $(I_{pc}/I_{max})\%$ versus frequency of a pulsed illumination of $\lambda = 650nm$ for nanowire D1.
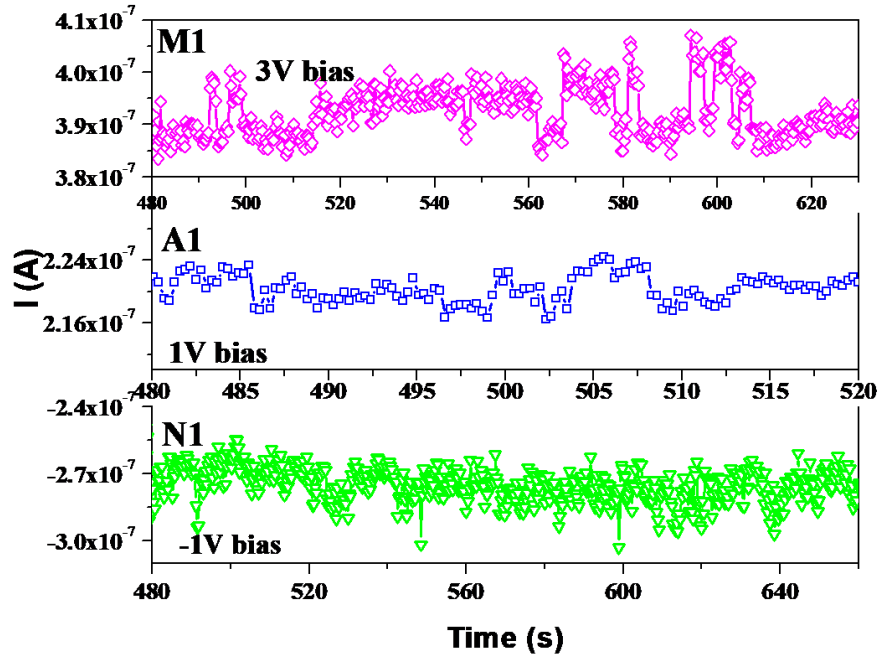

Figure 12. *I-t* curves from which we determine the *NEP*, when the signal to noise ratio is unity and the subsequent current noise in M1, A1 and N1.

A practical guide to find the minimum energy (or minimum number of photons) the NW device can detect, may be obtained from the observed Responsivity $\mathcal{R} = 3 \times 10^7$ A/W at 800 nm for NW A1 at an illumination intensity 57 μW/cm^2. For a detection band width of 0.5Hz (integration time $\approx$ 0.3 sec.) the rms current noise is $\approx$ 10 nA, as shown in Fig. 12. This implies that the detector can detect $\approx 0.3 \times 10^{-15}$ W and taking into account the integration time this will translate to 0.1×10^{-15} Joule. A photon of wavelength 850 nm carries energy 2.32 x 10^{-19} Joule. Thus the detector can detect a minimum of ~430 photons. The highest gain G_{pc} for the NWs occurs around 10μW/cm^2. For the detector with NW A1, the area $\mathcal{A}$ over which the light illumination is absorbed is $\approx 2.26 \times 10^{-9}$ cm^2. This translates to about 22×10^{-15} W, which gives an upper limit for its best performance.

Another alternate way to find the minimum power the sensed by the detector is to proceed from the measured Gain. The detector retains a finite measureable gain even for illumination intensity of 1μW/cm^2. Thus it can detect below 2×10^{-15} W. These estimates give us a good range of the minimum energy/power the single Ge NW detector can measure and measurement of ~10^{-15} Joule will be possible with these detectors, taking into consideration their *NEP* and detection band width.

6. Factors that may lead to uncertainty in the Responsivity and Gain

There are certain factors which may lead to underestimation of $\mathcal{R}$ which are discussed below:

- One of them is the power absorbed by the nanowire which is less than the incident power P.[20] The approximate fraction is estimated as 50-80% in absence of proper data. It is noted that P is an upper limit of the absorbed power, thus underestimating $\mathcal{R}$.

- Enhancement of the photoconduction on illumination has also been measured through the photocurrent gain as defined previously. It should be noted that a part of the enhanced device current also arises due to lowering of SBH (ϕ) as discussed in the previous section. The contribution to the enhancement of device current due to enhancement of the barrier penetration probability can be measured by a factor, $\kappa = \exp(|\Delta\phi|/k_{\mathrm{B}}T)$. Thus dividing the observed G_{pc} by this factor gives us the effective gain $G_{eff} \equiv \mathrm{G}_{pc}/\kappa$ (see Fig. 13(a)). In Fig. 13 both Gain parameters and their ratio G_{pc}/G_{eff} are plotted as a function of illumination intensity. At lower intensity $|\Delta\phi|$ being small, the difference is not much. However, at higher intensity where $|\Delta\phi|$ is comparable to k_BT, the correction is large. It shows an estimate of the uncertainty that can come from the lowering of SBH on illumination.

- We point out that in the device structures that have been used, there may be some additional contributions arising from the SiO$_2$ layer acting as a wave guide and thus collecting radiation over

an effective area that is larger than the nanowire. To rule out this effect we have tested the photoresponse by illumination away from the NW. We find that for illumination even at a distance of 2-3 times the diameter of the NW shows negligible response.

- Another uncertainty arising from such an effect is due physical cross-section of a laid wire as the light collection area because of the antenna effect[21,22] due to the underlying Silicon (below the 300 nm SiO_2 layer). Due to the antenna effect from the underlying Si substrate on top of SiO_2 there is back scattering of the incident EM wave. This may leads to an overestimation of the Responsivity due to scattered wave from the substrate re-entering the NW. We have used finite element method to simulate the scattered wave from a SiO_2/Si substrate. We estimate that the intensity of scattered wave is ~5.9% of the incident wave. The input intensity of $2654\mu W/m^2$ produces a back scattered intensity $159\mu W/m^2$. It is almost negligible and we can claim that this effect does not hamper the opto-electronic parameters obtained. The details of the simulation are given in **Appendix A**.
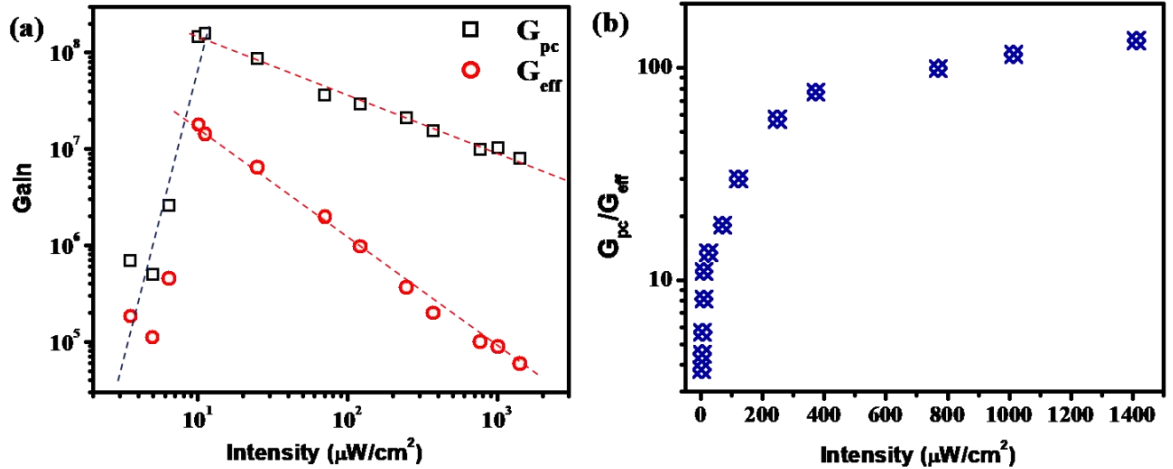

Figure 13. (a) Gain G_{pc} and Effective Gain G_{eff} versus Intensity for NW A1 at a wavelength of 650nm at 1V bias. The dotted lines are for guiding the eye. (b) Ratio of G_{pc}/G_{eff} in A1.

7. Dependence of photocurrent on illumination intensity

The Gain and the photocurrent have interesting dependences on the illumination intensity. We show below that the dependence of the I_{Pc} on illumination intensity can be qualitatively changed by annealing. This observation gives us useful information on the surface and interfaces on a Ge NW that is coated with a native oxide layer GeO_x (x ≤ 2).

In Fig. 14a, I_{Pc} has been plotted as a function of the illumination intensity J for the selected devices. The dependence of I_{pc} on J is given as,[23]

$$I_{pc} \propto J^\alpha \tag{10}$$

The exponent α depends on the factors like, process of generation of electron-hole pairs and trapping and recombination of charge carriers in the device. The fit to equation 10 is also shown in Fig. 14(a) which shows $\alpha < 1$ ($\alpha \sim 0.30$, 0.39 and 0.58 for N1, A1 and M1 respectively, given in Table 3). For all the devices except M1$_a$ (see Fig. 14(b)) which we discuss separately, one finds that $\alpha > 1$. The photo-response in nanowires is controlled by defects in them that can occur in the bulk of the NW and the surface. The sub-linear dependence on intensity arises from states that are located energetically near the Fermi level[1,23] and their filling by enhanced radiation intensity as more carriers generated control the dependence of I_{pc} on J.
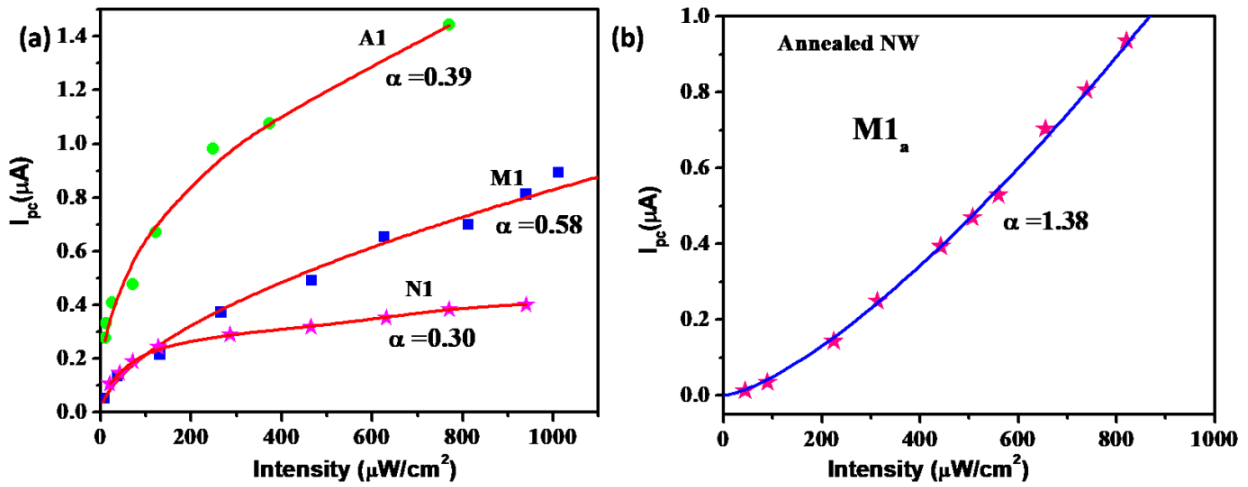

Figure 14. (a) Photocurrent (I_{pc}) as a function of intensity J in A1, M1 and N1 showing sub- linear dependence on J. (b) Post annealing, (M1$_a$), I_{pc} becomes super- linear ($\alpha = 1.38$).

These defects states can also lead to roll-off of the photo-response at higher J.[2] The defect limited sub-linear illumination intensity dependence is a bottle-neck in the process of enhancement of performance of single NW photodetector inspite of their high Responsivity that is achievable at low intensity. Photodetectors with super-linear intensity dependence ($\alpha > 1$) is rather rare although there are reports of such photo detectors.[24] It has been shown that existence of carrier trapping-detrapping centers within the band gap that have widely differing carrier capture rates, under certain conditions, can lead to a situation where it is possible to achieve super-linear photoresponse with $\alpha > 1$.[24,25] However, there are no reports of such super-linear photo response in NWs.

We have prior knowledge that there is a surface oxide layer on Ge of the form of GeO_x that has two types of defect states.[30] The "fast states" (relaxation time $\sim \mu$sec) occur at the Ge/GeO_x interface and "slow states (relaxation time $\sim m$sec) occur within the oxide layer. Control of these states by annealing can change the number of trap states with slow kinetics located within the surface oxides of Ge NW. Controlled thermal annealing was performed on the fabricated photodetector as well as on an ensemble of Ge NWs grown on Si substrate under ultrahigh vacuum (10^{-8} mbar) conditions at $\sim 400^0$C for 10 minutes. It is noted that since such a fabricated device is being annealed, a higher temperature ($> 400^0$C) as well as prolonged time of anneal (> 10 mins) breaks the device by thermal strain. In the next sub-section we show how annealing that change nature of the surface oxide can lead to $\alpha > 1$.

8. Nature of the surface oxide layer

Apart from the kinetics of the filling and de-filling of traps (located at the Ge/oxide interface and on the oxide layer), the surface plays another very crucial role; it forms a depletion layer which pins the Fermi level to the surface, resulting in surface band bending (SBB).[9,10] Thus a study of the chemical composition of the surface oxide layer is warranted.
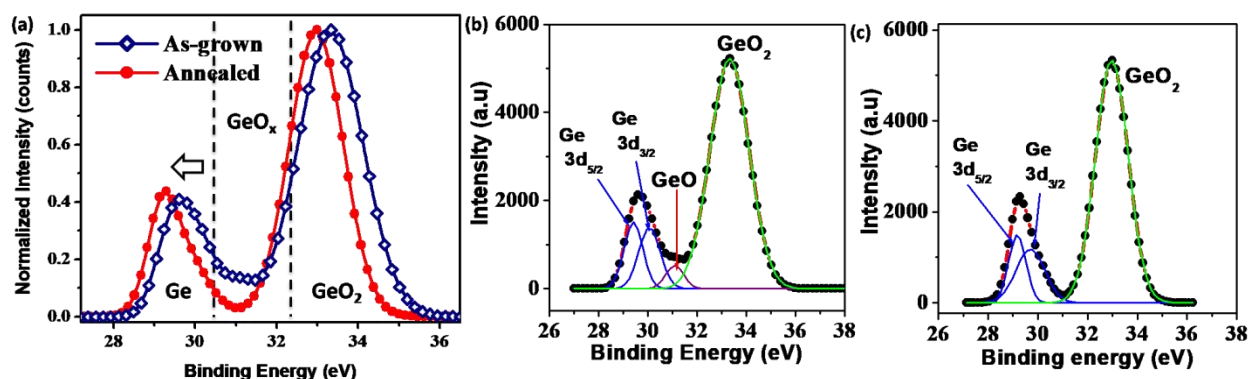

Figure 15. XPS spectrum of an ensemble of Ge NWs as-grown and annealed. The dashed lines roughly demarcate the Binding energy zones of Ge states. Multi-peak fits showing Ge 0+ peak is shown in blue, Ge 2+ peak in purple and Ge 4+ peak in green, while the experimental data is shown as black points in (b) as-grown NWs and in (c) annealed sample.

It is established (Chapter II, through Electron Energy Loss Spectroscopy) that the surface of the NW is surrounded by an oxide layer. We have performed a comparative XPS investigation on as grown as well as annealed Ge NWs using monochromatic AlK_α (1486.6eV) radiation. High resolution of Ge 3d photoelectron lines on the Ge NW is shown in Fig. 15. The XPS spectrum shows two prominent peaks corresponding to Ge^{0+} state and Ge in higher valence states. The Ge NW 3d XPS spectrum has multiple

peaks due to presence of oxides and sub-oxides. The de-convoluted Ge 3d photoelectron spectra (lines assumed to be Gaussian) are shown in Fig. 15(b) and 15(c). As-grown Ge NWs (Fig. 14(b)) shows oxide on the surface with Ge in 4+ (at ~33.3) and 2+ (at 31.1eV) states, along with Ge^0 3d peak (split by spin-orbit interaction).[26,27] XPS data shows that there is about 15% relative concentration of GeO (Ge^{2+} state) in the as-grown NWs. Post-annealing, dominantly Ge exists in stable 4+ state with peak position at 32.9eV in the form of GeO_2 along with Ge in 0+ state (Fig. 15(c)). There is no detectable trace of any sub-oxides, (predominantly GeO) which is known to volatilize from the surface[26,28,29] upon vacuum annealing at temperatures $\geq 400^0$ C. The main result is, controlled annealing at relatively low temperatures (~400^0C) leads to selective modification of the GeO_x on the Ge NW as revealed by XPS investigation.

8. Effect of controlled annealing on photoresponse

The $I - V$ curves for the as fabricated device, annealed device in dark and under illumination intensity of $820\mu W/cm^2$ and $\lambda = 650$ nm are shown in Fig. 16. It can be seen that the annealing enhances the device current by a more than two orders and there is also significant enhancement in the magnitude of the device photocurrent.
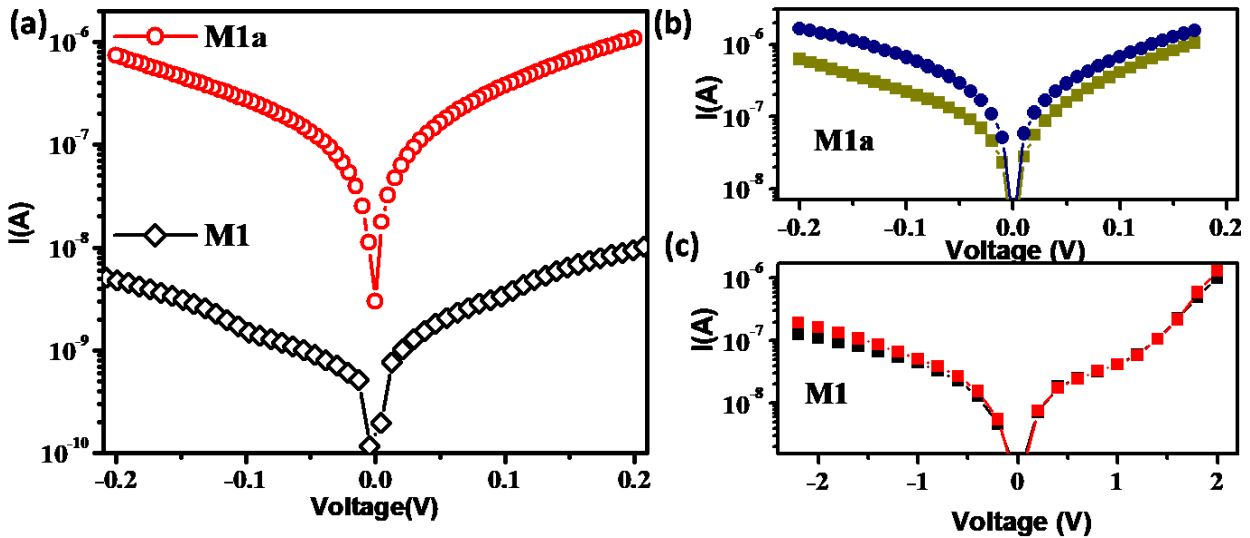

Figure 16. *I-V* curves for before (black) and after (red) annealing in M1. *I-V* curves in dark and under illumination intensity of $820\mu W/cm^2$ (λ=650nm) in (b) M1a: annealed and (c) M1 photodetector.

Quantitative analysis below shows that annealing as performed leads to improvement on a number of relevant device parameters that lead to enhancement of device parameters post-annealing. Analysis of the *I-V* curves were performed as discussed in Chapter IV. All the relevant parameters obtained by fitting the

data to are given in Table 2. There is a reduction in specific contact resistivity (ρ_c) by a factor of nearly 30 from 4.6mΩ-cm^2 to 0.15mΩ-cm^2 on annealing and also a decrease in the Schottky barrier height (φ) at the metal-semiconductor contact by 24 meV (~8.5%). The resistivity of the NW (ρ_{NW}) also reduces by a factor of 30, from 0.3Ω-cm to 0.01Ω-cm. Thus, annealing not only improves the electrical contacts, it also reduces defects in the bulk of the NW, which in turn is reflected in the reduction of NW resistivity. Substantial change occurs on illumination post-annealing in the SBH which in turn enhances the device output current.

9. A Noise Spectroscopy study on the NWs

The current biased low frequency $1/f$ noise spectroscopy was done with ac modulation technique.[31,32] Measurement of $1/f$ noise in the device before and after annealing at low frequency (< 10Hz) shows (Fig. 17) that the normalized Spectral power density ($\equiv \frac{S_V(f)}{V^2}$, where, $S_V(f)$ = Noise spectral power density) decreases significantly on annealing. For instance, at f =1Hz, the normalized spectral power decreases from 8.5x10^{-7} Hz^{-1} to 1.7x10^{-7} Hz^{-1}(Above $f = 1Hz$ the noise is dominated by the Nyquist Noise).[32]

Noise in a semiconductor can arise from fluctuators (generally from trap states that lead to generation-recombination of carriers) located in the bulk as well as on surface.[33-35] In a NW, due to enhanced surface contributions, it is reasonable to expect that a good part of the noise originates from surface states. The spectral range in the noise measurement shows that the fluctuators have a long relaxation time typically >20ms. From the extensive investigation done on Ge single crystals and surfaces, it is established that such fluctuators with long relaxation time occur in the GeO$_x$ layer on the surface of Ge.[30] Consequently annealing leads to reduction in Noise Equivalent power (NEP) and enhances the Specific Detectivity D^* by nearly an order of magnitude to ~ 10^{14}cmHz$^{1/2}$/W. The noise data thus leads to the important inference that the enhancement of the performance of the device arises from significant reduction of slow relaxing states.

In Ge, the trap states that occur at the interface of Ge/GeO$_x$[30] have high capture cross-section and capture time $\leq 1\mu sec$. These states are the "fast states" that control carrier recombination and annealing induced decrease of these states would enhance I_{pc} and $\mathcal{R}$ as has been observed. However, reduction of the low frequency noise data shows that the annealing also effectively reduces the "slow states" that are located in the GeO$_x$ layer. These states have capture time that can extend from *m*sec to even hours and determine the band bending at the surface and the kinetics of the charge balance on illumination.[26] Depletion of these states on annealing will not only reduce the low frequency noise, they will also reduce significantly

carrier capture over extended duration. These slow states limit photocurrent gain and saturate the power dependence of photocurrent at higher power. It is suggested that the important observation that annealing leads to super-linear dependence of photocurrent on the illumination intensity ($I_{pc} = kJ^\alpha, \alpha > 1$) is related to the observation of low frequency noise reduction on annealing that shows a substantial reduction of "slow states".
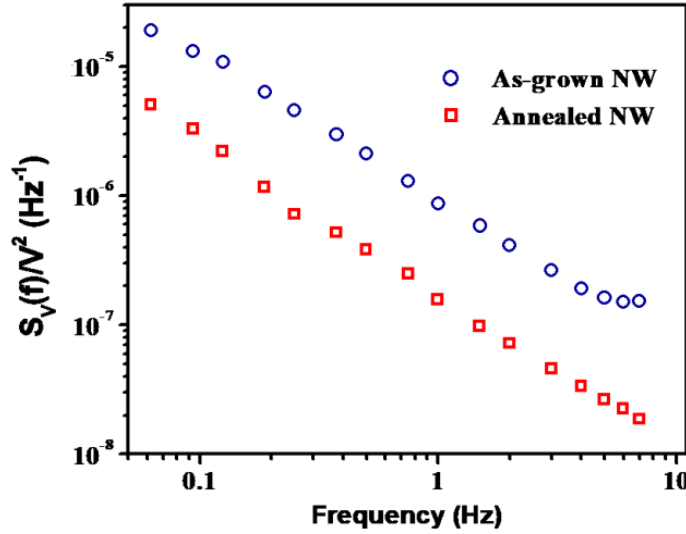

Figure 17. Normalized noise spectral power density in a Ge NW photodetector in as-grown device and in the annealed device.

10. Numerical model to quantify the photoresponse behavior

The role of "slow states" to control the illumination dependence of I_{pc} can be demonstrated by a numerical model of a photoconductor with three energy levels which lie within the band gap of Ge. Two of them are traps (for electrons and holes respectively) and the other is a recombination centre.[36-38] The details are given in **Appendix B**. For super-linearity to set in, carrier lifetime should increase with increasing generation rate or illumination intensity. It has been shown that such a situation occurs if,[37,38]

- Recombination centers become fully occupied while shifting of the quasi-Fermi level under illumination which reduces recombination pathways.
- Capture of carriers by the recombination centers is the slowest possible process.

In this case, the recombination centre (with density of states: N_3) is one that has a large lifetime thus its capture rate is very low (which corresponds to the slow states in Ge oxide layer) while the trap states have widely differing capture times (these are the fast states with density N at the interface of Ge/GeO$_x$ with lifetime ~ μsec).

Solving the rate equations for such a system shows that when all the states have equal density, $N_3 = N$, there is sublinear behavior of photocurrent ($\propto$ density of free carriers) with illumination (shown as photogeneration rate in Fig. 18). If we reduce density of slow states, i.e., $N_3 = 10^{-2}N$, then there is onset of super-linearity[31] and for the case $N_3 = 10^{12}N$, it is linear. Fig. 18 shows these three cases. This validates our noise spectroscopy observations that annealing reduces the number density of states with longer capture time.
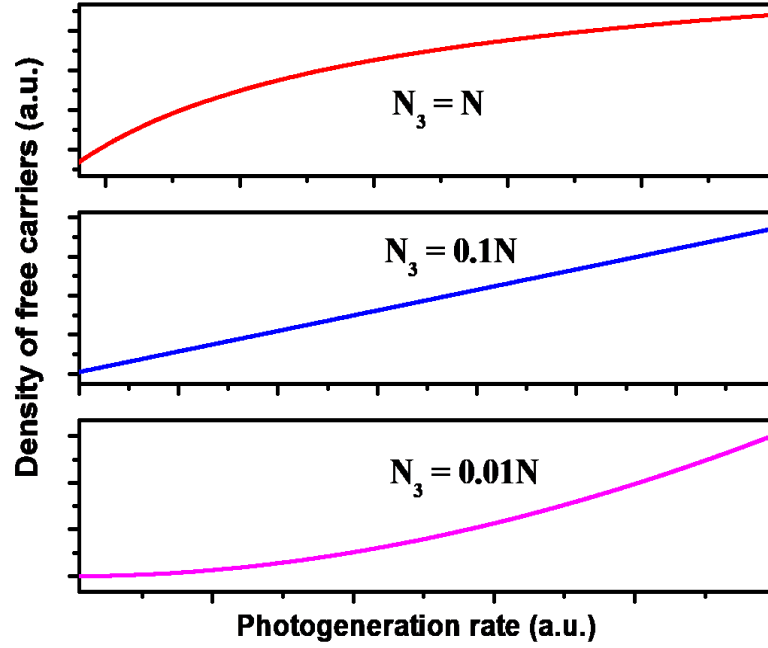

Figure 18. Free carriers as a function of generation rate for case (a) when $N_3 = N$ and (b) when $N_3 = 0.1N$ and (c) when $N_3 = 0.01N$.

Presence of sub-oxides on Ge leads to high density of defect (trap) and interface states[39,40]. It has been shown[40,41] that the traps arise in sub-oxides from deviation in local coordination from 8-N rules leading to substantial 3-fold coordination of Ge as well as Oxygen instead of 4 and 2-fold coordination respectively. These lead to formation of trap states that are charged. The trapping and de-trapping of electrons (and holes) from these charged states involve local bond relaxation and give rise to the "slow states" in the oxide layer[42]. The annealing process while reducing the sub-oxide GeO also leads to removal of these slow states. This reduces recombination pathways resulting in an increased carrier lifetime. This validates the hypothesis that links the "slow states" with observation of super-linear illumination intensity as well as $1/f$ noise spectroscopy.

11. Gain dependence on illumination intensity

Enhancement of the photoconduction on illumination has also been measured through the photocurrent gain as defined previously. An example of measured G_{pc} versus illumination intensity is shown in Fig.18 for the selected devices taken at wavelength 650 nm (other wavelengths have also been taken, though not shown here to avoid repetition). Since the data have been taken at different biases, we have normalized the Gain to 1V. G_{pc} initially increases with intensity, reaches a maximum and then reduces again at higher intensity. Nevertheless, we observe that the value of intensity where G_{pc} shows a peak is similar ~10μW/cm^2 for all the devices (see Fig. 19). G_{pc} reaches a maximum value in excess of 10^7. This is one of the highest value of Gain in a broadband spectrum reported till date.
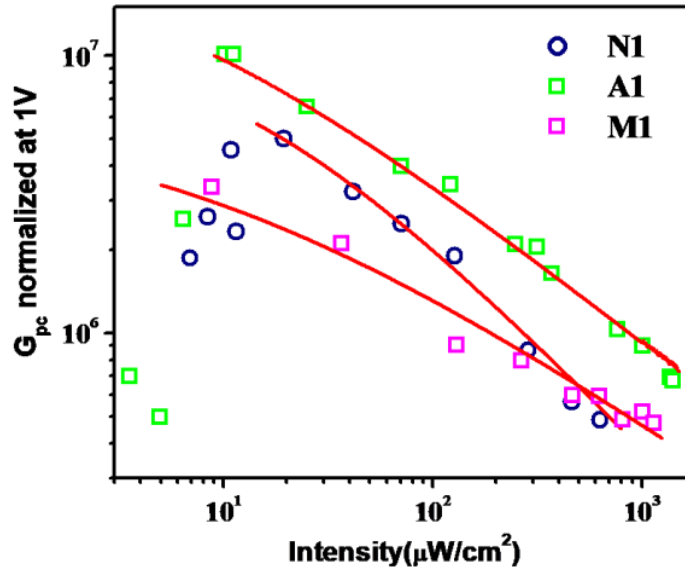

Figure 19. Gain for the selected nanowire devices as a function of illumination intensity. The dotted line is the fit to the equation 11.

For illumination intensity $\mathcal{J} >$ than the optimal value ($\mathcal{J}_0$), the gain decreases as a function of intensity. As a result beyond particular illumination intensity the gain decreases. The dependence of G_{pc} with $\mathcal{J}$ for $\mathcal{J} > \mathcal{J}_0$ is given by,[2]

$$G_{pc} = \frac{\tau_l/\tau_{tran}}{1+\left(\frac{\mathcal{J}}{\mathcal{J}_0}\right)^n} \tag{11}$$

where, the unsaturated intensity independent gain depends on the carrier transit time τ_{tran} , n is a phenomenological fitting parameter that depends on the recombination of carriers at the trap states and τ_l is the carrier lifetime. The fitting of the experimental data to the above equation also gives us the value of

the illumination intensity $\mathcal{I}_0$ where the gain saturates. The parameters obtained from the fits to equation 11 are given in Table 4. For all the NWs, the values of $\mathcal{I}_0$ are very similar. The value of $\tau_l/\tau_{tran} \sim 10^7$, shows that the lifetime of carriers (holes) are indeed enhanced due to capture of electrons at the trap states, driven by the radial field. In the 30 nm NW, there is a tenfold increase in $\mathcal{R}$ at the same bias as compared to N1 which has a 65 nm diameter. The above discussion clearly establishes the crucial role that a surface plays in photocarrier dynamics.

Table 4. Fit parameters for dependence of effective on illumination intensity.

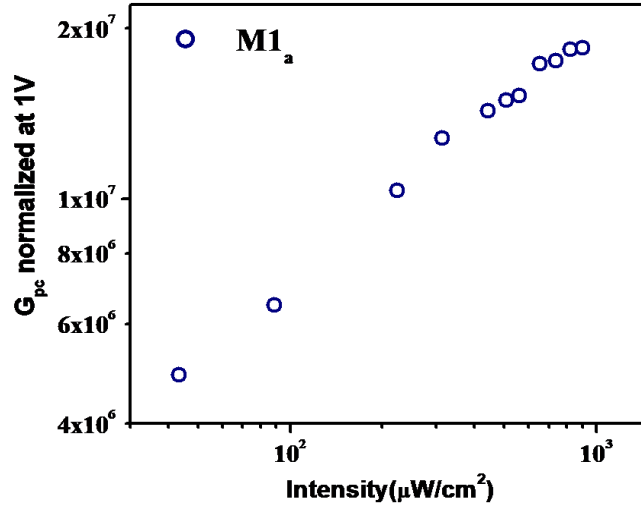| NW Name	τ_l/τ_{tran}	$\mathcal{I}_0(\mu W/cm^2)$	n
N1	1.0×10^7	9.0 ± 2	0.73
A1	2.5×10^7	8.3 ± 1.4	0.60
M1	1.8×10^7	8.5 ± 1.1	0.42

Figure 20. Gain for the annealed nanowire $M1_a$ devices as a function of illumination intensity.

The type of behaviour, where the Gain rolls-off at higher frequency is attributed to the presence of a **radial field** (created by a depletion layer on the surface, see Fig. 21(a)) and saturation of these surface states. As the illumination intensity increases, the carrier generation rate increases, the surface states get filled and the band bending that gives rise to the radial field is reduced leading to reduction in gain.

Gain dependence on illumination intensity in the annealed NW M1a is radically changed, which should be the case as we have a super-linear response. In this case, the Gain increases with intensity[11] as shown

in Fig. 20. (Note: The normalized Gain at 1V is shown here to highlight the effect that annealing reduces the working bias of the photodetector.)

D. DISCUSSIONS

1. Factors causing the high Gain

The extremely large value of $G_{pc} \geq 10^7$ achievable in the photodetectors is contributed by a number of factors.

- There is an important factor which we discussed due to the device size where the length l (distance between electrodes) being ~1-3μm, is greater than the recombination length d_{avg} that makes the transit time of the carrier $\tau_{transit} = l^2/\mu V$ short. As a result, devices with sizes in the range of ~1μm can collect carriers without sufficient recombination.

- Another additional factor that contributes to the enhanced photoresponse in NWs with a surface oxide layer is the partial enhancement of the electric field of the electromagnetic wave (EM) inside the nanowire;[1] it thus increases electron−hole pair generation. There is difference in refractive index between the core (Ge) and cladding (native oxide layer and air) resulting in a large numerical aperture which leads to confinement of incident light in the NW. This has been quantified in Si NWs[1] and our results for Ge NW are given in **Appendix C**, which shows that electric field of an EM wave increases drastically as the diameter of the NW reduces below 60 nm.

- **Photogating effect: "**Photogating is considered as a way of conductance modulation through photoinduced gate voltage".[43] If one type of photogenerated carrier gets trapped (due to impurity, interface states etc.) that prolongs their lifetime and also if it has a spatial distribution, it may be considered as an applied gate voltage since it modulates the channel conductance. In Ge, there are two types of surface states that govern the photoresponse. The states at the interface of GeO_x/Ge that are essentially trap states and the "slow states" (which are acceptor type) that lie in the GeO_x layer. This phenomenon, observed only in low dimensional materials[5,43,] is referred to as Photogating. It is a direct consequence of trap states and influences the photoresponse.

- The effect of impact ionization in a NW that increases the number of charge carriers through an avalanche mechanism, which will be discussed in Section D, 4.

- **Radial field:** The existence of a depletion layer on the surface of a NW (which is promoted by presence of a native oxide layer or one that is acquired during growth) plays an important role. It leads to surface Fermi level pinning induced band bending.[9,10] This process of carrier separation by a built-in radial field due to formation of a depletion layer at the surface (see Fig. 21(a)) is at the core of enhanced performance of the NWs as an efficient photodetector. The effective radial field separates the photogenerated carriers spatially. This inhibits carrier recombination and the holes can reach the electrodes without significant recombination. While in a forward biased contact (+ve), the barrier for holes is high, in the reverse biased junction (-ve), the holes get effectively collected (see Fig. 21 (b)). It is discussed below.
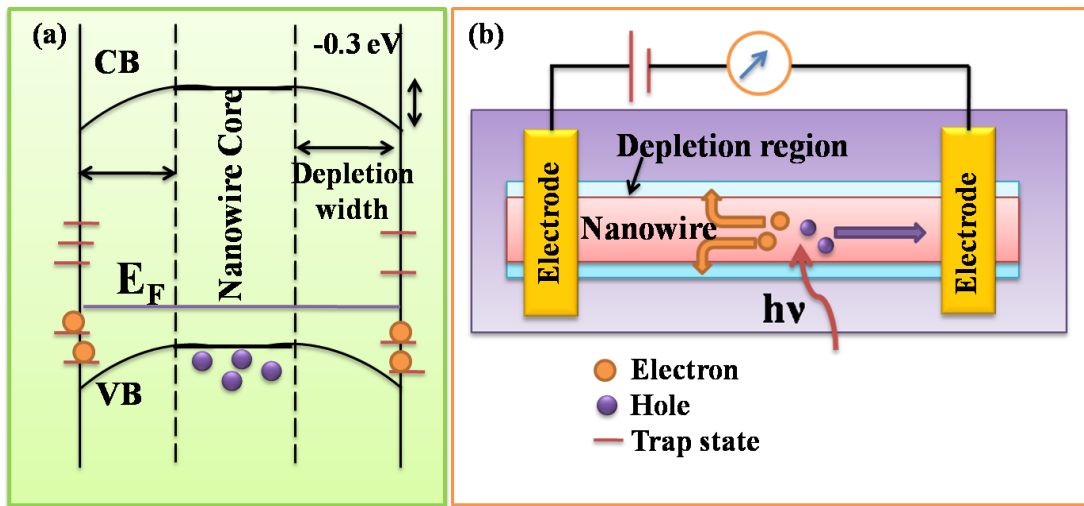

Figure 21. (a) Schematic of Radial field in a Ge nanowire, showing depletion of electrons at the nanowire core, resulting in band bending. (b) Schematic showing spatial separation of photogenerated electron-hole pair due to radial field formed by depletion layer at the surface.

2. The Radial Field

A very important effect due to presence of these surface states, that is negligible in bulk semiconductors, is depletion region at the surface. It constitutes a large fraction in a nanowire due to its small diameter (< 100nm). It is formed due to transfer of charge from interior states to surface states or any other states that lie within the band gap of Ge.[44] This depletes the surface and pins the Fermi level to the surface, resulting in surface band bending (SBB) or a lateral screening potential.[45] A schematic of the radial field is shown in Fig. 21 (a).

There have been observations (through XPS technique) of SBB in ZnO and GaAs NWs.[9,10] The SBB dictates the nature of radial field. In metal oxide NWs,[46] there is a short discussion on the radial field, but it is qualitative in nature. Recently, high Gain mechanism in Si NWs[47] was probed through photo-Hall measurements which show that electrons are localized in traps at the surface region, while holes are left in the channel region. They estimate a depletion width ~85 nm that reduces upon illumination. This is also the reason behind the decreasing G_{pc} (Fig. 19) upon increasing illumination. Upon illumination, the photogenerated pair is separated by the radial field and as electrons get trapped, the strength of the radial field decreases, that is, the depletion width decreases. Thus, an estimate of the depletion layer width in Ge NWs is essential. We conclude that the photoconductivity in semiconductor NWs is regulated by the depletion region width, photo-excited carrier density and presence of traps states.

3. Lateral confinement of electrons: Solution to the radial field using self-consistent Schrodinger-Poisson Equation

While the role of the surface states leading to SBB and their effects in enhancing the photoconductive gain has been discussed in earlier publications[9,10,47], the quantitative estimation of depletion width and assessment of the radial field has not been worked out before. This exercise will lead to *quantification* of the origin of the ultra-high photocurrent Gain in the nano-scale regime. We have used the Schrodinger-Poisson equation to solve for the radial field in a Ge NW through an iterative process.

The estimation of depletion width and assessment of the radial field helps us to quantify the origin of the ultra-high photocurrent Gain in the nano-scale regime. We have used the Schrodinger-Poisson equation to solve for the radial field in a Ge NW through an iterative process.

Carrier confinement in the radial direction in a NW depends on the temperature, doping and radius and most importantly on the pinning of the Fermi level (E_F).[45,48] We have used finite element method for solving this problem through COMSOL Multiphysics. Self-consistency is achieved by iteratively solving the two coupled equations. The Poisson's equation is solved to obtain the potential created by a given charge distribution (ρ) in a NW. The electric potential (V) from the electrostatics contributes to the potential energy term in the Schrödinger equation from which the wave function (ψ) and eigenvalues (λ) are calculated. The density function (n), which contributes to the space charge density in the electrostatics is determined from ψ, and considering a 1D cylindrical geometry is given by,[4]

$$n = \left(\frac{2m_e}{\pi \hbar^2 k_B T}\right)^{1/2} \sum_i F_{-1/2}\left(\frac{E_F - E_i}{k_B T}\right) |\psi_i|^2 \tag{12}$$

where, $F_{-1/2}$ is the Fermi-Dirac Integral and the other symbols have their usual meaning. Then, the Poisson equation is solved with this updated charge density (n') to get a new V (V'). The Schrödinger

equation and Poisson's equation are solved iteratively until a self-consistent solution[49] is obtained, with error between the Potentials (V and V') ~ 1µV.

We solve for the system in 1D using cylindrical symmetry. We have to make a few assumptions that are,

- There is uniform background of dopants ($N_d = 10^{18}$/cm^3)
- The Fermi level is at 0V at the centre of a NW (where r = 0).
- Potential at the surface (V_R) is pinned at some value with respect to $E_F = 0$.
- We solve at temperature equal to 300K.
- Bulk Ge material properties like dielectric constant etc has been used.

The boundary condition at the surface of the NW is given by the pinned Fermi level. We have used Fermi level pinning at -0.3eV since it is known from X-ray Photoelectron Spectroscopy measurements that the surface band bending is ~0.3eV in p-type Ge NWs.[26] The diameter of the NW is a typical 60 nm value while we solve the equation at 300K assuming all dopants are ionized.
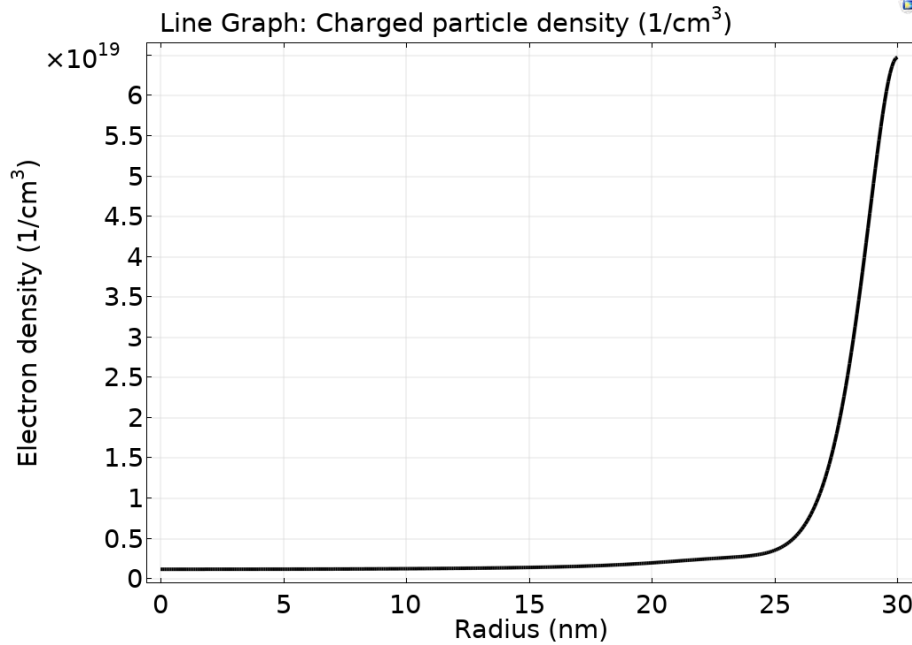

Figure 22. Electron density as a function of NW radius showing confinement of electrons at the surface.

Figure 22 shows the electron density in a 60nm NW due to presence of surface states. The surface (upto 10 nm) is electron rich while there is a depletion of electrons at the NW core. The SBB can be clearly seen from Figure 23, where the electric potential is shown as function of radius. The depletion width is ~ 30nm. Thus, for a 60 nm nanowire, the conduction channel is essentially 30 nm. The Radial field (see Fig. 24) increases sharply beyond 25 nm from the NW core and is quadratic in nature. The radial field quite

strong and reaches ~1.5×10^8 V/m at the surface of the NW. (Note: the negative value of radial field indicates band bending is downwards.)
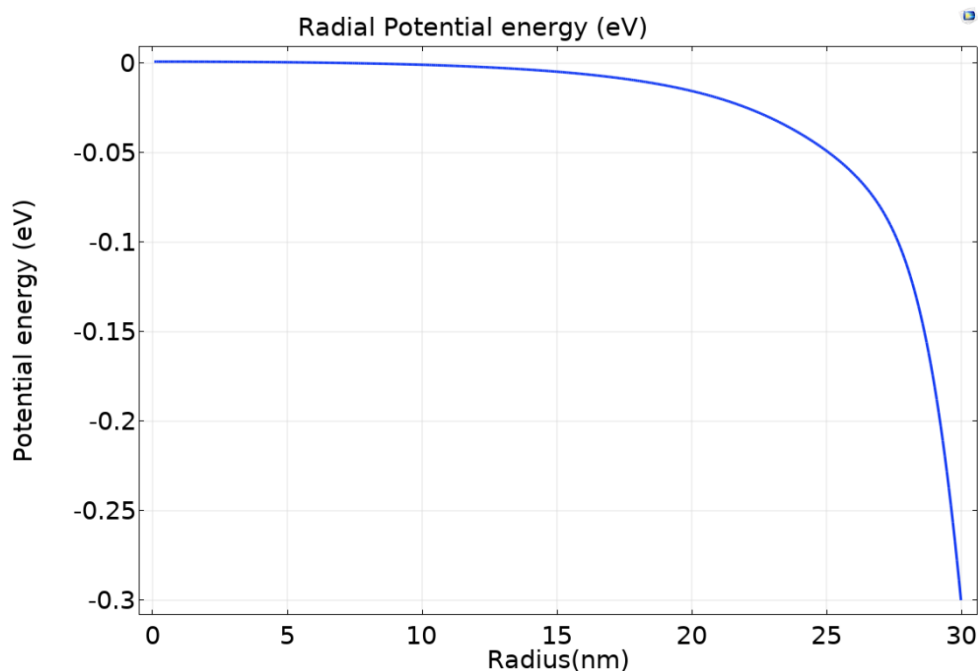

Figure 23. (a) Confining potential as a function of radius of the nanowire. The surface band bending ensures the potential = -0.3eV at the surface.
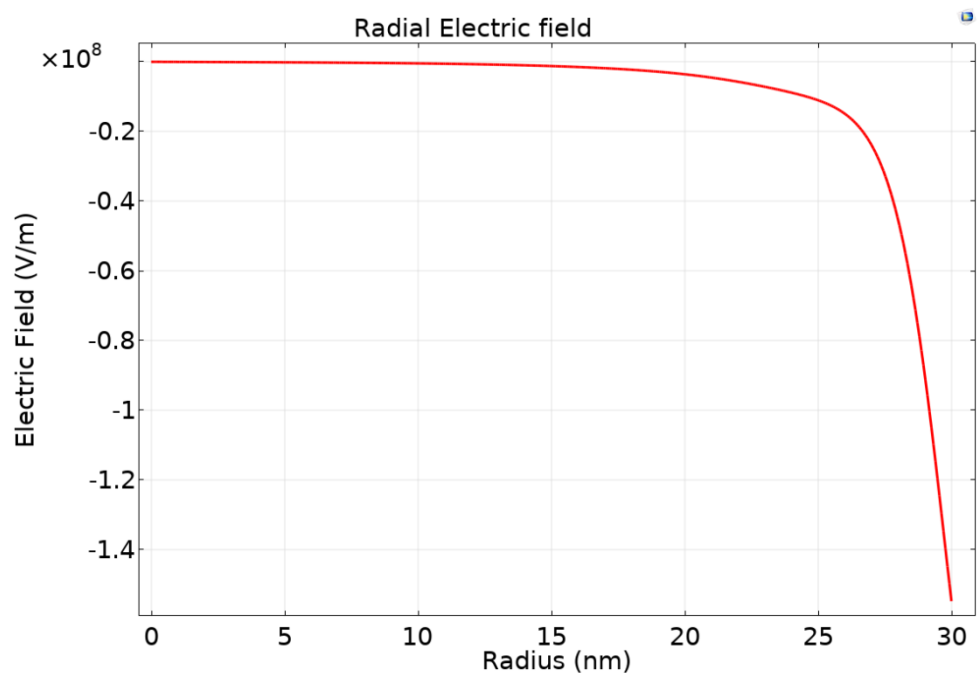

Figure 24. Radial field in a Ge NW pinned at 0.3eV.

To ascertain the correctness of the results, we have simulated the band bending in a 200 nm diameter Ge NW with E_F pinned at 0.3eV. It also shows a band bending and electron confinement at the surface. But in comparison to the core of the cylindrical wire, the fraction of the confined region is very less. This may be extrapolated to a bulk system, where a depletion region exists at the surface but is negligible. We have also simulated to see what happens if we assume E_F is not pinned i.e. $E_F = 0$ eV. The results show no band bending and no confining potential.

4. Impact of high electric field

Another factor that seems to be a likely cause of such high Responsivity is impact ionization[50] due to very high electric field at the depletion region that produces multiple electron-hole pairs through avalanche mechanism. In a p-Type/Intrinsic/n-Type Si NW,[50] it has been shown that the intrinsic region has a carrier multiplication $\sim10^3$-10^5 times more than the n-type and p-type regions. This sharp increase is attributed to an avalanche breakdown mechanism. The strong electric field $E \sim 4x10^5$V/cm in the intrinsic region effectively separates the photogenerated electron-hole pair that gives rise to the high photocurrent in the intrinsic region as compared to the p-type and n-type region. In an InP NW[51] that has a depletion region due to a p-n junction formed by doping during growth, shows light induced avalanche breakdown. Even though the depletion region is small (~200nm), it can multiply the electron-hole pair as they gain enough energy to commence the avalanche process. InP also has a low impact ionization coefficient that aids this process. The avalanche breakdown is quantified by a multiplication factor M, which ~ 20 when the applied bias approaches the breakdown voltage in a Si NW. In bulk Ge, the breakdown field $E_b \sim$ $4.5x10^5$V/cm for carrier concentration (n) of 10^{18}cm^{-3} and $1.5x10^5$V/cm for $n = 10^{15}$cm^{-3}.[52]

We have used a finite element method to determine the Electric field in a nanowire. We use a 2D rectangular block to design a 50nm NW with ~1μm gap between electrodes. We then define the voltage bias which is 2V at one end and grounded at the other. The material properties like carrier concentration, density of states etc are taken from bulk Ge values. We use Poisson's equation to calculate the electric potential across the NW.

The Electric field obtained in the photodetector is $E \sim 2x10^4$V/cm (see Fig. 25). Even though we do not reach the E_b in the Ge NWs, there may be an onset of the avalanche process. Another factor that plays an important role is the drift velocity of holes- which allows the photodetector to perform in the drift limited regime. In such high fields, the drift velocity may saturate. For example, the saturation drift velocity in a nominally doped Ge wafer is ~$6x10^6$cm/s at 300K at $E = 10^4$V/cm.[53,54] Thus, there is acceleration of photogenerated carriers to their saturation drift velocity as such high fields.
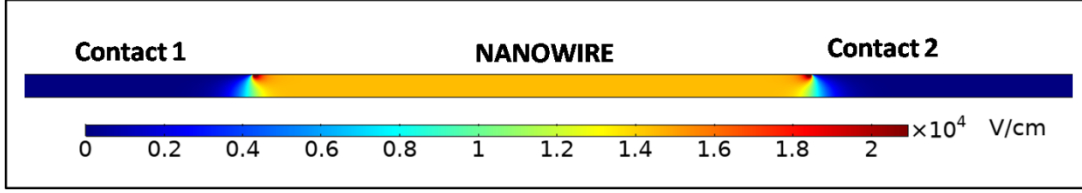
Figure 25. The Electric field at a bias of 2V in a Ge NW with typical dimensions used in this study.

E. CONCLUSIONS

We establish that photodetectors can be made from single Ge NWs that show ultrahigh Responsivity exceeding 10^7 A/W (nanowire diameter ~ 30 nm) over a broad spectral range 300 nm -1100 nm with finite response extending well into the NIR region at wavelength > 1100 nm. The relatively low current noise and such high Responsivity gives rise to a detector that can detect down to 10^{-15} W. The large optical gain exceeding 10^7 is achieved at a low optical illumination intensity ~ 10μW/cm^2. The device length ~1-3μm being smaller than the carrier diffusion length also facilitates collection of carriers effectively before recombination. One of the core enabling factors that leads to such a high gain is the surface oxide layer. The surface states in the oxide layer gives rise to a depletion layer that helps in separation of the photogenerated electron-hole pair. The states in oxide layer and at the interface, traps photogenerated carriers and leave the hole free to reach electrodes without recombination.

The performance of a photodetector can be engineered by a controlled high vacuum annealing of the NWs to 400^0 C. Post annealing, the detector shows an enhanced Specific Detectivity of ~10^{14}cm.Hz$^{1/2}$/W, comparable to commercially available detectors. While an overall enhanced response on annealing is not unexpected due to a number of enabling reasons like reduction in resistivity, contact resistance and Schottky barrier at metal-semiconductor contact, the overwhelmingly important result is the super-linear dependence of the photocurrent on intensity of illumination. We have shown that annealing reduces the concentration of recombination centers that govern the slow carrier kinetics, leading to super-linear photoresponse.

Thus we conclude that the surface states participate in the Fermi level pinning at the surface, which creates an upward SBB, as seen through Gain versus intensity behavior and validated by simulations. Our analysis clearly shows the effect of interface and surface states on the opto-electronic properties of Ge NWs.

REFERENCES FOR CHAPTER V

[1]K. Das, S. Mukherjee, S. Manna, S. K. Ray and A. K. Raychaudhuri, *Nanoscale,* **6**, 11232-11239, 2014

[2]C. Soci, A. Zhang, B. Xiang, S. A Dayeh, D. P. R. Aplin, J. Park, X. Y. Bao, Y. H. Lo and D. Wang *Nano Lett.*, **7***, 1003, 2007

[3]Z. Liu,T. Luo, B. Liang, G. Chen, G, Yu, X. Xie, D. Chen and G. Shen. *Nano Res.,* **6***, 775, 2013

[4]X. Zhang, Q. Liu, B. Liu, W. Yang, J. Li, P. Niu and X. Jiang, *J. Mater. Chem.C,* , **5**, 4319, 2017

[5]S. Thunich, L. Prechtel, D. Spirkoska, G. Abstreiter, A. Fontcuberta-i-Morral, and A. W. Holleitner, *Appl. Phys. Lett.* , **95**, 083111, 2009

[6]H. Otounye, W. Kim and W. D. Lu *Appl. Phys. Lett,* , **110**, 173104, 2017

[7]Y. H. Ahn and J. Park, J., *Appl. Phys. Lett.*, **91**, 162102, 2007

[8]R. Basori, K. Das, P. Kumar, K. S. Narayan and A. K. Raychaudhuri, *Optics. Exp.*, **22**, 4952, 2014

[9]C. Chen, J. R. D. Retamal, I-W. Wu, D. H. Lien, M. W. Chen, Y. Ding, Y. L. Chueh, C. I. Wu and J. H. He, *ACS Nano,* , **6** 9366-9372, 2012

[10]H. Y. Chen, R. S. Chen, N. K. Rajan, F. C. Chang, L. C. Chen, K. H. Chen, Y. J. Yang and M. A. Reed, *Phys. Rev. B.*, **84**, 205443, 2011

[11]J. S. Jie, W. J. Zhang, Y. Jiang, X. M. Meng, Y. Q. Li, and S. T. Lee, *Nano Lett.* **6**, 1887–1892, 2006

[12]H. A. Norde, *J. Appl. Phys.* **50**, 5052–5053, 1979

[13]S. Sett, K. Das and A. K. Raychaudhuri, *J. Appl. Phys.*, **121**, 124503, 2017

[14]Y. K. Shin, D. Lee, H. S. Lee, Y. J. Cho, C. J. Kim, H. J. Moon, *Optics. Exp.*,**19**, 6129, 2011

[15]D. B. Cuttriss, *Bell Syst. Techn. J.*, **40**, 509, 1961

[16]T. Wei, C. Huang, B. J. Hansen, Y. Lin and L. Chen*, Appl. Phys. Lett*. **96**, 013508, 2010

[17]Thor Labs website https://www.thorlabs.com/thorproduct.cfm?partnumber=FDS1010 (accessed May 2019)

[18]L. Cao, J. S. White, J. S. Park J. A. Schuller, B. M. Clemens and M. L. Brongersma, *Nat. Mat.,* **8**, 643, 2009

[19]K. Das, S Samanta, P. Kumar, K. S. Narayan, and A. K. Raychaudhuri, *IEEE Trans. Elec. Devices*, **61**, 1444, 2014

[20]G. G. Macfarlane, T. P. Mclean, J. E. Quarrington and V. Roberts, *Phys. Rev.,* **108**, 1377-1383, 1957

[21]Y. Wang, K. Kempa, B. Kimball, J. B. Carlson, G. Benham, W. Z. Li, T. Kempa, J. Rybczynski, A. Herczynski, and Z. F. Ren, *Appl. Phys. Lett.*, **85**, 2607, 2004

[22]G. Chen, J. Wu, Q. Lu, H. R. Gutierrez, Q. Xiong, M. E. Pellen, J. S. Petko, D. H. Werner and P. C. Eklund, *Nano Lett.,* **8**, 1341-1346, 2008

[23]A. Rose, *Concepts in Photoconductivity and Allied Problems* (Krieger, New York, 1978)

[24]V. Klee et. al., *Nano Lett.* **15**, 2619 , 2015

[25]J. A. Peters, N. K. Cho, Z. Liu, B. W. Wessels, H. Li, J. Androulakis, M. G. Kanatzidis, *J. Appl. Phys.* **112**, 063702, 2012

[26]D. Wang, Y. Chang, Q. Wang, J. Cao, D. B. Farmer, R. G. Gordon and H. Dai, *J. Am. Chem. Soc*. **126,** 11602-11611, 2004

[27]T. Hanrath and B. A. Korgel, *J. Phys. Chem. B* **109***, 5518-5524, 2005

[28]K. Kita, S. Suzuki, H. Nomura, T. Takahashi, T. Nishimura and A. Toriumi, *Jpn. J. Appl. Phys.* **47** 2349, 2008

[29]K. Kita, T. Takahashi, H. Nomura, S. Suzuki, T. Nishimura and A. Toriumi, *Appl. Surf. Science.* **254** 6100–6105, 2008

[30]R. H. Kingston, *J. Appl. Phys.* **27**, 101−114, 1956

[31]A. Bid, A. Bora and A. K. Raychaudhuri *Nanotechnology*, **17**, 152, 2006

[32]A. K. Raychaudhuri, *Current Opinion in Solid State and Materials Science,* **6**, 67–85, 2002

[33]A. L. McWhorter, *Semiconductor Surface Physics*, edited by B.H. Kingston (University of Pennsylvania, Philadelphia,1957)

[34]F. N. Hooge, *IEEE Trans. on Elec. Devices* **41**, 1926 – 1935, 1994

[35]M. R. Sakr, and X. P. A. Gao, *Appl. Phys. Lett.* **93**, 203503, 2008

[36]R. H. Bube, *J. Phy. Chem. Solids.***1**, 234-248, 1957

[37]F. Stockmann, *Phys. Stat. Sol.* **34,** 741, 1969

[38]F. Stockmann, *Phys. Stat. Sol.* **34,** 751, 1969

[39]V. V. Afanas'ev, Y. G. Fedorenko, and A. Stesmans, *Appl. Phys. Lett.* **87**, 032107, 2005

[40]J. F. Binder, P. Broqvist, and A. Pasquarello, *Appl. Phys. Lett.***97**, 092903, 2010

[41]P. Broqvist, J. F. Binder and A. Pasquarello, *Physica B,***407**, 2926–2931, 2012

[42]F. Binder, P. Broqvist, and A. Pasquarello, *Microelec. Eng.***88** 1428–1431, 2011

[43]N Guo, W Hu, L Liao, S P Yip , J C Ho, J Miao, Z Zhang, J Zou, T Jiang, S Wu, X Chen and W Lu, *Adv. Mater.*, **26**, 8203–8209, 2014

[44]A. Zangwill, *Physics at Surfaces*, (Cambridge University Press, 1987).

[45]J. H. Luscombe and M. Luban, *Appl. Phys. Lett.,* **57**, 61-63, 1990

[46]R. S. Chen, W. C. Wang, M. L. Lu, Y. F. Chen, H. C. Lin, K. H. Chen and L. C. Chen, *Nanoscale*, **5**, 6867-6873, 2013

[47]K. Chen, X. Zhao, A. Mesli, Y. He and Y. Dan, *ACS Nano*, **12**, 3436−3441, 2018

[48]J. H. Luscombe and A. M. Bouchard, *Phys. Rev. B.,* **46**, 263-268, 1992

[49]C. Liu, *Comsol Blog*, https://www.comsol.com/blogs/self-consistent-schrodinger-poisson-results-for-a-nanowire-benchmark/, 2018.

[50]C.Yang, C. J. Barrelet, F. Capasso and C. M. Lieber, *Nano. Lett*, **6**, 2929-2934, 2006

[51]S. Assefa, F. Xia and Y. A. Vlasov, *Nat. Lett.*, **464**, 80, 2010

[52]G. Bulgarini, M. E. Reimer, M. Hocevar, E. P. A. M. Bakkers, L. P. Kouwenhoven and V. Zwiller, *Nat. Photonics* **6**, 455–458, 2012

[53]K. G. McKay and K. B. McAfee, *Phys. Rev.* **91**, 1079, 1953

[54]L. Reggiani, C. Canali, F. Nava, and G. Ottaviani, *Phys. Rev. B* **16**, 2781, 1977.

CHAPTER VI

SELF-POWERED SINGLE GERMANIUM NANOWIRE PHOTODETECTOR

We have observed photoresponse in a single Ge nanowire photodetector in the absence of a bias voltage thus enabling a self-powered operation. We have used simulation to establish that the asymmetric SBH at the metal contacts in a metal-semiconductor-metal device is a major cause for the 'built-in' axial field that leads to separation of a light generated electron–hole pair. We also point out the physical origins that can lead to unequal barrier heights in seemingly identical nanowire/metal junctions.

A. INTRODUCTION

There is a recent surge in search for materials and novel technology that would give rise to self-powered devices.[1] These devices can effectively harness energy, either by harvesting it from thermal or similar sources or by conversion of one form of energy to another.[2-4] In this context, self-powered optical detectors that work in a broad spectral range are of great utility, in particular, if they can detect weak radiation without any external power. Photo-voltaic cells form a class of self-powered optical devices.[5] Self-powered broadband photodetectors have been fabricated using SnTe films[6] and GaN microwire arrays[7] with Si heterojunctions. Heterojunction devices use the internal *built-in* potential at the interface to separate and transport the photogenerated carriers, leading to photo-detection without external bias. Self-powered thin film metal-semiconductor-metal (MSM) photodetectors have been fabricated recently either with dissimilar electrode material for the two contacts or with widely varying area of contacts.[8,9] In these MSM devices, the Schottky Barrier (SB) plays a crucial role. There may be initially a Schottky Barrier Height (SBH) mismatch, due to different electrode material at both contacts.[8] Or else, even if the SB has the same height but, area of the Schottky contacts differ and it has been shown that for nano-sized Schottky junctions, their depletion regions are unequal. This in-turn modifies the local potential so that the effective barrier height gets modified.[9] Thus the important contribution to photocurrent comes from the built-in field due to unequal SBH which helps in separation of the photo-generated electron-hole pairs. A list of self-powered photodetectors reported in literature with photoresponse parameters is given in Table 1.

Recently, our group has reported a single Si NW based photodetector that shows a zero-bias Responsivity ($\mathcal{R}$) ~10^4A/W at 514 nm.[10] However there have been no other report of a self-powered nanowire

photodetector. The previous reports[8,9] show that an unequal SB is the main cause for photodetection but a quantitative modeling and/or nature of the built-in potential is missing.

Here we show that single semiconductor NW based self-biased photodetectors can have high photoresponse reaching $\mathcal{R} \approx 10^3$-10^5A/W in the broad spectral range from 300nm to 1100nm. We have also performed simulation using COMSOL Multiphysics software, which shows that owing to the difference SBH at the two MS junctions, an axial electric field arises in the NW even in absence of an external bias when the two contacts are separated by a distance comparable to the sum of their depletion widths. This field separates the photo generated electron-hole pairs and drives them to the respective electrodes.

Table 1. Comparative study of self-powered photodetectors

Type of device	Electrode 1	Electrode 2	Wavelength region (nm)	Maximum Responsivity (A/W)	Ref #
Ge NW	Cr/Au	Cr/Au	300-1100	4×10^5	Our work
Si NW	Cr/Au	Cr/Au	514	1.97×10^4	10
ZnO film	Au	Au	300-400	0.02	9
Ge substrate	Ti	Ni	1480	0.42	12
GaN film	Ni	Au	320-380	0.005	8
GaN microwire array/Si	Cu	Ag	320-850	0.47	7
SnTe film/Si	n-type Si	Au	254-1550	0.128	6
Graphene/Si	Cr/Au	Ag	532	3	11
GaAs	Au	Ti	500-850	0.0645	13
Si NW array	Au	Ti	800-1180	0.08	14
TiO$_2$ nanotubes/Se	-	-	280-700	0.088	15
Sb doped ZnO nanobelts	Au wire	Ag	UV light	-	16

B. Results and Discussions

1. Dark *I-V* curves of the devices and determination of the Schottky Barrier Height (SBH)

We have used three single Ge NW MSM devices for our study with diameter ranging from 30 – 90 nm and length between electrodes upto 2μm. We have used Cr(5nm)/Au(60nm) contact electrodes on two devices, namely *S1* and *S2*. Ni (60 nm) electrodes were used on device *S3*. The device parameters in dark are provided in Table 2. Since previous self-powered MSM devices have unequal barrier heights (due to

dissimilar metal contacts), which leads to photodetection at zero bias,[8] it is important that we determine the SBH at the two metal/NW junctions. We also show below that the asymmetric nature of the barriers lead to self-power operation.

The NW photodetectors are MSM devices which can be modeled as two back-to-back Schottky diodes, with SBHs ϕ_1 and ϕ_2 at both ends connected by the NW with resistance R_{NW} as discussed in Chapter IV. The *I-V* curves of the devices (shown in Fig. 1) have been used to evaluate the SBH at the MS junction by fitting it to the modified Richardson-Dushmann equation[17,18]. For a given NW, the values of the SBH at the two ends are different. To have a normalized measure of this asymmetry, we used a parameter $\gamma \equiv \frac{|(\phi_1 - \phi_2)|}{\langle\phi\rangle}$, where $\langle\phi\rangle = \frac{\phi_1 + \phi_2}{2}$ is the average value of the SB. The unequal SBH can be observed from the asymmetry in the *I-V* curves (Fig. 2). It is most pronounced in device *S1* (see Fig. 2(a)) which has the highest γ of ~58%. The SBH depends upon the resistivity of the NWs (as we have seen in Chapter IV) and even though, for the same material contact Au, the SBH is different in *S1* and *S2*.[18] Section 5 has a discussion regarding origin of unequal SBH in Ge NWs.

Table 2. Device parameters in dark.

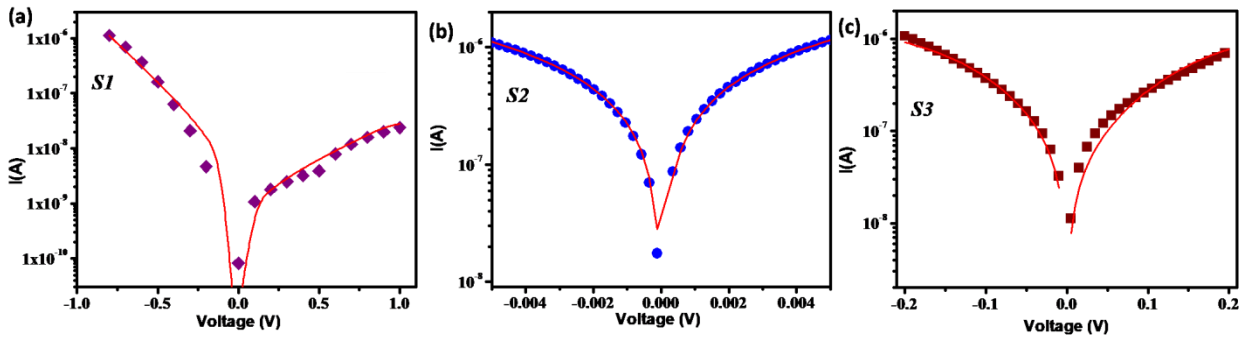| Sample	L (μm)	D (nm)	Both Electrodes	R_{NW}(kΩ)	φ_1 (eV)	φ_2 (eV)	γ (%)
S1	1.2	30	Cr/Au	850	0.384	0.212	58
S2	2	90	Cr/Au	1.1	0.175	0.145	19
S3	1.8	62	Ni	59.5	0.291	0.222	27

Figure 1. *I-V* characteristics in dark (shown as symbols) with corresponding MSM fits (shown as lines) for (a) *S1*, (b) S2 and (c) *S3*.

2. Photodetector performance

In Fig. 2(a), as an example, we show the current of device *S3* with no applied bias when illumination of different wavelengths are turned ON and OFF. The device shows appreciable photoresponse with a response time ≤300ms. (The response time is limited by stray capacitance of the long leads connecting the NW). An important characteristic of a photodetector is the Responsivity ($\mathcal{R} \equiv \frac{I_{pc}}{P}$), where I_{pc} is the photocurrent and P is the power incident on the photodetector. The Responsivity of *S3* is shown in Fig. 2(b) as a function of wavelength under self-biased condition. The illumination spot is 1mm in radius and illuminates the entire device. The illumination of the whole device cannot be avoided given its small size. The illumination of the contacts in such devices lowers the Schottky behaviour[19] which has been discussed in Chapter IV. Self-powered photoresponse was observed in all the three NW devices (data not shown to avoid duplications). The dark current and the current under illumination for all devices are given in Table III. Existence of substantial photocurrent at zero applied bias shows that the single Ge NW devices operate as self-powered photodetectors. Responsivity is given in table III at illumination wavelength of 650 nm. To the best of our knowledge it is highest reported value of $\mathcal{R}$ obtained in a self-powered photodetector. The wide spectrum in which $\mathcal{R}$ is large, makes it promising for applications, particularly where very low illumination power detection is needed.
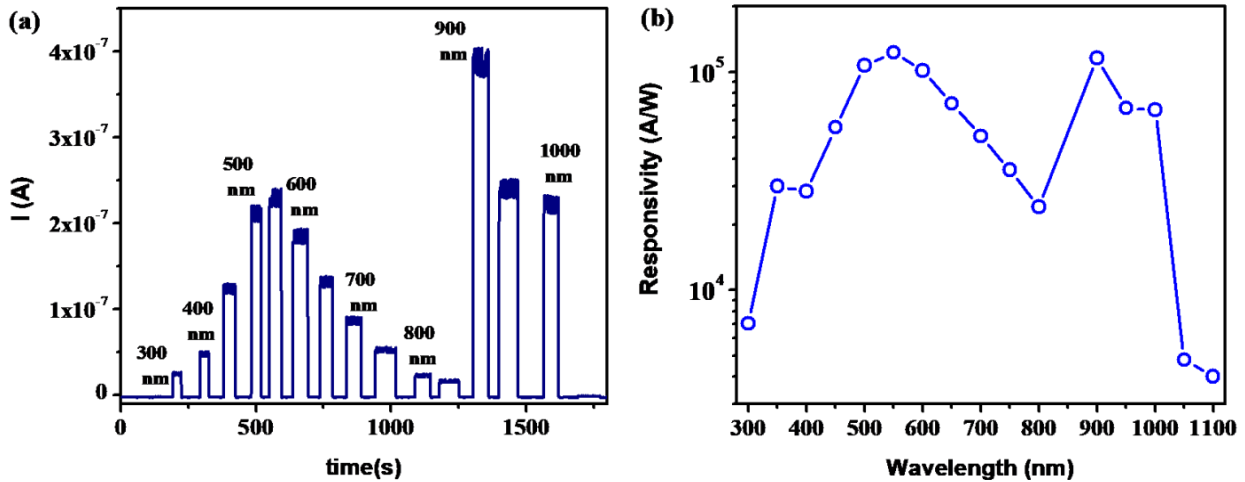

Figure 2. (a) *I-t* curves for device *S3* under illumination with monochromatic radiation from 300-1100 nm at intervals of 50 nm with power varying from 10μW-650μW, depending upon the Xenon lamp source characteristics when the lamp is switched ON and OFF. (b) Responsivity as a function of wavelength for nanowire *S3*.

110

Table 3. Photodetector parameters at zero bias.

Sample	Dark current (A)	Current under illumination (A)	$\mathcal{R}$(A/W) at λ=650nm
S1	3.1×10^{-10}	1.1×10^{-9}	2.3×10^3
S2	3.52×10^{-7}	1.20×10^{-6}	3.6×10^5
S3	2.7×10^{-9}	1.73×10^{-7}	2.1×10^5

3. Simulation of device performance using asymmetric Schottky Barrier

Self-powered photodetectors need existence of an electric field to separate the photogenerated electrons and holes which then diffuse to the respective electrodes. In a solar cell like a p-n junction cell or a heterostructure solar cell, the built-in potential exists in the depletion region at the junction/interface.[20] In self-powered NW photodetectors, in absence of any applied bias, this would need a *mechanism* that would give rise to the internal axial field. In a MSM device, it is proposed that such a field can arise from the MS contacts which show different SBH when formed on NWs, even when both contacts are made up of the same metal.

To quantify and validate our hypothesis, we performed a simulation using parameters for the device *S1*, which has the highest asymmetry in SBH (see table 2) with normalized asymmetry parameter $\gamma = 58\%$. There exists a finite potential at zero bias in the nanowire. The potential variation in the nanowire is shown as a 3-dimensional plot in Fig. 3, with color code showing the potential value. The inset shows surface potential along the longitudinal plane, with an arrow plot of the electric field E. A line plot of the potential (see Fig. 4(a)) shows that a linear potential develops along the NW length at zero applied bias and it is constant at the contact region. We have simulated the potential for other values of γ (see Fig. 4(a)), which shows enhancement of the built-in potential for larger γ. To establish generality of the results we have simulated device *S2* and *S3* and have got similar result.

The electric field calculated from the potential is constant in the NW in between the contact region. It increases linearly with increase in γ (see Fig. 4(b)). For the lowest $\gamma \sim 18\%$ in *S2*, $E \sim 2 \times 10^4$V/m which is larger than that in a heterojunction photodetector[6] with $E \sim 2.5 \times 10^2$V/m and compares well with that in microwire array detector with $E \sim 5 \times 10^4$V/m.[7] The Electric field E is in the direction from the electrode with SBH ϕ_2 to the electrode with SBH ϕ_1 (for $\phi_1 > \phi_2$) and electrons flow from the electrode with higher SBH (ϕ_1) to the electrode with lower SBH (ϕ_2).
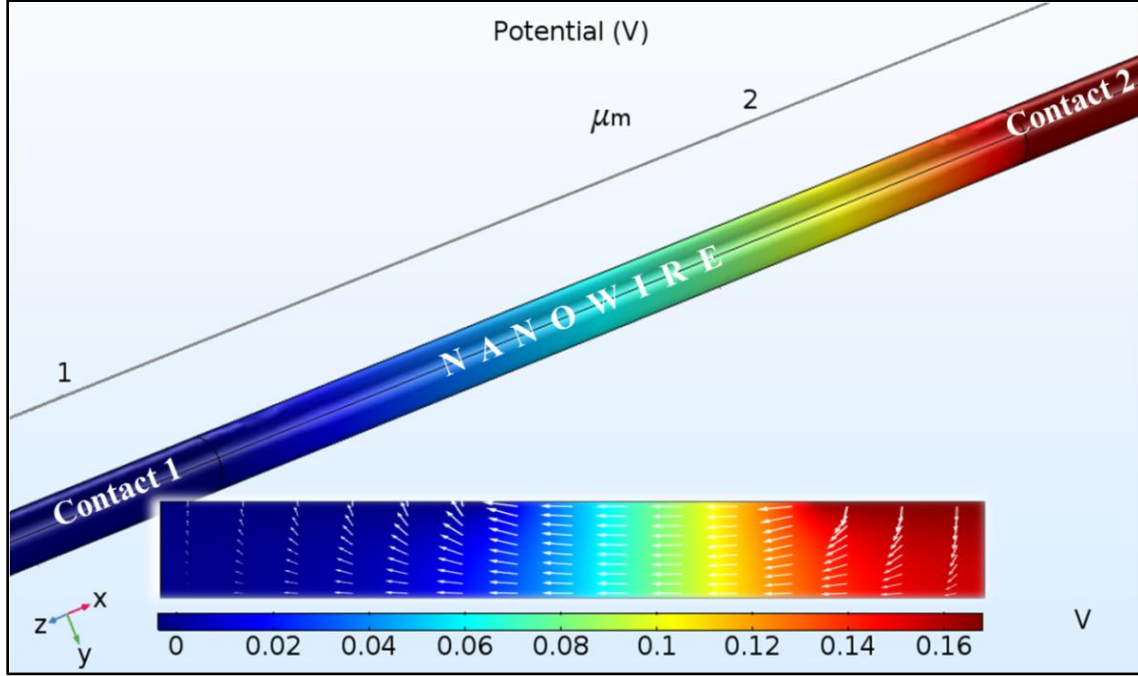
Figure 3. (a) Electric potential developed in the device *S1* at zero bias. Inset shows surface plot of the longitudinal section of the NW with color code of potential given in Volts. The surface arrow plot gives direction of the electric field developed in the nanowire (diameter exaggerated for clear image).
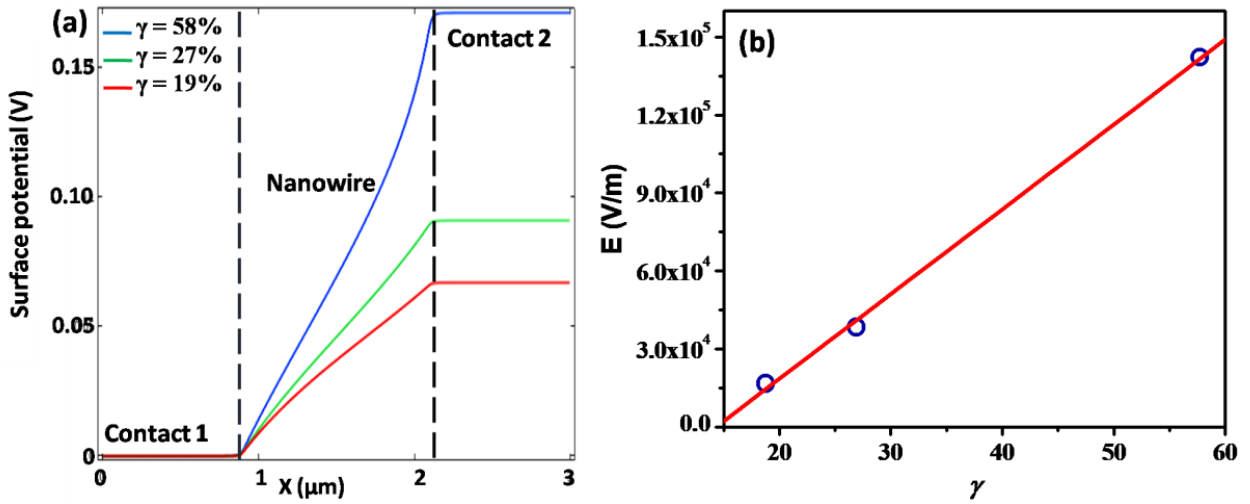

Figure 4. (a) Electric potential developed in *S1* at zero bias due to asymmetry in barrier height. The data show the potential for three asymmetry parameter values $\gamma = 19\%$, 27% and 58%. Enhancement in potential and hence field can be seen as γ is enhanced. (b) The electric field as function of asymmetry parameter with a linear fit in solid red line.

The existence of such a field however would need a device with micron size length, where the separation of the two collection electrodes/leads is of the same scale as the sum of depletion widths (W_D) at two ends. We have made an estimate of the depletion width in our device. The depletion width in a semiconductor is given by,[20] $W_D = \sqrt{2\varepsilon V_b / eN^*}$ where, N^* is the doping concentration of the NW, ε is the dielectric constant of Ge, V_b is the built-in voltage, given by $V_b = (\varphi_m - \varphi_s)/e$, and φ_m and φ_s is the work function of the metal and semiconductor respectively. In the absence of an accurate value of N^* for NWs, we have used the resistivity of the NWs (as calculated from fit parameter R_{NW}, given in table 1) to estimate the value of N^*, which is for bulk Ge.[21] While this leaves an element of uncertainty regarding the exact value of N^*, however, the uncertainty does not affect the main observation of the paper that a self-powered optical device can be made from a single Ge NW. The uncertainty in N^* may affect some of the numbers in the simulation part. For the work function of Ge, we have used $\varphi_S = 4.56\text{eV}$.[22] The depletion width W_D ranges from 100 - 300 nm for $N^* = 10^{22}\text{-}10^{23}\text{cm}^{-3}$.
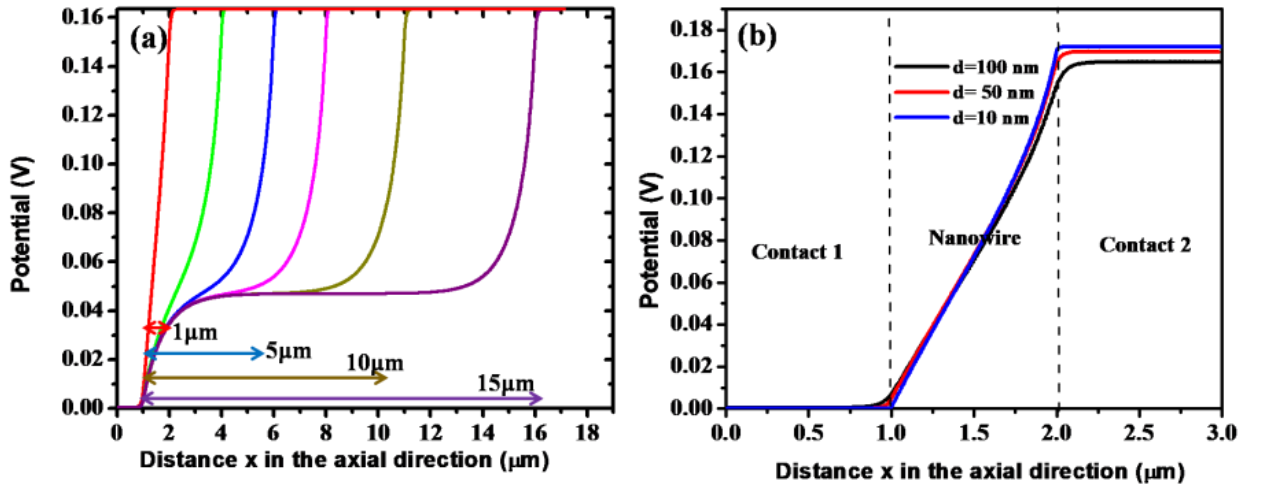

Figure 5. (a) The built-in potential as a function of length between the electrodes. The simulations have been done for length 1,3,5,7 10 and 15 μm. The arrow lines marks the length between the electrodes. (b) Potential as a function of nanowire diameter for a fixed channel length of 1μm.

The simulation data in Fig. 5(a) shows that with device length >> size of depletion region, this effect tappers off. The simulations have been done for length between 1-15 μm between electrodes and it can be clearly seen, that the potential in between electrodes gradually flattens beyond 5μm of the photodetector channel length. Hence, the built-in Electric field will cease to exist throughout the device length. Thus, when the depletion region covers almost $\frac{1}{5}$ to $\frac{1}{2}$ of the device length it is sufficient to obtain the axial field necessary for the photoresponse. Since we have investigated photodetectors with diameter variation from 30-90nm, it is pertinent to check through simulation the effect of diameter on the built-in field. Fig. 5(b)

shows that there is not much difference in E through the device length. Only, the potential at the MS interface becomes sharper as we go to lower diameter of the nanowire. The simulation provides us the necessary basis on which we show that the asymmetric barrier height is a sufficient (but may not be necessary) condition for a built-in potential in the NW at zero bias, that is essential for self-powered photodetection.

4. Origin of unequal SBH

A SBH mismatch due to different electrode material at both contacts can be caused intentionally. However, Fermi Level pinning (FLP) in bulk-Ge makes the SBH material independent and pins the SB to ~0.5eV.[23] In case of NWs, there has been experimental evidence for suppression of FLP.[18,24] It has been shown that contacts to Ge NWs are inhomogeneous (see Chapter IV) with a distribution of barrier heights.[18] The formation of a Schottky barrier depends on the initial stages of the metal layer deposition due to formation of defect state levels at the interface.[25,26] The high resolution TEM image of a Ge NW shows highly oriented d-planes with a surface oxide layer of varying from ~1-6nm (see Fig. 6). The oxide layer is marked in yellow line in the images and for both sides of the same NW shows non-uniform oxide thickness along the length. It is also corrugated and undulating. These corrugations lie within the electrode contact length ~ 1μm. The corrugations or "rumpling", leads to a shift in the oxygen atoms toward either the semiconductor or metal, which creates an additional dipole formation at the interface, that modifies the SBH.[27] There is a variation in the surface oxide thickness as well as the corrugation change on the surface of the NW along the length (see Fig. 6). The gradient in oxides thickness comes from the growth condition as the end anchored to Si substrate is the place where the growth first occurs, and gets more time to oxidize. Surface treatments like plasma etching can impart energy which causes surface modification as well as disorder in the semiconductor.[28] Such treatments are essential for NW devices fabricated by EBL, where remnant resists needs to be etched out for better lift-off. Thus the formation of the asymmetric SBH on Ge NW appears to be mainly dominated by structural inhomogenity as well as the oxide on the Ge NW surface. This adds an element of stochasticity in the barrier formation. Thus to have a "pre-designed" asymmetry and thus a predictable self-powered single NW photodetector, more research are needed in control of the NW surfaces and on the MS contact formation of NWs.
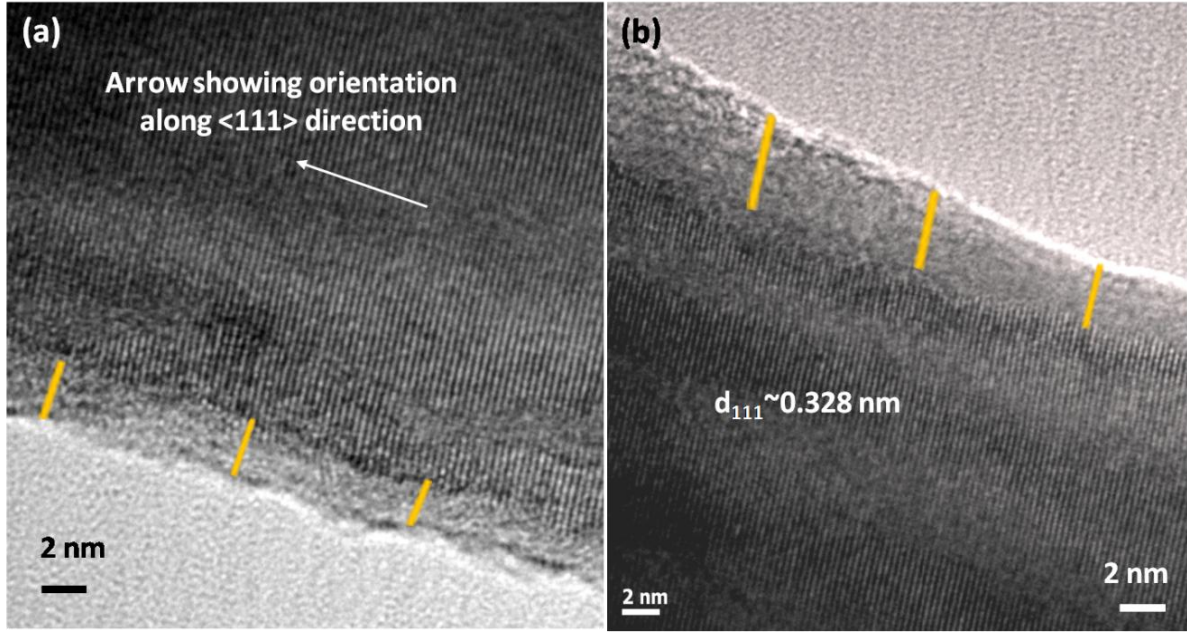
Figure 6. TEM image showing unequal oxide thickness (marked in yellow) on both sides of the same NW in (a) and (b), with crystalline Ge core and oriented along <111> direction.

4. CONCLUSIONS

We have shown that it is possible to obtain a self-powered photodetector with high responsivity using a single Ge NW fabricated in MSM device configuration. The MS junctions on the NW, due to surface conditions lead to formation of asymmetric barrier heights. This feature will be true for other semiconductor NW devices as well, which have a native/grown oxide layer. Using simulation we establish that the self-powered operation needs a finite current at zero bias and it is enabled by asymmetry in barrier heights at the two metal/NW junctions. The asymmetry in barrier leads to an axial field along the Ge NW that separates the photogenerated electron-hole pair and provides the necessary field for driving the carriers to respective electrodes. Another important factor is that the device length, which being short (~ few μm), is comparable to the sum of depletion widths at the MS interface, which helps to sustain the internal electric field throughout the device length. The observations and the phenomena reported here may enable high responsivity self-powered NW devices in other semiconductors as well.

REFERENCES FOR CHAPTER VI

[1]Xu S, Qin Y, Xu C, Wei Y, Yang R and Wang Z L 2010 *Nat. Nano*. **5** 366

[2]Han J, Fan F, Xu C, Lin S, Wei M, Duanand X, Wang Z L 2010 *Nanotechnology* **21** 405203

[3]Wu W, Bai S, Yuan M, Qin Y, Wang Z L and Jing T 2012 *ACS Nano*. **6** 6231

[4]Wang Z L 2012 *Adv. Mater.* **24** 280

[5]Fahrenbruch A L and Bube R H 1983 *Fundamentals in Solar Cells* (Academic Press, New York)

[6]Gu S, Ding K, Pan J, Shao Z, Mao J, Zhang X and Jie J 2017 *J. Mater. Chem. A.* **5** 11171

[7]Song W, Wang X, Chen H, Guo D, Qi M, Wang H, Luo X, Luo X, Li G and Li S 2017 *J. Mater. Chem. C.* **5** 11551

[8]Li D, Sun X, Song H, Li Z, Jiang H, Chen H, Miao G and Shen B 2011 *Appl. Phys. Lett.* **99** 261102

[9]Chen H Y, Liu K W, Chen X, Zhang Z , Fan M M, Jiang M M, Xie X H, Zhaoa H F and Shen D Z 2014 *J. Mater. Chem. C.* **2** 9689

[10]Das K, Mukherjee S, Manna S, Ray S K and Raychaudhuri A K 2014 *Nanoscale.* **6** 11232

[11]D Periyanagounder, P Gnanasekar, P Varadhan, J H Heb and J Kulandaivel, 2018 *J. Mater. Chem. C*, **6**, 9545

[12]Chui C O, Okyay A K, and Saraswat K C, 2003 *IEEE Photonics Tech Lett*. **15**, 1585

[13]Nusir A I and Manasreh M O, 2015 *IEEE Elect. Dev. Lett*. **36**, 1172

[14]Nusir A I, Bauman S J, Marie M S, Herzog J B, and Manasreh M O, 2017 *Appl. Phys. Lett*. **111**, 171103

[15]Zheng L, Hu K, Teng F, and Fang X, 2017 *Small* **13**, 1602488

[16]Yang Y, Guo W, Qi J, Zhao J, and Zhang Y 2010 *Appl. Phys. Lett*. **97**, 223113

[17]Norde H 1979 *J. Appl. Phys.* **50** 5052

[18]Sett S, Das K and Raychaudhuri A K 2017 *J. Appl. Phys.* **121** 124503

[19]Sett S, Ghatak A, Sharma D, Pavan Kumar G V, and Raychaudhuri A K, 2018 *J. Phys. Chem. C*, **122**, 15, 8564-8572

[20]Sze S M 1981 *Physics of Semiconductor Devices,* 2nd ed. (Wiley, London)

[21]Cutriss D B 1961 *Bell Syst. Techn. J.* **40** 509

[22]Serino C, Anderson M E, Saleh L A, Dziedzic R M, Mills H, Heidenreich L K, Spokoyny A M and Weiss P S 2017 *Appl. Mater. Interfaces.* **9** 34592

[23]Dimoulas A, Tsipas P, Sotiropoulas A and Evagelaou E K 2006 *Appl. Phys. Lett.* **89** 252110

[24]Gray M M K, Lutz T, Collins G, Biswas S, Holmes J D and Krstic V 2013 *Appl. Phys. Lett.* **103** 153101

[25]Brillson L J 1978 *Phys. Rev. Lett.* **40** 260

[26]Spicer W E, Lindau I, Skeath P, Su C Y and Chye P 1980 *Phys. Rev. Lett.* **44** 420

[27]M. Nunez and M. B. Nardelli, 2006. *Phys. Rev. B.*, **73**, 235422,

[28]Tung R T 2014 *App. Phys. Rev.* **1** 011304

CHAPTER VII

THERMAL PROPERTIES OF GERMANIUM NANOWIRES

We have measured the temperature dependent thermal conductivity $\kappa(T)$ in a single nanowire through a novel application of micro-Raman Spectroscopy. The experiment was done from 300K to above 600K. The method termed as Opto-thermal Spectroscopy utilizes the temperature dependence of Raman lines as a local probe for temperature. The method does not need any contacts to be made and provides a quick solution to existing methods of measuring single NW thermal conductivity using lithographically fabricated split platforms. We also analyzed quantitatively the temperature dependence of the thermal conductivity that shows $\kappa(T) \sim \frac{1}{T}$ which likely arises from Umklapp process. The magnitude of $\kappa(T)$ is determined by scattering of phonons from the rough surface of the NWs and $\kappa(T)$ is severely reduced from the bulk value. $\kappa(T)$ shows an inverse dependence on diameter as well as temperature. We also suggest a way to estimate approximately the thermal conductivity of Ge and Si NWs using the above observations, so that an actual experiment need not be done. The quantitative estimation of errors arising from the opto-thermal measurement and methods to mitigate them have been discussed.

The temperature dependence of the Raman line that was used as a thermometer was also analyzed using physics of anharmonic lattice and this is provided also some of the fundamental thermodynamic parameters of Ge NW.

A. INTRODUCTION

In the last decade there has been intense interest on heat transport in nanostructures, in particular nanowires (NWs), for their applications in nano-electronics and in such specific areas like thermoelectrics.[1,2] The experimental studies as well as theoretical investigations show that there can be large reduction of thermal conductivity (κ) from that of bulk in NWs when the size is reduced.[3] The reduction in thermal conductivity below a transverse length scale (like diameter in a NW) of 100nm or below can arise from strong diffuse surface scattering of phonons although this may not be the only cause. Effects of change in phonon dispersion relation and group velocity due to lateral confinement has also been proposed as a cause of reduction in thermal conductivity.[1,3]

A proper evaluation of thermal conductivity of nanostructures like NWs is important from the view of two opposing requirements. In nano-electronics and opto-electronics using NWs, low thermal conductivity is a matter of concern as this may lead to thermal hot spots due to high current density, whereas for applications in thermo-electrics one would need low thermal conductivity.

Thermal conduction in Si NWs has been investigated extensively using both experimental[4,5] as well as theoretical tools.[6] The main observation is that the thermal conductivity in Si NWs is low and can be even an order less than the bulk value.[6] The low thermal conductivity is believed to arise primarily from scattering of phonons at the boundary, which being diffusive in nature, reduces phonon lifetime.[7]

1. Review of measurement of thermal conductivity: experimental methods

Determination of thermal conductivity of bulk materials is a well-developed area in experimental physics, where, usually steady state methods are employed for determining the temperature gradient and heat flux across the bulk sample.[8,9] It requires accurate measurement of temperature at the hot end and at the heat sink and, determination of the amount of heat flowing through the sample. It is crucial to find the heat loss due to convection, radiation and thermal boundary resistance (TBR) between the sample and heat sink, due to which errors arise in finding the heat flux due to conduction by sample alone. In a transient state, pulsed power technique is used for heating the sample and a time dependent temperature difference is created.[10] Unfortunately, these techniques require precise and very careful measurements and are limited to particular sample geometry. Errors arise due to placement of thermometers and also for their size ($> 25\mu m$) while measuring small samples or thin films. In 1990, Cahill[11] developed an a.c. technique for measurement of thermal conductivity, known as the 3ω method. It uses a pre-fabricated metal network on the sample to act as a heater and also as a temperature sensor. The a.c. current at frequency ω heats up the metal line at a frequency 2ω, while the voltage across the metal line oscillates at 3ω. This method is highly accurate and is being used extensively.

The growth in research of experimental determination of thermal conductivity in NWs faces a bottle-neck in measurements particularly above room temperatures. Determination of thermal conductivity of NWs, in particular on single NW, is non-trivial and often complex as these need use of micro fabrication techniques. A micro-fabricated structure[12] is necessary to build suspended SiN_x membrane with SiN_x beams, and platinum lines acting as heater as well as electrical contacts to the nanowire/nano-sheet, which are placed on the suspended structure by a nano-manipulator. This technique relies heavily on the accuracy of the nanofabrication facility and needs expertise in handling. This method has been used widely and has undergone certain developments to determine the thermal conductivity of Si NWs,[4,5] Graphene,[13] CNT[14] and other nanomaterials. Even though these methods are accurate, they need elaborate

micro/nano fabrication. With a custom-designed thermally optimized sample stage, embedded radiation shield and better thermal anchor, it has been possible to measure thermal conductivity upto ~700 K.[15,16] A rapid and simpler non-contact method which can measure thermal conductivity at temperatures >> room temperature will thus be a favored option.

Flash laser Raman Spectroscopy was developed in 2015[17] where, a pulsed laser was used as a local heating source and an excitation laser produces a Raman signal. This method is only applicable when the characteristic Raman peak is temperature dependent. The local temperature is calculated from the relation between temperature and the shift of Raman characteristic peak. The unsteady thermal transport equation can be solved, but has two unknown parameters, laser absorption and thermal conductivity. For this purpose, a continuous laser is employed from which a steady state solution provides the laser absorption.[18] The temperature rise ratio as a function of laser spot radius and pulse duration extracts the thermal diffusivity from which the laser absorption can be calculated.[17]

Recently, a rapid, non-contact method known as Opto-thermal Raman Spectroscopy was used to measure the thermal conductivity of cantilevered Si NWs (clamped at one end) at 300K.[19] The results lie within 5% - 10% of thermal conductivity of Si NW measured using conventional electrical methods made on micro-fabricated platforms. The reported work, however, has not investigated the application of the method for temperatures above or below the room temperature. This method though somewhat "accuracy challenged",[20] is rapid, non-destructive and does not require elaborate micro/nanofabrication. In this method, the Raman peak shift is used as a thermometer and the laser employed to collect the Raman Spectrum is used as a heat source, whose power can be varied. As investigated in this work, we show that this method can also be used for $T > 300K$ which is a relevant temperature range for diverse applications.

2. Motivation

The investigations on thermal transport in NWs have been mostly done on Si NWs.[4,5,13] In contrast thermal transport in single Ge NW with good structural quality has not been investigated extensively. There has been a report of an $Si_{0.14}Ge_{0.86}$ alloy NW of diameter 205 nm that shows a considerably low thermal conductivity of ~1.8W/m.K at 300K.[21] There is only one report on thermal conductivity of a single Ge NW from 100K to 390K through a micro-chip measurement setup. It quotes a value of 2.26 W/m.K for a 20nm NW at 300K[22] which is ~40% lower than the predicted value of the same from theoretical consideration. This report of low thermal conductivity in Ge NW thus serves as a motivation to research it so that its applicability in thermo-electrics can be tested. Evaluation of thermal conductivity in Ge NWs also become important in view of local hot spots that can originate from low thermal

conductivity when such NWs are used in opto-electronic detectors where large current density (10^8-10^9 A/m^2)[23] may result from ultra-high responsivity observed in them giving rise to a local Joule heating.

Ge NW can be explored as a thermoelectric material for clean energy harvesting. Essentially, an investigation of the thermal transport properties, thermal expansion and electron-phonon interaction has great impact on the thermoelectric performance, which are lacking in case of Ge NWs. In that light, the electron-phonon interactions are of immense importance as a stepping stone to understanding the lattice dynamics. The important thermodynamic parameters and physical properties can be studied experimentally due to anharmonicity in crystals. The thermal expansion in a solid gives insight into the anharmonicity in the vibrational potential energy.[24] The mode Gruniesen parameter relates the vibrational frequency modes to specific heat and thermal expansion coefficient.[25] A non-invasive way to probe nanomaterials for extracting out lattice related properties can be performed through Raman Spectroscopy.[24,26]

In this work, thermal conductivity of a crystalline Ge NW was measured as a function of temperature from 300K to 600K for NWs using the opto-thermal spectroscopy. Results show the efficacy of size reduction (i.e. diameter reduction) in bringing about the reduction in thermal conductivity and also evaluate the temperature dependence of the thermal conductivity. We evaluated the results in frame work of physical theories of heat conduction in NWs. We have also estimated the uncertainty associated with the opto-thermal method.

3. Review of Raman Spectroscopy study on Ge NWs

Raman Spectroscopy study on Ge NWs is very limited. Raman spectra of Ge NWs show phonon confinement in NWs with average diameter < 20 nm.[27] A contribution to thermo-physical properties of Ge NWs has been performed. Tip-enhanced Raman scattering has been used for nanometer scale mapping of a single Ge NW.[28] Albeit an important material, Ge NWs suffers from a lacuna in the field of thermal transport. We study temperature dependence of Raman active Ge modes from which we determine the anharmonicity coefficients, optical phonon dynamics, vibrational modes and lattice expansion in ensemble of pure (with native oxide layer) as well as core-shell Ge-GeO$_2$ NWs of diameters varying between 30-120nm. Since this work does not directly involve the experimental determination of thermal conductivity, we have kept this segment in **Appendix E**.

B. EXPERIMENTAL SECTION

1. Establishing the 1D heat equation

The heat conduction is governed by the Fourier Equation given by,

$$\vec{\mathbb{Q}} = -\kappa\,(T)\vec{\nabla}\,T \tag{1}$$

where it $\vec{\mathbb{Q}}$ is the vector local heat flux density (W.m^{-2}) and $\vec{\nabla}\,T$ is the temperature gradient (K.m^{-1}) and it is assumed that the thermal conductivity $\kappa(T)$ does not have a spatial dependence. Thus $\kappa(T)$ has a unit Wm^{-1}K^{-1}. In one dimension heat flow, which is appropriate for the heat conduction in NW, the vector equation reduces to,

$$\mathbb{Q} = -\kappa\,(T)\left(\frac{dT}{dz}\right). \tag{2}$$

A more workable relation is what we use as Ohm's law in an electrical circuit where the temperature drop ΔT is like a voltage drop and the heat flux Q (not heat flux density $\mathbb{Q}$) is like a current so that we can introduce a thermal resistance R_T as,

$$\Delta\mathrm{T} = \ R_T Q = QR_{th} + \frac{LQ}{A\kappa} \tag{3}$$

where, $R_T \equiv R_{th} + \frac{1}{\kappa}\left(\frac{L}{A}\right)$ and the temperature drop $\Delta T (= T - T_o)$ is established over the length L of the nanowire with cross sectional area A, T_o is the cold end temperature and the thermal contact resistance is given as R_{th}.

2. Concept of Opto-thermal Method

In Opto-thermal Raman Spectroscopy, a focused laser is used to heat up at point in the NW and also collect the Raman Spectrum. The Raman peak position is used as a thermometer for our measurement. The power falling on the NW is calculated from the laser power that is measured by a flux meter. The schematic of the concept is shown in Fig. 1.

A single suspended NW is identified through a 100X microscopic objective and an Argon ion laser of 488nm is focused on the NW through the lens with a 0.9 numerical aperture. The laser spot has a Gaussian distribution with FWHM ~700 nm. From the position of the Raman peak, the temperature at the hot end (T_{hot}) at which the laser is focused can be determined through the calibrated Raman thermometer.

The laser beam falling on the NW has the form of a Gaussian given by, $J = J_0 \dfrac{e^{\frac{(x-x_o)^2}{2\sigma^2}}}{\sqrt{2\pi}\sigma}$, where x direction is along the length of the NW, x_o is the point at which the laser beam falls (center of beam), σ is the half width at half maxima. The power P (total heat falling on the NW) is calculated from the intensity of the laser beam I, given by, $I = J/\pi\sigma^2$, where J measured through the flux meter. Thus, the power on the NW can be approximated as, $P = I.S = J.\dfrac{\pi D}{2}.2\sigma$ where S is the area of the NW exposed to illumination. Finally, the heat flux (Q in equation 3) is, $Q = P\eta$, where η is the absorption efficiency, which is ~0.8 at 488nm for Ge NWs in the diameter range of (50-150nm).[29]
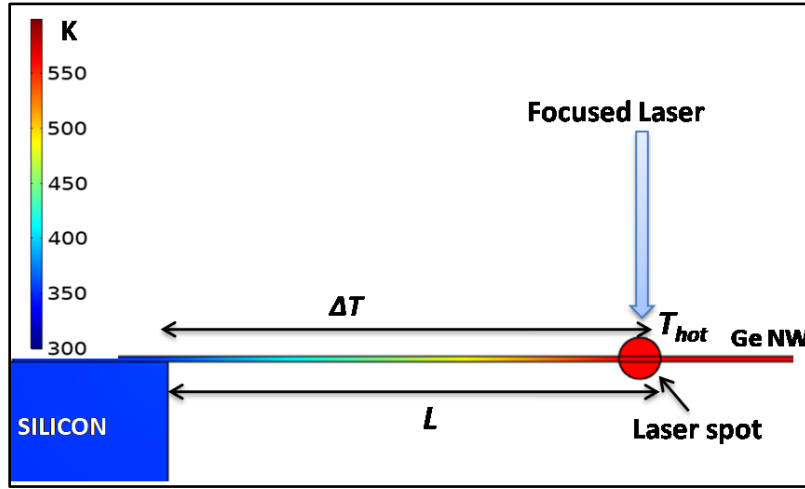

Figure 1. (a) Raman Spectroscopy set-up showing schematic of the Opto-thermal process. It shows a laser falling on a suspended NW on Si substrate, with temperature shown as color legend.

A realization of the utilization of equation 3 for measurement of the thermal conductivity can be done by measuring the Raman spectrum at a fixed power Q as a function of length of the distance of the point of illumination from the base NW (L). The slope of the $\Delta T'$ v/s L is then used to evaluate thermal conductivity. $\kappa(T)$ in this case is evaluated at the average temperature T' (see Eqn.3). To avoid errors, $\Delta T'$ was kept small. This method does not need determination of R_{th}.

In another realization of measurement using eqn. (3) we varied the heat flux Q at a fixed length L. This gives rise to (see equation 3). $\kappa(T)$ was determined from slope of the observed ΔT v/s Q curve.

3. Identifying and estimating the errors

The presence of the thermal contact resistance R_{th} creates a jump in temperature at the cold clamped end. The actual temperature T^* at the cold end of the NW, is given by,

$$T^* - T_0 = R_{th}Q \tag{4}$$

Determination of R_{th} properly mitigates a major source of error. We have determined R_{th} from experimental data using equation 3 and also using a finite element analysis. The temperature gradient in the NW of length L after correcting for the temperature rise at the contact is given by $\Delta T' = T - T^*$. The mean temperature at which thermal conductivity is measured is given by

$$T' = T^* + (\Delta T'/2) \tag{5}$$

We use simulation (given in **Appendix D)** to calculate the corrected $\Delta T'$ using the value of T^*.

One of the sources of error in applying eqn. (3) arises from finite size of the of heat source ((i.e., the finite size of the laser spot). It is not a point source but can be approximated as one when the width of the illumination region is $<< L$. Using this information and the fact that $> 95\%$ of the power is contained within an area of diameter 2σ, the effective size of the illumination region is ~ 0.7 μm. For measurement of thermal conductivity we used $L > 15$μm, which makes the error arising from this source $\leq 10\%$. Validation of point source approximation is shown through finite element method simulations given in **Appendix D**.

An important source of error in high temperature thermal conductivity experiments is heat loss through radiation as discussed in Section A, 2. Since the experiment was carried out under ambient atmospheric conditions, heat loss due to radiation needs to be accounted for. We have used finite element method to determine the heat loss through radiation processes (details given in **Appendix D**). The radiation heat loss in a NW at temperatures ~ 600 K is ~ 3 nW which is $\leq 2\%$ of the total power carrier by the NW.

4. Establishing the temperature sensor

In this method the temperature is measured from the shift of the Raman line which acts as a thermometer. To calibrate the Raman line shift with temperature, Ge NWs are dispersed onto a Cu grid thermally anchored to a substrate. The dispersion to a substrate is important as it defines the temperature of the NW on which Raman shift will be measured. The Raman spectrum was recorded in a Lab RAM HR spectrometer with 1800 gr/mm grating and Peltier cooled CCD detector. The Raman data has been collected by focusing a 488nm Argon ion laser onto a single Ge NW through a 50X objective lens (FWHM of laser is ~ 1.4μm). Low laser power ≤ 2 μW is used such that it gives a good signal to noise ratio yet avoids any local heating that may give rise to peak broadening and/or peak shift. We have recorded the Stokes line in this experiment The Raman spectra peak is fit using a Lorentzian function to extract the peak position (see Fig. 2). The peak position at room temperature ~ 300.5 cm^{-1} is from the

degenerate LO/TO mode at $q = 0$.[30] The diameter of the NWs are ≥ 50 nm and there are no effects of phonon confinement as observed from the spectra. Phonon confinement is observed in thinner NWs with diameter < 20 nm,[27] where an asymmetry in the peak shape is observed. We have also measured the Raman spectrum of a single suspended Ge NW at room temperature (see Fig. 2). It can be seen that the results are identical and the temperature equilibrated thermo-power does not depend on whether the NW is on a substrate or it is suspended.
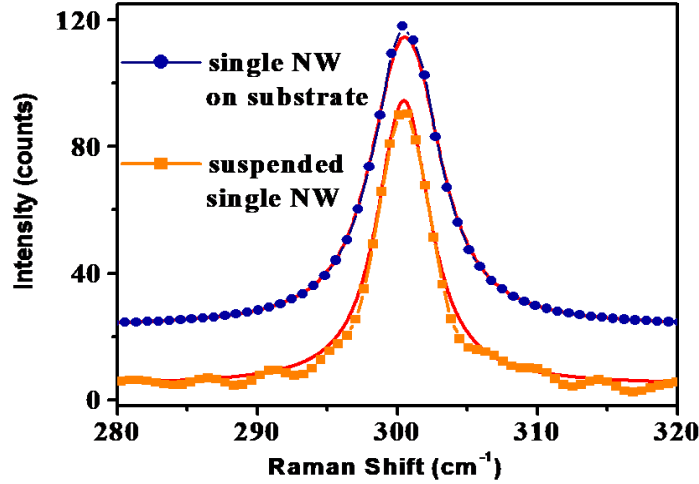

Figure 2. Raman Spectrum of a single Ge NW suspended and supported on Si substrate with a peak at ~300.5 cm^{-1} fit to a Lorentzian function (red solid line).
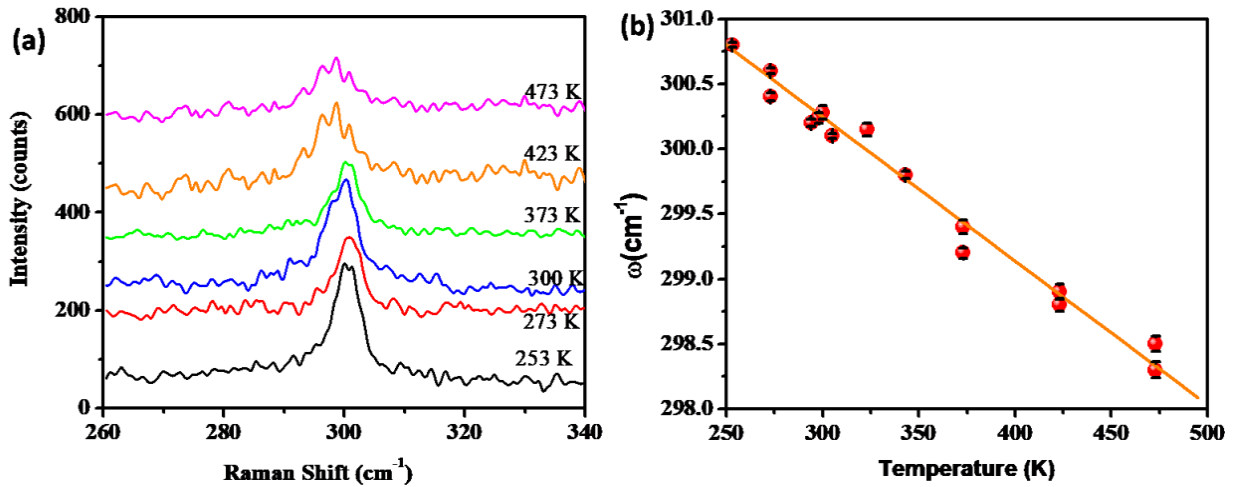

Figure 3. (a) Raman Spectra of some representative data is shown as a function of temperature in a single Ge NW. (b) Peak position versus temperature in a single Ge NW, with red line showing the linear fit to data.

The calibration of the Raman peak shift with temperature was performed on a single Ge NW dispersed onto a Cu grid through a temperature controlled stage. The temperature variation of the substrate from 250 K to 500 K was carried out in a vacuum chamber connected to a PID controlled heating stage, with N_2 vapor cooling facility. An example of the Raman line at different temperatures is given in Fig. 3(a). We get the peak position as a function of temperature from this measurement. This calibration acts as a temperature sensor for the NW as shown in Fig 3(b). We can observe the peak shift to a lower wavenumber as temperature of the NW increases. The peak position (ω) as a function of temperature (T) is shown in Fig. 3(b) for a single Ge NW. The slope of the straight line, $\Delta\omega/\Delta T = 0.0111\pm0.0004$ cm^{-1}/K serves as a calibrated thermometer. It is used to determine the temperature at any point in the NW through the peak position in the Raman Spectrum.

5. Suspended sample preparation

Ge NWs were grown by physical vapor transport by Vapor-Liquid-Solid mechanism and Au nanoparticle (NP) as seed catalyst on a Si substrate as described in Chapter II. NWs that grow near the edge of the substrate grow outward and are clamped at one end and are suspended in the other without any contact with the substrate as shown in Fig. 4. These NWs have been used for measurements of thermal conductivity because, absence of any support at the free end avoids spurious heat transport path which contributes to a source of error in such thermal measurement.
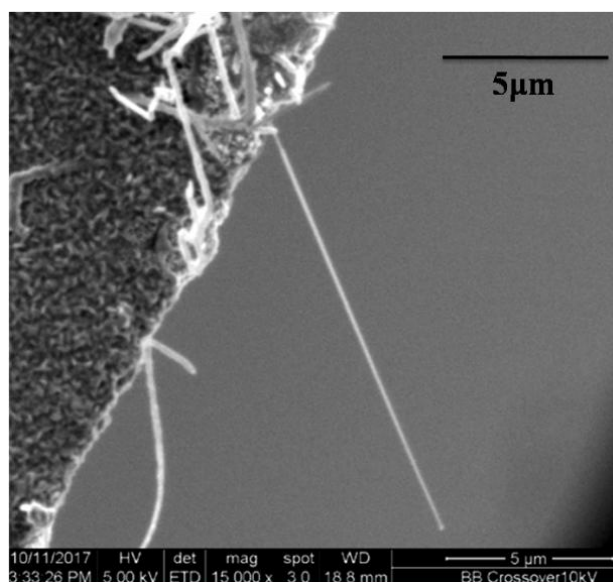

Figure 4. (a) SEM image of an edge of a Si substrate on which we have grown Ge NWs. The NW is clamped at one end and is suspended on the other, creating a cantilever.

C. RESULTS

1. Estimation of thermal conductivity through length variation method

An optical microscope image of the suspended NW with a focused laser for varying positions is shown in Figure 5. An example of a Raman spectrum (with local heating) in NW B is shown in Fig 6 (a). In the length variation method, since the active L varies from 2 – 20 μm, we use very low power ($J < 2$ μW) to avoid heating up regions lying outside the 2σ region. This ensures that we maintain the condition that $L \gg 2\sigma$ and minimize errors arising from L calculation. The active length L which is the distance of the illumination spot from the point of clamp on the substrate was obtained from x-y position markers accompanying the movable sample stage. The uncertainty in length comes from drift due to the sample stage vibrations. The temperature gradient ΔT is obtained from our calibrated Raman thermometer shown in Fig. 4(b)) and the plot of ΔT versus L (Fig. 6b) is obtained. Using the slope of this line, we can calculate the thermal conductivity of the NW using equation 1.The determination of the R_{th} is not needed in the length variation method and we calculate κ from the slope, although R_{th} can be evaluated from the method (see Table 1). The estimated R_{th} is similar for all the contacts ~ 0.4-0.5 K/nW.
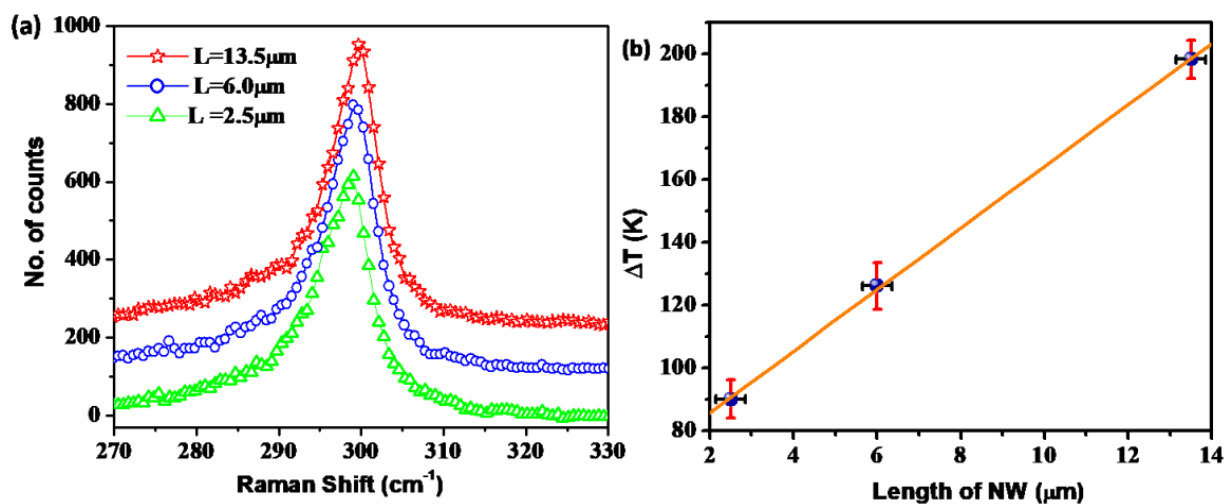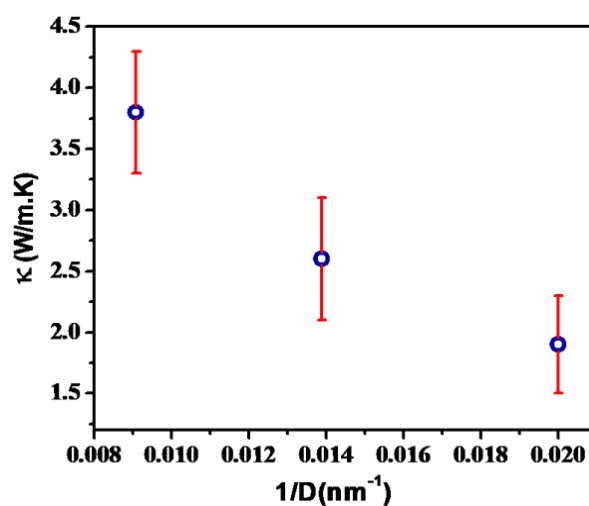

Figure 5. (b) A 488 nm Ar ion laser focused on a single cantilevered Ge NW at different positions.

Table 1 gives the essential fit parameters to Equation 3. The temperature T' at which the thermal conductivity is measured has been calculated using Equation 5. Within the total ΔT of ~100K, κ varies by $\leq 10\%$. Thus we assume that κ is independent of temperature within this temperature range. From the data in Table 1 we can get a quantitative estimate of variation of κ with diameter. (Note: Approximate relative variation in κ within the range 405K - 440K is < 5 % change. This is less than the uncertainty in the κ data.) The data is plotted in Figure 7 as κ versus $1/D$ and nearly linear dependence suggests that the thermal conductivity has an inverse dependence on the NW diameter.

Table 1. Ge NW with fit parameters to equation 3 for the length variation method.

NW	D (nm)	L (μm)	J (μW)	P (nW)	Slope (K/μm)	R_{th} (K/nW)	T' (K)	κ (W/m.K)
A	110	2.9-20	1.85	185±5	4.1±0.1	0.42±0.01	426	3.8±0.5
B	72	2.5-13.5	1.93	126±5	9.8±0.1	0.52±0.02	440	2.6±0.5
C	50	2.1-12	1.04	48±5	11.8±0.1	0.46±0.05	405	1.9±0.4

Figure 6. (a) Magnified Raman spectrum as a function of length (L) for a fixed power in NW B. (b) ΔT as a function of length for NW with linear fit to data in solid line.

Figure 7. Thermal conductivity of a single Ge NW as a function of inverse of diameter.

2. Estimation of thermal conductivity through power variation method

The Raman spectra for a fixed length L for varying powers were recorded for two NWs, A and B. The peak position as a function of laser power is plotted in Fig. 8a. As we increase power, the local temperature at position L increases leading to a peak shift $\Delta\omega$. From the $\Delta\omega$ we calculate ΔT as a function of laser power as shown in Fig. 8b. We use simulation results (given in Appendix E) as well as the experimental result (see Table 1) to calculate the corrected $\Delta T'$ using the value of T^*. We use equation 3 to determine the thermal conductivities of the NWs as function of temperature T' shown in Figure 9. The data shows an inverse dependence of κ on T.
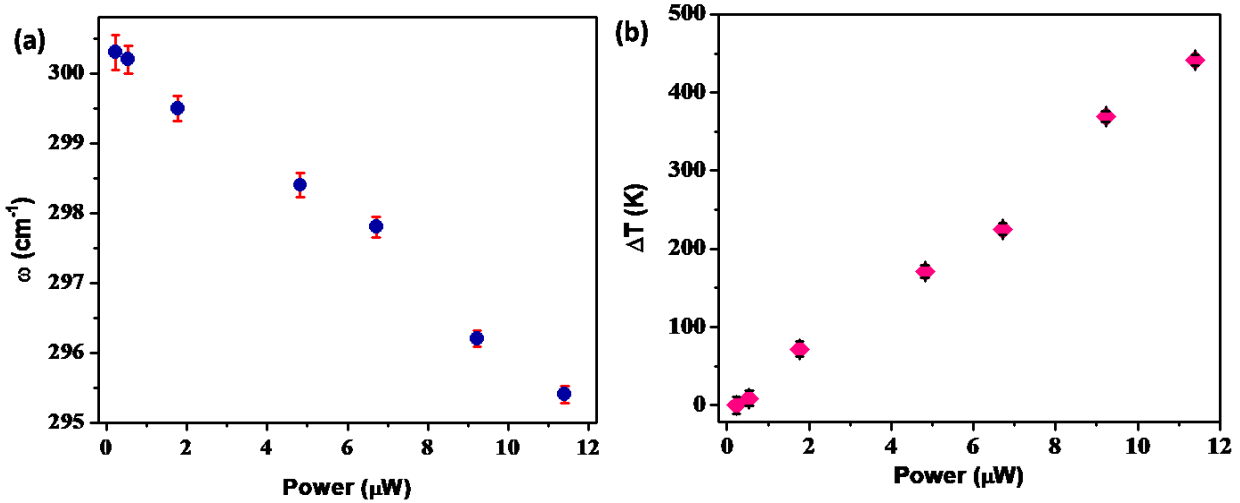

Figure 8. (a) Peak position as a function of laser power for a fixed length in NW A. (b) ΔT as a function of power for NW A.

The magnitude of κ of the Ge NWs ~ 4W/m.K (diameter 110nm) is less than that of the single crystalline Ge[14] by about a factor of 15 at room temperature and for the 50 nm diameter NW is lower by a factor of 30. This is an important quantitative evaluation. In addition, as pointed out before, we also make two important observations that κ has an inverse dependence on both T and D. In the next section we discuss the physical significance of these results.

D. DISCUSSIONS

1. Temperature dependence of thermal conductivity

In the temperature range $T > \theta_D$ (Debye temperature), $\kappa(T)$ of an insulating crystalline solid generally shows $1/T$ dependence which arises from inelastic Umklapp process.[31] The inverse T dependence of κ observed in the NWs (see Figure 9) thus can be postulated to arise from Umklapp process. To extract the

temperature dependence of $\kappa(T)$, we have fitted the thermal conductivity of the NWs to an equation of the form,

$$\kappa^{-1}(T) = \kappa_o^{-1} + \kappa_U^{-1}(T), \tag{6}$$

where $\kappa_U(T) = b/T$ is the temperature dependent term due to Umklapp scattering. The temperature independent part κ_o is a constant arising from elastic scattering of phonons such as boundary scattering. The transformed equation 6 in terms of $\kappa(T)$ is,

$$\kappa(T) = \frac{\kappa_o b /T}{\kappa_o + b/T} \tag{7}$$

The fit parameters of to Eqn. 7 are given in Table 2 and the fit data is shown in solid lines in Figure 9. In the following section we evaluate the postulates quantitatively to establish its correctness.
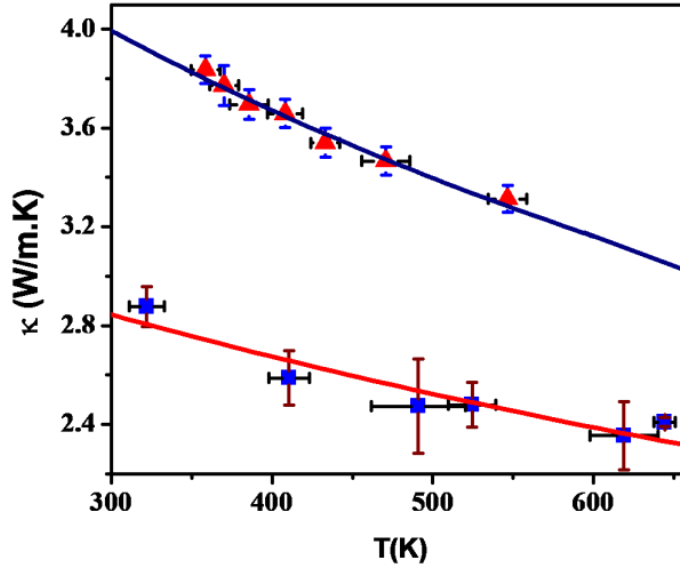

Figure 9. Thermal conductivity as a function of temperature in the NWs A and B. Solid lines are fit to equation 7.

If the inverse temperature dependence indeed arises from the Umklapp process, (see eqns. 6 and 7) then, κ_U for all temperatures above the Debye temperature can be expressed as,[31]

$$\kappa_U = \frac{\rho a \, v_c^3}{\gamma^2 T}, (T > \theta_D) \tag{8}$$

where ρ is the density, a is the lattice constant, γ is the Gruniesen parameter and v_c is the cumulative sound velocity in the material. The observed values of b can be used for finding v_c for the NWs. We use the standard macroscopic values of Ge i.e., $\rho = 5.32$ g/cm^3 and $\gamma = 1.4$. The lattice constant of Ge ($a =$

5.62 Å) can be evaluated from the *d*-plane spacing (from TEM study). We find that for the Ge NW with diameter of 110 nm, $v_c \sim$ 1430 m/s and for the Ge NW with diameter of 72 nm, $v_c \sim$ 1420 m/s, while in bulk Ge, $v_c \sim$ 2575 m/s. Considering the fact that there is no adjustable parameter in Eqn. 8 we think it is a good agreement, since the sound velocity is modified (typically softens) for a nano-system. Based on the above discussion and the quantitative reasonable value obtained from Umklapp theory it can be established that the inverse temperature dependence of the thermal conductivity ($\kappa \sim \frac{1}{T}$) indeed arises from the Umklapp process.

Table 2. Fit parameter to equation 5 shown in the κ versus T plot.

NW	Diameter (nm)	κ_o (W/m.K)	b (W/m)	v_c (m/s)
A	110	5.4±0.2	4553±304	1430±32
B	72	3.5±0.2	4455±775	1418±80

2. Boundary scattering and thermal conductivity

The temperature dependent part as discussed in the sub-section before arises from the Umklapp process that is comparable to what is observed in crystalline bulk albeit with reduced sound velocity. However the large part of thermal conductivity reduction in NWs appears to arise from scattering (diffused) at the NW boundary and is an elastic process. Previous investigations on ultrathin Si films/Si NWs and associated Monte Carlo[32]/MD simulations[33] have shown that the major cause for reduction in thermal conductivity in such size reduced systems can indeed be diffuse scattering from the boundary.

To check the contribution of the boundary scattering quantitatively, we have calculated the thermal conductivity of Ge NWs using the modified Callaway formalism for boundary scattering only. The thermal conductivity is given by,[5,34]

$$\kappa(T) = \sum_j \frac{k_B}{8\pi^3 v_j} \left(\frac{k_B T}{\hbar}\right)^3 (I_j) \tag{9}$$

where the summation index *j* is over all modes, v_j is the group velocity of the *j*[th] mode and other symbols have their usual meaning. The total thermal conductivity due to a longitudinal (*j=L*) mode and two transverse modes (*j=T*) gives,

$$\kappa = \kappa_L + 2\kappa_T. \tag{10}$$

The integral are defined as,

$$I_j = \int_0^{\theta_{D,j}/T} \int_0^{2\pi} \int_0^{\pi} \tau_{B,j} \frac{x^4 e^x}{(e^x-1)^2} Cos^2\theta Sin\theta d\theta dx \tag{11}$$

where $\theta_{D,j}$ is the Debye temperature for a particular mode *j*. The boundary scattering time (τ_B) term has been defined as,[33]

$$\tau_{B,j}^{-1} = \frac{v_j}{D}\left(\frac{1}{F}\right), \tag{12}$$

where *D* is the diameter and *F* is the Rugosity Factor[33] which is the ratio of diffuse to specular reflection. In this approximation for completely diffusive scattering (*F*=0) and $\tau_B^{-1} \rightarrow \infty$. Apart from *F* which is an adjustable parameter, θ_D has been taken from bulk value and v_j is the scaled sound velocity (according to the experimentally obtained ratio of v_c to the bulk v_c) which are given in Table 3.

Table 3. List of constants taken from Ref [6, 35] used for the thermal conductivity calculations

Material	Symbol	Value for Longitudinal mode	Value for Acoustic mode
Ge	θ_D	221 K	58 K
	Scaled v	3008 m/s	2026 m/s
Si	θ_D	586 K	240 K
	Scaled v	4637 m/s	3212 m/s

Table 4. Comparison of thermal conductivity from boundary scattering and experimental fit.

Diameter (*D*) (nm)	κ (W/m.K) at 300K from calculations using eqn. 9	κ_o (W/m.K) from fit to experimental data using eqn. 7
110	5.35 for *F* = 0.22	5.4±0.2
72	3.49 for *F* = 0.21	3.5±0.2

From Table 4 it can be seen that there is an excellent agreement with the observed value (within the experimental uncertainty) for *F*~ 0.2. We do not have an independent estimate of *F* for Ge NWs, but from previous molecular dynamics simulation of κ done on Si NWs with rectangular cross-section with area of cross-section varying from 2.58 nm² to 28.6 nm² and its comparison with calculations based on Boltzmann Transport Eqn. with boundary scattering, it was found that the two agree when the specularity factor *F*=0.45.[33] This difference can arise because Ge NW used by us has a rather larger area of cross-

section. This increases the amount of specular reflections from the boundary as compared to the diffuse scattering and reduces *F*. Also, the materials are different and the surface conditions are different.

3. Predictability of thermal conductivity for NWs

Predicting thermal conductivities of NWs without measurements will be a useful proposition even if it is done with some degree of known uncertainties because its measurement is quite complex and it is not possible to carry it out whenever some estimate of κ is needed. The results presented and the subsequent analysis allows us to predict thermal conductivity of semiconductor NWs with good crystallinity albeit with some degree of uncertainties. Given the fact that the thermal conductivity in these NWs is dominated by phonon conductivities, (due to its low electrical conductivity) boundary scattering and Umklapp scattering can be taken as the main source of phonon scattering for $T > \theta_D$ which is a valid approximation for most NWs at $T \sim 300$ K. Presence of electrons (in case of doped NWs) will provide a source of extra phonon scattering due to presence of dopants and also due to phonon-electron scattering which will likely decrease its thermal conductivity from the intrinsic value. Presence of lattice defects in case of these NWs has less structural quality will have similar effects.
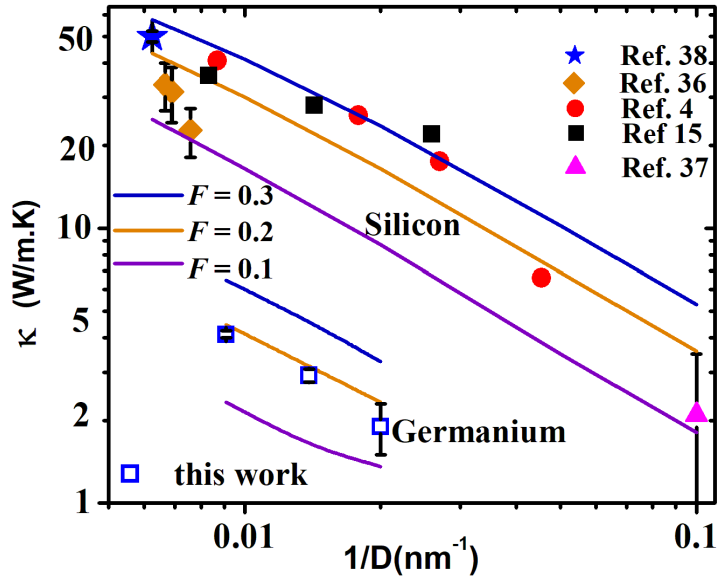

Figure. 10. Predictability of thermal conductivity of NWs at 300K with experimental data points of Si NWs from Ref [4, 15, 36-38].

The boundary scattering contribution can be estimated from a specularity factor of $F \approx 0.2$ which is a reasonable estimate for NWs. We do have a caveat that a much smaller value of F as may arise in NWs that have very rough surfaces (like those made by plasma or chemical etching). We find that the

temperature dependent part is weak and can be obtained from eqn. 8 of Umklapp scattering contribution with uncertainty though not very high from reduction of sound velocity from the bulk value in the NW.

We may thus suggest that eqn. 7 can be used to get a prediction of thermal conductivity of individual intrinsic (or lightly doped) semiconductor NWs with a given diameter where the term κ_0 can be estimated from boundary scattering (eqn. 9) and the term b/T estimated from the Umklapp process (eqn. 8). We have used these to estimate the value of $\kappa(T = 300\,K)$ using $0.1 \leq F \leq 0.3$ in Si and Ge NWs and the results are shown in Fig. 10. Alongside we have also shown experimental data in Si NWs[4,15, 37-39] and Ge NWs from our work. The estimated uncertainty is $\sim \pm 20\%$. This predictability when validated on different NWs may provide a tool to estimate this quantity in narrow semiconductor NWs without measurements.

E. CONCLUSIONS

In summary, we have measured thermal conductivity in single cantilevered Ge NWs through Opto-thermal Raman Spectroscopy utilizing the Raman line shift with temperature as calibrated temperature sensor. The thermal conductivity of the NWs is almost an order less than Si NWs of the same dimension. The NWs show an inverse dependence on diameter as well as on temperature, both of which have been quantitatively discussed. The thermal conductivity above Debye temperature is governed by two important scattering mechanisms; boundary scattering and Umklapp scattering. Armed with these two quantities that can be approximated from bulk values (making suitable modifications in parameters as are expected in NWs), the thermal conductivity of semiconductor NWs with different diameters can be predicted within ~20% uncertainty.

REFERENCES FOR CHAPTER VII

[1]D. G. Cahill, W. K. Ford, K. E. Goodson, G. D. Mahan, A. Majumdar, H. J. Maris, R. Merlin and S. R. Phillpot, *J. Appl. Phys.* **93**, 793, 2003

[2]D. G. Cahill, P. V. Braun, G. Chen, D. R. Clarke, S. Fan, K. E. Goodson, P. Keblinski, W. P. King, G. D. Mahan, A. Majumdar, H. J. Maris, S. R. Phillpot, E. Pop, and L. Shi, *Appl. Phys. Rev.* **1**, 011305, 2014

[3]W. Fon, K. C. Schwab, J. M. Worlock and M. L. Roukes, *Phys. Rev. B.*, **66**, 045302, 2002

[4]D. Li, Y. Wu, P. Kim, Li Shi, P. Yang and A.Majumdar, *Appl. Phys. Lett.*, **83**, 2934, 2003

[5]R. Chen, A. I. Hochbaum, P. Murphy, J. Moore, P. Yang, and A. Majumdar, *Phys. Rev. Lett.* **101**, 105501, 2008

[6]M. Kazan, G. Guisbiers, S. Pereira, M. R. Correia, P. Masri, A. Bruyant, S. Volz, and P. Royer, *J. Appl. Phys.* **107**, 083503, 2010

[7]J. Lim, K. Hippalgaonkar, S.C. Andrews, A. Majumdar and P. Yang, *Nano. Lett.*, **12**, 2475−2482, 2012

[8]C. J. Glassbrenner and Glen A. Slack, *Phys. Rev.* **134**, A1058, 1964

[9]W. Fulkerson, J. P. Moore, R. K. Williams, R. S. Graves, and D. L. McElroy, *Phys. Rev.* **167**, 765, 1968

[10]E Amin-Chalhoub et. al., J. *Phys. D: Appl. Phys.* **44** 355401, 2011

[11]D. Cahill, *Rev. Sci. Instrum.* **61**, 802, 1990

[12]L. Shi, Deyu Li, C. Yu, W. Jang, D.Kim, Z.Yao, P. Kim and A. Majumdar*, J. Heat Transfer* **125**, 881-888, 2003

[13]W. Jang, W. Bao, L. Jing, C. N. Lau and C. Dames, *Appl. Phys. Lett.* **103**, 133102, 2013

[14]L. Lu, W. Yi, and D. L. Zhang, *Rev. Sci. Instrum.* **72**, 2996, 2001

[15]J. Lee, W. Lee, J.Li, Y. Yu, Q. Kon, J. J. Urban and P. Yang, *Nano Lett.* **16**, 4133-4140, 2016

[16]X. Wang, J.n Yang, Y. Xiong, B. Huang, T. T Xu, D. Li and D. Xu, *Meas. Sci. Technol.* **29,** 025001, 2016

[17]J. Liu, H. Wang, Y. Hu, W. Ma, and X. Zhang, *Rev. Sci. Instrum.* **86**, 014901, 2015

[18]Q. Li, K. Xi, J. Zhang, Y. Zhang, Q. Li, K. Takahashi and X. Zhang, *Nanoscale*, **9**, 10784-10793, 2017

[19]G. S. Doerk, C. Carraro, and R. Maboudian, *ACS Nano*, **4,** 4908–4914, 2010

[20]T. Beechem, L.Yates and S. Graham, *Review of Scientific Instruments* **86**, 041101, 2015

[21]D. Wang, Q. Wang, A. Javey, R. Tu, H. Dai, H. Kim, P. C. McIntyre, T. Krishnamohan, and K. C. Saraswat, *Appl. Phys. Lett.* **83**, 2432–2434, 2003

[22]Z. Wang and N. Mingo, Appl. Phys. Lett. **97**, 101903, 2010

[23]S. Sett, A. Ghatak, D. Sharma, G. V. Pavan Kumar, and A. K. Raychaudhuri, *J. Phys. Chem. C.***122**, 8564-8572, 2018

[24]Amit S. Pawbake et. al., *ACS Appl. Mater. Interfaces*, **7**, 24185−24190, 2015

[25]J. F. Vetelino, K. V. Namjoshi, and S. S. Mitra, *J. Appl. Phys.* **41**, 5141, 1970

[26]F. Zhou, Y. Zhao, W. Zhou and D. Tang, *Appl. Sci.*, 8, 1794, 2018

[27]R. Jalilian, G. U. Sumanasekera, H. Chandrasekharan and M. K. Sunkara, *Phys. Rev. B,* **74**, 155421, 2006

[28]Y. Ogawa, Y. Yuasa, F. Minami, and S. Oda, *Appl. Phys. Lett.* **99**, 053112, 2011

[29]Cao, L.; White, J. S.; Park, J.-S.; Schuller, J. A.; Clemens, B. M.;Brongersma, M. L. *Nat. Mater.*, **8**, 643, 2009

[30]J. H. Parker Jr., D. W Feldman and M Ashkin, *Phys. Rev.* **155,** 712, 1967

[31]J. M Ziman, "*Electrons and Phonons",* (Clarendon Press, Oxford, UK)

[32]Y. Chen, D.Li, J.R. Lukes and A. Majumdar, *J. Heat Transfer* **127**, 1129-1137, 2005

[33]S Voltz and G Chen, *Appl. Phys. Lett.,* **75,** 2056, 1999

[34]*Thermal Conductivity: Theory, properties and applications,* Edited by T. M. Tritt (Kluwer Academic / Plenum Publishers, New York, 2004)

[35]P. N. Martin, Z. Aksamija, E. Pop and U. Ravaioli, *Nano Lett.,*10, 1120-1124, 2010

[36]J. P. Feser et al, *J. Appl. Phys*. **112**, 114306, 2012

[37]A. Kikuchi, A.Yao, I. Mori, I. Yamashita, T. Ono and S. Samukawa, *Proc. 16th Int. Conf. Nanotech*., **16**, 505, 2016

[38]Y. Zhao et al., *Nat. Commun.* **8**, 15919, 2017

CHAPTER VIII

APPROACH TO METAL-INSULATOR TRANSITION IN GERMANIUM NANOWIRES

The approach to metal-insulator transition was observed in Ge NWs which shows validity of scaling law. A size limit for 3D electronic conduction was established.

A. INTRODUCTION

The Metal-Insulator transition (MIT) is a challenging and interesting topic that has been investigated in bulk doped semiconductors for a long time.[1-3] The transition can be of Anderson type due to disorder and arises due to the quantum mechanical wave nature of the electrons or it may be of the Mott type due to correlation between interacting electrons.[1] At this point, an important length scale is the Bohr radius (a_H) of the electron around the impurity atom which defines the Mott minimum conductivity (σ_{Mott}). This is the critical value of conductivity above which, the system is metallic in nature. This type of localization can be achieved in a system by either increasing the disorder in it or by tuning the position of the Fermi level to lie beyond the mobility edge.[4] Disordered systems like alloys give us an opportunity to study the MIT transition, which is of Andersons' type. The MIT has been studied extensively in bulk Si and Ge with different dopants.[5] These experiments established that when the doping concentration n of carriers (like electrons and holes) falls below a critical concentration (n_c), MIT occurs. Such studies on bulk doped semiconductors formed the basis of the scaling theory of electron localization.[6] This theory established that a single parameter (conductance) can describe the MIT and it also developed a scaling equation for the electrical conductivity σ near the transition with ($n - n_c$).[7] It established 'correction to conductivity' and weak localization (WL) that occurs due to the quantum interference of electrons when disorder is high, and also the effect of temperature (T), which acts to weaken the quantum interference. While MIT in bulk doped semiconductors has been studied extensively, there have been very few studies on MIT in semiconductor NWs to evaluate the applicability/validity of the ideas of scaling theory and establish the parameter space (like the relevant length scales).

Electronic conduction in nanowires (NWs) is a topic of considerable current interest in nano-electronics and is also a problem of basic physics, in which some of the fundamental issues of electronic conduction in semiconductors can be addressed.[8,9] The performance of NWs with a small width is affected by size

when important length scales associated with electronic conduction are comparable to the physical dimensions of the NW.[10] The issue of WL has been looked at in single semiconductor NWs like Si,[11] InAs,[12] GaN,[13] ZnO[14] and In$_2$O$_3$.[15] Measurements were carried out down to low temperatures and the nature of WL and the temperature dependence of Thouless Length (L_{Th}) were studied. In the size range of the NWs used (diameter $\leqslant$30 nm), the electron transport (and accompanying WL correction) was found to be that of a 1D disordered conductor or one with a cross-over from 1D to 2D behavior. The Thouless length was found to have a temperature dependence $\sim T^{-1/3}$, which arises when the Nyquist mechanism is the primary mechanism for electron de-phasing.[16] Most of the investigations were performed in NWs on the insulating side of the MIT and the conductivity showed variable range hopping (VRH).[17]

The effect of size on electronic conduction in Ge NWs has not been investigated before. Furthermore, Ge is a fast developing material for application in high-speed electronics and other nano-electronic devices,[18-20] and it is felt that a study of this issue will be an important addition in this area. Our investigations to study the metal-insulator transition are performed with NWs that have higher conductivity and are on the metallic side of the transition. The NWs lying on the metallic side have a spread in conductivity over which the scaling law of conductivity can be tested with reasonable accuracy as the MIT is approached from the metallic side. This investigation, carried out on Ge NWs, has a different scope and perspective than the above-mentioned studies on other semiconductor NWs. The NWs used in this study have a larger diameter (>45 nm), so that one can establish a lower size limit for the validity of scaling theories of localization (as formulated for 3D systems).

B. RESULTS AND DISCUSSIONS

1. The Au-Ge alloy

Ge NWs were grown using the VLS method as described in Chapter II. It is known that NWs can be unintentionally doped due to diffusion from the metal catalyst and acquires deep level acceptor states.[21,22] There have been some studies on the migration of Au-Ge alloy within an intrinsic Ge NW with temperature by in-situ TEM analysis.[23,24] In this particular case, the growth takes place at around 600^{0}C where diffusion coefficient of Au in Ge is $1.77 \times 10^{-3} \mu$m^2/s at that temperature.[25] Since the growth time is 1000s–2000s, it is possible that Au diffuses inside Ge during growth over its length (1–2 μm), leading to unintentional doping.

Structural characterizations using Transmission Electron Microscopy through the High Angle Annular Diffraction Field (HAADF) image of a NW (Fig. 1(a)) we can clearly see the Au tip as well as the presence of Au that has segregated inside the NW during cooling. X-ray Diffraction (XRD) is also performed on the NWs grown on Si substrate and shows peaks that are traceable to International Centre for Diffraction Data (see Fig. 1(b)). It shows the peak from (111) plane of Ge having maximum intensity. There is a peak of Au-Ge alloy corresponding to the (321) plane and an Au peak (111) coming from the Au NP which are un-reacted on the Si substrate. The other low intensity peaks are of GeO_2. Ge NWs grown using the VLS method can be unintentionally doped and may behave as doped Ge–Au alloy NWs.
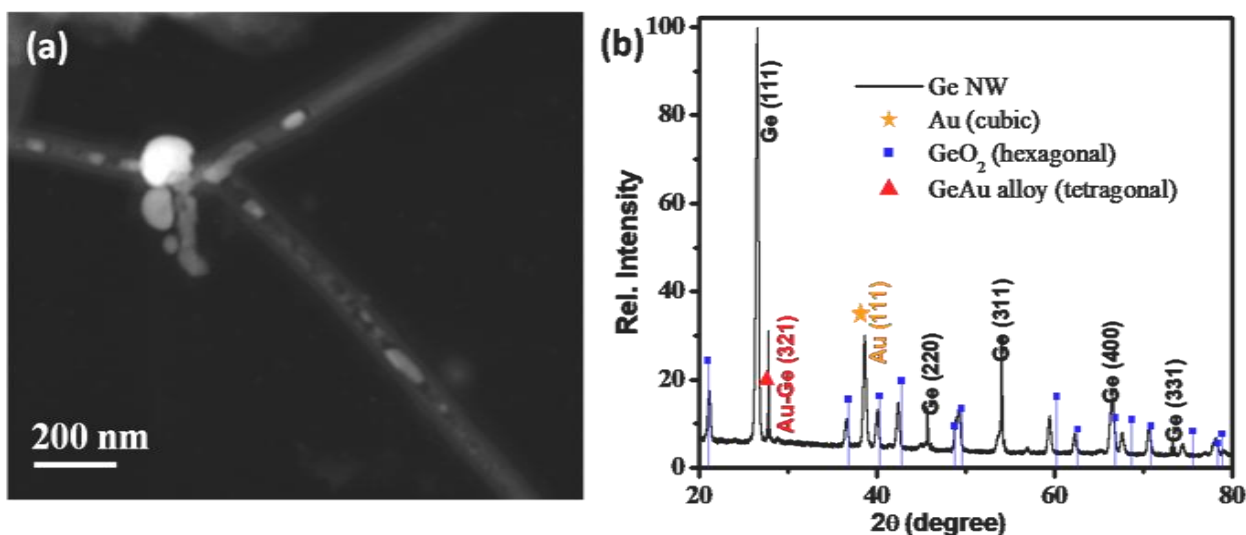
Figure1. (a) HAADF image where Gold can be seen on the tip as well as within the body of a NW. (b) XRD pattern of an ensemble of Ge NWs showing the Ge (111) peak, an Au-Ge alloy peak, Au (111) peak and other GeO_2 peaks.

2. Temperature dependent resistivity

Low temperature (down to 6K) electrical transport measurements were performed on three single Ge NWs which show a finite conduction at $T \rightarrow 0$. These NWs has reasonably low resistivities. Table 1 also shows the carrier concentration (n). The dependence of carrier concentration on resistivity in semiconductors is a developed and well-researched area. Thus, from the resistivity of bulk Ge, we have determined the value of N using well established data.[26] There is no available data on Ge NWs, from which we can extract out the resistivity. Hall measurement gives the correct value of carrier concentration but in case of a nanowire, there are limitations in measurement of the same. Fabrication of Hall bar in a NW (of diameter < 100nm) is a challenging task and a successful measurement of carrier concentration by Hall effect in a NW is limited to just a couple of reports so far,[27,28] with NW diameter > 100 nm. Even

when such measurements are made on such NW Hall-bars, there are errors that arise. In fact even interpretation of Hall data in narrow nanowires have their own source of uncertainties that arise from exact alignment of Hall probe that increase uncertainties in exact Hall probe spacing distances. It has been shown recently theoretically[29] that: (i) influence of diffusion currents in nanowires with radius comparable with the screening length of carriers and (ii) eddy currents in non-planar Hall contacts can result in a severe reduction of the measured Hall voltage leading to overestimation of effective carrier concentration. While this leaves an element of uncertainty regarding the exact value of *N*, however, the uncertainty does not affect the main observation made in this thesis.

NW3 that has $\rho \sim 10$ mΩcm, while the other NWs have $\rho << 1$ mΩcm. From the $\rho-T$ curves for the three NWs shown in Fig. 2, we observe that the NWs have negative temperature Coefficient of Resistivity (TCR). However, at low temperature, the resistivity saturates to a temperature-independent value, indicating a finite conductivity σ_0 as $T \rightarrow 0$, indicating a metallic state ($\sigma(T = 0) \neq 0$).[7] Thus these NWs lie on the metallic side of the MIT. The negative TCR of the NWs does not show activated behavior, as checked using the logarithmic temperature derivative.[30] NW2 is seen to approach saturation, although it is not directly visible for the lowest temperature used (~6 K). However, when the data are analyzed digitally one can see the approach to saturation since the derivative dρ/dT decreases continuously and approaches zero. In the $\sigma-T$ plot at low temperature (Fig. 3), the curves are fit to a 3D WL model and from there it is clear that there is a finite constant conductivity that appears as an intercept on the *y*-axis as the temperature approaches 0 K.

Table 1. Device nomenclature with NW dimensions.

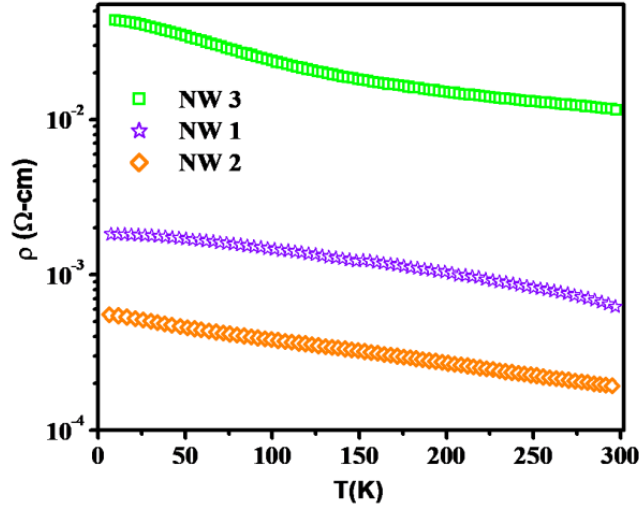| Name	Diameter (nm)	Length (μm)	ρ_{RT}(Ωcm)	n (cm^{-3})
NW1	65	2.0	6.0×10^{-4}	5×10^{19}
NW2	45	1.5	1.9×10^{-4}	4.5×10^{20}
NW3	100	2.5	1.1×10^{-2}	6×10^{17}

Figure 2. Resistivity verses temperature data for all the NW1 (violet), NW2 (orange) and NW3 (green).

3. The weak localization model

For a system in which disorder is present, the weak localization is an effect of the backscattering of electrons from the disordered lattice which gives a coherent standing wave pattern and resistance thus increases.[1] In most cases, there is a mobility edge present below which energy, the states are localized. Then, the position of the Fermi level (E_F) with respect to the edge becomes very important.[3] Even though the system may have a finite DOS, it may not be conducting if E_F lies below the mobility edge.[1,4] In our case, the NWs are on the metallic side of the transition. The amount of Au diffusion in the NW tunes the E_F such that the system is metallic. To analyze the electronic transport property of the NWs, we consider fitting the data with the model for low temperature conductivity due to weak localization (WL).[7] The inelastic scattering brought about by a static random periodic potential due to impurity in the system can be incorporated by introducing a length scale L_{Th}, the Thouless length, which is the path of an electron diffusing between de-phasing inelastic collisions.[7,31] NWs with a finite $\sigma(T = 0) = \sigma_0$ and a negative TCR are expected to show signature of WL in their T dependence, particularly at low T when phase-breaking mechanisms die out. To verify this we analyze the electronic transport in the NWs by fitting the $\sigma - T$ data with the WL relation for correction to conductivity, which is applicable for 3D transport, and is given by,[7]

$$\sigma = \sigma_0 + kT^{\frac{p}{2}} \tag{1}$$

where, $k = \frac{2e^2}{ah\pi^2}$ and $L_{th} = aT^{-\frac{p}{2}}$. The factor a thus gives us the length scale associated with the de-phasing process. The exponent p depends predominantly on the dimensionality and also the inelastic

scattering process, and σ_0 is the Drude conductivity. The experimental data along with fitted curves for the three NWs are given in Fig. 3. The fit parameters are given in Table 2. The value of $p \sim 4$ in all cases and agrees well with the predicted value of $p = 4$ for WL when the dominant inelastic scattering is due to electron– phonon interaction.[32]
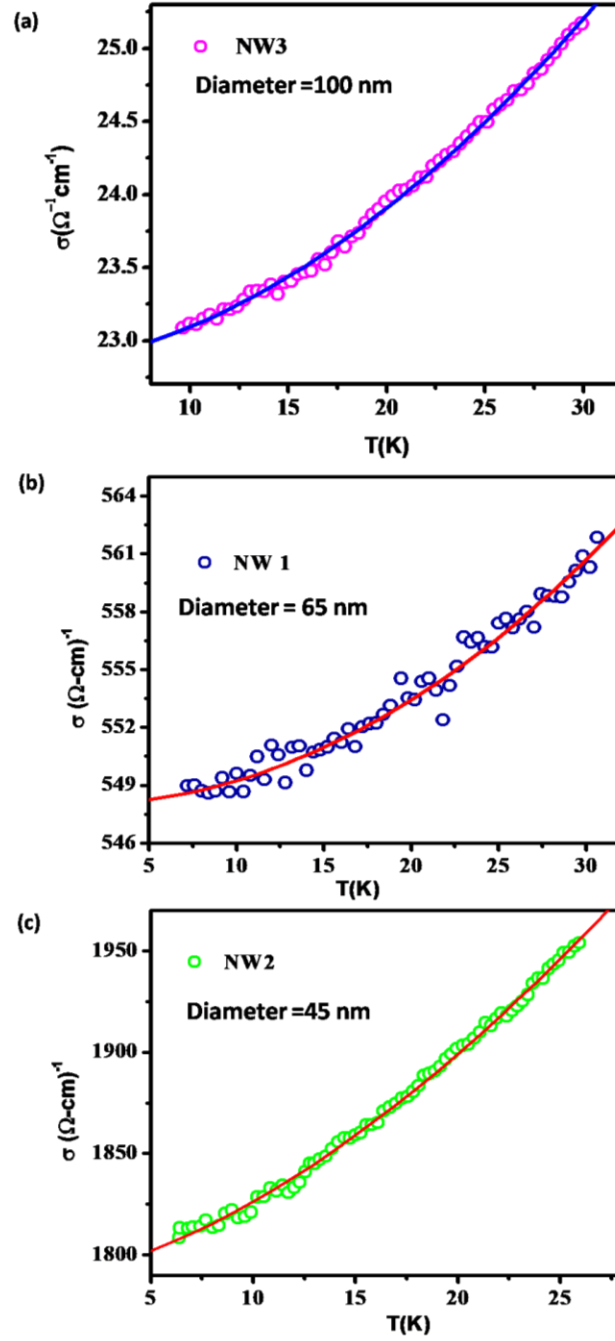

Figure 3. The low temperature conductivity with model fitted data (line) for (a) NW3, (b) NW1 and (c) NW2.

Table 2. The fit parameters for low-temperature conductivity.

Name	$\sigma_0 (\Omega cm)^{-1}$	σ_0 / σ_{Mott}	k	p	a (x10^4)
NW1	547.9 ± 0.3	48.5	0.01 ± 0.005	4.2 ± 0.1	7.8
NW2	1790 ± 1	158.7	0.89 ± 0.09	3.2 ± 0.03	0.08
NW3	22.8 ± 0.3	2	0.0036 ± 0.0004	3.82 ± 0.03	21.4

3. Scaling model of conductivity

Using the value of the Hydrogenic Bohr radius a_H = 6.4 nm of an electron around an impurity atom in Ge,[33] we evaluated the Mott minimum metallic conductivity in doped Ge, $\sigma_{Mott} \approx 1130$ $(\Omega m)^{-1}$. In Table 2 we show the ratio σ_0 / σ_{Mott}, which for NW3 is >1, while for NW1 and NW2 it is >>1. This reaffirms that the Ge NWs indeed lie on the metallic side, while NW3 lies close to the transition but is still on the metallic side.

To visualize the approach to the critical region from the metallic side in Fig. 4a we plotted the zero temperature conductance σ_0 as a function of $\left|1 - \frac{n}{n_c}\right|$,[1] where n_c is the critical electron concentration for MIT in Ge. We used a value of n_c averaged over different dopants using published data.[34] We used values taken from extensive studies on bulk Ge. While this leaves an element of uncertainty regarding the exact value of n_c in the context of NWs, in the absence of such a number for NWs, a bulk value for n_c can be a viable estimate. The zero temperature conductivity was found to follow the scaling law,

$$\sigma_0 \sim \left(1 - \frac{n}{n_c}\right)^{\nu}. \tag{2}$$

From the fit to the data we found that ν= 0.62, which is close to the theoretical value of 0.5.[6] It is noted that there are not too many points that are warranted for a precise determination of the exponent ν and validity of the scaling law, nevertheless its applicability in the approach to the critical region of MIT is interesting. This has not been tested in NWs before.

In the bulk, the critical concentration in Ge is not defined exactly and varies with the donor atoms due to the spread in the ionization energies of the donor centers.[5] Furthermore, the critical exponent varies (0.5<ν<1.2) depending on the degree of compensation. Table 3 gives the level of compensation and the value of ν for impurity-doped bulk Ge. For an uncompensated system, a value of ~0.5 is reported for ν[35] for bulk Ge, which is in agreement with our experimentally obtained value of ν= 0.62. In Fig. 4b we plot

the $\sigma - T$ data for the NWs—together with bulk doped Ge (single crystal)[36] and Au–Ge alloy (polycrystalline film)[37] —close to the transition region. The percentage of Au in the alloy is 28% for a polycrystalline film. The arsenic-doped Ge crystal has an electronic concentration of $4.5 \times 10^{17} cm^{-3}$.[38] The bulk, film and NWs have $n > n_c$ and all lie on the metallic side of the transition with a finite conductivity at low temperature. This graph establishes that the universal behavior of Ge as a doped semiconductor is retained in these NWs.

Figure 4: (a) Dependence of zero temperature conductivity σ_0 on the electronic concentration and fit to the scaling law. (b) Conductivity v/s temperature data for NW1, NW2 and NW3 along with published data of Ge-Au alloy[37] (dotted line) and n-type bulk Arsenic doped Ge.[38]

Table 3. Scaling parameters for bulk germanium.

Dopant	Degree of compensation	Scaling exponent v	Ref #
Arsenic	Low	0.5	38
Arsenic	High	1.2	38
Antimony	Low	0.9	39
Gallium	Uncompensated	0.5	35
Gallium	Low	0.97	40

4. The Thouless length

We obtained the Thouless length L_{Th} (Fig. 5) from the T dependence of σ using the value of a (see equation 2). In the cases of NW1 and NW2, with less disorder, L_{Th} at low temperature grows to an appreciable value $\rightarrow$ few μ m. In the case of the NW3 that lies on the verge of transition, the increase of L_{Th} with T is much smaller and is in the range of a few hundreds of nm. The comparison of the temperature dependent values of L_{Th} with the physical size of the NWs (diameter and length) show that in all the NWs the physical length is $>L_{Th}$. For NW1 and NW2, L_{Th} and the physical length becomes comparable and at much lower temperatures ($<1K$) one would expect the onset of phase coherent transport.

Figure 5. Temperature dependence of Thouless length L_{Th} as obtained from weak localization fits and its comparison with physical size of samples.

Thus from the analysis of the data it is possible to estimate some approximate physical size (length $\geqslant 0.5$ μm) and temperature zone ($T < 10$ K) where one would expect phase coherent transport in Ge NWs. Generally two length scales will decide whether one can obtain 1D behavior in them. These are the Thouless length L_{Th} and the Bohr radius a_H. The fit to the WL expression gives us L_{Th}, as discussed above. At low temperature in NW1 and NW2, the L_{Th} becomes larger than the diameter of the NWs. One would expect deviation from 3D behavior. However, we did not observe such a deviation. It may occur at even lower temperatures, where $L_{Th}>>$ diameter. The physical size of the samples used in this work is much larger than another fundamental scale, namely the Bohr radius. Since both the diameter and the length are

$>a_H$, we would not expect any changes in the basic parameters related to MIT behavior. Our investigation thus establishes that above a certain size scale, the theories developed for the bulk Ge MIT are still valid.

C. CONCLUSIONS

Germanium nanowires form an important ingredient in nanoelectronics. In this context, understanding of the physics of electronic transport in single Ge nanowires that are in the "metallic" side of the insulator-metal transition is of great significance. This investigation answers an important aspect of the electronic conduction in Ge nanowires regarding applicability of theories of weak localization and scaling theories that have been developed to deal with disordered conductors.

This study carried out on single Ge nanowires, investigates the validity range of scaling theories in the nanowires and establishes a limit of size for applicability of the theory for 3D behavior in Ge Nanowires. The weak negative temperature coefficient of resistivity has been linked to weak localization behavior from which the Thouless length has been obtained which provides an estimation of the length scale over which phase coherent transport can be expected. Importantly a scaling exponent ν of ~0.6 has been obtained from the dependence of conductivity on concentration, which is expected from scaling theories for uncompensated semiconductors.

Constructive quantum interference tends to localize electrons as they diffuse coherently in weakly disordered systems. Such weak localization effect has been widely observed in various disordered electronic systems. Electrons have to maintain their phase coherence for quantum-interference effects to take place. Therefore, the weak localization diminishes at high temperatures where frequent electron-phonon and electron-electron scatterings destroy the coherence. Furthermore, a magnetic field introduces different phases for electron traveling in time-reversed paths and thus suppresses the weak localization and enhances the sample conductance. Because the weak localization correction to conductance is directly related to the phase coherence length L_ϕ, analyzing the weak field magneto-conductance is often used to extract L_ϕ, which is a key parameter for any device operation based on electron coherence in nanostructures. Even though we have not been able to obtain the phase coherence length, we have established the validity range for scaling theories in the NWs also a size limit for the applicability of the theory for 3D behavior.

REFERENCES FOR CHAPTER VIII

[1]B. Kramer and A. McKinnon 1993 *Rep. Prog. Phys*. 56, 1469

[2]N. F. Mott and E. A. Davis, Electronic Processes in non-crystalline materials (Clarendon Press, Oxford 1977).

[3]N. F. Mott, *Metal-Insulator Transitions* (Taylor and Francis, London, 1990)

[4]F. Gebhard, *The Mott Metal-Insulator Transition* (Springer, Heidelberg, 2000).

[5]M. N. Alexander and D. F. Holcomb 1968 *Rev. Mod. Phys*. 40, 815

[6]E. Abrahams, P. W. Anderson, D. C. Licciardello and T. V. Ramakrishnan 1979 *Phys. Rev. Lett*. 42, 673

[7]P. A. Lee, T. V. Ramakrishnan 1985 *Rev. Mod. Phys*. 57, 287

[8]W. Lu and C. M. Lieber 2007 *Nat. Mat*. 6, 841

[9]C. Thelander, P. Agarwal, S. Brongersma, J. Eymery, L. F. Feiner, A. Forchel, M. Scherer, W. Riess, B. J. Ohlsson, U. Gosele, and L. Samuelson 2006 *Mat. Today*. 9, 28

[10]M. M. Mirza, D. A. MacLaren, A. Samarelli, B. M. Holmes,H. Zhou, S. Thoms,D. MacIntyre, and D. J. Paul 2014 *Nano. Lett*. 14, 6056

[11]F. J. Ruess, B. Weber, K. E. J. Goh, O. Klochan, A. R. Hamilton and M. Y. Simmons 2007 *Phys. Rev. B*. 76, 085403

[12]D. Liang, M. R. Sakr and X. A. Gao 2009 *Nano. Lett*. 9, 1709

[13]Y. Huang, X. Duan, Y. Cui, and C.M. Lieber 2002 *Nano. Lett.* 2, 101

[14]R. S. Thompson, D. Li, C M. Witte and J. G. Lu 2009 *Nano. Lett*. 9, 3991

[15]A. J. Chiquito, A. J. C. Lanfredi, R. F. M. deOliveira , L. P. Pozzi and E. R. Leite 2007 *Nano. Lett*. 7, 1439

[16]B. L. Altshuler, A. G. Aronov and D. E. Khmelnitsky 1982 *J. Phys. C: Solid State Phys*. 15, 7367

[17]N. F. Mott 1968 *J. Non-Cryst. Solids*. 1, 1

[18]U. Wang, Q. Wang, A. Javey, R. Tu, H. Dai, H. Kim, P. C. McIntyre, T. Krishnamohan and K. C. Saraswat 2003 *Appl. Phys. Lett*. 83, 2432

[19]G. Y. Yoon, T. K. Kim, I. Hwang, H. S. Lee, B. W. Hwang, J. M. Moon, Y. J. Seo , S. W. Lee, M. H. Jo and S. H. Lee 2014 *Appl. Mater. Interfaces* 6, 3150

[20]L. Z. Pei and Z. Y. Cai 2012 *Recent Pat. Nanotech*. 6, 44

[21]S. Barth, M. M. Kolesnik, K. Donegan, K. Krsti, and J. D. Holmes 2011 *Chem. Mater*. 23, 3335–3340

[22]M. Simanullang, G. B. M. Wisna, K. Usami, W. Cao, Y. Kawano, K. Banerjee, S. Oda 2016 *J. Mater. Chem*. C. 4, 5102−5108.

[23]Yu-Lun Chueh et. al., *Nano Lett.* 2010, 10, 393-397

[24]Q Liu, R Zou, J Wu, K Xu, A Lu, Y Bando, D Golberg and J Hu, *Nano Lett.*2015, **15**, 2809-2816

[25]H. Bracht, N. A. Stolwijk, and H. Mehrer 1991 *Phys. Rev*. 43, 14465

[26]D. Cutriss 1961 *Bell Syst. Techn. J*. 40, 509

[27]K. Storm, F. Halvardsson, M. Heurlin, D. Lindgren, A. Gustafsson, P. M. Wu, B. Monemar and L. Samuelson 2012 *Nat. Nanotech*. 7, 718-722

[28]Ch. Bloomers, T. Grap, M. I. Lepsa, J. Moers, St. Trellenkamp, D. Grutzmacher, H. Luth and Th. Schapers 2012 *Appl. Phys. Lett*, 101, 152106

[29]C. Fernandes, H. E. Ruda, and A. Shik 2014 *J. Appl. Phys*. 115, 234304

[30]A. Mobius 1985 *J. Phys. C: Solid State Phys*. 18, 4639

[31]D. L. Thouless 1977 *Phys. Rev. Lett*. 39, 1167

[32]J. J. Lin and J. P. Bird 2002 *J. Phys.: Condens. Matter*. 14, R501

[33]R. Vrijen, E. Yablonovitch, K. Wang, H. W. Jiang, A. Balandin, V. Roychowdhury, T. Mor and D. DiVincenzo 2000 *Phys. Rev. A*. 62, 012306

[34]P. P. Edwards and M. J. Sienko 1978 *Phys. Rev. B*. 17, 2575

[35]M. Watanabe, Y. Ootuka, K. M. Itoh and E. E. Haller 1998 *Phys. Rev. B* 58 9851

[36]A. G. Zabrodskii and K. N. Zinoveva 1984 *Sov. Phys. JETP* 59, 425

[37]B. W. Dodson, W. I. McMillan, J. M. Mochel and R.C Dynes 1981 *Phys. Rev. Lett*. 46, 46

[38]R. Rentzsch, Ch. Reich, A. N. Ionov, V. Ginodman, I. Shlimak, P. Fozooni and M. J. Lea 1999 *Phys. Sol. State* 41 757

[39]I. Shlimak, M. Kaveh, R. Ussyshkin, V. Ginodman and L. Resnick 1996 *Phys. Rev. Lett* 77 1103

[40]K. M. Itoh, M. Watanabe, Y. Ootuka, E. E. Haller and T. Ohtsuki 2004 *J. Phys. Soc. Japan* 73 173

CHAPTER IX

DISCUSSIONS

A summary of the work done in this thesis is presented here. It has a short discussion on the new observations and a quick insight into the physics behind them.

The important observations of this thesis are:

1. Growth of oxide-free Germanium Nanowires (NWs) by a non-toxic method using direct vapor transport in the presence of reducing agents.
2. Formation of electrical contacts to side-contacted single Ge NWs through lithography which has low Schottky barrier height ($\varphi = 0.15$eV) and low specific contact resistivity ($\rho_c = 10^{-6}\Omega$cm^2).
3. Observation of ultra-high photoresponse (($\mathcal{R}$) ~10^7A/W) in a single Ge NW with surface oxide controlled opto-electronic properties that is tunable through manipulation of sub-oxide content.
4. Observation of self-powered photodetection in a single Ge NW.
5. Utilization of micro-Raman Spectroscopy to study thermal conductivity in single Ge NW and prediction of thermal conductivity of semiconductor NWs.
6. Observation of approach to metal-insulator transition and validity of scaling law for a doped semiconductor nanowire.

We have investigated the physics behind each of the above observations and have built-on the existing knowledge, and added new knowledge wherever applicable in understanding the transport properties of Ge NWs. From the material science point of view, we have been able to grow good quality single crystalline Ge NWs for our study. This step is crucial since it forms the backbone for all experimental measurements. It is known that Ge NWs are very prone to oxide formation, thus a simple method to prevent formation of oxide during the growth process was employed through the use of reducing gas H$_2$ and oxygen-getters in the growth environment. What we cannot control is the native oxide formation on Ge post growth, to a self-limiting thickness.

We have investigated the important issues of electrical contacts made on single NWs. Fabrication of low barrier and low resistance contact on Ge is a challenging issue and has been studied extensively in bulk due to Fermi level pinning (FLP). However, the knowledge of bulk contact formation cannot be extrapolated into nanoregime because there is suppression of Fermi level pinning in NWs. Thus a dedicated contact evaluation on Ge NWs is necessary and important as has been done in this thesis. We have quantitatively assed the barrier heights, ideality factors and specific contact resistivities of contacts

made on single Ge NW and evaluated their evolution with temperature, which has not been investigated previously. The junction characteristics have been analyzed which shows how a contact with low barrier height of ~0.15eV and a low specific contact resistivity of $10^{-6}\Omega cm^2$ can be obtained in NWs with low resistance. The metal semiconductor junction shows an ideality factor close to unity. The specific contact resistance increases on cooling but the barrier shows suppression as the nanowire is cooled, along with an enhancement of the ideality factor. We analyze the temperature dependence of these parameters using a model that assumes a Gaussian distribution of barrier heights in the contact region.

We have investigated photoconductive properties of single Ge NWs of diameter < 100 nm in the spectral range of 300-1100 nm and in the broadband Near Infra-red spectrum showing peak Responsivity ($\mathcal{R}$) in excess of 10^7A/W at a minimal bias of 2V. The highest optical gain of $< 10^8$ A/W was achieved in a nanowire of diameter 30 nm at a low illumination intensity of $10\mu W/cm^2$. The origin of the ultra-large $\mathcal{R}$ arises from a combination of various physical effects of which the ones unique and important are:

- Presence of radial field due to surface depletion layer that leads to band bending and contributes to separation of photogenerated electron-hole pair.

- States residing in the surface oxide layer controls act as recombination centre for the photogenerated carrier.

- States at the Ge/GeO$_x$ interface controls the photoconductive gain by acting as traps.

This conclusion of the Radial field has been drawn from the observation of power dependence of the optical gain, which decreases beyond a certain threshold intensity. This indicates that the gain is controlled by a radial field formed due to surface states. We have quantified the Radial field in a Ge NW by using self-consistent Schrodinger-Poisson equation. It shows that there is depletion of electrons in the NW core resulting in band bending. The Radial field obtained in a typical Ge NW of diameter ~ 60 nm is ~10^{-6} V/m.

The density of trap states was tuned to engineer the photoconductive gain in Ge NWs to achieve super-linear photoresponse. The Ge/GeO$_2$ interface alters at temperatures $\geq 400^0$C due to de-sorption of GeO (that have 3-fold coordination and controls the slow kinetics). This reduces the concentration of the slow states and causes onset of super-linearity. Annealing also reduces bulk trap states and improves the metal/NW contact such that there is tremendous improvement in overall photodetector performance.

We have observed a significantly high performing self-powered device based on a single NW and we investigate the physics behind the performance of the self-powered device. This investigation showed that

it is possible to achieve self-powered photodetection using a single Germanium nanowire (diameter < 100nm) with micron size (1μm-2μm) device length with $\mathcal{R} \sim 10^3\text{-}10^5$A/W. We have shown that the photodetector configured as a metal-semiconductor-metal device has an asymmetry in the Schottky Barrier height. This asymmetry provides the necessary "built-in" axial field to separate the photogenerated electron-hole pair, leading to photodetection under zero external bias. The above idea was validated by a simulation study to establish that the origin of this effect indeed lies in the asymmetry in the Schottky Barrier Height at the two metal-semiconductor contacts. The simulation also shows that electric field inside the nanowire can only arise in micron/sub-micron length device where the device length is comparable to the to the total depletion widths at the contacts. The formation of asymmetric barriers on Ge NW appears to be mainly dominated by structural inhomogenity and presence of oxide layer on the Ge NW surface. This adds an element of stochasticity in the barrier formation and needs to be investigated further for pre-designed self-powered devices.

We investigate the thermal conductivity of a single Ge NW using a novel application of Raman Spectroscopy. The Raman active temperature dependent vibrational mode of Ge acts as a thermometer while the intense micro-laser that falls on the NW, heats it. The Opto-thermal method to determine thermal conductivity is rapid and non-destructive but is known to be erroneous. We have developed certain methods to overcome and eliminate the errors arising from this measurement method. The effect of thermal boundary resistance has been eliminated by performing a "length dependent method" experiment, and also through simulations. The errors arising due to an extended heat source (laser with FWHM ~700nm) has been investigated and accounted for. We have analyzed the effects of errors and provide a solution to reduce them through simulations. By improving the data-acquiring process through certain precautions we can minimize the error.

The thermal conductivity of Ge NWs lies within 2-3.8W/m.K for diameter between 50-110nm around room temperature. The temperature dependence of thermal conductivity is expressed as a sum of a temperature independent term arising from boundary scattering and a T^{-1} term arising due to Umklapp scattering at high temperatures. We have been able to predict the thermal conductivity of semiconductor nanowires through calculation of the above parameters that gives a quick estimate within a ~ 20% uncertainty. The investigation shows the importance of Ge NWs for application as a good thermoelectric material for which further investigations are warranted. This study also shows the ease with which a thermal conductivity measurement may be performed by use of a table top instrument only through a non-destructive and rapid technique.

We have investigated the electronic transport in Ge NWs which lie beyond the insulating regime of the insulator-metal transition. The study provides a platform to test the validity of the scaling laws and weak localization theory which has not been done before in Ge NWs. The low temperature conductivity follows a 3D weak localization behavior from which we have extracted the Thouless length, an important parameter that dictates onset of phase coherent electron transport. We have determined the scaling exponent which is nearly 0.6 and is close to the theoretically expected value in uncompensated semiconductors. These parameters obtained helps us to estimate the length scale and temperature scale below which Ge NWs can show coherent electron transport.

CHAPTER X

CONCLUSIONS AND FUTURE PROSPECTS

This thesis is a combination of basic physics and application development. We have investigated the low temperature electrical conduction in Ge NWs and studied its thermal conductivity. We have developed a method for fabrication of low specific contact resistivity electrical contacts in a single Ge nanowire (NW). We have investigated the opto-electronic properties of Ge NWs and observed some unique and exciting physics which has been explored in details. The Ge surface oxide layer promotes charge separation (through a radial field) and carrier trapping (through different trap states) that highly enhances its photoresponse. The photoconductive gain has been controlled through the surface oxide layer and tuned by a process of annealing. These observations give an insight into the physics that governs the ultra-high photoresponse in semiconductor NWs. A systematic study of the same, with a rigorous diameter variation (while keeping other factors constant) can provide an experimental insight into the radial field. It will be a useful addition to the existing results of the Schrodinger-Poisson solution to the radial field.

Ge NWs hold a potential application in thermoelectric due to its low thermal conductivity of ~ 4W/m.K (diameter ~ 100nm). A more detailed analysis of the thermal properties of Ge NWs is warranted for a better understanding of its heat transport mechanisms. While in Si NW, a figure of merit *ZT* is ~0.6, in Ge NWs this essential number is lacking. There is a void in the study of its thermal properties, even though they surpass Si. This thesis is an initial stepping stone towards the direction of thermal property study of Ge NWs.

APPENDIX A

Simulation to determine intensity of scattered wave from a nanowire on a SiO₂/Si substrate.

Due to the antenna effect from the underlying Si substrate on top of SiO_2 (300 nm) there is back scattering of the incident EM wave. This may leads to an overestimation of the Responsivity due to scattered wave from the substrate re-entering the NW. We have used the finite element method (software COMSOL Multiphysics), Wave optics module to simulate through finite element method the scattered wave from a SiO_2/Si substrate. We have defined the geometry and input appropriate boundary conditions to find solution to the wave equation. We have used a linearly polarized EM wave of frequency 650 nm and amplitude 1V/m as the input wave along the y-direction. The 3D image of scattered field is shown in Fig. A1. It shows an interference pattern inside the Si which is slowly decaying out towards infinity in all directions. The line plot of the intensity of input wave and scattered wave in SiO_2 and the air above is shown in Fig A2.

Figure A1. (a) Scattered EM wave shown as a 3D plot with color legend showing the amplitude of the EM wave in V/m.
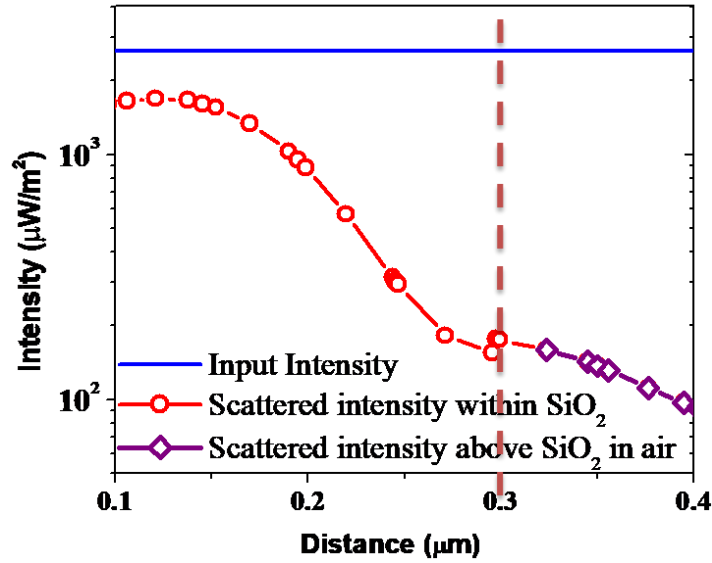
Figure A2. Line plot of intensity scattered wave in the region of interest.

For calculating the scattered intensity of light, we have used the dimensions of a 45 nm NW with length 2μm. The input intensity of $2654μW/m^2$ produces a back scattered intensity $159μW/m^2$. The percentage of scattered power re-entering the NW due to the underlying substrate is ~5.9%. It is almost negligible and we can claim that this effect does not hamper the opto-electronic parameters obtained. Thus Responsivity of $3x10^7$ A/W (as discussed in Chapter V) can get scaled down to not less than 10^7 A/W due to these effects. Thus the large photoresponse is an intrinsic property of a Ge NW.

References

[1] G. G. Macfarlane, T. P. Mclean, J. E. Quarrington and V. Roberts, *Phys. Rev.,* **108**, 1377-1383, 1957

[2] Y. Wang, K. Kempa, B. Kimball, J. B. Carlson, G. Benham, W. Z. Li, T. Kempa, J. Rybczynski, A. Herczynski, and Z. F. Ren, *Appl. Phys. Lett.*, **85**, 2607, 2004

APPENDIX B

Model for photocurrent in annealed Ge nanowire

We consider a photoconductor with three different kinds of levels; there is recombination centre (level 3, which is empty in dark) and two trap states: one of electrons (level 1) and the other one for holes (level 2) at different energetic positions within the band gap. There is thermal trapping and de-trapping in levels 1 and 3. The schematic is shown below:
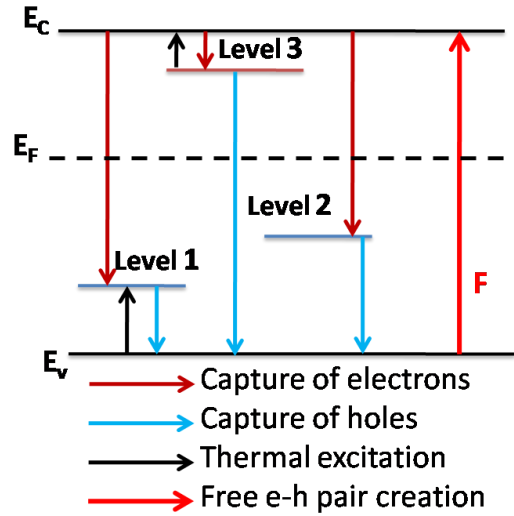

Figure B1. Schematic of the photoconductor model with different energy levels.

We know that in Germanium, there are fast states that can trap electrons and holes and are designated here as level 1 and level 2 with density of states N (let $N=10^{15}/cm^3$). The states have similar electron and hole capture cross-section and hence recombination rate β. Level 3 indicates the slow states in Ge (with density of states N_3) which has a much lesser recombination rate β'. Since the relaxation time of the fast states $\sim10^{-6}$ sec and for slow states it is $\geq 10^{-3}$ sec, it is a reasonable assumption to take $\beta = 10^{-4}\beta'$. There is a thermal excitation and de-excitation from level 1 and level 3, which is negligible for level 2, which is a deep level. We follow the rate equations as given by Bube[1] and discuss the situation when the photoresponse changes from sublinear to super-linear.

In the as-grown Ge NW photodetector, we get a sublinear behavior. Such a situation can only arise if,

- $N_3 >> N$
- $N_3 = N$

It has been evaluated upto $N_3 =10^2N$.

In the annealed Ge NW, we get super-linear behavior. Such a situation arises if,

- $N_3 << N$

It has been evaluated for $N_3 = 0.01N$ which shows onset of super-linear behavior. It holds for other values of N_3 till, $N_3 = 10^{-8}N$.

The results of this solution agree well with our experimental observations that, upon annealing, there is a reduction in GeO which corresponds to a reduction in the slow states. Therefore, the onset of super-linearity, marked by the condition that $N_3 = 0.01N$, corroborated well with our observations and we conclude that indeed, annealing leads to onset of super-linearity through reduction of states with slow kinetics.

References

[1]R. H. Bube, *J. Phy. Chem. Solids.* **1**, 234-248, 1957

APPENDIX C

Concentration of electric field due to electromagnetic wave inside a nanowire with a cladding

In addition to the factors discussed in Chapter IV for the ultra-high photoresponse in Ge NWs, there is another additional factor contributes to enhanced photoresponse in narrow nanowires. There is partial enhancement of the electric field of the illuminating light which increases electron-hole pair generation. We have used Maxwell's equations to find the analytical solution to the electric wave propagation inside a Ge NW with an oxide layer surrounding it. We have calculated the electric field in the cladding at 2.5 nm inside the GeO_2 layer and in the core at 3 nm from the central axis of the NW, which is 1 μm in length.

We have determined the amplitude of electric field inside the NW at the core as well as the oxide as a function of nanowire diameter. We have taken a 2D model of rectangular slab of variable width (d), which is the Ge core diameter with 5 nm width of GeO_2 layer (cladding) on both sides of it. It takes into account an electromagnetic wave of wavelength 650 nm incident on the NW from one edge. The method assumes the electric wave propagation along the axis of the NW (z-direction) following the equation,[1]

$$E_z = E_y e^{-ik_x x},$$

where, the y-component is along the radial direction. The NW has a surrounding oxide layer, which acts as cladding and causes a wave guiding effect in it (see Fig. C1).
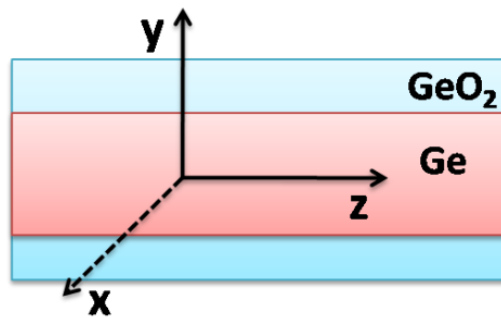

Figure C1. Schematic showing the coordinates in the Ge NW model which we used for calculations.

Hence, E_y it is defined at the two regions as,[1]

$$E_y = A cos(k_y y) \text{ (in the Ge NW core) and}$$

$$E_y = B e^{-(\eta y + \frac{d}{2})} \text{ (in the } GeO_2 \text{ cladding).}$$

The continuity equation at the interface of the core and cladding gives us the wave guiding condition, solving which, we can determine η and in turn, the value of E_z. We have taken 3×10^4 photons falling on unit area of the NW per unit time, to find the value of the constants A and B.

From Figure C2, we can see that the amplitude of electric field is always greater in the core than the cladding. The electric field in the nanowire increases drastically as diameter reduces below 60 nm. In the 30nm wire the enhancement of the field is around 1.5 times than that in the 65 nm wire.

Figure C2. Amplitude of Electric field in the Ge NW core and the GeO$_2$ cladding layer

Reference

[1]K. Das, S. Mukherjee, S. Manna, S. K. Ray and A. K. Raychaudhuri,. *Nanoscale*, **6**, 11232-11239. 2014

APPENDIX D

Simulations to solve 1D heat equation in a nanowire by laser heating

We use finite element method to solve the heat diffusion equation in a single Ge NW suspended from a Si substrate at ambient conditions. The purpose of the simulation is three fold:

- Estimation of heat loss due to radiation.
- Determining temperature (T^*) at the cold end arising from thermal boundary resistance.
- Validation of point source approximation of the laser beam that allows use of equation 1 for determining thermal conductivity.

We have used a NW of diameter 110 nm with distance $L = 7\mu m$ from base of Si to centre of laser beam for our device geometry. We use thermal boundary resistance between Si/Ge equal to 5.89×10^{-9} Km^2/W.[1] The surface plot of the temperature of a NW is shown in Fig. D1. The side color legend gives temperature. Since the experiment was carried out under ambient atmospheric conditions, heat loss due to radiation and convection needs to be accounted for. We have used finite element method to determine the heat loss through convection and radiation processes.
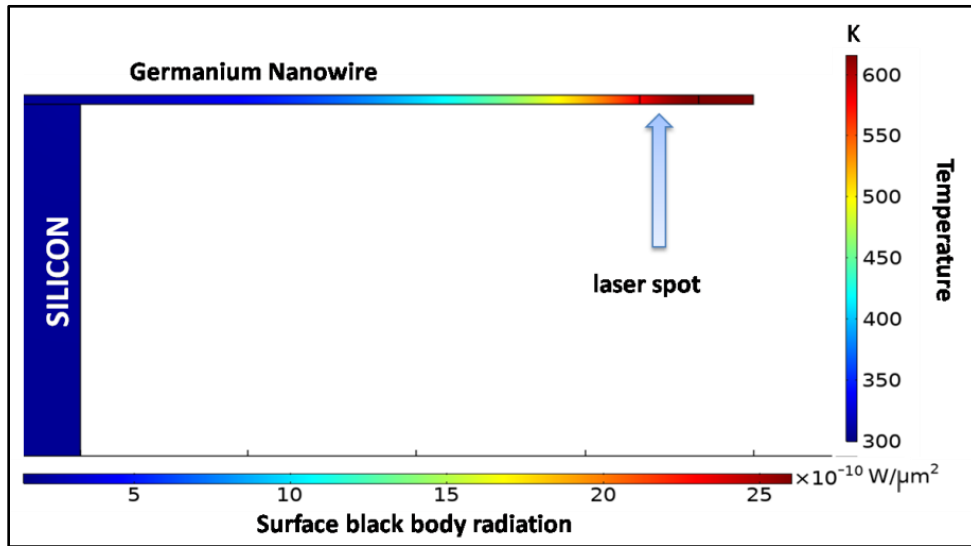

Figure D1. Surface plot of temperature and radiation intensity in a single cantilevered Ge NW.

We have also performed the same calculations using vacuum as the surrounding environment and there is no modifications in the temperature profile upto one decimal place. Thus, the thermal conductivity of NWs can be measured under ambient atmospheric conditions and corrections due to heat loss are

negligible. Nevertheless, the heat loss due to radiation since $T > 300K$ is accountable. The surface radiation intensity (bottom color legend) is shown in Fig. D1. The radiation heat loss in a NW at temperature ~ 600 K is ~3 nW which is ≤ 2 % of the total heat carried by the NW. In terms of a thermal resistance, it translates to 3 orders less than the thermal boundary resistance between Si and Ge interface.
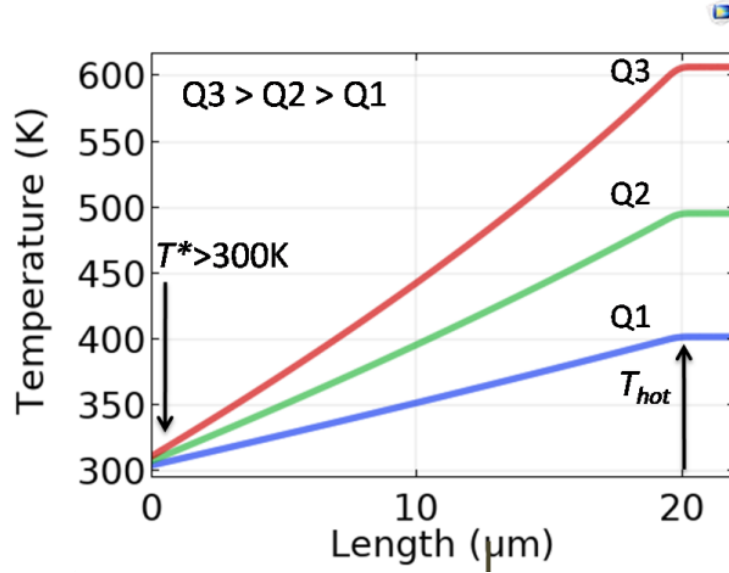

Figure D2. The temperature profile along the NW as a function of power.
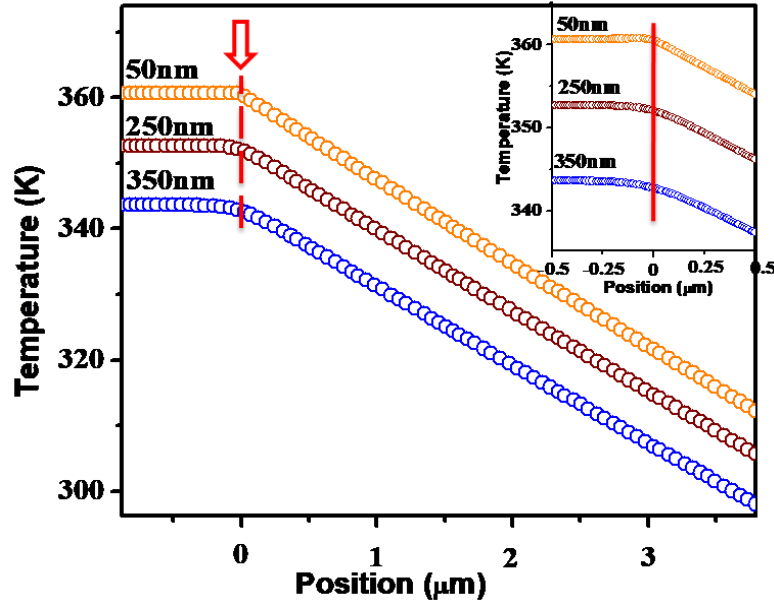

Figure D3. Temperature profile in a NW as laser half-width is varied from 50 – 350 nm with inset showing the region of 500nm from the centre of the laser beam. The curves have been shifted for clarity.

The temperature profile of the NW along its length is shown in Fig. D2 for different heat flux Q. There is a linear temperature gradient and the temperature at the base of the NW (x-axis position at 0) shows temperature of the NW > 300K. We use this temperature T^* as a correction term and calculate $\Delta T'$. Figure S3 shows the temperature gradient in a NW for different spot sizes. We have taken three values of σ = 50, 250 and 350 nm, and the temperature profile shows that the gradient remains similar if we take integrated power falling on the NW to be constant at all times. The error in temperature is < 1K for our experimental condition of assuming a point contact for σ = 350 nm.

Reference

[1]K. R. Hahn, M. Puligheddu and L. Colombo, *Phys. Rev. B.,* **91**, 195313, 2015

APPENDIX E

Temperature dependent Raman Spectroscopy in pristine and core-shell Germanium Nanowires

Essentially, an investigation of the thermal transport properties, thermal expansion and electron-phonon interaction has great impact on the thermoelectric performance, which are lacking in case of Ge NWs. In that light, the electron-phonon interactions are of immense importance as a stepping stone to understanding the lattice dynamics. The important thermodynamic parameters and physical properties can be studied experimentally due to anharmonicity in crystals. The thermal expansion in a solid gives insight into the anharmonicity in the vibrational potential energy. The mode Gruniesen parameter relates the vibrational frequency modes to specific heat and thermal expansion coefficient. A non-invasive way to probe nanomaterials for extracting out lattice related properties can be performed through Raman Spectroscopy.

In this work, we study temperature dependence of Raman active Ge modes from which we determine the anharmonicity coefficients, optical phonon dynamics, vibrational modes and lattice expansion in ensemble of pure (with native oxide layer) as well as core-shell Ge-GeO$_x$ NWs of diameters varying between 30-120nm.

1. Structural characterization

Depending on the use of H$_2$ as the carrier gas, as discussed in Chapter II, we have synthesized two types of NWs- one with presence of a thick Ge oxide layer (5-10nm) as the core-shell type structure indicated as *cs-Ge* NWs and the other with a thin native Ge oxide layer (1-2nm) designated as *na-Ge* NW. The room temperature Raman spectra of an ensemble of NWs (shown in Chapter II) clearly shows two different types of NWs – one only a pure Ge peak with Raman Shift at 300.2±0.5[1] while the other one has GeO$_2$ peaks at 123.3±0.2, 167.0±0.3, 262.4±0.6 and 444.4±0.4 cm^{-1}.[2] XPS depth profiling study was carried out on the *cs-Ge* NWs and *na-Ge* NWs in order to have a complete knowledge about the depth dependent overall oxide concentration profile. High resolution spectra of Ge 3d photoelectron lines recorded for both NWs are shown in Figure E1. The de-convoluted Ge 3d photoelectron spectra (lines assumed to be Gaussian) in the *na-Ge* can be resolved into four Gaussian components. Resolved photoelectron peaks at ~29.5eV and ~30.0eV correspond to Ge 3d$_{5/2}$ and Ge 3d$_{3/2}$ spin orbit doublets due to Ge^o chemical state.[3] The peaks of Ge 3d at higher binding energy (BE) of 31.1 eV and 33.3eV correspond to a higher oxidation state of Ge i.e., Ge^{2+} and Ge^{4+}.[3] In the *cs-Ge* NWs, there is only Ge^{4+}

peak at 32.7eV. Since XPS gives information from upto few nm from the sample surface (1-3nm), we get Ge elemental peak in the *na-Ge* NWs, which shows that the native oxide layer upto ~few (1-3nm) nm in thickness, while the *cs-Ge* NWs do not show any elemental Ge content. There is a slight shift to a lower BE in the *cs-Ge* NWs corresponding to a greater upward band bending effect in them.
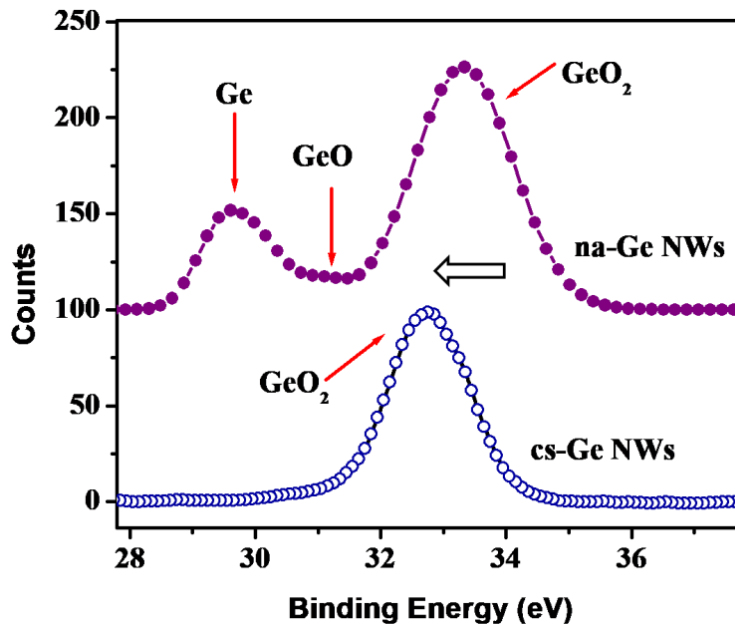

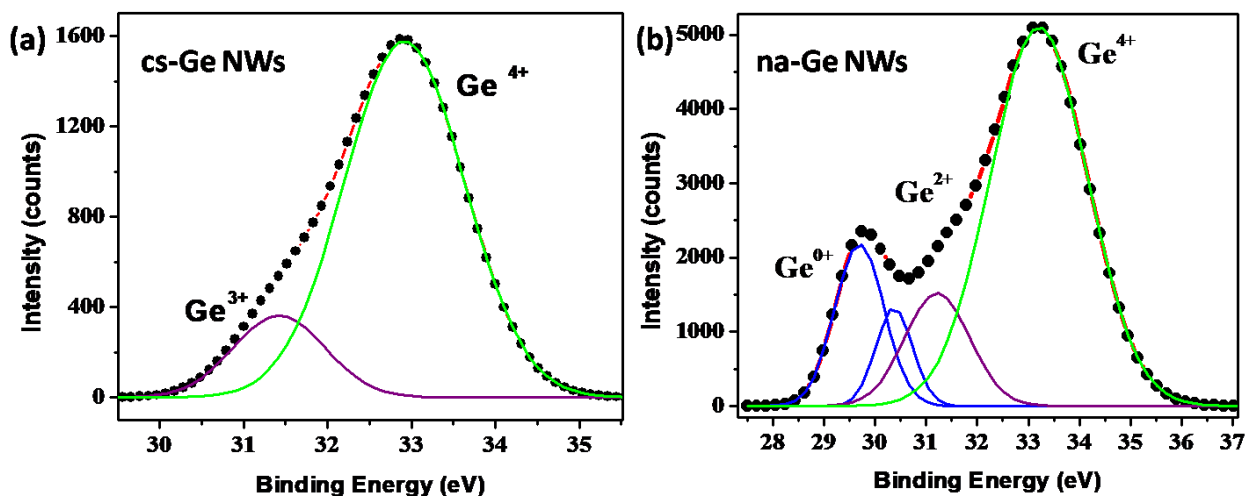**Figure E1.** XPS spectrum of the *cs-Ge* NWs and *na-Ge* NWs.

Figure E2. XPS profile of (a) *cs-Ge* NW and (b) *na-Ge* NWs after 60s of sputtering along with the fitted peaks showing the different valence states of Ge.

As the oxide layer is very crucial for our study, we have performed XPS depth profiling study in order to have a complete knowledge about the depth dependent overall concentration profile of the two types of Ge NWs. The etch rate of Ge ~ 1nm/min for Ar ion milling. As we go into the oxide layer by Ar ion milling, the XPS patterns become wide with an asymmetry towards lower Binding Energy side which suggests the existence of multiple valence states of Ge across the thickness of the NWs (Spectra for both NWs after 60s of ion milling is shown in Figure E2).
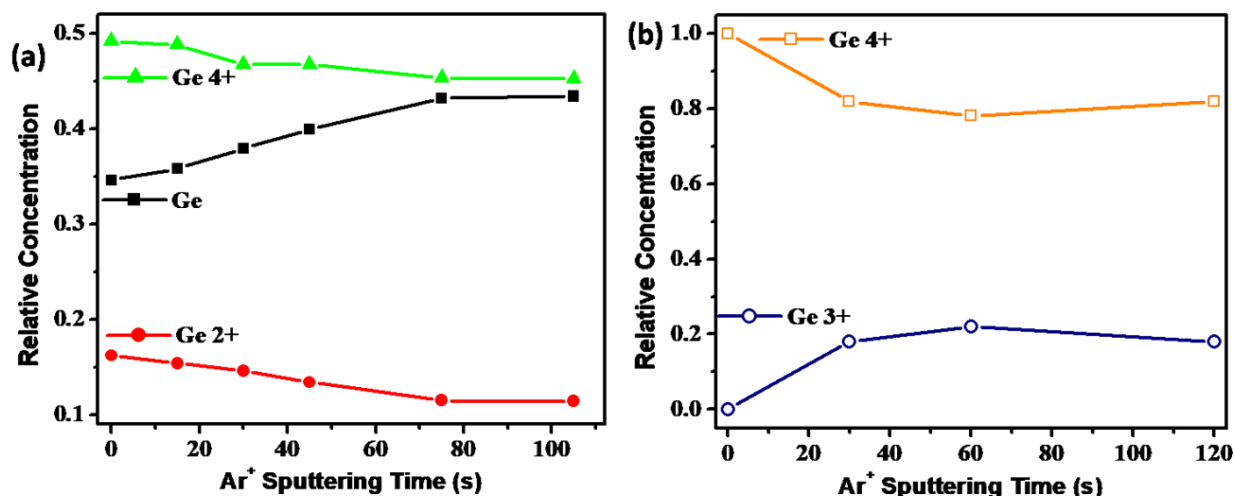

Figure E3. Relative concentration of Ge chemical states plotted as function of Ar ion milling time in (a) *na-Ge* NWs and (b) *cs-Ge* NWs.

The depth dependent relative concentration of Ge and O states in the NWs is depicted in Figure E3 (a) and (b) for *na-Ge* and *cs-Ge* NWs. In *na-Ge* NW, the surface is more enriched with oxygen than the interior of the NWs and as we move from surface to the interior Ge^{0+} concentration increases. In the *cs-Ge* NWs, even after milling for 2 mins (corresponding to ~2nm etch) there is no sign of Ge in its elemental state, though there is presence of Ge^{3+}, showing an oxygen deficient native oxide layer. The relative concentration plot is not an artifact or result of the ion milling process because if it were so, then the concentration profiles would be an increasing function of sputtering time. In the contrary, from Figure 6 we observe the concentration of all the chemical states of Ge stabilizes.

2. Temperature dependent Raman Spectroscopy

In Figure E4, we plot the temperature dependent Raman Spectrum of an ensemble of *na-Ge* NWs and as-Ge NWs for a wide range of temperature, from 83K to 823K, at intervals of 50K. The intensity of the Stokes line increases as we decrease temperature. The two other features are: gradual increase in peak

position (ω) and decrease of linewidth (Γ) with lowering of temperature. A typical Raman peak fit is shown at 300K for the *na-Ge* NWs in Figure E5 (a). The data has been fit using a Lorentzian function with width Γ. In the *na-Ge* NWs, below 183K, the degeneracy of Longitudinal Optical (LO)/Transverse Optical (TO) is lifted and the Raman peak broadens with a slight asymmetry. The intensity of both peaks increases as we go to lower temperature and it can be clearly distinguished at 83K (see Fig. E5(b)), where a clear shoulder is seen ~308cm^{-1}. This feature is not visible for Ge-cs NWs.

The ω and Γ have been extracted from the Raman spectrum and plotted as a function of temperature in Figure E6. There is softening of the phonon modes as we go to $T < 120K$. Due to anharmonicity in vibrational potential energy, a rise in temperature leads to an increase in the average amplitude of atomic vibrations. This corresponds to the increase in the average value of inter-atomic separation that arises only if the potential has cubic or higher order terms. This is also the cause of thermal expansion in a lattice as temperature increases. The decay of the optical phonon to two or more acoustic phonons is due to anharmonicity which causes variation in ω and Γ with temperature. Their relation is given by the modified Balkanski formula,[4]

$$\omega(T) = \omega_o + A\left(1 + \frac{2}{e^x - 1}\right) + B(1 + \frac{3}{e^y - 1} + \frac{3}{(e^y - 1)^2}) \tag{1}$$

$$\Gamma(T) = \Gamma1 + C\left(1 + \frac{2}{e^x - 1}\right) + D(1 + \frac{3}{e^y - 1} + \frac{3}{(e^y - 1)^2}) \tag{2}$$

where, $x = \frac{h\omega_o}{2*2\pi KT}$ and $y = \frac{h\omega_o}{3*2\pi KT}$, ω_o is the peak position at 0K, A, B, C and D are coefficients of anharmonicity. A and C correspond to the three phonon decay process and B and D corresponds to the four phonon decay process. The fitted curves to the above equation are given in Fig. E6. The parameter $\Gamma1$ is additional linewidth broadening due to diameter distribution, phonon confinement, disorder, stress etc. C and D are related to the recombination rate of the acoustic phonons generated from the optical phonon decay and its lifetime is given by $\tau, = h/2\pi C$.[5] Since we are dealing with NWs, it is important to note that there is already a broadening as well as red-shift in the room temperature Raman spectrum. This is due to relaxation of $q = 0$ selection rule as other wave vectors also participate that causes downshift and asymmetry in the Raman spectrum caused by a varying Electric field inside the NW (diameter < 100nm). The natural linewidth comes from the finite lifetime of a state. The broadening of linewidth also comes from disorder, inhomogenity and anharmonicity. The fits of the peak position and linewidth are given in Table 1 for *cs-Ge* and *na-Ge* NW. We first fit the equation for peak position and using the best fit value of ω_o, the equation for linewidth is fitted. The ratio of B/A or C/D should be < 1, which implies that the probability of two phonon decay is higher than the three phonon one.
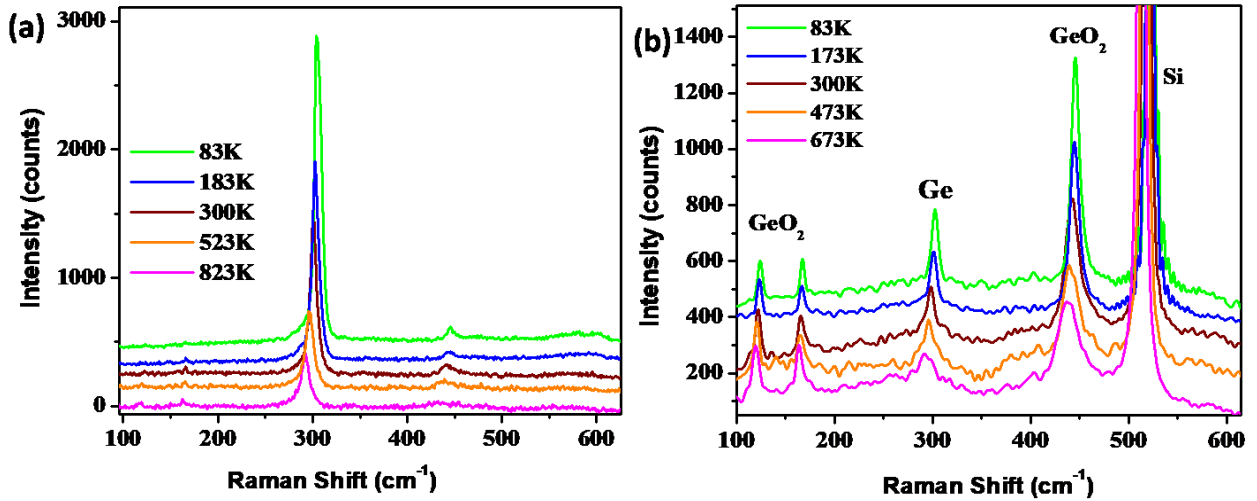
Figure E4. Temperature dependent Raman Spectrum of (a) *na-Ge* NWs and (b) *cs-Ge* NWs for a wide range of temperature, with only five data points shown here for better visualization.
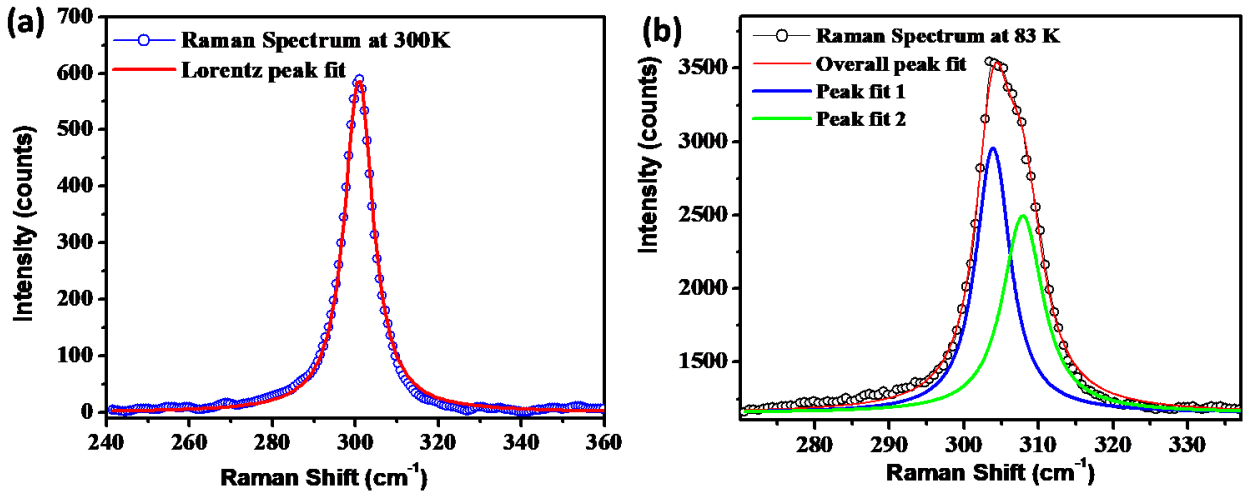

Figure E5. Raman peak fit at (a) 300K and at (b) 83 K showing the splitting of the LO/TO mode in *na-Ge* NWs.

The *na-Ge* NWs fit well with the assumption of the optical phonon decaying into two acoustic ones of half its frequency, with mean lifetime (τ)~ 1.2ps. The anharmonicity is enhanced in the *cs-Ge* NWs, since for the best fit, three phonon as well as four phonon coupling is necessary. The onset of anharmonicity effects shows up a much higher temperature in the Ge-cs NWs. The ω and Γ versus temperature plot is no longer linear below 300K. Also, the linewidth broadening is higher in the *cs-Ge* NW due to both anharmonic terms in the vibrational potential energy as well as from stress that could be developed in the NW due to surrounding oxide layer.
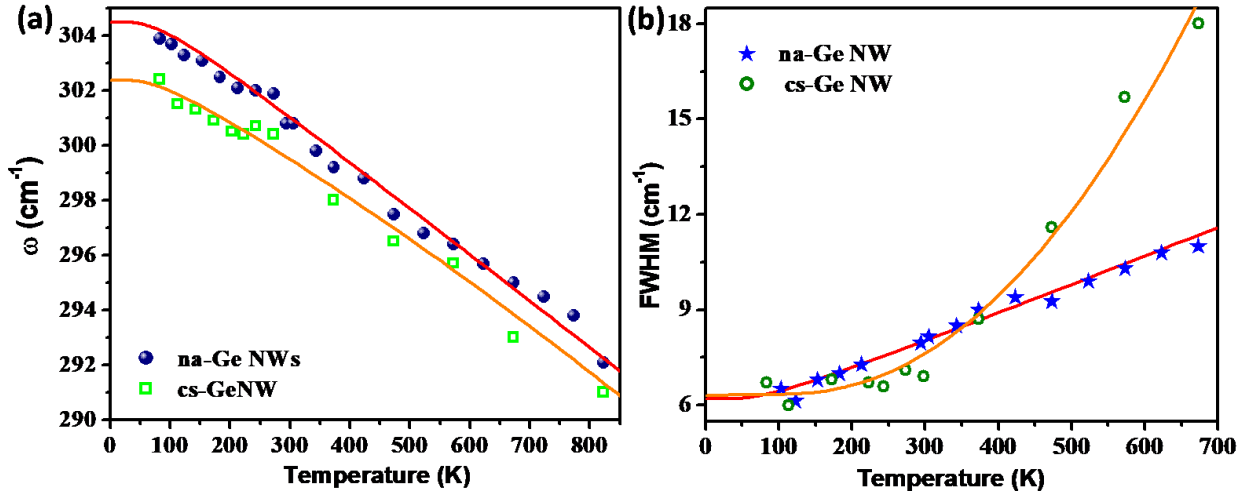
Figure E6. (a) Peak position as a function of temperature for both types of Ge NWs and fits given in bold lines. (b) FWHM as a function of temperature for both types of Ge NWs and fits given in bold lines.

Table 1. Fit parameters to temperature dependence of linewidth and peak position

Sample	ω_o (cm^{-1})	A (cm^{-1})	B (cm^{-1})	C (cm^{-1})	D (cm^{-1})	Γ_1 (cm^{-1})	B/A	D/C
cs-Ge NW	303.8	-1.44	-0.019	-1.3	0.302	7.31	0.013	0.23
na-Ge NW	306.4	-1.88	-	1.0064	-	5.164	0	0

The expression for lattice expansion in a solid is solely due to presence anharmonic terms in the vibrational potential energy which causes a shift in the frequency of normal vibrational phonon modes. The mode Gruneisen parameter γ_i for the ith mode with phonon frequency ω_i is given by,[6]

$$\gamma_i = -\frac{dln\,\omega_i}{dlnV} \tag{3}$$

where V is the volume of the crystal. If ω_i is purely a function of V, then the mode Gruniesen parameter can be expressed in the form of thermal expansion coefficient α as,

$$\gamma_i = -\frac{1}{3\alpha\omega_i}\left(\frac{\partial\omega_i}{\partial T}\right)_P \tag{4}$$

We can convert the experimental data for frequency shift as a function of temperature to determine the product of thermal expansion coefficient and mode Gruniesen parameter. Figure E7 shows the product of these two important quantities. In case γ_i can be determined experimentally, the thermal expansion coefficient can be easily extracted from the above plot.

The product of $\alpha\gamma$ allow us to calculate a very important physical parameter, the mean free path of phonons (λ_{mfp}) given by,[7]

$$\lambda_{mfp} \sim \frac{a}{3\alpha\gamma T}, \quad (T > \theta_D) \tag{5}$$

for an isotropic material (see Fig. E5 b). For T~ 300K, λ_{mfp} = 12nm which gradually decreases to 4nm at ~800K. The λ_{mfp} follows a $1/T$ behavior beyond 200K, where Umklapp scattering dominates and reduces the mean free path.
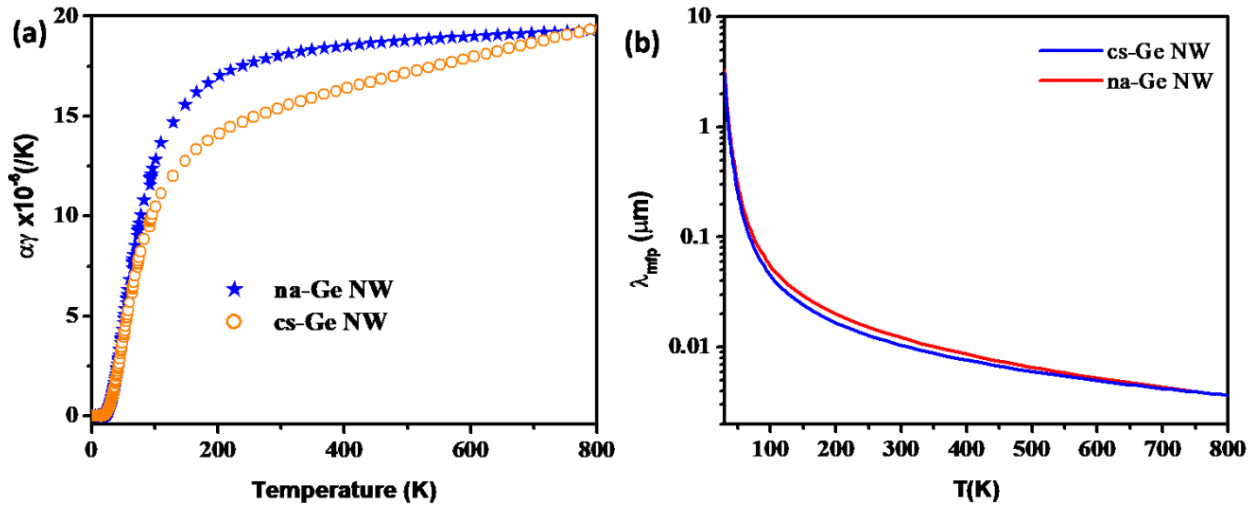

Figure E7. (a) Product of $\alpha\gamma$ and (b) λ_{mfp} as a function of temperature

In summary, we show the temperature dependent Raman Spectroscopy is an important and useful tool to study the thermodynamic properties of Ge NWs. The softening of phonon modes was observed in Ge NWs with increasing temperature, due to anharmonicity. We have determined the anharmonicity coefficients and phonon lifetimes of Ge NWs as well as provide a temperature versus peak position calibration that can serve as a local temperature sensor. We have been experimentally able to determine the product of two important parameters $\gamma_i \alpha$ from which, useful information like mean free path of phonons may be extracted out to study the thermal properties of Ge NWs.

References

[1] J. H. Parker, Jr., D. W. Feldman, and M. Ashkin, *Phys. Rev*. **155**, 712, 1967.

[2] P. Gillet and Andre Le Cleach*, J. Geophys. Res,* **95**, 21,635-21,655, 1990.

[3] D. Wang, Y. Chang, Q. Wang, J. Cao, D. B. Farmer, R. G. Gordon and H. Dai, *J. Am. Chem. Soc.*, **126**, 11602-11611, 2004

[4] M. Balkanski, R. F. Wallis, and E. Haro, *Phys. Rev. B.,* **28**, 1928, 1983.

[5]T. R. Hart, R. L. Aggarwal, and B. Lax, *Phys. Rev. B***1**, 638, 1970

[6]J. F. Vetelino, K. V. Namjoshi, and S. S. Mitra, *J. Appl. Phys.***41**, 5141, 1970

[7]J. M Ziman, "*Electrons and Phonons",* (Clarendon Press, Oxford, UK)